Development of efficient photoelectrodes for photoelectrochemical water splitting and hydrogen generation

（光電気化学的水分解および水素生成に向けた高効率光電極の開発）

July, 2024

Doctor of Philosophy (Engineering)

Marwa Mohamed Mohamed Abouelela

マルワ　モハメド　モハメド　アボウエレラ

Toyohashi University of Technology

別紙４－１（課程博士（英文））

Date of Submission（month day, year）: July 8th, 2024

Department of Electrical and Electronic Information Engineering	Student ID Number	D209202
Applicant's name	Marwa Mohamed Mohamed Abouelela	

Supervisors	Atsunori Matsuda Go Kawamura Tan Wai Kian

Abstract（Doctor）

Title of Thesis	Development of efficient photoelectrodes for photoelectrochemical water splitting and hydrogen generation

Approx. 800 words

Photoelectrochemical water splitting (PEC-WS) technique that uses solar energy and photoelectrodes immersed in an electrolyte has sparked an increased interest to generate chemical energy, such as H_2 in one step. The important requirements to achieve an efficient PEC-WS system are (1) absorbing a wide wavelength range of solar energy; (2) excellent e^-/h^+ pairs separation and mobility; (3) low overpotential for H_2 and O_2 evolution reaction; (4) high stability; (5) scalable techniques and (6) low-cost materials. The main objective of this thesis is to present simple methods for designing efficient and stable photoanodes for PEC-WS that generate large amount of H_2. Our approach focuses on improving the optical and electrical properties of some metal oxides by the deposition of appropriate quantity of metal chalcogenides (MCs) and plasmonic metal nanoparticles (NPs). The distinctive electrical and optical characteristics of MCs have made them promising choice for light absorbers. The decoration of metal oxide semiconductors with plasmonic metal NPs has also been reported as an auspicious approach for promoting the PEC performance by the transfer of plasmonic energy from the plasmonic metal NPs to the metal oxide semiconductor.

This thesis consists of four studies for designing and investigating photoanodes for PEC-WS; (1) Anodized nanoporous (ANPor) WO_3 was decorated with Bi_2S_3 quantum dots (QDs) and investigated as a photoanode for PEC-WS under ultraviolet-visible (UV-Vis) illumination. The ANPor WO_3 photoanode decorated with ten cycles of Bi_2S_3 QDs exhibited the highest current density of 16.28 mA cm^{-2} at 0.95 V vs. reversible hydrogen electrode (RHE), which is ~ 19 times than pure ANPor WO_3 (0.85 mA cm^{-2}). Furthermore, ANPor WO_3/Bi_2S_3 QDs (10) photoanode demonstrated the highest ABPE of 4.1% at 0.66 V vs. RHE, while pure ANPor WO_3 displayed 0.3% at 0.85 V vs. RHE. This was ascribed to the proper deposited quantity of Bi_2S_3 QDs which remarkably enhanced the Vis light absorption, and the formation of type-II band alignment between WO_3 and Bi_2S_3 QDs which improved e^-/h^+ pairs separation and migration.

(2) The unique morphology of ZnO nanopagoda arrays (NPGs) was prepared using aqueous downward growth technique, followed by deposition of various quantities of Ag NPs.

The deposition of an optimal quantity of Ag NPs over ZnO NPGs demonstrated the highest photocurrent of 2.15 mA cm^{-2} at 1.23 V vs RHE, meanwhile pure ZnO NRs and NPGs attained 0.90 and 1.43 mA cm^{-2}, respectively. This remarkable increase in photocurrent density was extensively analyzed using various PEC and optical determinations as well as electromagnetic simulation. As a result, this improved PEC performance was ascribed to two reasons; firstly, ZnO NPGs can mitigate the charge recombination rate owing to the reduced structural defects and enhance the light absorption ability owing to their distinct superstructure properties. Secondly, the deposition of plasmonic Ag NPs can improve the interfacial charge transfer and raise the ability to absorp Vis light due to their LSPR effect.

(3) ZnO NPGs was modified with Ag and Ag_2S NPs and investigated as a photoanode for the PEC system. The crystal structure, morphology, elemental composition, optical characteristics, and PEC performance of the prepared samples were studied. The results revealed that, the successful deposition of Ag and Ag_2S NPs on the surface of ZnO NPGs not only improved the Vis light absorption but also ameliorated the e^-/h^+ pairs separation and transfer. The optimum amount of Ag-Ag_2S NPs on ZnO NPGs attained the maximum photocurrent of 2.91 mA cm^{-2} at 1.23 V vs. RHE, about five times than pure ZnO NPGs. It also exhibited the improved ABPE of 0.43% at 0.6 V vs. RHE. This study presented a facile preparation process of a unique ZnO NPGs and enhanced PEC performance through the synergistic effect of the LSPR of Ag NPs and Vis light sensitization of Ag_2S NPs.

(4) An effective type II heterojunction between Bi_2Se_3 QDs and TiO_2 nanotube arrays (TNTAs) was formed by depositing Bi_2Se_3 QDs on the surface of TNTAs. The TNTAs/Bi_2Se_3 QDs photoanode displayed the highest photocurrent density of 1.75 mA cm^{-2}, which is 3.8 times higher than pure TNTAs (0.46 mA cm^{-2}) at 1.23 V vs. RHE. They also achieved a high H_2 generation amount of 355.8 μmol after 5 hours, which is 3.3 times higher than pure TNTAs (105.3 μmol) at 1.23 V vs. RHE. TNTAs and TNTAs/Bi_2Se_3 QDs photoanodes both demonstrated superb stability for over 7 hours. The TNTAs/Bi_2Se_3 QDs photoanode demonstrated higher IPCE in the UV region than pure TNTAs and extended the light response to the Vis region owing to its lower charge recombination rate and the Vis light absorption ability derived from Bi_2Se_3 QDs. The superb PEC performance of TNTAs/Bi_2Se_3 QDs photoanode was also owing to its suitable bandgap energy, which improved the Vis light absorption, and its efficient charge transfer, that alleviated the e^-/h^+ pairs recombination. Consequently, this thesis paves the way for facile approaches to construct efficient photoanodes for PEC-WS and H_2 generation.

Table of Contents

List of Figures and Schemes

List of Tables

List of abbreviations

PEC-WS	Photoelectrochemical water splitting
CB	Conduction band
VB	Valence band
PC	Photocatalytic
e^-/h^+	Electron/hole
NPs	Nanoparticles
LSPR	Localized surface plasmon resonance
1D	One-dimensional
OER	Oxygen evolution reaction
HER	Hydrogen evolution reaction
E_{RHE}	Potential versus reversible hydrogen electrode
E_{NHE}	Potential versus normal hydrogen electrode.
NHE	Normal hydrogen electrode
STH	Solar-to-hydrogen conversion
SPR	Surface plasmon resonance
HEI	Hot electron injection
PIRET	Plasmon induced resonance energy transfer
UV	Ultra-violet
NIR	Near-infrared
3D	Three-dimensional
NTAs	Nanotube arrays
NRs	Nanorods
MCs	Metal chalcogenides
WBSs	Wide bandgap semiconductors
QDs	Quantum dots
NCs	Nanocrystals
PL	Photoluminescence
Vis	Visible
NPor	Nanoporous
ANPor	Anodic nanoporous
SILAR	Successive ionic layer adsorption and reaction
NPGs	Nanopagoda arrays

ABPE	Applied bias photon-to-current efficiency
XRD	X-ray diffractometer
XPS	X-ray photoelectron spectroscopy
SEM	Scanning electron microscope
EDX	Energy-dispersive X-ray spectroscopy
TEM	Transmission electron microscope
HRTEM	High-resolution TEM
DRS	Diffuse reflectance spectroscopy
LSV	Linear sweep voltammetry
EIS	Electrochemical impedance spectroscopy
M-S	Mott−Schottky
Vs. RHE	Versus the reversible hydrogen electrode
R_{ct}	Interfacial charge transfer resistances
E_{fb}	Flat band potentials
1D	One-dimensional
2D	Two-dimensional
FTO	Fluorine-doped tin oxide
STEM-EDX	Scanning TEM-EDX
FDTD	Finite-difference time-domain
IPCE	Incident photon-to-current efficiency
NPs	Nanoparticles
NRs	Nanorods
TNTAs	TiO_2 nanotube arrays
DI	Deionized

Chapter 1. General Introduction

1.1. Overall introduction of photoelectrochemical water splitting technology

There is a noticeable depletion of nonrenewable energy sources, which are mainly composed of fossil fuels such as coal, gas, and oil, due to the increase in population and industrial fields [1]. Therefore, proactive incorporation of renewable energy sources is so vital to meet the world's energy needs. The most abundant renewable energy source is sunlight (~1.2 × 1014 kJ arrives at the Earth's surface per second) [2]. The transformation of sunlight into electricity, heat, or fuel is an important way of utilizing renewable energy [3]. Multiple pathways exist for converting sunlight into chemical energy, such as photocatalysis, photovoltaic devices, and photoelectrocatalysis [4–6]. Since the 1972 innovative study of Honda and Fujishima [7], photoelectrochemical water splitting (PEC-WS) using solar light for H_2 generation has been an attractive strategy to address the world's energy crisis. During the PEC-WS process, TiO_2 was used as a photoanode, and Pt was used as a cathode. When the surface of the TiO_2 was exposed to ultra-violet (UV) irradiation ($\lambda < 415$ nm), electrons and holes were generated. These generated electrons were transferred through an external circuit to the Pt cathode while the anodic potential was applied. H_2 and O_2 were produced at the cathode, and photoanode respectively. In the presence of enough photon energy, photogenerated electrons can be transported to the conduction band (CB), forming holes in the valence band (VB). These electrons can reduce the protons to form H_2 molecules, while holes can oxidize water to form O_2 molecules. Since this pioneering study, many investigations of the WS procedure utilizing semiconductors have been published.

The rising consumption of hydrogen and its application in the transportation fuel sector is driving up the demand for hydrogen as fuel on a global scale. The technologies used in the manufacturing, storage, and transportation of hydrogen must be improved to meet the rising demand. Despite of the notable advancements in hydrogen storage and delivery, the utilization of hydrogen energy is impeded by the absence of viable and affordable production methods [8]. Hydrogen can be generated utilizing many techniques classified into two groups depending on the raw materials used. The first category involves strategies that use fossil fuels, such as hydrocarbon reforming and hydrocarbon pyrolysis. The second category involves the technologies that utilize renewable sources such as biomass and water [9,10]. Sustainable hydrogen production from the WS strategy has garnered a lot of interest due to its high energy density and ability to be used without carbon emission [11,12]. The PEC-WS cell can transform

water (H_2O) and sunlight directly to H_2, and O_2. The generated H_2 from the PEC-WS process can mitigate the global warming issue by decreasing reliance on fossil fuels [13–18]. Oxygen is a vital treatment for patients in all healthcare systems [19]. The COVID-19 epidemic has recently resulted in a significant increase in the world's oxygen demand. The reasons behind the low solar conversion efficiency are as follows: (1) restricted light absorption of semiconductors; (2) ineffective usage of photogenerated charge carriers leading to rapid charge recombination; and (3) inadequate surface redox reactions [20]. To solve these issues, scientists have studied various semiconductor materials and developed cutting-edge solutions to these issues.

1.2. Fundamentals of photoelectrochemical water splitting

PEC solar fuel generation offers a straightforward route for renewable solar energy conversion to chemical energy compared with traditional photovoltaic techniques [21,22]. This is attributed to the simplicity of the PEC cell, which consists of at least two electrodes (anode and cathode) and a membrane for product separation. At least, one of the electrodes should be a semiconductor which able to absorb photon energy that is larger than its bandgap. The photopotential generated by electron/hole (e^-/h^+) pairs separation can undergo electrochemical solar to fuel generation [21]. Additionally, a PEC cell can be designed in a tandem configuration that involves n-type photoanode and p-type photocathode semiconductors to enhance the light absorption capability and the system's photopotential [23]. Moreover, the PEC-WS technology presents some more advantages than photocatalytic (PC)-WS (PC-WS), such as (1) the self or external bias can alleviate e^-/h^+ pairs recombination which can enhance the charge separation and transport; (2) H_2 and O_2 can be easily separated by accumulating at two distinct electrodes; (3) the application of semiconductor thin films on a variety of conductive substrates that makes it suitable for future industrial use; and (4) it does not need to be stirred; therefore, it uses less power compared to PC-WS technique which uses powder materials and often requires stirring [24]. In 1972, Fujishima and Honda discovered the PEC-WS, which used TiO_2 and Pt as a photoanode and a cathode, respectively, submerged in an electrolyte. TiO_2 photoanode absorbed photon's energy and formed enough potential to split H_2O into H_2 and O_2 [7]. Numerous researchers have explained the fundamentals of the PEC-WS technique [25–28], as well as various semiconductor-based photoelectrodes like metal oxides [29–33], and metal chalcogenides [34–38], have been studied. However, the PEC-WS technique is still challenging as the electrodes are in direct contact with the electrolyte. As a result, it's necessary to increase the electrodes' stability against corrosion [39]. The most important prerequisites for attaining a competitive PEC-WS system are (1) capturing a large

scale of solar energy; (2) superior e^-/h^+ pairs separation and transfer; (3) low overpotential for H_2 and O_2 evolution reaction; (4) achieving a high level of stability; (5) scalable techniques and (6) cost-effective materials [28,40]. Photocurrent-voltage determination is substantial for evaluating the performance of the PEC-WS process of various photoelectrodes [40]. Despite metal oxide semiconductors ($BiVO_4$, TiO_2, and Fe_2O_3) being affordable and can demonstrate good stability for electrochemical processes [41–47], they manifest low efficiency for H_2 generation under sunlight irradiation due to their poor light absorption and restricted charge transfer mobility. Therefore, numerous strategies have been reported to overcome these issues and improve their PEC performance, for instance, (i) controlling morphology and size of studied materials, (ii) loading of cocatalysts, (iii) doping with metals and non-metals, (iv) heterojunction using semiconductors with narrow bandgap materials [48,49].

1.2.1. Fundamental processes of photoelectrochemical water splitting

PEC-WS is a laborious process with multiple steps that need to be controlled to maximize the effectiveness of the apparatus. This section discusses the three basic PEC-WS processes as depicted in **Figure 1-1a**,**b**; (1) light absorption and charge carriers photogeneration, (2) charge separation and transfer, and (3) WS redox reactions.

1.2.1.1. Light absorption and charge carriers photogeneration

The semiconductor's electronic structure interacts with the electromagnetic wave when light enters the semiconductor. As a result of this interaction, some electrons are excited from the VB to the CB generating holes in the VB [26]. The difference in the energy between the CB and the VB of the semiconductor is defined as the bandgap energy. When photon energy surpasses a semiconductor's bandgap energy, the excited electrons transmit the extra energy to nearby atoms via thermal vibration, to be stabilized in CB [28]. A variety of metal oxide semiconductors have been examined as photoelectrodes because of their good chemical resistance. However, their light absorption is restricted to the UV field due to their broad bandgap energy. As a result, low PEC-WS efficiency has been demonstrated in under sunlight [50]. To overcome this issue, some research studies have concentrated on employing narrow bandgap semiconductors [51–53]. The heterojunction between narrow bandgap and wide bandgap semiconductors has demonstrated a noteworthy enhancement for both counterparts in terms of mitigating the drawbacks of individual semiconductors inside a composite and augmenting PEC-WS efficiency [54]. **Figure 1-1c** shows the bandgap energy and band edge position of some interesting metal oxides, nitrides, and chalcogenides concerning the redox potentials of H_2O. Another strategy to extend the light absorption of the material is the deposition of plasmonic metal nanoparticles (NPs) which demonstrate localized surface

plasmon resonance (LSPR) [55–57]. The LSPR effect is the oscillation of surface electrons in the plasmonic metal NPs with irradiated light. The LSPR effect can boost the PEC-WS performance through; (1) enhancement of localized electric field, (2) improvement of light absorption, and (3) tranfer of hot electrons [58]. Numerous research investigations have studied the application of plasmonic metal NPs in the PEC-WS, where the type, shape, and size, of the metal, regulated the amount of light absorption in the visible (Vis) spectrum [57,59–62].

1.2.1.2. Charge carriers separation and transfer

To effectively split H_2O and produce H_2 and O_2, the photogenerated e^-/h^+ pairs in the photoelectrode must be separated prior arriving to at the active sites to prevent their recombination. The recombination process happens when the excited electrons return to the holes in the VB after losing their energy [28]. The recombination process is the primary obstacle to the transfer of charge carriers to the active sites in the photoelectrode, as the high level of recombination makes it challenging to extract current from charge carriers [28,63,64]. The crystal structure, particle size, and crystallinity of the material affect the separation and transmission of photogenerated e^-/h^+ pairs. Materials that have high crystallinity and few defects show high PC activity as the defects work as trapping centers, speeding up the recombination rate of e^-/h^+ pairs. Nanomaterials have a short diffusion distance among charge carriers and active sites, lowering the possibility of recombination. As well as, they have a high surface-to-volume ratio, that enhances the interaction between e^-/h^+ pairs and active sites [63]. Moreover, the morphology of the deposited materials, defect structures, and the composition of the electrolyte affect the transmission of e^-/h^+ pairs [65–68]. For example, nanomaterials with one-dimensional (1D) structures like nanotubes can improve e^-/h^+ pairs transport through the linear transport route [66].

Applying an external potential or creating an internal built-in potential can enhance e^-/h^+ pairs separation and inhibit their recombination. Various approaches to generate internal potential include the heterojunction construction between different materials, doping of elements, and metal integration onto the semiconductor [69]. Some structures that can create built-in electric field are (1) p–n homojunction, where a semiconductor material has two different areas with different features (i.e., p-type and n-type silicon), (2) p–n heterojunction involves the combination between two different materials with different features (i.e., n-type WO_3 and p-type silicon), (3) Schottky junction, where a semiconductor material equilibrates with the free electrons energy level of the metal (i.e., nickel metal and n-type silicon), (4) semiconductor-liquid junction, where the semiconductor material equilibrates with the

adsorbed ions on the surface, forming a Helmholtz double layer (i.e., n-type WO_3 in a basic electrolyte) [28]. Heterojunction formation among two semiconductors can be considered an effective approach to promote e^-/h^+ pairs separation, and it can be classified depending on the energy band alignment into three sorts [70,71]; (1) Straddling-gap heterojunctions (type-I), where photogenerated electrons and holes are transferred from semiconductor A to semiconductor B (**Figure 1-2a**), leading to a high accumulation of e^-/h^+ pairs in semiconductor B and causing extreme charge recombination. (2) Staggered-gap heterojunctions (type-II), where photogenerated electrons in semiconductor B are transmitted to semiconductor A; while, the photogenerated holes on semiconductor A are transferred to semiconductor B, leading to effective e^-/h^+ pairs separation (**Figure 1-2b**), (3) Broken-gap heterojunctions (type-III), where there is no directional migration of photogenerated charge carriers between semiconductor A and semiconductor B (**Figure 1-2c**).

1.2.1.3. Water splitting redox reactions

The photogenerated e^-/h^+ pairs can be separated by the built-in electric field. When a photoanode is used, holes migrate to the photoelectrode's surface to perform the oxygen evolution reaction (OER), and electrons are collected through the back contact to reduce the protons at the counter electrode and generate H_2 as depicted in **Figure 1-1a**. Meanwhile, a photocathode is used, electrons transfer to the surface to undergo the hydrogen evolution reaction (HER) as shown in **Figure 1-1b** [28,72,73]. The reaction of WS is a non-spontaneous reaction and it can happen when an external potential is applied among two electrodes (anode and cathode) immersed in an electrolyte to carry out the OER and HER. The complete WS reaction needs the Gibbs free energy (ΔG) of 237.2 kJ/mol, which is related to a thermodynamic reversible potential of 1.23 V, which is a theoretical value at ionic concentration, gas pressure, and temperature of 1 molar, 1 atm, and 25 °C, respectively. The potential value changes with the pH of the electrolyte in accordance to the Nernst equation:

$$E_{RHE} = E_{NHE} + 0.059 \times pH, \qquad \text{(Eq.1-1)}$$

where E_{RHE} is the potential versus reversible hydrogen electrode, and E_{NHE} is the potential versus normal hydrogen electrode. The two half-reactions for the overall WS to generate H_2 and O_2 regarding to the pH of the electrolyte are illustrated as follows [28,74];

In acidic conditions

$$\text{OER: } 2H_2O - 4e^- \longrightarrow O_2 + 4H^+, \quad (E^0 = 1.23 \text{ V vs. NHE at pH = 0}), \qquad \text{(Eq.1-2)}$$

$$\text{HER: } 2H^+ + 2e^- \longrightarrow H_2, \quad (E^0 = 0.00 \text{ V vs. NHE at pH = 0}), \qquad \text{(Eq.1-3)}$$

In basic conditions

OER: $4OH^- - 4e^- \longrightarrow O_2 + 2H_2O$, ($E^0$ = 0.40 V vs. NHE at pH = 14), (Eq.1-4)

HER: $2H_2O + 2e^- \longrightarrow H_2 + 2OH^-$, ($E^0$ = −0.83 V vs. NHE at pH = 14). (Eq.1-5)

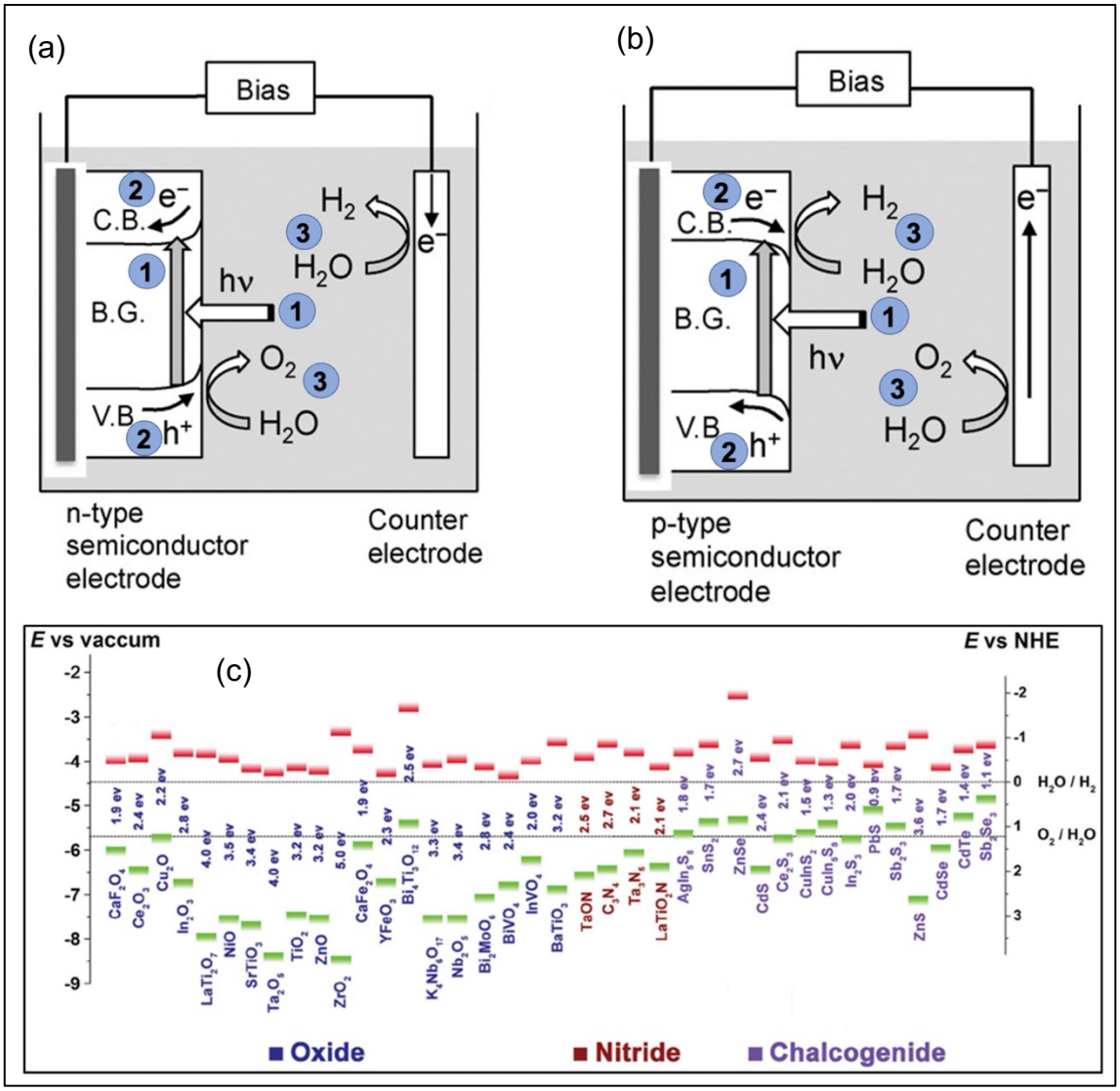

Figure 1-1. The major PEC-WS processes in a PEC cell consist of (a) n-type and (b) p-type semiconductor electrodes [72]. Copyright 2010, Elsevier; (c) band edge positions and bandgap energy of a variety of semiconductors corresponding to the vacuum and the normal hydrogen electrode (NHE). The green points indicate the VB, while the red points indicate the CB. Water redox potentials are represented by two dashed lines [75]. Copyright 2015, WILEY-VCH Verlag GmbH & Co. KGaA, Weinheim.

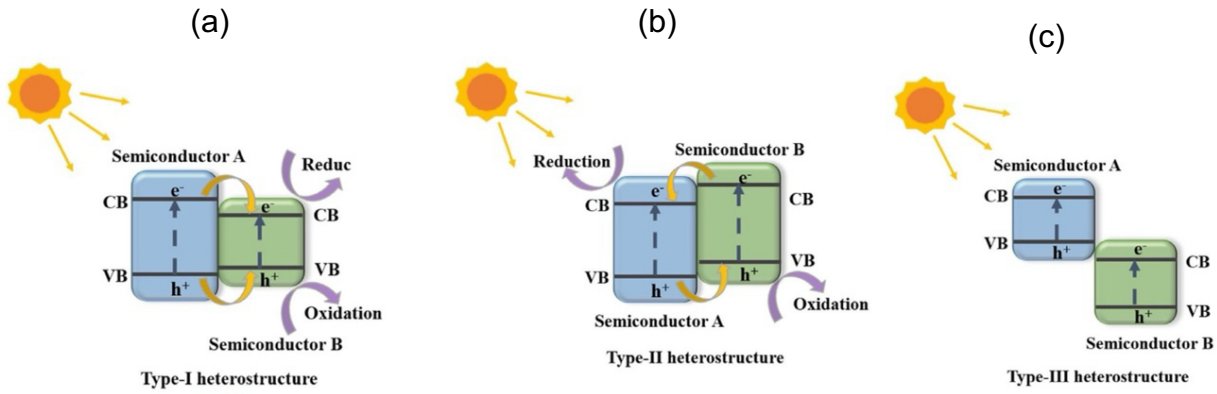

Figure 1-2. The band alignment diagram of the three sorts of heterojunctions; (a) type-I, (b) type-II, and (c) type-III heterojunction [70]. @Shengnan Li. et al. (Licensed under CC BY 4.0).

1.2.2. Substance requirements

The semiconductor substance is the most important component in all solar conversion systems. It is responsible for absorbing photon energy and producing excited electrons (e^-) and holes (h^+). These photogenerated e^-/h^+ pairs can move in opposing directions with the generation of photopotential, which promotes fuel production like H_2 [21]. The solar-to-hydrogen conversion (STH) efficiency of the PEC cell mostly depends on (1) light absorption, (2) photogeneration of e^-/h^+ pairs, and (3) separation and movement of e^-/h^+ pairs [73]. When selecting a semiconductor to serve as a photoelectrode, there are several considerations should be followed;

1.2.2.1.Potential requirement

Under standard conditions, the splitting of one molecule of H_2O to H_2 and ½ O_2 demands ΔG of 237.2 kJ/mol, which regards ΔE = 1.23 V per electron transported. The employed semiconductors should collect light radiation with photon energy larger than 1.23 eV and use it to split H_2O. This process generates four h^+ per O_2 molecule (4×1.23 = 4.92 eV) or two e^- per H_2 molecule (2×1.23 = 2.46 eV) [15]. The bandgap energy of the selected semiconductor should be 1.23 to 2.4 eV to be able to absorb Vis light, which makes up about half of the solar spectrum [26]. It's also important to take into account some energy losses, such as the overpotential loss at the photoelectrode and the ionic conductivity loss in the electrolyte. consequently, 1.6-2.0 V is the necessary potential for WS [76].

1.2.2.2. Structure of the band edge

The band edge position and charge carrier diffusion lengths are important factors during the selection of suitable material for the PEC-WS process. The CB should be more negative

than the H_2 production potential, meanwhile, the VB should be more positive than the O_2 potential potential [22,77].

1.2.2.3. Crystallinity and surface area

The crystallinity and surface active sites of semiconductors are very crucial for e^-/h^+ pairs transfer and OER/HER reactions [76]. substances with high crystallinity and low defects can inhibit the e^-/h^+ pairs recombination [78]. The OER/HER reaction rate should be higher than the backward reaction, which mostly relies on the number of active sites [26]. Shi et al. showed that annealing at 540 °C improved the crystallinity of $BiVO_4$ film, reduced e^-/h^+ pairs recombination, and boosted PEC-WS performance under light illumination [79]. Iqbal et al. [80] and Kim et al. [81] showed how increasing the prepared photoanode's crystallinity enhanced the PEC-WS performance.

1.2.2.4. Materials' cost and stability

Photoelectrodes must be constructed from easily accessible and reasonably priced components that can achieve long-term PEC-WS performance in the presence of produced gases [21]. It is favored to utilize electrodes made of materials that are widely available on Earth. In either basic or acidic electrolytes, the employed semiconductor photoelectrodes should exhibit stability. Sometimes, to prolong the photoelectrodes' lifetime, a coating layer that is capable of transmitting light is necessary [76]. Sun et al. illustrated that the homogenous coating of $BiVO_4$ photoanode with super hydrophilic CoFe-phytic acid complex significantly reduced the photocorrosion and acted as an efficient cocatalyst, that promotes the water oxidation kinetics [82]. The formed current density as a function of time under light illumination can be utilized to evaluate the stability of the photoelectrode; for instance, Au/CdSe nanodumbbell photoanode displayed a steady photocurrent density of 1.3 mA/cm^2 at 0.4 V vs. RHE for five days due to its remarkable structure stability [83].

1.3. Investigated category of materials

1.3.1. Plasmonic metal nanoparticles based photoelectrodes

Despite the great effort of many researchers who have focused on developing efficient PC and PEC systems, the resultant systems suffer from low efficiency, instability, and high manufacturing costs. Occasionally, metal oxide semiconductors demonstrate limited light absorption range (owing to their low absorption coefficients and wide bandgap energy), short charge carrier lifetimes and diffusion lengths, and sluggish catalytic surface reactions [21]. Hence, the challenges facing the WS technology are fast e^-/h^+ pairs recombination, wide bandgap energy of investigated semiconductors, and reverse reactions (i.e., H_2O formation

from H_2 and O_2) [84]. Numerous research studies have focused on improving the optical, electronic, and catalytic characteristics of semiconductors [85–87].

One of the attractive approaches is to decorate semiconductors with plasmonic metal NPs [88–90]. These metal NPs can enhance the capability of the light absorption of the semiconductor (i.e., raise its absorption coefficients) either by scattering or concentrating the incident light radiation into the semiconductor [89–91]. Also, plasmonic metal NPs able to absorb Vis light with a wavelength longer (lower energy) than the semiconductor's bandgap energy and transfer this plasmonic energy to the semiconductor in various forms like "hot electrons" (i.e., electrons that have energy larger than the metal's Fermi level) [92,93] via a dipole-dipole interaction [94], significantly broaden the absorption range of the semiconductor photoelectrode. Simultaneously, the plasmonic metal NPs can dramatically improve the electronic characteristics [95] and catalytic activity of semiconductors [96]. Various semiconductor- plasmonic metal NPs composites have been investigated for solar WS technology [59,86,94,97–100].

The intriguing properties of semiconductor-plasmonic metal NPs composites involve the generation of the LSPR and a near-electric field at the metal and semiconductor interface (Schottky junction) supporting the transfer of hot-electrons in either direction [101,102]. Plasmonic photocatalysts can absorb light with a broad range of wavelengths as the plasmonic metal NPs have several oscillating electrons on their surface in resonance with the incident light photons and can capture these photons efficiently [103]. This effect can be defined as LSPR effect [104]. Additionally, the plasmonic metal NPs promote the e^-/h^+ pairs separation and transfer and diminish their recombination [105]. When plasmonic metal NPs are incorporated with a semiconductor, the surface plasmons can cause both radiative and nonradiative decay. The surface plasmonic energy can be transported from the plasmonic metal NPs to the semiconductor and contribute to the WS operation. The transport of plasmonic energy happens by four mechanisms [57,91]; light trapping mechanisms (light scattering and light concentration), hot electron injection (HEI), and Plasmon induced resonance energy transfer (PIRET). Regarding the mechanism of light scattering, the plasmonic metal NPs cause radiative decay and generate photons that are scattered into the semiconductor. This process ameliorates the semiconductor's optical path length. Conversely, in the mechanism of light concentration, the plasmonic NPs serve as optical antennas that enclose the fallen electromagnetic field around the semiconductor, improving the photogeneration of e^-/h^+ pairs in the semiconductor. In the HEI mechanism, the hot electrons are produced by the nonradiative decay of the plasmonic NPs. The energy of these produced hot electrons is affected by the

crystallinity, surface area, shape, and particle size of the plasmonic metal NPs. In the PIRET mechanism, the near-field energy is nonradiatively transmitted to the semiconductor through dipole-dipole interaction with weak band-edge states. The effectiveness of light trapping and PIRET mechanisms mostly relies on the spectral overlap between the plasmonic metal NPs and the semiconductor; band energy alignment is not needed.

1.3.1.1. Characteristics of plasmonic metal NPs

plasmonic metal NPs strongly react with the incident photons which results in the LSPR effect. The intensity of the LSPR effect is based on the type, shape, and size, of the plasmonic metal NPs [106–109]. Controlling the shape and size of plasmonic metal NPs can remarkably influence the range of light absorption in the solar spectrum [110,111]. Under solar-light irradiation, e^- and h^+ are generated. The main obstacle at this stage is the fast e^-/h^+ pairs recombination [112,113]. Generally, charge recombination is often suppressed in substances with tiny particle sizes and low defects. Defects on the substance surface act as active sites to adsorb e^-/h^+ pairs and accelerate their recombination, as a result, diminishing PC and PEC activity. Photocatalysts with high crystallinity are preferred for WS reactions due to their few surface defects. Additionally, photocatalysts with a nanoscale particle size can decrease the diffusion distances for e^- and h^+ to arrive at the surface active sites, resulting in reducing the chance of e^-/h^+ pairs recombination and promoting the surface reactions owing to their large specific surface area [63,64].

1.3.1.1.1. Surface area

Substances that have a large surface area are beneficial for WS reactions because they may offer plenty of active sites. As the predominant reaction in water splitting is not the adsorption of reactant molecules, this characteristic would have less impact than other variables like particle size and crystallinity [114]. DeSario et al. reported that three-dimensional (3D) Au–TiO_2 aerogels photocatalyst significantly enhanced the PC-WS under Vis light owing to the preserved porous structure and specific surface area of pristine TiO_2 aerogel [115]. Substances with large surface areas can effectively absorb light and inwardly scatter it [116], ameliorating the light absorption capability [89,117–121].

1.3.1.1.2. Crystallinity

High crystalline substances manifest greater WS efficiency than amorphous or low crystalline substances. Highly crystalline TiO_2 nanotube arrays (TNTAs) showed higher photocurrent density compared to amorphous TNTAs [122]. Partially crystalline or amorphous substances facilitate the e^-/h^+ pairs recombination [123–125]. Hence, substances with high crystallinity are favored for WS reactions to suppress the recombination of e^-/h^+ pairs. Gong

et al. have observed that a multistep anodization strategy developed the crystallinity of TNTAs. TNTAs fabricated through three steps of electrochemical anodization demonstrated a higher photocurrent density, that was 2.2 times higher than that produced by TNTAs fabricated through one step electrochemical anodization. Moreover, it produced a higher quantity of H_2 with improved e^-/h^+ pairs transfer efficiency [126]. Therefore, the material's structural characteristics have a significant impact on photocurrent production; as crystallinity increases, the defects and e^-/h^+ pairs recombination rate decrease.

1.3.1.1.3. Particle size

The effectiveness of PC-WS and PEC-WS is significantly influenced by the particle size of plasmonic photocatalysts. The size of Au NPs affected the hot-electron migration [127]. Zhang et al. investigated how the particle size of Au influences the plasmonic behavior of Au NPs/$BiVO_4$ photoanode for the PEC-WS process. They changed the particle size of Au from 10 to 80 nm. The results manifested that Au NPs with a particle size of 30 nm showed the best enhancement for the plasmonic field concentration and PEC-WS performance due to the overlap of the near-electric field and the interband excitation in $BiVO_4$. Conversely, the scattering effect played a vital role when Au NPs have a particle size greater than 60 nm [128]. The particle size of Au in Au-ZnO nanostructures remarkably affected the H_2 production rate. The Au-ZnO flower structure with the smallest Au particle size of 5.4 nm presented the highest H_2 production rate [129].

1.3.1.1.4. Shape

The shape of the plasmonic metal NPs substantially affects the LSPR frequency, which promotes light absorption through the solar spectrum. It also affects the rate of e^-/h^+ pairs photogeneration [130,131]. Pu et al. studied the decoration of different shapes of Au nanostructures with TiO_2 nanowire for PEC-WS under light irradiation (300 - 800 nm). The PEC performance of Au nanorods (NRs), Au NPs, and a mix of Au NRs and NPs on the TiO_2 nanowire were studied and compared with that of bare TiO_2. Au NPs/TiO_2 nanowire enhanced the PEC performance in the UV and Vis zones. Conversely, Au NRs/TiO_2 nanowire boosted the PEC performance only in the Vis zone. The photoelectrode fabricated using a mixture of Au NRs and NPs/TiO_2 nanowires enhanced PEC performance in all UV−Vis ranges [132]. Light can be absorbed more efficiently by CuO with a sheet-like structure than CuO with a spherical structure. The bandgap energy of CuO drops as particle size gets smaller [133]. The separation of charge carriers and, consequently, the PC activity of photocatalysts is significantly influenced by the morphology of nanostructured materials. Sampaio et al. clarified that Au-ZnO flower morphology demonstrated a higher H_2 production rate (427 μmol

h^{-1} g_{cat}^{-1}) than bare ZnO, Au–ZnO needle morphology, and Au-ZnO rods morphology. This was attributed to the sophisticated flower morphology of Au-ZnO, which scattered the incident light, resulting in improving the structure's light absorption ability and PC performance [129].

1.3.1.2. Semiconductor-plasmonic metal nanoparticles composites

Composites made of semiconductor and metal or metal oxide have recently shown a high rate of H_2 production [134]. The deposition of metal or metal oxide on the surface of the semiconductor works as a co-catalyst or a photosensitizer that improves the catalytic activity, either by suppressing the rate of e^-/h^+ pairs recombination through capturing the electrons migrated from the semiconductor or by developing the semiconductor's light absorption capability. The co-catalyst has a higher work function than the semiconductor and offers more active sites, so, electrons flow to it more readily, increasing the rate of H_2 production [135]. TiO_2-based composites achieved good PC-WS performance due to their unique characteristics, involving good stability, and appropriate edge potentials of CB and VB [136,137]. Additionally, numerous semiconductors metal oxides, nitrides, phosphates, and sulfides have been studied as photocatalysts/photoelectrodes for the WS process. Doping semiconductors with transition metal ions such as V^{5+}, Cr^{3+}, and Ni^{2+} can enhance the WS performance through improving semiconductor's ability to absorb Vis light. Loading of Co-catalysts like Pt, Au, and NiO suppressed the back reaction and enhanced the H_2 production [114]. The doping of $SrTiO_3$ with plasmonic metal NPs significantly improved its WS performance under Vis light [138,139].

Ag and Au are predominant in photocatalysis applications because they act as photosensitizers due to their distinct features, like their optoelectronic characteristics (involving LSPR) and good chemical stability [88,89,140,141]. Noble metals NPs such as Pt, Ag, Rh, Au, and Ru, have displayed high efficiency for H_2 generation through the LSPR effect and Schottky junction [142–145]. These plasmonic noble metals can be deposited onto numerous semiconductors (e.g., $BiVO_4$, ZnO, Fe_2O_3, WO_3, TiO_2, and SnO_2) with various morphologies and applied for H_2 generation. The created Schottky junction in semiconductor-noble metal composites has a crucial role in boosting the rate of H_2 generation. Noble metals have limited carrier lifetimes and activity due to their spontaneous aggregation propensity. Moreover, Their practical application is restricted by their high cost. Hence, eco-friendly and low-cost plasmonic metal NPs are needed for scalable applications [84].

Inexpensive non-noble transition metals are appealing substitutes for pricey noble metals in PEC-WS and PC-WS applications, owing to their high work functions and strong electrical conductivity. Therefore, they can ameliorate electrons transfer and trapping. Despite the challenging preparation conditions that restrict their practical utilization, they work as co-

catalysts and concurrently inhibit the photocorrosion of photoelectrodes during PEC-WS [13,146]. The deposited Cu NPs on several semiconductors, including $SrTiO_3$, TiO_2, ZnO, and g-C_3N_4, [147–150], worked as an efficient co-catalyst by accelerating the e^-/h^+ pairs separation and transfer at the interface, resulting in improving the catalytic performance. Tian et al. fabricated Cu/TiO_2 photocatalyst using two different techniques (wet impregnation and ion exchange) and investigated their PC performance. Cu captured the generated electrons in TiO_2, so improved the electron separation and migration in the CB of TiO_2. It was observed that the Cu/TiO_2 photocatalyst synthesized by ion exchange technique was more efficient than that synthesized by wet impregnation, which was ascribed to the good dispersion of Cu on the surface of TiO_2 [151]. Ni and Co both demonstrated good efficiency for H_2 production [152]. Fe and Co NPs have also been applied for PEC-WS and PC-WS [152–154]. Al displayed a plasmonic effect in the UV region and it broadened to the near-infrared (NIR) region [155–157] and has been used extensively as a photocatalyst [155,158,159].

1.3.2. Metal chalcogenides based photoelectrodes

Chalcogenides compounds are composed of chalcogens (S, Se, Te) as anions and electropositive cations [20]. Metal chalcogenides (MCs) can be classified into three groups regarding their chemical composition; metal mono- (MX), di- (MX_2), and tri- (MX_3) chalcogenides. M stands for the metal element, and X for the chalcogen. Each group has distinct crystal features and characteristics that can be used in various optoelectronic applications [160]. MCs have attracted researchers' attention because of their remarkable light absorption ability and distinct energy levels. So, MCs have been investigated in numerous energy producing and storage applications, involving catalysis, photovoltaics, batteries, and artificial photosynthesis systems [161]. Compared to metal oxides, MCs have been deemed more promising photocatalysts because of their greater light absorption coefficient, preferred energy level alignment, and abundance of active sites [20,162–165]. Furthermore, transition MCs applied as photoanodes in the optimized PEC system can theoretically achieve the best solar-to-hydrogen efficiency [21]. MCs photoelectrodes have been widely applied for the PEC-WS technique [166–168]. For instance, MoS_2 is an auspicious and cheap alternative to Pt electrodes for H_2 production from EC- and PEC-WS techniques [169]. CdS has garnered significant attention for PC- and PEC-WS under Vis light, due to its advantageous properties, including a reasonable bandgap, a suitable band position, and a high efficiency of H_2 production [170–172]. However, it suffers from fast e^-/h^+ pairs recombination and photocorrosion. Transition MCs have a lot of compositions with various lattice features and unique electronic structures [173]. As a result, they have been used in various energy-related

applications [165]. The configuration, optical characteristics of transition MCs, and their performance in several fields of photonics and optoelectronics were reported in many reviews [160,174–177]. Other reviews have concentrated on the application of transition MCs for H_2 generation using the WS technique [8,178–181].

1.3.2.1. The role of Metal chalcogenides in adjusting the bandgap energy of hydride heterostructure

MCs have generated a lot of attention in many fields, as a consequence of their unique optical characteristics. MCs have bandgap energy between 0.3 and 3.8 eV, based on their composition [75,182]. The light absorption wavelength of the substance depends on its bandgap energy. Substances with a wide bandgap energy can absorb a short wavelength, meanwhile, substances with a narrow bandgap energy can absorb the long wavelength of the incident light [183]. **Figure 1-3** illustrates the relation between the material's bandgap energy and the predicted wavelength of absorbed light. The relation between bandgap energy (eV) and wavelength (nm) of the incident light can be illustrated as follows [40];

$$h\upsilon\,(\mathrm{eV}) = \frac{1239.8\ (\mathrm{eV}x\ \mathrm{nm})}{\lambda\ (\mathrm{nm})} \qquad \text{(Eq.1-6)}$$

Various types of MCs photoelectrode can exhibit great activity for H_2 production owing to their adjustable bandgap energy [184,185]. Jiang et al. [186] explained that the bandgap energy and absorption edge of CdS were remarkably affected by altering the hydrothermal synthesis time due to changes in the crystal size. CdS which was synthesized through the hydrothermal time of 4 h, had the highest absorption edge of 560 nm and the smallest bandgap energy owing to their large particle size. The combination of wide bandgap semiconductors (WBSs) with narrow bandgap energy semiconductors having suitable energy band positions is an efficient strategy to ameliorate the light absorption, e^-/h^+ pairs transfer, and maximize the PEC energy conversion efficiency by generating type-II heterojunction [187–190]. The type-II heterojunction provides a long lifetime of charge carriers as the minimum CB and the maximum VB are present in different positions of the heterojunction [191].

Recently, various transition MCs quantum dots (QDs) formed nanocomposites with several WBSs which significantly improved the light absorption capability of WBSs and facilitated e^-/h^+ pairs separation [161,192–194]. The deposition of layer-by-layer CdSe QDs on TNTAs generated type-II heterojunction between CdSe QDs and TNTAs, resulting in red-shifted the absorption band edge, enhanced light absorption ability of TNTAs, and promotes the e^-/h^+ pairs separation and transfer [161]. The light absorption ability of the ZnO photoanode was considerably improved after the deposition of CdSe/ ZnSe [195], CdSe/CdS [196], and

CdS/CdSe nanofilm [197], with an obvious bandgap decrease and improvement in the PEC performance. When Bi_2S_3 NRs uniformly distributed over WO_3 nanoplates, a type-II heterojunction was created, excellent light absorption and charge separation were attained [198]. Mollavali et al. observed that the growth of NiS, CdS, and ZnS NPs over C, N-co-doped -TiO_2 NTAs surface notably decreased the bandgap energy and boosted the PEC-WS performance [187]. D. Rani et al. noted that the heterojunction between CdSe QDs and $BaTiO_3$ expanded the light absorption wavelength to 550 nm with a quick bandgap drop to 2.25 eV [199]. Wu et al. showed that the heterojunction constructed between $CuSbS_2$ and $Zn_{0.2}Cd_{0.8}S$ doped with Fe extended the light absorption and demonstrated excellent PEC stability after loading Co-Pi [200]. Shen et al. explained the effect of CdSe NPs deposition in expanding the light absorption of TNTAs photoelectrode from the UV to the Vis range [201]. Bare TNTAs had an absorption band edge of 400 nm, while after decoration with Au nanocrystals (NCs), the absorption peak was expanded to 520 nm owing to the LSPR effect of Au NCs. The further deposition of CdSe NPs displayed a remarkable red shift to 700 nm. This was ascribed to the superb synergy between CdSe NPs and Au NCs decorated on the TNTAs surface. Andrea et al. decorated TiO_2 with diverse cadmium chalcogenides (CdS, CdSe, and CdTe) QDs to develop its light absorption ability [202]. The results showed that CdSe QDs/TiO_2 demonstrated the highest light absorption capacity (300-650 nm) compared to other single-modified photoelectrodes. Conversely, fabricated photoelectrodes with CdS-CdSe QDs or CdS-CdTe QDs displayed a wider range of light absorption with suitable energy levels, facilitating e^-/h^+ pairs separation and improving PEC performance. The recent development of metal mono-chalcogenides, metal di-chalcogenides, and metal tri-chalcogenide based photoelectrodes for the PEC-WS technique are illustrated in **Table 1-1**, **Table 1-2**, and **Table 1-3** respectively.

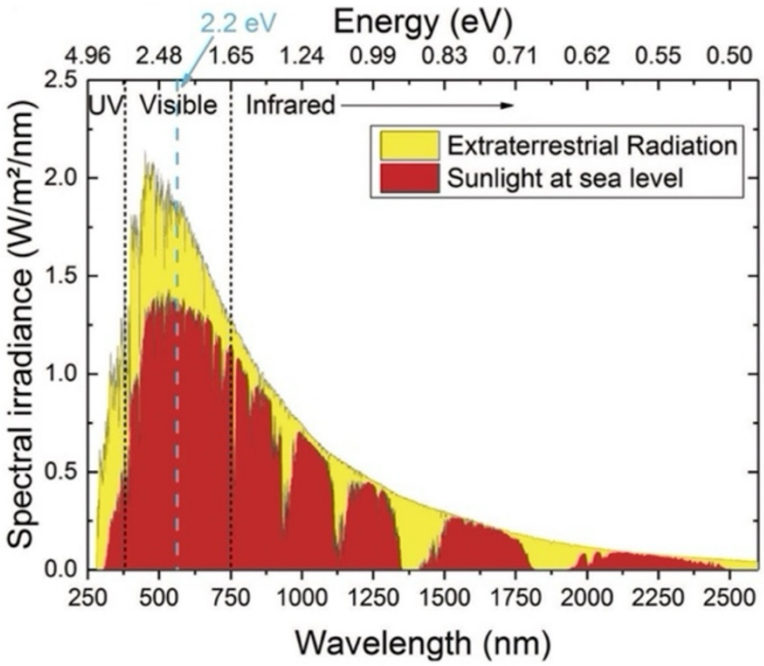

Figure 1-3. Spectral irradiance versus wavelength of solar energy in space and at sea level. The top axis displays the relation with the energy of incident photons [183]. @Friedhelm Finger et al. (Licensed under CC BY 4.0).

1.3.2.2. Drawbacks of metal chalcogenides application

Under light irradiation, MCs alone exhibit limited photocatalytic activity because of the high recombination rate of e^-/h^+ pairs and photocorrosion that leads to poor energy conversion efficiency [203,204]. Three strategies were reported to ameliorate e^-/h^+ pairs separation and mitigate the photocorrosion rate of the photoelectrodes [258,259]. (i) The use of electrolytes contain sacrificial reagents which able to catch the extra holes that can cause the photocorrosion of the photoelectrode [205–207]. For instance, Na_2SO_3/Na_2S acted as a sacrificial reagent that captured the extra holes and oxidized sulfides (S^{2-}); to disulfides (S_2^{2-}). Thus, it mitigated the photocorrosion of Bi_2S_3. Moreover, Na_2SO_3 reduced S_2^{2-} to S^{2-}, which increased of generated quantity of H_2 at the counter electrode [208–210].

$$S_2^{2-} + SO_3^{2-} \longrightarrow S^{2-} + S_2O_3^{2-} \qquad \text{(Eq.1-7)}$$

(ii) Noble metals [211–216], or non-noble metals [217–222] loading on the semiconductors. These doped metals act as co-catalysts that promote the OER by decreasing the water oxidation overpotential, leading to quickly consuming the holes present on the surface of the semiconductor and thereby rapidly consume the holes present on the semiconductor surface [223]. (iii) The application of a protective layer on the photoelectrode surface [224–228]. This protective cover requires to be extremely homogeneous, highly conductive, and chemically

inert. For example, the passivation layer of ZnS prevented the photocorrosion of CdS NPs [187,229,230]. The shell layer in the core/shell heterojunction inhibits the dissociation of surface ions in the core [20,69,231]. Sheng et al. reported that the wrapping of CdS NRs with MoS_2/In_2S_3 nanosheets which were vertically arranged as a shell, significantly reduced the intensity of the photoluminescence (PL) peak that confirmed the effective e^-/h^+ pairs separation [231].

1.4. The aim and structure of this thesis

The PEC-WS technique is a remarkable strategy that uses semiconductor photoelectrodes immersed in an electrolyte to absorb solar energy and split water, generating eco-friendly and storable chemical energy, such as H_2 without carbon dioxide emission. To achieve an effective PEC-WS system, semiconductor photoelectrodes with a high light absorption capacity, quick e^-/h^+ pairs separation and transfer, and adequate chemical stability must be designed. The main goal of this thesis is to present facile approaches for designing stable, and effective photoanodes for PEC-WS that produce a high quantity of H_2. Our strategy focuses on improving the optical and electrical characteristics of some metal oxides by the appropriate deposition of MCs and plasmonic metal NPs.

The distinctive electrical and optical properties of MCs have made them attractive options for light absorbers. The decoration of anodic nanoporous (ANPor) WO_3 with MC QDs that has narrow bandgap can remarkably improve the light absorption ability, facilitate e^-/h^+ pairs transfer, and mitigate the charge recombination. We synthesized ANPor WO_3 using an anodic oxidation method. Using successive ionic layer adsorption and reaction (SILAR) procedure an adequate quantity of Bi_2S_3 QDs was deposited on the ANPor WO_3 surface and was investigated for PEC-WS as a photoanode under UV-Vis irradiation. The detailed results are shown in Chapter 2.

Additionally, the doping of semiconductors with plasmonic metal NPs has been reported as an auspicious approach for promoting the PEC activity of the semiconductor by the transmission of plasmonic energy from the plasmonic metal NPs to the semiconductor. The PEC-WS performance can be improved by adjusting the nanostructure of the semiconductor photoelectrodes and sensitizing them with plasmonic metal NPs. We transformed ZnO nanorods (NRs) to ZnO nanopagoda arrays (NPGs) followed by Ag NPs deposition. This study illustrates how the transformation from ZnO NRs to ZnO NPGs and the doping of Ag NPs improve the photocurrent and PEC conversion efficiency under light irradiation. The detailed results are explained in Chapter 3.

We also investigated the impact of concurrently depositing Ag and Ag_2S NPs over ZnO NPGs. The obtained data displayed that the successful deposition of Ag and Ag_2S NPs on the surface of ZnO NPGs not only improved the Vis light absorption but also facilitated the e^-/h^+ pairs separation and migration. The detailed results are illustrated in Chapter 4.

Moreover, we constructed an effective type II heterojunction between Bi_2Se_3 QDs and TNTAs by depositing a suitable amount of Bi_2Se_3 QDs on the surface of TNTAs. The TNTAs/Bi_2Se_3 QDs photoanode displayed outstanding PEC performance due to its suitable bandgap, which enhanced the Vis light absorption, and its efficient e^-/h^+ pairs transfer, which mitigated their recombination rate. The detailed results are disclosed in Chapter 5.

Table 1-1. The latest metal mono-chalcogenide based photoelectrodes studied for the PEC-WS.

Photoelectrode	Fabrication	Morphology	Electrolyte	Light source	Applied bias	Photocurrent (mA/cm^2)	Ref.
$Cu_2Se/CdSe/TiO_2$ (photoanode)	Anodization, electrochemical deposition	Nanotubes	0.5 M Na_2S	500 W Xe lamp	0.1 V vs. SCE	28	[232]
TiO_2 NRs/CdSQDs (photoanode)	Chemical bath deposition	Nanorods	0.25 M Na_2S/0.35 M Na_2SO_3	300 W Xe lamp	1.0 V vs. RHE	6.8	[233]
Fe_2O_3/CdS/Co-Pi (photoanode)	Hydrothermal, chemical bath deposition, photo-assisted deposition	Nanorods	1. M NaOH + 0.1 M Na_2S	300 W Xe lamp	0.7 V vs. RHE	3.29	[207]
$CdS@MoS_2/In_2S_3$ (photoanode)	Hydrothermal	Nanosheets, Nanorods	5 M H_2SO_4/lactic acid	300 W Xe lamp	0.14 V vs. RHE	1.5–2.0	[231]
C, N-codoped-TiO_2/NiS/CdS/ZnS NPs (photoanode)	Anodization, SILAR	Nanotubes, Nanoparticles	0.28 M Na_2S/ 0.32 M Na_2SO_3	150 W Xe ozone-free lamp	0 V vs. Ag/AgCl	18.79	[187]
CdS/Cu_2O (photoanode)	Hydrothermal, SILAR,	Nanorods	Na_2S (0.35 M)/Na_2SO_3 (0.25 M)	300 W Xe lamp	0 V vs. Ag/AgCl	4.2	[234]
$CdS/ZnFe_2O4/Cu_2O$ (photoanode)	Hydrothermal, CBD	Nanorods	Na_2S (0.35 M)/Na_2SO_3 (0.25 M)	300 W Xe lamp	0 V vs. Ag/AgCl	3.3	[235]
PbS/Mn-doped CdS QDs/TiO_2 (photoanode)	Hydrothermal, SILAR	Mesoporous, QDs	0.25 M Na_2S/0.35 M Na_2SO_3	AM 1.5 G solar simulator	0.6 V vs. RHE	22.1	[236]
$CdSe/TiO_2$ NTs (photoanode)	Anodization, CBD	Nanotubes	1 M KOH	150 W Xe lamp	0.4 V vs. Ag/AgCl	1.6	[237]
SnO_2–TiO_2/ CdSe/CdS core-shell QDs (photoanode)	Hot injection, SILAR, electrophoretic deposition	Mesoporous, QDs	0.25 M Na_2S and 0.35 M Na_2SO_3	300 W Xe lamp	1 V vs. RHE	~4.7	[238]
Fe-$Zn_{0.2}Cd_{0.8}S$/$CuSbS_2$/ Co-Pi (photoanode)	Hydrothermal, electrochemical deposition,	Nanowalls	Na_2S/Na_2SO_3	CHF-XM500, 100 mW/cm^2	0.9 V vs. RHE	0.31	[200]
$Zn_{0.5}Cd_{0.5}S/TiO_2$ (photoanode)	Anodization, SILAR	Nanotubes	0.25 M Na_2S/0.35 Na_2SO_3	300 W Xe lamp, $\lambda > 400$ nm	1.23 V vs. RHE	10.95	[239]

TiO_2/CdS/CdSe/ZnS (photoanode)	Spray pyrolysis, hot injection, SILAR	Nanoparticles	0.25 M Na_2SO_3/0.35 M Na_2S	–	0 V	3.9	[202]
ZnO NR-$Zn_{1-x}Cd_xS$ PNS (photoanode)	Solvothermal	Nanorods, Porous nanosheets	0.25 M Na_2S +0.35 M Na_2SO_3	100 Mw/cm^2 simulated sunlight source	0 V vs. Ag/AgCl	6.60	[240]
N-RGO-$Cd_{0.6}Zn_{0.4}S$ (photoanode)	Solvothermal	Spherical nanoparticles	Na_2S (0.35 M)/Na_2SO_3 (0.25 M)	300 W Xe lamp	–	0.92	[241]
RGO-$Cd_xZn_{1-x}S$ (photoanode)	Thermal sulfurization	Agglomerated nanoparticles	0.35 M Na_2S and 0.25 M Na_2SO_3	HAL-320 Xe lamp	0.542 V vs. RHE	6.5	[242]
ZnSe/C/TiO_2 NTAs (photoanode)	Anodization, deposition	Nanotubes	0.25 M Na_2SO_3 and 0.35 M Na_2S	300 W Xe lamp	0.5 V vs. SCE	1.05	[243]
FeSnOS-$BiVO_4$ (photoanode)	Electrodeposition, spin-coating	Worm-like shape	0.5 M Na_2SO_4	–	at 1.23 V vs. RHE	3.1	[244]
ZnO/CdS/CdSe (photoanode)	CBD	Nanosheets	0.25 M Na_2S/0.35 M Na_2SO_3	100 W Xe lamp	0 V vs Ag/AgCl	4.0	[196]
$CdSe(en)_{0.5}$/$CdIn_2S_4$/TiO_2 (photoanode)	Solvothermal	Nanodiscs	0.1 M Na_2S and 0.02 M Na_2SO_3	100 Mw/cm^2 simulated sunlight irradiation	0 V vs. Ag/AgCl,	2.43	[245]
PbS/CdS/ZnO NWAs (photoanode)	SILAR	Nanowires	0.1 M Na_2SO_3/0.1 M Na_2S	100 mW/cm^2 halogen lamp	1.2 V vs. Ag/AgCl	1.42	[188]
TiO_2-CdSe-Au (photoanode)	Anodization, cyclic voltammetric deposition, magnetron sputtering	Nanotubes	0.1 M Na_2S	300 W Xe lamp	0 V vs. Ag/AgCl	8.4	[201]
CdSeQDs/$BaTiO_3$ (photoanode)	Hot injection, hydrothermal.	Irregular shape NPs	1 M Na_2S	300 W Xe lamp	0.8 V. vs. Ag/AgCl	12	[199]
ZnO-CdS-Ce (photoanode)	Electrodeposition, SILAR	Nanosheets, Nanorods	0.35 M Na_2SO_3/0.24 M Na_2S	300 W Xe lamp	–	8.9	[246]

InSe/graphene (photoanode)	Exfoliation and encapsulation	–	NaOH	AAA solar simulator	1.23 V vs. RHE	10	[247]
ZnO/CdS/CdSe (photoanode)	Hydrothermal, SILAR and CBD	Nanorods	0.25 M $Na_2S.9H_2O$, and 0.35 M Na_2SO_3	100 mW/cm^2	−0.2 V vs. Ag/AgCl	6.244	[197]
ZnO/Au/CdS NTAs (photoanode)	Electrochemical deposition, hydrothermal reduction, CBD	Nanotubes	Na_2S (0.25 M) and M Na_2SO_3 (0.35 M)	300 W Xe lamp	No bias	6.5	[192]
ZnO/CdS/Au NTAs (photoanode)	CBD, Au reduction	Nanotubes	0.25 M Na_2S and 0.35 M Na_2SO_3	350 W Xe lamp	1.2 V vs. Ag/AgCl	21.53	[194]
CdSe/ZnSe/ZnO NTAs (photoanode)	Electrochemical deposition, consecutive ion-replacement reaction	Nanotubes	Na_2SO_3 (0.5 M) and Na_2S (0.5 M)	300 W Xe lamp	0.25 V vs. Ag/AgCl	3.2	[195]
MoSx-CdS/Cu_2ZnSnS_4 (photocathode)	Spray pyrolysis, sulfurization, CBD, electrodeposition	Microstructure	0.2 M Na_2HPO_4/ NaH_2PO_4	Solar simulator	0.6 V vs. RHE	18	[248]

Table 1-2. The latest metal di-chalcogenide based photoelectrodes studied for the PEC-WS.

Photoelectrode	Fabrication	Morphology	Electrolyte	Light source	Applied bias	Photocurrent (mA/cm^2)	Ref.
Cu_2O/g-C_3N_4/WS_2 (photocathode)	Electrodeposition, Exfoliation	Nanosheets	1 M Na_2SO_4	Xe lamp ($\lambda \geq 420$ nm)	−0.55 V vs. RHE	−9.5	[249]
MoS_2NSs/ZnO NWs (photoanode)	Sputtering, hydrothermal	Nanosheets, Nanowires	0.5 M Na_2SO_4	100 W Xe arc lamp	0 V vs. SCE	0.25	[250]
3D TiO_2 NFs/2D $MoSe_2$ (photoanode)	Impregnation	Nanoflowers	1 M NaOH	150 W Xe lamp	1.2 V vs. Ag/AgCl	1.40	[251]
ReS_2/Si (photocathode)	Chemical vapor deposition	Nanosheets	0.5 H_2SO_4	300 W Xe lamp	0 V vs. RHE	18.5	[252]
10% CdSe QDs/WS_2 NF (photocathode)	Hydrothermal, hot injection	Nanoflowers	0.5 M H_2SO_4	300 W Xe lamp ($\lambda >$ 420 nm)	0 V vs. RHE	−1.12	[253]
Au–FeS_2 (photocathode)	Hot injection	Nanosheets	0.2 M H_2SO_4	150 W Xe lamp	0.08 V vs. RHE	10	[254]
MoS_2/CoTe (photoanode)	Hydrothermal, ultrasonication	Flower-like feature	0.5 M H_2SO_4	300 W Xe lamp $\lambda > 420$	1.23 V vs. RHE	2.791	[255]
$NaNbO_3$/MoS_2 (photocathode)	Hydrothermal	Cubic-like structure	0.5 M Na_2SO_4	150 W Xe arc lamp	−1.0 V	4.54	[256]
Pt/TiO_2/Sb_2Se_3 (TGA 5) (photocathode)	Spin-coating	Needle-like shape	0.1 M H_2SO_4	solar light illumination (AM 1.5 G, Newport Corporation)	0 V vs. RHE	−12.5	[38]
TiO_2/MoS_2 (photoanode)	Hydrothermal, MOCVD	Nanowires, Flakes	0.3 M KH_2PO_4 buffered with KOH solution	150 W Xe arc lamp	0 V vs. Hg/Hg_2Cl_2	215	[257]
TiO_2/CdS/MoS_2 (photoanode)	Hydrothermal, CBD, SILAR	Nanosheets, Nanorods, Nanocrystals	0.35 M Na_2SO_3 /0.25 M Na_2S	Solar simulator (100 mW/cm^2)	0.9 V vs. RHE	3.25	[258]
MoS_2/GaN (photoanode)	MOCVD	–	1 M NaOH	300 W Xe lamp	0 V vs. Ag/AgCl	5.2	[259]
TiO_2/Bi NPs/Sb_2S_3 (photoanode)	Doctor-blade technique, CBD	No specific shape	0.1 M Na_2SO_3 and 0.1 M Na_2SO_4,	150 W Xe lamp	1.23 V vs. RHE	4.21	[260]
MoS_2/MoO_2 (photocathode)	Hydrothermal	Spherical nanoflowers	0.1 M Na_2SO_4	300 W Xe arc lamp	−1.8 V vs. SCE	-10.3	[261]

A-$Fe_2O_3/SnS_2/Cu_2O$ (photoanode)	Hydrothermal, dip-coating	Nanorod,Nanosheet	1 M NaOH	300 W Xe lamp	1.23 VRHE	2.98	[262]
C60-decorated $SnS_2/CuInS_2$ (photocathode)	Hydrothermal	Nanosheet	0.5 M Na_2SO_4	300 W Xe lamp	−0.45 V vs. RHE	4.51	[263]
n^+p-Si/Ti/Ru MoS_2 (photocathode)	Spin-coating, CVD	Nanoplates	0.5 M H_2SO_4	500 W Xe lamp	0 V vs. RHE	−43	[264]

Table 1-3. The latest metal tri-chalcogenide based photoelectrodes studied for the PEC-WS.

Photoelectrode	**Fabrication**	**Morphology**	**Electrolyte**	**Light source**	**Applied bias**	**Photocurrent (mA/cm^2)**	**Ref.**
Bi_2S_3/(001) TiO_2 (photoanode)	Hydrothermal	Nanoplates, Nanorods	0.36 M Na_2SO_3 and 0.25 M Na_2S	150 W Xe lamp	0.9 V vs. Ag/AgCl	2.035	[265]
WO_3/Bi_2S_3 (photoanode)	Hydrothermal, SILAR, CBD	Nanorods, Nanoplates	0.1 M Na_2S and 0.1 M Na_2SO_3	Simulated solar light	0.9 V vs. RHE	5.95	[198]
V-Bi_2S_3 (photoanode)	In situ solution-processed reaction	Nanowires	0.1 M Na_2S and 0.1 M Na_2SO_3	300 W Xe lamp	−0.2 V vs. Ag/AgCl	10	[266]
MoS_2/Sb_2Se_3 (photocathode)	Close-spaced sublimation, sputtering	Nanorods	0.5 M Na_2SO_4	AM 1.5 G solar simulator	0 V vs. RHE	−10	[267]
α-Fe_2O_3NRs/Sb_2S_3/Co-Pi (photoanode)	Hydrothermal, photo-assisted electrodeposition	Nanorods	1 M NaOH	–	1.23 V vs. RHE	1.14	[268]
Bi_2S_3NS/Ag interlayer/Zr:Fe_2O_3 NR (photoanode)	hydrothermal	Nanorods, Nanosheets	–	Solar light source (AM 1.5 G, 100 mW/cm^2	−0.4 V vs. Ag/AgCl	1.27	[269]
AuNPs/Bi_2S_3NRs (photoanode)	Hydrothermal, seed-mediated growth, drop-casting	Nanorods, Nanoparticles	0.1 M Na_2S/ 0.1 M Na_2SO_3	Solar light source	1.23 V vs. RHE	9.61	[270]
Sb_2S_3/5%Mo−WO_3 (photoanode)	Hydrothermal, spin-coating	Nanoplates, Nanoparticles	0.1 M Na_2SO_4	300 W Xe lamp	1.23 V vs. RHE	0.42	[271]
ZnO/ Cu_2SnS_3 (photoanode)	Hydrothermal	Nanorods, Nanocrystals	0.5 M Na_2SO_4	Simulated sunlight (100 mW/cm^2)	1.23 V vs. NHE	4.75 mA cm-2	[272]

g-C_3N_4/Bi_2S_3/BiNPs (photoanode)	Doctor blading technique, SILAR, drop-casting.	Flower-like structure, Flat sheets,	0.1 M Na_2SO_4/Na_2SO_3	150 W Xe lamp	1.23 V vs. RHE	7.11	[273]
Au-Cu_3BiS_3 (photocathode)	Solvothermal	Nanoflowers	0.1 M KCl/0.1 M $Eu(NO_3)_3$	300 W Xe lamp	–	0.2	[274]
Bi_2S_3/ZnS/ZnO (photoanode)	Hydrothermal, sulphurization, SILAR	Nanosheets, nanorods	0.1 M Na_2S and 0.1 M Na_2SO_3	300 W Xe lamp	0.2 V vs. Ag/AgCl	220	[275]
WO_3/Cu/Bi_2S_3 (photoanode)	Hydrothermal, electrophoretic deposition, doctor blade	Nanoplatelets	0.1 M Na_2SO_3 and Na_2SO_4	150 W Xe arc lamp	1.23 V vs. RHE	10.6	[276]
In_2S_3@Bi_2S_3 (photoanode)	Solvothermal process.	Nanosheets, Nanorods	0.2 M Na_2SO_4	AM 1.5G illumination	1.23 V vs. RHE	2.0	[277]
Sb_2O_3/Sb_2S_3/FeOOH (photoanode)	Impregnation, CBD, post-sulfidation.	Rod-like feature	1 M Na_2SO_4	300 W Xe lamp	1.23 V vs. RHE	0.45	[278]
PVP treated WO_3/In_2S_3 (photoanode)	Hydrothermal, water bath reaction	Nanowalls, Nanosheets	0.1 M Na_2SO_4	Solar simulated illumination (AM 1.5 G, 100 Mw/cm^2)	1.23 V vs. RHE	1.61	[279]
$CdIn_2S_4$ (photoanode)	Hydrothermal	Plates	0.35 M Na_2SO_3 and 0.25 M Na_2S	300 W Xe arc lamp	1.23 V vs. RHE	5.73	[167]
TiO_2/Bi_2S_3 (photoanode)	Hydrothermal, SILAR, solvothermal	Rosette rod	0.1 M Na_2S and Na_2SO_3	Xe lamp, 100 mW/cm^2	1.23 V vs. RHE	3.98	[206]
PANI/Bi_2S_3 NFs (photoanode)	Hydrothermal, chemisorption	Nanoflowers	0.5 M Na_2SO_4	Halogen lamp (100 mW/cm^2)	0.8 V vs. NHE	6.95	[280]
RuO_x/TiO_2/Sb_2Se_3/Au/FTO (photocathode)	Close space sublimation (CSS),ALD, galvanostatic photo-deposition	Microstructure	H_2SO_4, pH ~ 1	Simulated solar light	0 V vs. RHE	30	[281]
$Sb_2(S_xSe_{1-x})_3$ (photocathode)	Vapor transport deposition, postsulfurization	Nanorod	0.5 MNa_2SO_4	300 W Xenon lamp	0 V vs. RHE	0.8	[282]

References

[1] H. Ahmad, S.K. Kamarudin, L.J. Minggu, M. Kassim, Hydrogen from photo-catalytic water splitting process: A review, Renewable and Sustainable Energy Reviews 43 (2015) 599–610. https://doi.org/10.1016/j.rser.2014.10.101.

[2] R.E. Blankenship, D.M. Tiede, J. Barber, G.W. Brudvig, G. Fleming, M. Ghirardi, M.R. Gunner, W. Junge, D.M. Kramer, A. Melis, T.A. Moore, C.C. Moser, D.G. Nocera, A.J. Nozik, D.R. Ort, W.W. Parson, R.C. Prince, R.T. Sayre, Comparing Photosynthetic and Photovoltaic Efficiencies and Recognizing the Potential for Improvement, Science (1979) 332 (2011) 805–809. https://doi.org/10.1126/science.1200165.

[3] N.S. Lewis, Research opportunities to advance solar energy utilization, Science (1979) 351 (2016). https://doi.org/10.1126/science.aad1920.

[4] F. Xiao, J. Miao, H.B. Tao, S. Hung, H. Wang, H. Bin Yang, J. Chen, R. Chen, B. Liu, One-Dimensional Hybrid Nanostructures for Heterogeneous Photocatalysis and Photoelectrocatalysis, Small 11 (2015) 2115–2131. https://doi.org/10.1002/smll.201402420.

[5] F.-X. Xiao, B. Liu, In situ etching-induced self-assembly of metal cluster decorated one-dimensional semiconductors for solar-powered water splitting: unraveling cooperative synergy by photoelectrochemical investigations, Nanoscale 9 (2017) 17118–17132. https://doi.org/10.1039/C7NR06697J.

[6] A.M. Rabie, M.R. Abukhadra, A.M. Rady, S.A. Ahmed, A. Labena, H.S.H. Mohamed, M.A. Betiha, J.-J. Shim, Instantaneous photocatalytic degradation of malachite green dye under visible light using novel green Co–ZnO/algae composites, Research on Chemical Intermediates 46 (2020) 1955–1973. https://doi.org/10.1007/s11164-019-04074-x.

[7] A. FUJISHIMA, K. HONDA, Electrochemical Photolysis of Water at a Semiconductor Electrode, Nature 238 (1972) 37–38. https://doi.org/10.1038/238037a0.

[8] L. Lin, P. Sherrell, Y. Liu, W. Lei, S. Zhang, H. Zhang, G.G. Wallace, J. Chen, Engineered 2D Transition Metal Dichalcogenides—A Vision of Viable Hydrogen Evolution Reaction Catalysis, Adv Energy Mater 10 (2020). https://doi.org/10.1002/aenm.201903870.

[9] P. Pei, M. Wang, D. Chen, P. Ren, L. Zhang, Key technologies for polymer electrolyte membrane fuel cell systems fueled impure hydrogen, Progress in Natural Science: Materials International 30 (2020) 751–763. https://doi.org/10.1016/j.pnsc.2020.08.015.

[10] P. Nikolaidis, A. Poullikkas, A comparative overview of hydrogen production processes, Renewable and Sustainable Energy Reviews 67 (2017) 597–611. https://doi.org/10.1016/j.rser.2016.09.044.

[11] C. Tang, M.-M. Titirici, Q. Zhang, A review of nanocarbons in energy electrocatalysis: Multifunctional substrates and highly active sites, Journal of Energy Chemistry 26 (2017) 1077–1093. https://doi.org/10.1016/j.jechem.2017.08.008.

[12] I. Roger, M.A. Shipman, M.D. Symes, Earth-abundant catalysts for electrochemical and photoelectrochemical water splitting, Nat Rev Chem 1 (2017) 0003. https://doi.org/10.1038/s41570-016-0003.

[13] M.J. Kenney, M. Gong, Y. Li, J.Z. Wu, J. Feng, M. Lanza, H. Dai, High-Performance Silicon Photoanodes Passivated with Ultrathin Nickel Films for Water Oxidation, Science (1979) 342 (2013) 836–840. https://doi.org/10.1126/science.1241327.

[14] O. Khaselev, J.A. Turner, A Monolithic Photovoltaic-Photoelectrochemical Device for Hydrogen Production via Water Splitting, Science (1979) 280 (1998) 425–427. https://doi.org/10.1126/science.280.5362.425.

[15] M.G. Walter, E.L. Warren, J.R. McKone, S.W. Boettcher, Q. Mi, E.A. Santori, N.S. Lewis, Solar Water Splitting Cells, Chem Rev 110 (2010) 6446–6473. https://doi.org/10.1021/cr1002326.
[16] K.S. Joya, Y.F. Joya, K. Ocakoglu, R. van de Krol, Water-Splitting Catalysis and Solar Fuel Devices: Artificial Leaves on the Move, Angewandte Chemie International Edition 52 (2013) 10426–10437. https://doi.org/10.1002/anie.201300136.
[17] C. Liu, B.C. Colón, M. Ziesack, P.A. Silver, D.G. Nocera, Water splitting–biosynthetic system with CO 2 reduction efficiencies exceeding photosynthesis, Science (1979) 352 (2016) 1210–1213. https://doi.org/10.1126/science.aaf5039.
[18] H.H. Farrag, S.Y. Sayed, N.K. Allam, A.M. Mohammad, Emerging nanoporous anodized stainless steel for hydrogen production from solar water splitting, J Clean Prod 274 (2020) 122826. https://doi.org/10.1016/j.jclepro.2020.122826.
[19] T. Duke, S.M. Graham, M.N. Cherian, A.S. Ginsburg, M. English, S. Howie, D. Peel, P.M. Enarson, I.H. Wilson, W. Were, Union Oxygen Systems Working Group, Oxygen is an essential medicine: a call for international action., Int J Tuberc Lung Dis 14 (2010) 1362–8.
[20] V. Navakoteswara Rao, P. Ravi, M. Sathish, M. Vijayakumar, M. Sakar, M. Karthik, S. Balakumar, K.R. Reddy, N.P. Shetti, T.M. Aminabhavi, M.V. Shankar, Metal chalcogenide-based core/shell photocatalysts for solar hydrogen production: Recent advances, properties and technology challenges, J Hazard Mater 415 (2021) 125588. https://doi.org/10.1016/j.jhazmat.2021.125588.
[21] K. Sivula, R. van de Krol, Semiconducting materials for photoelectrochemical energy conversion, Nat Rev Mater 1 (2016) 15010. https://doi.org/10.1038/natrevmats.2015.10.
[22] M.G. Walter, E.L. Warren, J.R. McKone, S.W. Boettcher, Q. Mi, E.A. Santori, N.S. Lewis, Solar Water Splitting Cells, Chem Rev 110 (2010) 6446–6473. https://doi.org/10.1021/cr1002326.
[23] A.J. Nozik, Photochemical diodes, Appl Phys Lett 30 (1977) 567–569. https://doi.org/10.1063/1.89262.
[24] X. Chen, Z. Zhang, L. Chi, A.K. Nair, W. Shangguan, Z. Jiang, Recent Advances in Visible-Light-Driven Photoelectrochemical Water Splitting: Catalyst Nanostructures and Reaction Systems, Nanomicro Lett 8 (2016) 1–12. https://doi.org/10.1007/s40820-015-0063-3.
[25] R. Passalacqua, S. Perathoner, G. Centi, Semiconductor, molecular and hybrid systems for photoelectrochemical solar fuel production, Journal of Energy Chemistry 26 (2017) 219–240. https://doi.org/10.1016/j.jechem.2017.03.004.
[26] A. Hellman, B. Wang, First-Principles View on Photoelectrochemistry: Water-Splitting as Case Study, Inorganics (Basel) 5 (2017) 37. https://doi.org/10.3390/inorganics5020037.
[27] T. Yao, X. An, H. Han, J.Q. Chen, C. Li, Photoelectrocatalytic Materials for Solar Water Splitting, Adv Energy Mater 8 (2018). https://doi.org/10.1002/aenm.201800210.
[28] C. Ros, T. Andreu, J.R. Morante, Photoelectrochemical water splitting: a road from stable metal oxides to protected thin film solar cells, J Mater Chem A Mater 8 (2020) 10625–10669. https://doi.org/10.1039/D0TA02755C.
[29] T.-F. Hou, M.A. Johar, R. Boppella, M.A. Hassan, S.J. Patil, S.-W. Ryu, D.-W. Lee, Vertically aligned one-dimensional ZnO/V_2O_5 core–shell hetero-nanostructure for photoelectrochemical water splitting, Journal of Energy Chemistry 49 (2020) 262–274. https://doi.org/10.1016/j.jechem.2020.02.004.

[30] S. Lin, H. Ren, Z. Wu, L. Sun, X.-G. Zhang, Y.-M. Lin, K. H. L. Zhang, C.-J. Lin, Z.-Q. Tian, J.-F. Li, Direct Z-scheme WO_3-nanowire-bridged TiO_2 nanorod arrays for highly efficient photoelectrochemical overall water splitting, Journal of Energy Chemistry 59 (2021) 721–729. https://doi.org/10.1016/j.jechem.2020.12.010.

[31] X. Liu, H. Wang, W. Qiu, Q. Wu, H. Wang, S. Xue, Dentritic hemaitite thinfilms with ferrous lactate overlayers for efficient photoelectrochemical water splitting, Solar Energy 231 (2022) 897–907. https://doi.org/10.1016/j.solener.2021.11.049.

[32] S. Banerjee, S. Padhan, R. Thangavel, Dopant inculcated ZnO based photoelectrodes for revitalizing photoelectrochemical water splitting, Mater Chem Phys 277 (2022) 125548. https://doi.org/10.1016/j.matchemphys.2021.125548.

[33] T.H. Jeon, D. Monllor–Satoca, G. Moon, W. Kim, H. Kim, D.W. Bahnemann, H. Park, W. Choi, Ag(I) ions working as a hole-transfer mediator in photoelectrocatalytic water oxidation on WO3 film, Nat Commun 11 (2020) 967. https://doi.org/10.1038/s41467-020-14775-2.

[34] J. Miao, B. Liu, Cadmium selenide-sensitized upright-standing mesoporous zinc oxide nanosheets for efficient photoelectrochemical H2 production, Journal of Energy Chemistry 25 (2016) 371–374. https://doi.org/10.1016/j.jechem.2016.02.013.

[35] Z. Zhou, P. Li, X. Gao, J. Chen, K. Akhtar, E.M. Bakhsh, S.B. Khan, Y. Shen, M. Wang, Constructing two-dimensional heterojunction through decorating covalent organic framework with MoS2 for enhanced photoelectrochemical water oxidation, J Environ Chem Eng 10 (2022) 106900. https://doi.org/10.1016/j.jece.2021.106900.

[36] S. Tiwari, S. Kumar, A.K. Ganguli, Role of MoS_2/rGO co-catalyst to enhance the activity and stability of Cu2O as photocatalyst towards photoelectrochemical water splitting, J Photochem Photobiol A Chem 424 (2022) 113622. https://doi.org/10.1016/j.jphotochem.2021.113622.

[37] S. Majumder, M. Gu, K. Hyeon Kim, Facile fabrication of $BiVO_4$/Bi_2S_3/$NiCoO_2$ for significant photoelectrochemical water splitting, Appl Surf Sci 574 (2022) 151562. https://doi.org/10.1016/j.apsusc.2021.151562.

[38] W. Yang, J. Ahn, Y. Oh, J. Tan, H. Lee, J. Park, H. Kwon, J. Kim, W. Jo, J. Kim, J. Moon, Water Splitting: Adjusting the Anisotropy of 1D Sb_2Se_3 Nanostructures for Highly Efficient Photoelectrochemical Water Splitting (Adv. Energy Mater. 14/2018), Adv Energy Mater 8 (2018). https://doi.org/10.1002/aenm.201870061.

[39] S. Ardo, D. Fernandez Rivas, M.A. Modestino, V. Schulze Greiving, F.F. Abdi, E. Alarcon Llado, V. Artero, K. Ayers, C. Battaglia, J.-P. Becker, D. Bederak, A. Berger, F. Buda, E. Chinello, B. Dam, V. Di Palma, T. Edvinsson, K. Fujii, H. Gardeniers, H. Geerlings, S.M. H. Hashemi, S. Haussener, F. Houle, J. Huskens, B.D. James, K. Konrad, A. Kudo, P.P. Kunturu, D. Lohse, B. Mei, E.L. Miller, G.F. Moore, J. Muller, K.L. Orchard, T.E. Rosser, F.H. Saadi, J.-W. Schüttauf, B. Seger, S.W. Sheehan, W.A. Smith, J. Spurgeon, M.H. Tang, R. van de Krol, P.C.K. Vesborg, P. Westerik, Pathways to electrochemical solar-hydrogen technologies, Energy Environ Sci 11 (2018) 2768–2783. https://doi.org/10.1039/C7EE03639F.

[40] Z. Chen, H.N. Dinh, E. Miller, Photoelectrochemical Water Splitting, Springer New York, New York, NY, 2013. https://doi.org/10.1007/978-1-4614-8298-7.

[41] Y.-Y. Wang, Y.-X. Chen, T. Barakat, Y.-J. Zeng, J. Liu, S. Siffert, B.-L. Su, Recent advances in non-metal doped titania for solar-driven photocatalytic/photoelectrochemical

water-splitting, Journal of Energy Chemistry 66 (2022) 529–559. https://doi.org/10.1016/j.jechem.2021.08.038.
[42] S.S. Kalanur, H. Seo, Work function tuned, surface Cs intercalated BiVO4 for enhanced photoelectrochemical water splitting reactions, Journal of Energy Chemistry 68 (2022) 612–623. https://doi.org/10.1016/j.jechem.2021.12.039.
[43] H. Sopha, M. Krbal, S. Ng, J. Prikryl, R. Zazpe, F.K. Yam, J.M. Macak, Highly efficient photoelectrochemical and photocatalytic anodic TiO2 nanotube layers with additional TiO_2 coating, Appl Mater Today 9 (2017) 104–110. https://doi.org/10.1016/j.apmt.2017.06.002.
[44] Y. Lu, C.-Y. Chiang, E. Huang, Vertically nanotwinned TiO_2 photoanodes with enhanced charge transport for efficient solar water splitting, Appl Mater Today 20 (2020) 100707. https://doi.org/10.1016/j.apmt.2020.100707.
[45] T.W. Kim, K.-S. Choi, Nanoporous $BiVO_4$ Photoanodes with Dual-Layer Oxygen Evolution Catalysts for Solar Water Splitting, Science (1979) 343 (2014) 990–994. https://doi.org/10.1126/science.1246913.
[46] S.C. Warren, K. Voïtchovsky, H. Dotan, C.M. Leroy, M. Cornuz, F. Stellacci, C. Hébert, A. Rothschild, M. Grätzel, Identifying champion nanostructures for solar water-splitting, Nat Mater 12 (2013) 842–849. https://doi.org/10.1038/nmat3684.
[47] G. Wang, H. Wang, Y. Ling, Y. Tang, X. Yang, R.C. Fitzmorris, C. Wang, J.Z. Zhang, Y. Li, Hydrogen-Treated TiO_2 Nanowire Arrays for Photoelectrochemical Water Splitting, Nano Lett 11 (2011) 3026–3033. https://doi.org/10.1021/nl201766h.
[48] L. Xi, K. Lange, Surface Modification of Hematite Photoanodes for Improvement of Photoelectrochemical Performance, Catalysts 8 (2018) 497. https://doi.org/10.3390/catal8110497.
[49] S. Cho, J.-W. Jang, K.-H. Lee, J.S. Lee, Research Update: Strategies for efficient photoelectrochemical water splitting using metal oxide photoanodes, APL Mater 2 (2014). https://doi.org/10.1063/1.4861798.
[50] S. Jeong, J. Song, S. Lee, Photoelectrochemical Device Designs toward Practical Solar Water Splitting: A Review on the Recent Progress of BiVO4 and BiFeO3 Photoanodes, Applied Sciences 8 (2018) 1388. https://doi.org/10.3390/app8081388.
[51] H. Zhao, H. Fu, X. Yang, S. Xiong, D. Han, X. An, MoS_2/CdS rod-like nanocomposites as high-performance visible light photocatalyst for water splitting photocatalytic hydrogen production, Int J Hydrogen Energy 47 (2022) 8247–8260. https://doi.org/10.1016/j.ijhydene.2021.12.171.
[52] W. Li, X. Chu, F. Wang, Y. Dang, X. Liu, T. Ma, J. Li, C. Wang, Pd single-atom decorated CdS nanocatalyst for highly efficient overall water splitting under simulated solar light, Appl Catal B 304 (2022) 121000. https://doi.org/10.1016/j.apcatb.2021.121000.
[53] J.D. Butson, P.R. Narangari, M. Lysevych, J. Wong-Leung, Y. Wan, S.K. Karuturi, H.H. Tan, C. Jagadish, InGaAsP as a Promising Narrow Band Gap Semiconductor for Photoelectrochemical Water Splitting, ACS Appl Mater Interfaces 11 (2019) 25236–25242. https://doi.org/10.1021/acsami.9b06656.
[54] M. Mohamed Abouelela, G. Kawamura, A. Matsuda, Metal chalcogenide-based photoelectrodes for photoelectrochemical water splitting, Journal of Energy Chemistry 73 (2022) 189–213. https://doi.org/10.1016/j.jechem.2022.05.022.
[55] S. Saji, Z. Yin, Non-Noble Plasmon Enhancement (NNPE) for PEC Energy Conversion, in: Atomic and Nano Scale Materials for Advanced Energy Conversion, Wiley, 2022: pp. 411–428. https://doi.org/10.1002/9783527831401.ch17.

[56] J. Cai, R. Li, J. Cao, J. Liu, J. Han, M. Huang, Plasmonic Au-decorated hierarchical p-NiO/n-ZnO heterostructure arrays for enhanced photoelectrochemical water splitting, Physica E Low Dimens Syst Nanostruct 135 (2022) 114974. https://doi.org/10.1016/j.physe.2021.114974.
[57] M.M. Abouelela, G. Kawamura, A. Matsuda, A review on plasmonic nanoparticle-semiconductor photocatalysts for water splitting, J Clean Prod 294 (2021) 126200. https://doi.org/10.1016/j.jclepro.2021.126200.
[58] S.Y. Jeong, H.-M. Shin, Y.-R. Jo, Y.J. Kim, S. Kim, W.-J. Lee, G.J. Lee, J. Song, B.J. Moon, S. Seo, H. An, S.H. Lee, Y.M. Song, B.-J. Kim, M.-H. Yoon, S. Lee, Plasmonic Silver Nanoparticle-Impregnated Nanocomposite BiVO $_4$ Photoanode for Plasmon-Enhanced Photocatalytic Water Splitting, The Journal of Physical Chemistry C 122 (2018) 7088–7093. https://doi.org/10.1021/acs.jpcc.8b00220.
[59] G. Kawamura, A. Matsuda, Synthesis of Plasmonic Photocatalysts for Water Splitting, Catalysts 9 (2019) 982. https://doi.org/10.3390/catal9120982.
[60] B.S. Kalanoor, H. Seo, S.S. Kalanur, Multiple ion doping in $BiVO_4$ as an effective strategy of enhancing photoelectrochemical water splitting: A review, Mater Sci Energy Technol 4 (2021) 317–328. https://doi.org/10.1016/j.mset.2021.08.010.
[61] M.G. Lee, C.W. Moon, H. Park, W. Sohn, S.B. Kang, S. Lee, K.J. Choi, H.W. Jang, Dominance of Plasmonic Resonant Energy Transfer over Direct Electron Transfer in Substantially Enhanced Water Oxidation Activity of $BiVO_4$ by Shape-Controlled Au Nanoparticles, Small 13 (2017). https://doi.org/10.1002/smll.201701644.
[62] S. Kim, Y. Yu, S.Y. Jeong, M.G. Lee, H.W. Jeong, Y.M. Kwon, J.M. Baik, H. Park, H.W. Jang, S. Lee, Plasmonic gold nanoparticle-decorated $BiVO_4$ /ZnO nanowire heterostructure photoanodes for efficient water oxidation, Catal Sci Technol 8 (2018) 3759–3766. https://doi.org/10.1039/C8CY00685G.
[63] T. Jafari, E. Moharreri, A. Amin, R. Miao, W. Song, S. Suib, Photocatalytic Water Splitting—The Untamed Dream: A Review of Recent Advances, Molecules 21 (2016) 900. https://doi.org/10.3390/molecules21070900.
[64] A. Kudo, Y. Miseki, Heterogeneous photocatalyst materials for water splitting, Chem. Soc. Rev. 38 (2009) 253–278. https://doi.org/10.1039/B800489G.
[65] B. Iandolo, B. Wickman, I. Zorić, A. Hellman, The rise of hematite: origin and strategies to reduce the high onset potential for the oxygen evolution reaction, J Mater Chem A Mater 3 (2015) 16896–16912. https://doi.org/10.1039/C5TA03362D.
[66] S. Mahalingam, H. Abdullah, Electron transport study of indium oxide as photoanode in DSSCs: A review, Renewable and Sustainable Energy Reviews 63 (2016) 245–255. https://doi.org/10.1016/j.rser.2016.05.067.
[67] B. Wickman, A. Bastos Fanta, A. Burrows, A. Hellman, J.B. Wagner, B. Iandolo, Iron Oxide Films Prepared by Rapid Thermal Processing for Solar Energy Conversion, Sci Rep 7 (2017) 40500. https://doi.org/10.1038/srep40500.
[68] A. J. Frank, N. Kopidakis, J. van de Lagemaat, Electrons in nanostructured TiO_2 solar cells: transport, recombination and photovoltaic properties, Coord Chem Rev 248 (2004) 1165–1179. https://doi.org/10.1016/j.ccr.2004.03.015.
[69] J. Low, J. Yu, M. Jaroniec, S. Wageh, A.A. Al-Ghamdi, Heterojunction Photocatalysts, Advanced Materials 29 (2017). https://doi.org/10.1002/adma.201601694.

[70] S. Li, W. Xu, L. Meng, W. Tian, L. Li, Recent Progress on Semiconductor Heterojunction-Based Photoanodes for Photoelectrochemical Water Splitting, Small Science 2 (2022). https://doi.org/10.1002/smsc.202100112.
[71] M. Xiao, B. Luo, Z. Wang, S. Wang, L. Wang, Recent Advances of Metal-Oxide Photoanodes: Engineering of Charge Separation and Transportation toward Efficient Solar Water Splitting, Solar RRL 4 (2020). https://doi.org/10.1002/solr.201900509.
[72] R. Abe, Recent progress on photocatalytic and photoelectrochemical water splitting under visible light irradiation, Journal of Photochemistry and Photobiology C: Photochemistry Reviews 11 (2010) 179–209. https://doi.org/10.1016/j.jphotochemrev.2011.02.003.
[73] J. Jian, G. Jiang, R. van de Krol, B. Wei, H. Wang, Recent advances in rational engineering of multinary semiconductors for photoelectrochemical hydrogen generation, Nano Energy 51 (2018) 457–480. https://doi.org/10.1016/j.nanoen.2018.06.074.
[74] X. Liu, J. Chi, B. Dong, Y. Sun, Recent Progress in Decoupled H_2 and O_2 Production from Electrolytic Water Splitting, ChemElectroChem 6 (2019) 2157–2166. https://doi.org/10.1002/celc.201801671.
[75] Q. Lu, Y. Yu, Q. Ma, B. Chen, H. Zhang, 2D Transition-Metal-Dichalcogenide-Nanosheet-Based Composites for Photocatalytic and Electrocatalytic Hydrogen Evolution Reactions, Advanced Materials 28 (2016) 1917–1933. https://doi.org/10.1002/adma.201503270.
[76] P. Ma, D. Wang, THE PRINCIPLE OF PHOTOELECTROCHEMICAL WATER SPLITTING, in: Nanomaterials for Energy Conversion and Storage, WORLD SCIENTIFIC (EUROPE), 2018: pp. 1–61. https://doi.org/10.1142/9781786343635_0001.
[77] S.S. Kalanur, L.T. Duy, H. Seo, Recent Progress in Photoelectrochemical Water Splitting Activity of WO_3 Photoanodes, Top Catal 61 (2018) 1043–1076. https://doi.org/10.1007/s11244-018-0950-1.
[78] S. Guldin, S. Hüttner, P. Tiwana, M.C. Orilall, B. Ülgüt, M. Stefik, P. Docampo, M. Kolle, G. Divitini, C. Ducati, S.A.T. Redfern, H.J. Snaith, U. Wiesner, D. Eder, U. Steiner, Improved conductivity in dye-sensitised solar cells through block-copolymer confined TiO_2 crystallisation, Energy Environ. Sci. 4 (2011) 225–233. https://doi.org/10.1039/C0EE00362J.
[79] L. Shi, S. Zhuo, M. Abulikemu, G. Mettela, T. Palaniselvam, S. Rasul, B. Tang, B. Yan, N.B. Saleh, P. Wang, Annealing temperature effects on photoelectrochemical performance of bismuth vanadate thin film photoelectrodes, RSC Adv 8 (2018) 29179–29188. https://doi.org/10.1039/C8RA04887H.
[80] A. Iqbal, N.M. Hamdan, Investigation and Optimization of Mxene Functionalized Mesoporous Titania Films as Efficient Photoelectrodes, Materials 14 (2021) 6292. https://doi.org/10.3390/ma14216292.
[81] J.Y. Kim, G. Magesh, D.H. Youn, J.-W. Jang, J. Kubota, K. Domen, J.S. Lee, Single-crystalline, wormlike hematite photoanodes for efficient solar water splitting, Sci Rep 3 (2013) 2681. https://doi.org/10.1038/srep02681.
[82] H. Sun, W. Hua, Y. Li, J.-G. Wang, Conformal coating of superhydrophilic metal-organic complex toward substantially improved photoelectrochemical water oxidation, Chemical Engineering Journal 427 (2022) 131004. https://doi.org/10.1016/j.cej.2021.131004.
[83] H. Wang, Y. Gao, J. Liu, X. Li, M. Ji, E. Zhang, X. Cheng, M. Xu, J. Liu, H. Rong, W. Chen, F. Fan, C. Li, J. Zhang, Efficient Plasmonic Au/CdSe Nanodumbbell for Photoelectrochemical Hydrogen Generation beyond Visible Region, Adv Energy Mater 9 (2019). https://doi.org/10.1002/aenm.201803889.

[84] N.L. Reddy, V.N. Rao, M. Vijayakumar, R. Santhosh, S. Anandan, M. Karthik, M.V. Shankar, K.R. Reddy, N.P. Shetti, M.N. Nadagouda, T.M. Aminabhavi, A review on frontiers in plasmonic nano-photocatalysts for hydrogen production, Int J Hydrogen Energy 44 (2019) 10453–10472. https://doi.org/10.1016/j.ijhydene.2019.02.120.

[85] W.J. Youngblood, S.-H.A. Lee, K. Maeda, T.E. Mallouk, Visible Light Water Splitting Using Dye-Sensitized Oxide Semiconductors, Acc Chem Res 42 (2009) 1966–1973. https://doi.org/10.1021/ar9002398.

[86] J. Li, S.K. Cushing, P. Zheng, T. Senty, F. Meng, A.D. Bristow, A. Manivannan, N. Wu, Solar Hydrogen Generation by a CdS-Au-TiO_2 Sandwich Nanorod Array Enhanced with Au Nanoparticle as Electron Relay and Plasmonic Photosensitizer, J Am Chem Soc 136 (2014) 8438–8449. https://doi.org/10.1021/ja503508g.

[87] M. de Respinis, K.S. Joya, H.J.M. De Groot, F. D'Souza, W.A. Smith, R. van de Krol, B. Dam, Solar Water Splitting Combining a $BiVO_4$ Light Absorber with a Ru-Based Molecular Cocatalyst, The Journal of Physical Chemistry C 119 (2015) 7275–7281. https://doi.org/10.1021/acs.jpcc.5b00287.

[88] P. Zhang, T. Wang, J. Gong, Mechanistic Understanding of the Plasmonic Enhancement for Solar Water Splitting, Advanced Materials 27 (2015) 5328–5342. https://doi.org/10.1002/adma.201500888.

[89] S.C. Warren, E. Thimsen, Plasmonic solar water splitting, Energy Environ. Sci. 5 (2012) 5133–5146. https://doi.org/10.1039/C1EE02875H.

[90] S. Linic, P. Christopher, D.B. Ingram, Plasmonic-metal nanostructures for efficient conversion of solar to chemical energy, Nat Mater 10 (2011) 911–921. https://doi.org/10.1038/nmat3151.

[91] M. Valenti, E. Kontoleta, I.A. Digdaya, M.P. Jonsson, G. Biskos, A. Schmidt-Ott, W.A. Smith, The Role of Size and Dimerization of Decorating Plasmonic Silver Nanoparticles on the Photoelectrochemical Solar Water Splitting Performance of $BiVO_4$ Photoanodes, ChemNanoMat 2 (2016) 739–747. https://doi.org/10.1002/cnma.201600026.

[92] C. Clavero, Plasmon-induced hot-electron generation at nanoparticle/metal-oxide interfaces for photovoltaic and photocatalytic devices, Nat Photonics 8 (2014) 95–103. https://doi.org/10.1038/nphoton.2013.238.

[93] S. Mubeen, J. Lee, N. Singh, S. Krämer, G.D. Stucky, M. Moskovits, An autonomous photosynthetic device in which all charge carriers derive from surface plasmons, Nat Nanotechnol 8 (2013) 247–251. https://doi.org/10.1038/nnano.2013.18.

[94] S.K. Cushing, J. Li, F. Meng, T.R. Senty, S. Suri, M. Zhi, M. Li, A.D. Bristow, N. Wu, Photocatalytic Activity Enhanced by Plasmonic Resonant Energy Transfer from Metal to Semiconductor, J Am Chem Soc 134 (2012) 15033–15041. https://doi.org/10.1021/ja305603t.

[95] H.M. Chen, C.K. Chen, C.-J. Chen, L.-C. Cheng, P.C. Wu, B.H. Cheng, Y.Z. Ho, M.L. Tseng, Y.-Y. Hsu, T.-S. Chan, J.-F. Lee, R.-S. Liu, D.P. Tsai, Plasmon Inducing Effects for Enhanced Photoelectrochemical Water Splitting: X-ray Absorption Approach to Electronic Structures, ACS Nano 6 (2012) 7362–7372. https://doi.org/10.1021/nn3024877.

[96] M. Haro, R. Abargues, I. Herraiz-Cardona, J. Martínez-Pastor, S. Giménez, Plasmonic versus catalytic effect of gold nanoparticles on mesoporous TiO_2 electrodes for water splitting, Electrochim Acta 144 (2014) 64–70. https://doi.org/10.1016/j.electacta.2014.07.146.

[97] W.R. Erwin, H.F. Zarick, E.M. Talbert, R. Bardhan, Light trapping in mesoporous solar cells with plasmonic nanostructures, Energy Environ Sci 9 (2016) 1577–1601. https://doi.org/10.1039/C5EE03847B.
[98] M. Valenti, D. Dolat, G. Biskos, A. Schmidt-Ott, W.A. Smith, Enhancement of the Photoelectrochemical Performance of $CuWO_4$ Thin Films for Solar Water Splitting by Plasmonic Nanoparticle Functionalization, The Journal of Physical Chemistry C 119 (2015) 2096–2104. https://doi.org/10.1021/jp506349t.
[99] A. Piot, S.K. Earl, C. Ng, S. Dligatch, A. Roberts, T.J. Davis, D.E. Gómez, Collective excitation of plasmonic hot-spots for enhanced hot charge carrier transfer in metal/semiconductor contacts, Nanoscale 7 (2015) 8294–8298. https://doi.org/10.1039/C5NR01592H.
[100] E. Thimsen, F. Le Formal, M. Grätzel, S.C. Warren, Influence of Plasmonic Au Nanoparticles on the Photoactivity of Fe_2 O_3 Electrodes for Water Splitting, Nano Lett 11 (2011) 35–43. https://doi.org/10.1021/nl1022354.
[101] M. Xiao, R. Jiang, F. Wang, C. Fang, J. Wang, J.C. Yu, Plasmon-enhanced chemical reactions, J Mater Chem A Mater 1 (2013) 5790. https://doi.org/10.1039/c3ta01450a.
[102] G. Kawamura, T. Arai, H. Muto, A. Matsuda, Charge behavior in a plasmonic photocatalyst composed of Au and TiO_2, Catal Sci Technol 8 (2018) 1813–1818. https://doi.org/10.1039/C8CY00120K.
[103] M. Gao, P.K.N. Connor, G.W. Ho, Plasmonic photothermic directed broadband sunlight harnessing for seawater catalysis and desalination, Energy Environ Sci 9 (2016) 3151–3160. https://doi.org/10.1039/C6EE00971A.
[104] J. Katyal, R.K. Soni, Size- and shape-dependent plasmonic properties of aluminum nanoparticles for nanosensing applications, J Mod Opt 60 (2013) 1717–1728. https://doi.org/10.1080/09500340.2013.856483.
[105] Y. Tian, T. Tatsuma, Mechanisms and Applications of Plasmon-Induced Charge Separation at TiO_2 Films Loaded with Gold Nanoparticles, J Am Chem Soc 127 (2005) 7632–7637. https://doi.org/10.1021/ja042192u.
[106] L. Brus, Noble Metal Nanocrystals: Plasmon Electron Transfer Photochemistry and Single-Molecule Raman Spectroscopy, Acc Chem Res 41 (2008) 1742–1749. https://doi.org/10.1021/ar800121r.
[107] C. Burda, X. Chen, R. Narayanan, M.A. El-Sayed, Chemistry and Properties of Nanocrystals of Different Shapes, Chem Rev 105 (2005) 1025–1102. https://doi.org/10.1021/cr030063a.
[108] M.A. El-Sayed, Some Interesting Properties of Metals Confined in Time and Nanometer Space of Different Shapes, Acc Chem Res 34 (2001) 257–264. https://doi.org/10.1021/ar960016n.
[109] K.L. Kelly, E. Coronado, L.L. Zhao, G.C. Schatz, The Optical Properties of Metal Nanoparticles: The Influence of Size, Shape, and Dielectric Environment, J Phys Chem B 107 (2003) 668–677. https://doi.org/10.1021/jp026731y.
[110] Y. Xia, Y. Xiong, B. Lim, S.E. Skrabalak, Shape-Controlled Synthesis of Metal Nanocrystals: Simple Chemistry Meets Complex Physics?, Angewandte Chemie International Edition 48 (2009) 60–103. https://doi.org/10.1002/anie.200802248.
[111] M. Rycenga, C.M. Cobley, J. Zeng, W. Li, C.H. Moran, Q. Zhang, D. Qin, Y. Xia, Controlling the Synthesis and Assembly of Silver Nanostructures for Plasmonic Applications, Chem Rev 111 (2011) 3669–3712. https://doi.org/10.1021/cr100275d.

[112] Z. Zou, J. Ye, K. Sayama, H. Arakawa, Direct splitting of water under visible light irradiation with an oxide semiconductor photocatalyst, Nature 414 (2001) 625–627. https://doi.org/10.1038/414625a.
[113] A. Kudo, Y. Miseki, Heterogeneous photocatalyst materials for water splitting, Chem. Soc. Rev. 38 (2009) 253–278. https://doi.org/10.1039/B800489G.
[114] T. Jafari, E. Moharreri, A. Amin, R. Miao, W. Song, S. Suib, Photocatalytic Water Splitting—The Untamed Dream: A Review of Recent Advances, Molecules 21 (2016) 900. https://doi.org/10.3390/molecules21070900.
[115] P.A. DeSario, J.J. Pietron, D.E. DeVantier, T.H. Brintlinger, R.M. Stroud, D.R. Rolison, Plasmonic enhancement of visible-light water splitting with Au–TiO_2 composite aerogels, Nanoscale 5 (2013) 8073. https://doi.org/10.1039/c3nr01429k.
[116] M.L. Anderson, R.M. Stroud, C.A. Morris, C.I. Merzbacher, D.R. Rolison, Tailoring Advanced Nanoscale Materials Through Synthesis of Composite Aerogel Architectures, Adv Eng Mater 2 (2000) 481–488. https://doi.org/10.1002/1527-2648(200008)2:8<481::AID-ADEM481>3.0.CO;2-O.
[117] Y. Lin, G. Yuan, R. Liu, S. Zhou, S.W. Sheehan, D. Wang, Semiconductor nanostructure-based photoelectrochemical water splitting: A brief review, Chem Phys Lett 507 (2011) 209–215. https://doi.org/10.1016/j.cplett.2011.03.074.
[118] S. Nishimura, N. Abrams, B.A. Lewis, L.I. Halaoui, T.E. Mallouk, K.D. Benkstein, J. van de Lagemaat, A.J. Frank, Standing Wave Enhancement of Red Absorbance and Photocurrent in Dye-Sensitized Titanium Dioxide Photoelectrodes Coupled to Photonic Crystals, J Am Chem Soc 125 (2003) 6306–6310. https://doi.org/10.1021/ja034650p.
[119] J.J. Pietron, A.M. Stux, R.S. Compton, D.R. Rolison, Dye-sensitized titania aerogels as photovoltaic electrodes for electrochemical solar cells, Solar Energy Materials and Solar Cells 91 (2007) 1066–1074. https://doi.org/10.1016/j.solmat.2007.02.021.
[120] S.C. Roy, O.K. Varghese, M. Paulose, C.A. Grimes, Toward Solar Fuels: Photocatalytic Conversion of Carbon Dioxide to Hydrocarbons, ACS Nano 4 (2010) 1259–1278. https://doi.org/10.1021/nn9015423.
[121] Á. Valdés, J. Brillet, M. Grätzel, H. Gudmundsdóttir, H.A. Hansen, H. Jónsson, P. Klüpfel, G.-J. Kroes, F. Le Formal, I.C. Man, R.S. Martins, J.K. Nørskov, J. Rossmeisl, K. Sivula, A. Vojvodic, M. Zäch, Solar hydrogen production with semiconductor metal oxides: new directions in experiment and theory, Phys. Chem. Chem. Phys. 14 (2012) 49–70. https://doi.org/10.1039/C1CP23212F.
[122] N. Liu, S.P. Albu, K. Lee, S. So, P. Schmuki, Water annealing and other low temperature treatments of anodic TiO_2 nanotubes: A comparison of properties and efficiencies in dye sensitized solar cells and for water splitting, Electrochim Acta 82 (2012) 98–102. https://doi.org/10.1016/j.electacta.2012.06.006.
[123] R.P. Lynch, A. Ghicov, P. Schmuki, A Photo-Electrochemical Investigation of Self-Organized TiO_2 Nanotubes, J Electrochem Soc 157 (2010) G76. https://doi.org/10.1149/1.3276455.
[124] J.R. Jennings, A. Ghicov, L.M. Peter, P. Schmuki, A.B. Walker, Dye-Sensitized Solar Cells Based on Oriented TiO_2 Nanotube Arrays: Transport, Trapping, and Transfer of Electrons, J Am Chem Soc 130 (2008) 13364–13372. https://doi.org/10.1021/ja804852z.
[125] L. Forro, O. Chauvet, D. Emin, L. Zuppiroli, H. Berger, F. Lévy, High mobility *n* -type charge carriers in large single crystals of anatase (TiO_2), J Appl Phys 75 (1994) 633–635. https://doi.org/10.1063/1.355801.

[126] J. Gong, Y. Lai, C. Lin, Electrochemically multi-anodized TiO_2 nanotube arrays for enhancing hydrogen generation by photoelectrocatalytic water splitting, Electrochim Acta 55 (2010) 4776–4782. https://doi.org/10.1016/j.electacta.2010.03.055.
[127] K. Qian, B.C. Sweeny, A.C. Johnston-Peck, W. Niu, J.O. Graham, J.S. DuChene, J. Qiu, Y.-C. Wang, M.H. Engelhard, D. Su, E.A. Stach, W.D. Wei, Surface Plasmon-Driven Water Reduction: Gold Nanoparticle Size Matters, J Am Chem Soc 136 (2014) 9842–9845. https://doi.org/10.1021/ja504097v.
[128] L. Zhang, L.O. Herrmann, J.J. Baumberg, Size Dependent Plasmonic Effect on BiVO4 Photoanodes for Solar Water Splitting, Sci Rep 5 (2015) 16660. https://doi.org/10.1038/srep16660.
[129] M.J. Sampaio, J.W.L. Oliveira, C.I.L. Sombrio, D.L. Baptista, S.R. Teixeira, S.A.C. Carabineiro, C.G. Silva, J.L. Faria, Photocatalytic performance of Au/ZnO nanocatalysts for hydrogen production from ethanol, Appl Catal A Gen 518 (2016) 198–205. https://doi.org/10.1016/j.apcata.2015.10.013.
[130] A. Sousa-Castillo, M. Comesaña-Hermo, B. Rodríguez-González, M. Pérez-Lorenzo, Z. Wang, X.-T. Kong, A.O. Govorov, M.A. Correa-Duarte, Boosting Hot Electron-Driven Photocatalysis through Anisotropic Plasmonic Nanoparticles with Hot Spots in Au–TiO_2 Nanoarchitectures, The Journal of Physical Chemistry C 120 (2016) 11690–11699. https://doi.org/10.1021/acs.jpcc.6b02370.
[131] H. Harutyunyan, A.B.F. Martinson, D. Rosenmann, L.K. Khorashad, L. V. Besteiro, A.O. Govorov, G.P. Wiederrecht, Anomalous ultrafast dynamics of hot plasmonic electrons in nanostructures with hot spots, Nat Nanotechnol 10 (2015) 770–774. https://doi.org/10.1038/nnano.2015.165.
[132] Y.-C. Pu, G. Wang, K.-D. Chang, Y. Ling, Y.-K. Lin, B.C. Fitzmorris, C.-M. Liu, X. Lu, Y. Tong, J.Z. Zhang, Y.-J. Hsu, Y. Li, Au Nanostructure-Decorated TiO_2 Nanowires Exhibiting Photoactivity Across Entire UV-visible Region for Photoelectrochemical Water Splitting, Nano Lett 13 (2013) 3817–3823. https://doi.org/10.1021/nl4018385.
[133] S.P. Meshram, P.V. Adhyapak, U.P. Mulik, D.P. Amalnerkar, Facile synthesis of CuO nanomorphs and their morphology dependent sunlight driven photocatalytic properties, Chemical Engineering Journal 204–206 (2012) 158–168. https://doi.org/10.1016/j.cej.2012.07.012.
[134] M.J. Villaseñor, Á. Ríos, Nanomaterials for water cleaning and desalination, energy production, disinfection, agriculture and green chemistry, Environ Chem Lett 16 (2018) 11–34. https://doi.org/10.1007/s10311-017-0656-9.
[135] N. Lakshmana Reddy, V. Navakoteswara Rao, M. Mamatha Kumari, R.R. Kakarla, P. Ravi, M. Sathish, M. Karthik, S. Muthukonda Venkatakrishnan, Inamuddin, Nanostructured semiconducting materials for efficient hydrogen generation, Environ Chem Lett 16 (2018) 765–796. https://doi.org/10.1007/s10311-018-0722-y.
[136] L. Sang, Y. Zhao, C. Burda, TiO_2 Nanoparticles as Functional Building Blocks, Chem Rev 114 (2014) 9283–9318. https://doi.org/10.1021/cr400629p.
[137] Y. Ma, X. Wang, Y. Jia, X. Chen, H. Han, C. Li, Titanium Dioxide-Based Nanomaterials for Photocatalytic Fuel Generations, Chem Rev 114 (2014) 9987–10043. https://doi.org/10.1021/cr500008u.
[138] T. Takata, K. Domen, Defect Engineering of Photocatalysts by Doping of Aliovalent Metal Cations for Efficient Water Splitting, The Journal of Physical Chemistry C 113 (2009) 19386–19388. https://doi.org/10.1021/jp908621e.

[139] K. Furuhashi, Q. Jia, A. Kudo, H. Onishi, Time-Resolved Infrared Absorption Study of $SrTiO_3$ Photocatalysts Codoped with Rhodium and Antimony, The Journal of Physical Chemistry C 117 (2013) 19101–19106. https://doi.org/10.1021/jp407040p.
[140] M. Valenti, M.P. Jonsson, G. Biskos, A. Schmidt-Ott, W.A. Smith, Plasmonic nanoparticle-semiconductor composites for efficient solar water splitting, J Mater Chem A Mater 4 (2016) 17891–17912. https://doi.org/10.1039/C6TA06405A.
[141] W. Hou, S.B. Cronin, A Review of Surface Plasmon Resonance-Enhanced Photocatalysis, Adv Funct Mater 23 (2013) 1612–1619. https://doi.org/10.1002/adfm.201202148.
[142] J. Yu, L. Qi, M. Jaroniec, Hydrogen Production by Photocatalytic Water Splitting over Pt/TiO_2 Nanosheets with Exposed (001) Facets, The Journal of Physical Chemistry C 114 (2010) 13118–13125. https://doi.org/10.1021/jp104488b.
[143] J. Wu, S. Lu, D. Ge, L. Zhang, W. Chen, H. Gu, Photocatalytic properties of Pd/TiO_2 nanosheets for hydrogen evolution from water splitting, RSC Adv 6 (2016) 67502–67508. https://doi.org/10.1039/C6RA10408H.
[144] W.-T. Chen, A. Chan, Z.H.N. Al-Azri, A.G. Dosado, M.A. Nadeem, D. Sun-Waterhouse, H. Idriss, G.I.N. Waterhouse, Effect of TiO_2 polymorph and alcohol sacrificial agent on the activity of Au/TiO2 photocatalysts for H_2 production in alcohol–water mixtures, J Catal 329 (2015) 499–513. https://doi.org/10.1016/j.jcat.2015.06.014.
[145] Z. Bian, T. Tachikawa, P. Zhang, M. Fujitsuka, T. Majima, Au/TiO_2 Superstructure-Based Plasmonic Photocatalysts Exhibiting Efficient Charge Separation and Unprecedented Activity, J Am Chem Soc 136 (2014) 458–465. https://doi.org/10.1021/ja410994f.
[146] S.-S. Yi, X.-B. Zhang, B.-R. Wulan, J.-M. Yan, Q. Jiang, Non-noble metals applied to solar water splitting, Energy Environ Sci 11 (2018) 3128–3156. https://doi.org/10.1039/C8EE02096E.
[147] P. Zhang, T. Song, T. Wang, H. Zeng, In-situ synthesis of Cu nanoparticles hybridized with carbon quantum dots as a broad spectrum photocatalyst for improvement of photocatalytic H_2 evolution, Appl Catal B 206 (2017) 328–335. https://doi.org/10.1016/j.apcatb.2017.01.051.
[148] P. Gomathisankar, K. Hachisuka, H. Katsumata, T. Suzuki, K. Funasaka, S. Kaneco, Enhanced photocatalytic hydrogen production from aqueous methanol solution using ZnO with simultaneous photodeposition of Cu, Int J Hydrogen Energy 38 (2013) 11840–11846. https://doi.org/10.1016/j.ijhydene.2013.06.131.
[149] D.-N. Bui, J. Mu, L. Wang, S.-Z. Kang, X. Li, Preparation of Cu-loaded $SrTiO_3$ nanoparticles and their photocatalytic activity for hydrogen evolution from methanol aqueous solution, Appl Surf Sci 274 (2013) 328–333. https://doi.org/10.1016/j.apsusc.2013.03.054.
[150] K.K. M., B. K., N. G., S. B., V. A., Plasmonic resonance nature of $Ag\text{-}Cu/TiO_2$ photocatalyst under solar and artificial light: Synthesis, characterization and evaluation of H_2O splitting activity, Appl Catal B 199 (2016) 282–291. https://doi.org/10.1016/j.apcatb.2016.06.050.
[151] H. Tian, X.L. Zhang, J. Scott, C. Ng, R. Amal, TiO_2 -supported copper nanoparticles prepared via ion exchange for photocatalytic hydrogen production, J. Mater. Chem. A 2 (2014) 6432–6438. https://doi.org/10.1039/C3TA15254E.
[152] P.D. Tran, L. Xi, S.K. Batabyal, L.H. Wong, J. Barber, J.S. Chye Loo, Enhancing the photocatalytic efficiency of TiO_2 nanopowders for H2 production by using non-noble

transition metal co-catalysts, Physical Chemistry Chemical Physics 14 (2012) 11596. https://doi.org/10.1039/c2cp41450c.
[153] Y. Yang, P. Gao, Y. Wang, L. Sha, X. Ren, J. Zhang, P. Yang, T. Wu, Y. Chen, X. Li, A simple and efficient hydrogen production-storage hybrid system (Co/TiO_2) for synchronized hydrogen photogeneration with uptake, J Mater Chem A Mater 5 (2017) 9198–9203. https://doi.org/10.1039/C7TA00818J.
[154] M. Melchionna, A. Beltram, A. Stopin, T. Montini, R.W. Lodge, A.N. Khlobystov, D. Bonifazi, M. Prato, P. Fornasiero, Magnetic shepherding of nanocatalysts through hierarchically-assembled Fe-filled CNTs hybrids, Appl Catal B 227 (2018) 356–365. https://doi.org/10.1016/j.apcatb.2018.01.049.
[155] X. Zhou, Z.T. Gossage, B.H. Simpson, J. Hui, Z.J. Barton, J. Rodríguez-López, Electrochemical Imaging of Photoanodic Water Oxidation Enhancements on TiO_2 Thin Films Modified by Subsurface Aluminum Nanodimers, ACS Nano 10 (2016) 9346–9352. https://doi.org/10.1021/acsnano.6b04004.
[156] X. Li, M. Bi, L. Cui, Y. Zhou, X. Du, S. Qiao, J. Yang, 3D Aluminum Hybrid Plasmonic Nanostructures with Large Areas of Dense Hot Spots and Long-Term Stability, Adv Funct Mater 27 (2017). https://doi.org/10.1002/adfm.201605703.
[157] Y. Chen, X. Xin, N. Zhang, Y. Xu, Aluminum-Based Plasmonic Photocatalysis, Particle & Particle Systems Characterization 34 (2017). https://doi.org/10.1002/ppsc.201600357.
[158] Q. Hao, C. Wang, H. Huang, W. Li, D. Du, D. Han, T. Qiu, P.K. Chu, Aluminum plasmonic photocatalysis, Sci Rep 5 (2015) 15288. https://doi.org/10.1038/srep15288.
[159] E.R. Encina, N. Passarelli, E.A. Coronado, Plasmon enhanced light absorption in aluminium@Hematite core shell hybrid nanocylinders: the critical role of length, RSC Adv 7 (2017) 2857–2868. https://doi.org/10.1039/C6RA27594J.
[160] Y. Cui, Z. Zhou, T. Li, K. Wang, J. Li, Z. Wei, Versatile Crystal Structures and (Opto)electronic Applications of the 2D Metal Mono-, Di-, and Tri-Chalcogenide Nanosheets, Adv Funct Mater 29 (2019). https://doi.org/10.1002/adfm.201900040.
[161] S. Hou, X.-C. Dai, Y.-B. Li, M.-H. Huang, T. Li, Z.-Q. Wei, Y. He, G. Xiao, F.-X. Xiao, Charge transfer modulation in layer-by-layer-assembled multilayered photoanodes for solar water oxidation, J Mater Chem A Mater 7 (2019) 22487–22499. https://doi.org/10.1039/C9TA08107K.
[162] Q.-L. Mo, S. Hou, Z.-Q. Wei, X.-Y. Fu, G. Xiao, F.-X. Xiao, Fine tuning of charge motion over homogeneous transient metal chalcogenides heterostructured photoanodes for photoelectrochemical water splitting, Chemical Engineering Journal 433 (2022) 133641. https://doi.org/10.1016/j.cej.2021.133641.
[163] Q.-L. Mo, X. Lin, Z.-Q. Wei, X.-C. Dai, S. Hou, T. Li, F.-X. Xiao, All-in-one: branched macromolecule-protected metal nanocrystals as integrated charge separation/motion centers for enhanced photocatalytic selective organic transformations, J Mater Chem A Mater 8 (2020) 16392–16404. https://doi.org/10.1039/D0TA05297C.
[164] Z. Hu, Z. Wu, C. Han, J. He, Z. Ni, W. Chen, Two-dimensional transition metal dichalcogenides: interface and defect engineering, Chem Soc Rev 47 (2018) 3100–3128. https://doi.org/10.1039/C8CS00024G.
[165] S. Chandrasekaran, L. Yao, L. Deng, C. Bowen, Y. Zhang, S. Chen, Z. Lin, F. Peng, P. Zhang, Recent advances in metal sulfides: from controlled fabrication to electrocatalytic, photocatalytic and photoelectrochemical water splitting and beyond, Chem Soc Rev 48 (2019) 4178–4280. https://doi.org/10.1039/C8CS00664D.

[166] Y.B. Kim, S.H. Jung, D.S. Kim, N.G. Deshpande, H.S. Lee, H.K. Cho, Interleaved biphasic p–n blended copper indium selenide photoelectrode and its application in pulse-driven photoelectrochemical water splitting, Appl Catal B 285 (2021) 119839. https://doi.org/10.1016/j.apcatb.2020.119839.
[167] H. Wang, Y. Xia, H. Li, X. Wang, Y. Yu, X. Jiao, D. Chen, Highly active deficient ternary sulfide photoanode for photoelectrochemical water splitting, Nat Commun 11 (2020) 3078. https://doi.org/10.1038/s41467-020-16800-w.
[168] X. Hu, G. Li, J.C. Yu, Design, Fabrication, and Modification of Nanostructured Semiconductor Materials for Environmental and Energy Applications, Langmuir 26 (2010) 3031–3039. https://doi.org/10.1021/la902142b.
[169] J. McAllister, N.A.G. Bandeira, J.C. McGlynn, A.Y. Ganin, Y.-F. Song, C. Bo, H.N. Miras, Tuning and mechanistic insights of metal chalcogenide molecular catalysts for the hydrogen-evolution reaction, Nat Commun 10 (2019) 370. https://doi.org/10.1038/s41467-018-08208-4.
[170] K. Wu, Y. Du, H. Tang, Z. Chen, T. Lian, Efficient Extraction of Trapped Holes from Colloidal CdS Nanorods, J Am Chem Soc 137 (2015) 10224–10230. https://doi.org/10.1021/jacs.5b04564.
[171] Y. Lei, X. Wu, S. Li, J. Huang, K.H. Ng, Y. Lai, Noble-metal-free metallic MoC combined with CdS for enhanced visible-light-driven photocatalytic hydrogen evolution, J Clean Prod 322 (2021) 129018. https://doi.org/10.1016/j.jclepro.2021.129018.
[172] R. Marschall, Semiconductor Composites: Strategies for Enhancing Charge Carrier Separation to Improve Photocatalytic Activity, Adv Funct Mater 24 (2014) 2421–2440. https://doi.org/10.1002/adfm.201303214.
[173] S. Anantharaj, S.R. Ede, K. Sakthikumar, K. Karthick, S. Mishra, S. Kundu, Recent Trends and Perspectives in Electrochemical Water Splitting with an Emphasis on Sulfide, Selenide, and Phosphide Catalysts of Fe, Co, and Ni: A Review, ACS Catal 6 (2016) 8069–8097. https://doi.org/10.1021/acscatal.6b02479.
[174] S. Manzeli, D. Ovchinnikov, D. Pasquier, O. V. Yazyev, A. Kis, 2D transition metal dichalcogenides, Nat Rev Mater 2 (2017) 17033. https://doi.org/10.1038/natrevmats.2017.33.
[175] K.F. Mak, J. Shan, Photonics and optoelectronics of 2D semiconductor transition metal dichalcogenides, Nat Photonics 10 (2016) 216–226. https://doi.org/10.1038/nphoton.2015.282.
[176] X. Xu, W. Yao, D. Xiao, T.F. Heinz, Spin and pseudospins in layered transition metal dichalcogenides, Nat Phys 10 (2014) 343–350. https://doi.org/10.1038/nphys2942.
[177] F.H.L. Koppens, T. Mueller, Ph. Avouris, A.C. Ferrari, M.S. Vitiello, M. Polini, Photodetectors based on graphene, other two-dimensional materials and hybrid systems, Nat Nanotechnol 9 (2014) 780–793. https://doi.org/10.1038/nnano.2014.215.
[178] J. Yin, J. Jin, H. Lin, Z. Yin, J. Li, M. Lu, L. Guo, P. Xi, Y. Tang, C. Yan, Optimized Metal Chalcogenides for Boosting Water Splitting, Advanced Science 7 (2020) 1903070. https://doi.org/10.1002/advs.201903070.
[179] L. Jin, H. Zhao, Z.M. Wang, F. Rosei, Quantum Dots-Based Photoelectrochemical Hydrogen Evolution from Water Splitting, Adv Energy Mater 11 (2021) 2003233. https://doi.org/10.1002/aenm.202003233.

[180] J. Joe, H. Yang, C. Bae, H. Shin, Metal Chalcogenides on Silicon Photocathodes for Efficient Water Splitting: A Mini Overview, Catalysts 9 (2019) 149. https://doi.org/10.3390/catal9020149.
[181] S.M. Ho, M.A. Mahadik, J.S. Jang, V.N. Singh, Metal Oxide based Chalcogenides Heterostructure Thin Film Photoanodes for Photoelectrochemical Solar Hydrogen Generation, Asian Journal of Chemistry 31 (2019) 18–24. https://doi.org/10.14233/ajchem.2019.21647.
[182] I.-H. Toor, S. Khan, Optical and Structural Properties of Metal Chalcogenide Semiconductor Nanostructures, in: Metal Chalcogenide Nanostructures for Renewable Energy Applications, John Wiley & Sons, Inc., Hoboken, NJ, USA, 2014: pp. 123–145. https://doi.org/10.1002/9781119008934.ch6.
[183] F. Finger, K. Welter, F. Urbain, V. Smirnov, B. Kaiser, W. Jaegermann, Photoelectrochemical Water Splitting using Adapted Silicon Based Multi-Junction Solar Cell Structures: Development of Solar Cells and Catalysts, Upscaling of Combined Photovoltaic-Electrochemical Devices and Performance Stability, Zeitschrift Für Physikalische Chemie 234 (2020) 1055–1095. https://doi.org/10.1515/zpch-2019-1453.
[184] W. Wang, H. Chen, J. Wu, H. Wang, S. Li, B. Wang, Y. Li, H. Lin, L. Wang, Unique hollow heterostructured CdS/$Cd_{0.5}Zn_{0.5}S$-$Mo_{1-x}W_xS_2$: Highly-improved visible-light-driven H_2 generation via synergy of $Cd_{0.5}Zn_{0.5}S$ protective shell and defect-rich $Mo_{1-x}W_XS_2$ cocatalyst, Nano Res 15 (2022) 985–995. https://doi.org/10.1007/s12274-021-3585-7.
[185] S. Chen, T. Liu, Z. Zheng, M. Ishaq, G. Liang, P. Fan, T. Chen, J. Tang, Recent progress and perspectives on Sb_2Se_3-based photocathodes for solar hydrogen production via photoelectrochemical water splitting, Journal of Energy Chemistry 67 (2022) 508–523. https://doi.org/10.1016/j.jechem.2021.08.062.
[186] J. Jiang, H. Wang, H. An, G. Du, Controlled Growth of CdS Nanostep Structured Arrays to Improve Photoelectrochemical Performance, Front Chem 8 (2020). https://doi.org/10.3389/fchem.2020.577582.
[187] M. Mollavali, C. Falamaki, S. Rohani, Efficient light harvesting by NiS/CdS/ZnS NPs incorporated in C, N-co-doped-TiO_2 nanotube arrays as visible-light sensitive multilayer photoanode for solar applications, Int J Hydrogen Energy 43 (2018) 9259–9278. https://doi.org/10.1016/j.ijhydene.2018.03.102.
[188] A.M. Holi, A.A. Al-Zahrani, A.S. Najm, P. Chelvanathan, N. Amin, PbS/CdS/ZnO nanowire arrays: Synthesis, structural, optical, electrical, and photoelectrochemical properties, Chem Phys Lett 750 (2020) 137486. https://doi.org/10.1016/j.cplett.2020.137486.
[189] S. Majumder, N.D. Quang, T. Thi Hien, N.D. Chinh, H. Yang, C. Kim, D. Kim, Nanostructured β-Bi_2O_3/PbS heterojunction as np-junction photoanode for enhanced photoelectrochemical performance, J Alloys Compd 870 (2021) 159545. https://doi.org/10.1016/j.jallcom.2021.159545.
[190] U. Alam, N. Verma, Direct Z-scheme-based novel cobalt nickel tungstate/graphitic carbon nitride composite: Enhanced photocatalytic degradation of organic pollutants and oxidation of benzyl alcohol, Colloids Surf A Physicochem Eng Asp 630 (2021) 127606. https://doi.org/10.1016/j.colsurfa.2021.127606.
[191] Q. Wang, K. Dou, X. Shi, Band alignment in multilayered semiconductor homojunctions supported on metals, J Mater Chem C Mater 8 (2020) 959–967. https://doi.org/10.1039/C9TC04512K.

[192] Y. Li, Q. Wang, J. Jin, Z. Zhang, S. Gao, Construction of TiO2 nanotube arrays co-sensitized by Sb2S3-Bi2S3 microspheres by UV-assisted photodeposition for the enhanced photoelectrochemical performance, Ceram Int 44 (2018) 12825–12830. https://doi.org/10.1016/j.ceramint.2018.04.090.
[193] Y. Wang, W. Wang, J. Fu, Y. Liang, L. Yao, T. Zhu, Integrating the plasmonic sensitizer and electron relay into ZnO/Au/CdS sandwich nanotube array photoanode for efficient solar-to-hydrogen conversion with 3.2% efficiency, Renew Energy 168 (2021) 647–658. https://doi.org/10.1016/j.renene.2020.12.076.
[194] R.-B. Wei, P.-Y. Kuang, H. Cheng, Y.-B. Chen, J.-Y. Long, M.-Y. Zhang, Z.-Q. Liu, Plasmon-Enhanced Photoelectrochemical Water Splitting on Gold Nanoparticle Decorated ZnO/CdS Nanotube Arrays, ACS Sustain Chem Eng 5 (2017) 4249–4257. https://doi.org/10.1021/acssuschemeng.7b00242.
[195] M. Lin, W. Wang, Passivation of ZnSe nanoparticles in sandwiched CdSe/ZnSe/ZnO nanotube array photoanode to substantially enhance solar photoelectrochemical water splitting for hydrogen evolution, Colloids Surf A Physicochem Eng Asp 614 (2021) 126206. https://doi.org/10.1016/j.colsurfa.2021.126206.
[196] C.T. Altaf, M. Faraji, A. Kumtepe, N. Abdullayeva, N. Yilmaz, E. Karagoz, A. Bozbey, H. Kurt, M. Sankir, N.D. Sankir, Highly efficient 3D-ZnO nanosheet photoelectrodes for solar-driven water splitting: Chalcogenide nanoparticle sensitization and mathematical modeling, J Alloys Compd 828 (2020) 154472. https://doi.org/10.1016/j.jallcom.2020.154472.
[197] C. Li, S. Chen, X. Gao, W. Zhang, Y. Wang, Fabrication, characterization and photoelectrochemical properties of CdS/CdSe nanofilm co-sensitized ZnO nanorod arrays on Zn foil substrate, J Colloid Interface Sci 588 (2021) 269–282. https://doi.org/10.1016/j.jcis.2020.12.078.
[198] Y. Wang, W. Tian, L. Chen, F. Cao, J. Guo, L. Li, Three-Dimensional WO_3 Nanoplate/Bi_2S_3 Nanorod Heterojunction as a Highly Efficient Photoanode for Improved Photoelectrochemical Water Splitting, ACS Appl Mater Interfaces 9 (2017) 40235–40243. https://doi.org/10.1021/acsami.7b11510.
[199] D. Soumya Rani, M.R. Meera, Photo-electrochemical water splitting behavior of CdSeQDs sensitized ferroelectric BaTiO3 perovskite heterostructure, Mater Today Proc 37 (2021) 1248–1253. https://doi.org/10.1016/j.matpr.2020.06.436.
[200] P. Wu, Z. Liu, M. Ruan, Z. Guo, L. Zhao, Cobalt-phosphate modified Fe-Zn0.2Cd0.8S/CuSbS2 heterojunction photoanode with multiple synergistic effect for enhancing photoelectrochemical water splitting, Appl Surf Sci 476 (2019) 716–723. https://doi.org/10.1016/j.apsusc.2019.01.150.
[201] Q. Shen, G. Gao, J. Xue, Y. Li, Q. Li, Q. Zhao, X. Liu, H. Jia, Photoelectrocatalytic hydrogen production of heterogeneous photoelectrodes with different system configurations of CdSe nanoparticles, Au nanocrystals and TiO_2 nanotube arrays, Int J Hydrogen Energy 45 (2020) 26688–26700. https://doi.org/10.1016/j.ijhydene.2020.07.015.
[202] A. Cerdán-Pasarán, T. López-Luke, I. Zarazúa, E. De la Rosa, R. Fuentes-Ramírez, K.C. Sanal, A. Alatorre-Ordaz, Co-sensitized TiO_2 electrodes with different quantum dots for enhanced hydrogen evolution in photoelectrochemical cells, J Appl Electrochem 49 (2019) 475–484. https://doi.org/10.1007/s10800-019-01299-x.
[203] Q. Li, X. Li, S. Wageh, Ahmed.A. Al-Ghamdi, J. Yu, CdS/Graphene Nanocomposite Photocatalysts, Adv Energy Mater 5 (2015) 1500010. https://doi.org/10.1002/aenm.201500010.

[204] Z. Xie, X. Liu, W. Wang, X. Wang, C. Liu, Q. Xie, Z. Li, Z. Zhang, Enhanced photoelectrochemical and photocatalytic performance of TiO_2 nanorod arrays/CdS quantum dots by coating TiO2 through atomic layer deposition, Nano Energy 11 (2015) 400–408. https://doi.org/10.1016/j.nanoen.2014.11.024.
[205] F. Zhan, W. Liu, H. Li, Y. Yang, M. Wang, Ce-doped CdS quantum dot sensitized TiO_2 nanorod films with enhanced visible-light photoelectrochemical properties, Appl Surf Sci 455 (2018) 476–483. https://doi.org/10.1016/j.apsusc.2018.05.226.
[206] A. Ahmad, F. Tezcan, G. Yerlikaya, Zia-ur-Rehman, H. Paksoy, G. Kardaş, Three dimensional rosette-rod TiO_2/Bi_2S_3 heterojunction for enhanced photoelectrochemical water splitting, J Alloys Compd 868 (2021) 159133. https://doi.org/10.1016/j.jallcom.2021.159133.
[207] P. Kuang, L. Zhang, B. Cheng, J. Yu, Enhanced charge transfer kinetics of Fe_2O_3/CdS composite nanorod arrays using cobalt-phosphate as cocatalyst, Appl Catal B 218 (2017) 570–580. https://doi.org/10.1016/j.apcatb.2017.07.002.
[208] F. Gao, Q. Chen, X. Zhang, H. Wang, T. Huang, L. Zhou, ZnO/TiO_2 core–shell heterojunction for CdS and PbS quantum dot-cosensitized solar cells, Current Applied Physics 18 (2018) 546–550. https://doi.org/10.1016/j.cap.2018.02.020.
[209] P. Gomathisankar, K. Hachisuka, H. Katsumata, T. Suzuki, K. Funasaka, S. Kaneco, Photocatalytic Hydrogen Production from Aqueous Na_2S + Na_2SO_3 Solution with B-Doped ZnO, ACS Sustain Chem Eng 1 (2013) 982–988. https://doi.org/10.1021/sc400061w.
[210] M.A. Mahadik, P.S. Shinde, M. Cho, J.S. Jang, Metal oxide top layer as an interfacial promoter on a $ZnIn_2S_4$/TiO_2 heterostructure photoanode for enhanced photoelectrochemical performance, Appl Catal B 184 (2016) 337–346. https://doi.org/10.1016/j.apcatb.2015.12.001.
[211] M. Luo, Y. Liu, J. Hu, H. Liu, J. Li, One-Pot Synthesis of CdS and Ni-Doped CdS Hollow Spheres with Enhanced Photocatalytic Activity and Durability, ACS Appl Mater Interfaces 4 (2012) 1813–1821. https://doi.org/10.1021/am3000903.
[212] J. Yang, H. Yan, X. Wang, F. Wen, Z. Wang, D. Fan, J. Shi, C. Li, Roles of cocatalysts in Pt–PdS/CdS with exceptionally high quantum efficiency for photocatalytic hydrogen production, J Catal 290 (2012) 151–157. https://doi.org/10.1016/j.jcat.2012.03.008.
[213] T.-T. Yang, W.-T. Chen, Y.-J. Hsu, K.-H. Wei, T.-Y. Lin, T.-W. Lin, Interfacial Charge Carrier Dynamics in Core−Shell Au-CdS Nanocrystals, The Journal of Physical Chemistry C 114 (2010) 11414–11420. https://doi.org/10.1021/jp103294c.
[214] M. de Oliveira Melo, L.A. Silva, Visible light-induced hydrogen production from glycerol aqueous solution on hybrid Pt–CdS–TiO_2 photocatalysts, J Photochem Photobiol A Chem 226 (2011) 36–41. https://doi.org/10.1016/j.jphotochem.2011.10.012.
[215] H. Park, Y.K. Kim, W. Choi, Reversing CdS Preparation Order and Its Effects on Photocatalytic Hydrogen Production of CdS/Pt-TiO_2 Hybrids Under Visible Light, The Journal of Physical Chemistry C 115 (2011) 6141–6148. https://doi.org/10.1021/jp2015319.
[216] J. Chen, X.-J. Wu, L. Yin, B. Li, X. Hong, Z. Fan, B. Chen, C. Xue, H. Zhang, One-pot Synthesis of CdS Nanocrystals Hybridized with Single-Layer Transition-Metal Dichalcogenide Nanosheets for Efficient Photocatalytic Hydrogen Evolution, Angewandte Chemie 127 (2015) 1226–1230. https://doi.org/10.1002/ange.201410172.
[217] J. Jin, J. Yu, D. Guo, C. Cui, W. Ho, A Hierarchical Z-Scheme CdS-WO_3 Photocatalyst with Enhanced CO_2 Reduction Activity, Small 11 (2015) 5262–5271. https://doi.org/10.1002/smll.201500926.

[218] H. Yu, X. Huang, P. Wang, J. Yu, Enhanced Photoinduced-Stability and Photocatalytic Activity of CdS by Dual Amorphous Cocatalysts: Synergistic Effect of Ti(IV)-Hole Cocatalyst and Ni(II)-Electron Cocatalyst, The Journal of Physical Chemistry C 120 (2016) 3722–3730. https://doi.org/10.1021/acs.jpcc.6b00126.
[219] S. Hong, D.P. Kumar, D.A. Reddy, J. Choi, T.K. Kim, Excellent photocatalytic hydrogen production over CdS nanorods via using noble metal-free copper molybdenum sulfide (Cu2MoS4) nanosheets as co-catalysts, Appl Surf Sci 396 (2017) 421–429. https://doi.org/10.1016/j.apsusc.2016.10.171.
[220] J.-J. Zhou, R. Wang, X.-L. Liu, F.-M. Peng, C.-H. Li, F. Teng, Y.-P. Yuan, In situ growth of CdS nanoparticles on UiO-66 metal-organic framework octahedrons for enhanced photocatalytic hydrogen production under visible light irradiation, Appl Surf Sci 346 (2015) 278–283. https://doi.org/10.1016/j.apsusc.2015.03.210.
[221] Y. Zhu, Y. Wang, Z. Chen, L. Qin, L. Yang, L. Zhu, P. Tang, T. Gao, Y. Huang, Z. Sha, G. Tang, Visible light induced photocatalysis on CdS quantum dots decorated TiO_2 nanotube arrays, Appl Catal A Gen 498 (2015) 159–166. https://doi.org/10.1016/j.apcata.2015.03.035.
[222] Y. Xie, G. Ali, S.H. Yoo, S.O. Cho, Sonication-Assisted Synthesis of CdS Quantum-Dot-Sensitized TiO_2 Nanotube Arrays with Enhanced Photoelectrochemical and Photocatalytic Activity, ACS Appl Mater Interfaces 2 (2010) 2910–2914. https://doi.org/10.1021/am100605a.
[223] J. Yang, D. Wang, H. Han, C. Li, Roles of Cocatalysts in Photocatalysis and Photoelectrocatalysis, Acc Chem Res 46 (2013) 1900–1909. https://doi.org/10.1021/ar300227e.
[224] Y.W. Chen, J.D. Prange, S. Dühnen, Y. Park, M. Gunji, C.E.D. Chidsey, P.C. McIntyre, Atomic layer-deposited tunnel oxide stabilizes silicon photoanodes for water oxidation, Nat Mater 10 (2011) 539–544. https://doi.org/10.1038/nmat3047.
[225] L. Chen, J. Yang, S. Klaus, L.J. Lee, R. Woods-Robinson, J. Ma, Y. Lum, J.K. Cooper, F.M. Toma, L.-W. Wang, I.D. Sharp, A.T. Bell, J.W. Ager, p-Type Transparent Conducting Oxide/n-Type Semiconductor Heterojunctions for Efficient and Stable Solar Water Oxidation, J Am Chem Soc 137 (2015) 9595–9603. https://doi.org/10.1021/jacs.5b03536.
[226] L. Ji, M.D. McDaniel, S. Wang, A.B. Posadas, X. Li, H. Huang, J.C. Lee, A.A. Demkov, A.J. Bard, J.G. Ekerdt, E.T. Yu, A silicon-based photocathode for water reduction with an epitaxial $SrTiO_3$ protection layer and a nanostructured catalyst, Nat Nanotechnol 10 (2015) 84–90. https://doi.org/10.1038/nnano.2014.277.
[227] K. Sun, F.H. Saadi, M.F. Lichterman, W.G. Hale, H.-P. Wang, X. Zhou, N.T. Plymale, S.T. Omelchenko, J.-H. He, K.M. Papadantonakis, B.S. Brunschwig, N.S. Lewis, Stable solar-driven oxidation of water by semiconducting photoanodes protected by transparent catalytic nickel oxide films, Proceedings of the National Academy of Sciences 112 (2015) 3612–3617. https://doi.org/10.1073/pnas.1423034112.
[228] S. Tong, J. Liu, C. Zhang, Platelet-rich plasma inhibits inflammatory factors and represses rheumatoid fibroblast-like synoviocytes in rheumatoid arthritis, Clin Exp Med 17 (2017) 441–449. https://doi.org/10.1007/s10238-017-0449-2.
[229] S.-K. Kim, M.-K. Son, S. Park, M.-S. Jeong, K. Prabakar, H.-J. Kim, Surface modification on TiO_2 nanoparticles in CdS/CdSe Quantum Dot-sensitized Solar Cell, Electrochim Acta 118 (2014) 118–123. https://doi.org/10.1016/j.electacta.2013.11.191.

[230] D. Zhong, W. Liu, P. Tan, A. Zhu, Y. Liu, X. Xiong, J. Pan, Insights into the synergy effect of anisotropic {001} and {230}facets of $BaTiO_3$ nanocubes sensitized with CdSe quantum dots for photocatalytic water reduction, Appl Catal B 227 (2018) 1–12. https://doi.org/10.1016/j.apcatb.2018.01.009.
[231] W. Sheng, Y. Song, M. Dou, J. Ji, F. Wang, Constructing 1D hierarchical heterostructures of MoS_2/In_2S_3 nanosheets on CdS nanorod arrays for enhanced photoelectrocatalytic H_2 evolution, Appl Surf Sci 436 (2018) 613–623. https://doi.org/10.1016/j.apsusc.2017.11.281.
[232] B. Chong, W. Zhu, Y. Liu, L. Guan, G.Z. Chen, Highly efficient photoanodes based on cascade structural semiconductors of $Cu_2Se/CdSe/TiO_2$: a multifaceted approach to achieving microstructural and compositional control, J Mater Chem A Mater 4 (2016) 1336–1344. https://doi.org/10.1039/C5TA09179A.
[233] Y.-L. Chen, Y.-H. Chen, J.-W. Chen, F. Cao, L. Li, Z.-M. Luo, I.-C. Leu, Y.-C. Pu, New Insights into the Electron-Collection Efficiency Improvement of CdS-Sensitized TiO_2 Nanorod Photoelectrodes by Interfacial Seed-Layer Mediation, ACS Appl Mater Interfaces 11 (2019) 8126–8137. https://doi.org/10.1021/acsami.8b22418.
[234] L. Wang, W. Wang, Y. Chen, L. Yao, X. Zhao, H. Shi, M. Cao, Y. Liang, Heterogeneous p–n Junction CdS/Cu_2O Nanorod Arrays: Synthesis and Superior Visible-Light-Driven Photoelectrochemical Performance for Hydrogen Evolution, ACS Appl Mater Interfaces 10 (2018) 11652–11662. https://doi.org/10.1021/acsami.7b19530.
[235] L. Yao, W. Wang, T. Zhu, Y. Wang, Y. Liang, J. Fu, J. Wang, Y. Cheng, S. Liu, A rational design of $CdS/ZnFe_2O_4/Cu_2O$ core-shell nanorod array photoanode with stair-like type-II band alignment for highly efficient bias-free visible-light-driven H2 generation, Appl Catal B 268 (2020) 118460. https://doi.org/10.1016/j.apcatb.2019.118460.
[236] J.-Y. Kim, Y.J. Jang, J. Park, J. Kim, J.S. Kang, D.Y. Chung, Y.-E. Sung, C. Lee, J.S. Lee, M.J. Ko, Highly loaded PbS/Mn-doped CdS quantum dots for dual application in solar-to-electrical and solar-to-chemical energy conversion, Appl Catal B 227 (2018) 409–417. https://doi.org/10.1016/j.apcatb.2018.01.041.
[237] C.W. Lai, K.S. Lau, P.M. Chou, $CdSe/TiO_2$ nanotubes for enhanced photoelectrochemical activity under solar illumination: Influence of soaking time in CdSe bath solution, Chem Phys Lett 714 (2019) 6–10. https://doi.org/10.1016/j.cplett.2018.10.054.
[238] K. Basu, H. Zhang, H. Zhao, S. Bhattacharya, F. Navarro-Pardo, P.K. Datta, L. Jin, S. Sun, F. Vetrone, F. Rosei, Highly stable photoelectrochemical cells for hydrogen production using a SnO_2–TiO_2/quantum dot heterostructured photoanode, Nanoscale 10 (2018) 15273–15284. https://doi.org/10.1039/C8NR02286K.
[239] L. Cao, K. Xu, M. Fan, Zn0.5Cd0.5S nanoparticles modified TiO_2 nanotube arrays with efficient charge separation and enhanced light harvesting for boosting visible-light-driven photoelectrochemical performance, J Power Sources 482 (2021) 228956. https://doi.org/10.1016/j.jpowsour.2020.228956.
[240] R.P. Patil, M.A. Mahadik, W.-S. Chae, S.H. Choi, J.S. Jang, Self-templated fabrication of 2-D dual nanoarchitecture Zn1-xCdxS porous nanosheet and ZnO nanorod for photoelectrochemical hydrogen production, Appl Surf Sci 539 (2021) 148267. https://doi.org/10.1016/j.apsusc.2020.148267.
[241] D. Akyüz, R.M. Zunain Ayaz, S. Yılmaz, Ö. Uğuz, C. Sarıoğlu, F. Karaca, A.R. Özkaya, A. Koca, Metal chalcogenide based photocatalysts decorated with heteroatom doped reduced graphene oxide for photocatalytic and photoelectrochemical hydrogen production,

Int J Hydrogen Energy 44 (2019) 18836–18847. https://doi.org/10.1016/j.ijhydene.2019.04.049.
[242] R. Zunain Ayaz, D. Akyüz, Ö. Uğuz, İ. Tanşık, C. Sarıoğlu, F. Karaca, A.R. Özkaya, A. Koca, Photoelectrochemical performance of thermally sulfurized CdxZn1-xS photoanode: Enhancement with reduced graphene oxide support, Renew Energy 162 (2020) 182–195. https://doi.org/10.1016/j.renene.2020.07.102.
[243] E. Liu, X. Zhang, P. Xue, J. Fan, X. Hu, Carbon membrane bridged ZnSe and TiO_2 nanotube arrays: Fabrication and promising application in photoelectrochemical water splitting, Int J Hydrogen Energy 45 (2020) 9635–9647. https://doi.org/10.1016/j.ijhydene.2020.01.207.
[244] R. Hu, L. Meng, J. Zhang, X. Wang, S. Wu, Z. Wu, R. Zhou, L. Li, D.-S. Li, T. Wu, A high-activity bimetallic OER cocatalyst for efficient photoelectrochemical water splitting of $BiVO_4$, Nanoscale 12 (2020) 8875–8882. https://doi.org/10.1039/D0NR01616K.
[245] H.-S. Bae, R.P. Patil, W.-S. Chae, J. Ryu, M.A. Mahadik, J.S. Jang, Morphology control and phase transformation of ZIS/TiO_2 into CdSe(en)0.5/CIS/TiO_2 photoanode for enhanced solar hydrogen generation, Chemical Engineering Journal 385 (2020) 123871. https://doi.org/10.1016/j.cej.2019.123871.
[246] P. Sheng, L. Yao, P. Yang, D. Yang, C. Lu, K. Cao, W. Li, The origin of enhanced photoelectrochemical activity in metal-ion-doped ZnO/CdS quantum dots, J Alloys Compd 822 (2020) 153700. https://doi.org/10.1016/j.jallcom.2020.153700.
[247] H. Zheng, Y. Lu, K.-H. Ye, J. Hu, S. Liu, J. Yan, Y. Ye, Y. Guo, Z. Lin, J. Cheng, Y. Cao, Atomically thin photoanode of InSe/graphene heterostructure, Nat Commun 12 (2021) 91. https://doi.org/10.1038/s41467-020-20341-7.
[248] K. Feng, D. Huang, L. Li, K. Wang, J. Li, T. Harada, S. Ikeda, F. Jiang, MoS_x-CdS/Cu_2ZnSnS_4-based thin film photocathode for solar hydrogen evolution from water, Appl Catal B 268 (2020) 118438. https://doi.org/10.1016/j.apcatb.2019.118438.
[249] X. Xu, Y. Liu, Y. Zhu, X. Fan, Y. Li, F. Zhang, G. Zhang, W. Peng, Fabrication of a Cu_2O/g-C_3N_4/WS_2 Triple-Layer Photocathode for Photoelectrochemical Hydrogen Evolution, ChemElectroChem 4 (2017) 1498–1502. https://doi.org/10.1002/celc.201700014.
[250] H. Li, W. Dong, J. Zhang, J. Xi, G. Du, Z. Ji, MoS_2 nanosheet/ZnO nanowire hybrid nanostructures for photoelectrochemical water splitting, Journal of the American Ceramic Society 101 (2018) 3989–3996. https://doi.org/10.1111/jace.15540.
[251] H. Li, C. Yang, X. Wang, J. Zhang, J. Xi, G. Du, Z. Ji, Mixed 3D/2D dimensional TiO_2 nanoflowers/$MoSe_2$ nanosheets for enhanced photoelectrochemical hydrogen generation, Journal of the American Ceramic Society 103 (2020) 1187–1196. https://doi.org/10.1111/jace.16807.
[252] W. Huang, Q. Zhou, S. Su, J. Li, X. Lu, X. Gao, X. Wang, M. Jin, G. Zhou, Z. Zhang, J. Liu, Ion Beam Defect Engineering on ReS_2 /Si Photocathode with Significantly Enhanced Hydrogen Evolution Reaction, Adv Mater Interfaces 6 (2019) 1801663. https://doi.org/10.1002/admi.201801663.
[253] M. Tekalgne, A. Hasani, Q. Van Le, T.P. Nguyen, K.S. Choi, T.H. Lee, H.W. Jang, Z. Luo, S.Y. Kim, CdSe Quantum Dots Doped WS_2 Nanoflowers for Enhanced Solar Hydrogen Production, Physica Status Solidi (a) 216 (2019) 1800853. https://doi.org/10.1002/pssa.201800853.
[254] I. Mondal, S.Y. Moon, H. Lee, H. Kim, J.Y. Park, Two-dimensional FeS_2 -encapsulated Au: a quasi-epitaxial heterojunction for synergistic catalytic activity under

photoelectrocatalytic water reduction, J Mater Chem A Mater 7 (2019) 19258–19268. https://doi.org/10.1039/C9TA02065A.
[255] E. Sitara, H. Nasir, A. Mumtaz, M.F. Ehsan, M. Sohail, S. Iram, S.A.B. Bukhari, Efficient Photoelectrochemical Water Splitting by Tailoring MoS_2/CoTe Heterojunction in a Photoelectrochemical Cell, Nanomaterials 10 (2020) 2341. https://doi.org/10.3390/nano10122341.
[256] S. Kumar, T. Malik, D. Sharma, A.K. Ganguli, $NaNbO_3$/MoS_2 and $NaNbO_3$/$BiVO_4$ Core−Shell Nanostructures for Photoelectrochemical Hydrogen Generation, ACS Appl Nano Mater 2 (2019) 2651–2662. https://doi.org/10.1021/acsanm.9b00098.
[257] D.-B. Seo, S. Kim, T.N. Trung, D. Kim, E.-T. Kim, Conformal growth of few-layer MoS2 flakes on closely-packed TiO_2 nanowires and their enhanced photoelectrochemical reactivity, J Alloys Compd 770 (2019) 686–691. https://doi.org/10.1016/j.jallcom.2018.08.151.
[258] S.S.M. Bhat, S.A. Pawar, D. Potphode, C.-K. Moon, J.M. Suh, C. Kim, S. Choi, D.S. Patil, J.-J. Kim, J.C. Shin, H.W. Jang, Substantially enhanced photoelectrochemical performance of TiO_2 nanorods/CdS nanocrystals heterojunction photoanode decorated with MoS_2 nanosheets, Appl Catal B 259 (2019) 118102. https://doi.org/10.1016/j.apcatb.2019.118102.
[259] M.A. Hassan, M.-W. Kim, M.A. Johar, A. Waseem, M.-K. Kwon, S.-W. Ryu, Transferred monolayer MoS_2 onto GaN for heterostructure photoanode: Toward stable and efficient photoelectrochemical water splitting, Sci Rep 9 (2019) 20141. https://doi.org/10.1038/s41598-019-56807-y.
[260] P. Subramanyam, M. Deepa, S.S.K. Raavi, H. Misawa, V. Biju, C. Subrahmanyam, A photoanode with plasmonic nanoparticles of earth abundant bismuth for photoelectrochemical reactions, Nanoscale Adv 2 (2020) 5591–5599. https://doi.org/10.1039/D0NA00641F.
[261] Z. Wu, M. Ouyang, D. Wang, X. Liu, Boosted photo-electro-catalytic hydrogen evolution over the MoS_2/MoO_2 Schottky heterojunction by accelerating photo-generated charge kinetics, J Alloys Compd 832 (2020) 154970. https://doi.org/10.1016/j.jallcom.2020.154970.
[262] L. Li, Y. Chen, X. Liu, Q. Wang, L. Du, X. Chen, G. Tian, Cu_2O decorated α-Fe2O3/SnS2 core/shell heterostructured nanoarray photoanodes for water splitting, Solar Energy 220 (2021) 843–851. https://doi.org/10.1016/j.solener.2021.04.022.
[263] F. Zhang, Y. Chen, W. Zhou, C. Ren, H. Gao, G. Tian, Hierarchical SnS_2/$CuInS_2$ Nanosheet Heterostructure Films Decorated with C_{60} for Remarkable Photoelectrochemical Water Splitting, ACS Appl Mater Interfaces 11 (2019) 9093–9101. https://doi.org/10.1021/acsami.8b21222.
[264] F. Zhang, X. Yu, J. Hu, L. Lei, Y. He, X. Zhang, Coupling Ru-MoS_2 heterostructure with silicon for efficient photoelectrocatalytic water splitting, Chemical Engineering Journal 423 (2021) 130231. https://doi.org/10.1016/j.cej.2021.130231.
[265] G. Huang, J. Zhang, F. Jiang, Z. Zhang, J. Zeng, X. Qi, Z. Shen, H. Wang, Z. Kong, J. Xi, Z. Ji, Excellent photoelectrochemical activity of Bi_2S_3 nanorod/TiO_2 nanoplate composites with dominant {001} facets, J Solid State Chem 281 (2020) 121041. https://doi.org/10.1016/j.jssc.2019.121041.
[266] Y.-Y. Geng, C.-L. Tao, S.-F. Duan, J. San Martin, Y. Lin, X. Zhu, Q.-Q. Zhang, X.-W. Kang, S.-S. He, Y.-X. Zhao, X. Li, L. Niu, D.-D. Qin, Y. Yan, D.-X. Han, V-rich Bi_2S_3 nanowire with efficient charge separation and transport for high-performance and robust

photoelectrochemical application under visible light, Catal Today 350 (2020) 47–55. https://doi.org/10.1016/j.cattod.2019.08.008.
[267] L. Guo, P.S. Shinde, Y. Ma, L. Li, S. Pan, F. Yan, Scalable Core–Shell MoS_2/Sb_2Se_3 Nanorod Array Photocathodes for Enhanced Photoelectrochemical Water Splitting, Solar RRL 4 (2020) 1900442. https://doi.org/10.1002/solr.201900442.
[268] D. Chen, Z. Liu, M. Zhou, P. Wu, J. Wei, Enhanced photoelectrochemical water splitting performance of α-Fe_2O_3 nanostructures modified with Sb_2S_3 and cobalt phosphate, J Alloys Compd 742 (2018) 918–927. https://doi.org/10.1016/j.jallcom.2018.01.334.
[269] M.A. Mahadik, J.W. Park, W.-S. Chae, S.H. Choi, H.-S. Chung, M. Cho, J.S. Jang, Facile synthesis of Bi_2S_3 nanosheet/Zr:Fe_2O_3 nanorod heterojunction: Effect of Ag interlayer on the change transport and photoelectrochemical stability, Journal of Industrial and Engineering Chemistry 70 (2019) 311–321. https://doi.org/10.1016/j.jiec.2018.10.031.
[270] P. Subramanyam, T. Vinodkumar, M. Deepa, Ch. Subrahmanyam, Gold nanoparticle decorated bismuth sulfide nanorods for enhanced photoelectrochemical hydrogen production, J Mater Chem C Mater 7 (2019) 6398–6405. https://doi.org/10.1039/C9TC00759H.
[271] H. Du, C. Yang, W. Pu, H. Zhao, J. Gong, Highly Active Sb_2S_3-Attached Mo–WO_3 Composite Film for Enhanced Photoelectrocatalytic Water Splitting at Extremely Low Input Light Energy, ACS Sustain Chem Eng 7 (2019) 9172–9181. https://doi.org/10.1021/acssuschemeng.8b06545.
[272] W. Sun, Y. Ye, Y. You, J. Xu, A top-down synthesis of wurtzite Cu_2SnS_3 nanocrystals for efficient photoelectrochemical performance, J Mater Chem A Mater 6 (2018) 8221–8226. https://doi.org/10.1039/C8TA00851E.
[273] P. Subramanyam, B. Meena, D. Suryakala, M. Deepa, C. Subrahmanyam, Plasmonic nanometal decorated photoanodes for efficient photoelectrochemical water splitting, Catal Today 379 (2021) 1–6. https://doi.org/10.1016/j.cattod.2020.01.041.
[274] J. Li, Y. Zhao, X. Han, D. Xiao, A facile strategy for fabricating particle-on-flower Au-Cu_3BiS_3 nanostructures for enhanced photoelectrocatalytic activity in water splitting, New Journal of Chemistry 45 (2021) 1231–1239. https://doi.org/10.1039/D0NJ03448G.
[275] S. Sadhasivam, N. Anbarasan, M. Mukilan, P. Manivel, K. Jeganathan, Bi2S3 anchored ZnS/ZnO nanorod arrays photoanode for enhanced visible light driven photo electrochemical properties, Int J Hydrogen Energy 45 (2020) 30080–30090. https://doi.org/10.1016/j.ijhydene.2020.08.026.
[276] P. Subramanyam, B. Meena, G.N. Sinha, M. Deepa, C. Subrahmanyam, Decoration of plasmonic Cu nanoparticles on WO_3/Bi_2S_3 QDs heterojunction for enhanced photoelectrochemical water splitting, Int J Hydrogen Energy 45 (2020) 7706–7715. https://doi.org/10.1016/j.ijhydene.2019.05.168.
[277] Y. Xiong, L. Yang, D.K. Nandakumar, Y. Yang, H. Dong, X. Ji, P. Xiao, S.C. Tan, Highly efficient photoelectrochemical water oxidation enabled by enhanced interfacial interaction in 2D/1D In_2S_3 @Bi_2S_3 heterostructures, J Mater Chem A Mater 8 (2020) 5612–5621. https://doi.org/10.1039/D0TA00149J.
[278] Y. PENG, J. CHEN, L. JIANG, T. WANG, H. YANG, F. LIU, M. JIA, Preparation of Sb_2O_3/Sb_2S_3/FeOOH composite photoanodes for enhanced photoelectrochemical water oxidation, Transactions of Nonferrous Metals Society of China 30 (2020) 1625–1634. https://doi.org/10.1016/S1003-6326(20)65325-0.

[279] W. Tian, C. Chen, L. Meng, W. Xu, F. Cao, L. Li, PVP Treatment Induced Gradient Oxygen Doping in In_2S_3 Nanosheet to Boost Solar Water Oxidation of WO_3 Nanoarray Photoanode, Adv Energy Mater 10 (2020) 1903951. https://doi.org/10.1002/aenm.201903951.
[280] S. Sharma, D. Kumar, N. Khare, Three-dimensional hierarchical PANI/Bi_2S_3 nanoflowers heterojunction for enhanced photoelectrochemical water splitting, J Alloys Compd 865 (2021) 158779. https://doi.org/10.1016/j.jallcom.2021.158779.
[281] W. Yang, J.H. Kim, O.S. Hutter, L.J. Phillips, J. Tan, J. Park, H. Lee, J.D. Major, J.S. Lee, J. Moon, Benchmark performance of low-cost Sb_2Se_3 photocathodes for unassisted solar overall water splitting, Nat Commun 11 (2020) 861. https://doi.org/10.1038/s41467-020-14704-3.
[282] Y. Cheng, C. Xin, J. Zhao, J. Wang, M. Gong, H. Miao, X. Hu, Constructing lateral sulfur-gradient $Sb_2(S_xSe_{1-x})_3$ heterostructures for Sb_2Se_3 nanorod photocathodes with enhanced photoelectrochemical properties, Electrochim Acta 403 (2022) 139610. https://doi.org/10.1016/j.electacta.2021.139610.

Chapter 2. Photoelectrochemical water splitting using anodic nanoporous WO_3/Bi_2S_3 quantum dots photoanode

2.1. Introduction

The consumption of fossil fuels has skyrocketed in recent years due to the world's population growth and fast economic development. Consequently, it is necessary to investigate new sources of renewable fuels with high energy density and minimal environmental effects [1]. One of the most interesting and accessible approaches now is solar energy, especially for developing nations that have powerful and sustained sun radiation as well as suffer from severe energy and environmental issues. Therefore, creating eco-friendly, solar-powered, technologies is essential and helpful for tackling the problems facing humanity [2]. PEC-WS technique can transform solar photons into useful chemical fuels without producing pollutants. Therefore, it is an appealing technique for addressing future energy demands [3–5]. To achieve outstanding PEC-WS efficiency, the following prerequisites must be fulfilled; (1) light absorption, (2) e^-/h^+ pairs separation and transfer, and (3) oxidation and reduction surface reactions [6,7]. Selecting the appropriate photoelectrode materials is a critical step toward optimizing the performance of the PEC-WS system because their properties like light absorption ability and chemical stability can impact directly the system's efficiency [8,9]. Numerous materials have been studied for the PEC-WS process, for example, WO_3 [10,11], TiO_2 [12,13], α-Fe_2O_3 [14–16], $BiVO_4$ [17,18], ZnO [19–21], and $SrTiO_3$ [22]. WO_3 stands out among these materials as a potential photoanode for PEC-WS and H_2 production due to its special features; (1) it has a moderate bandgap (2.5–2.8 eV) [23,24]. (2) it exhibits reasonable hole diffusion length (≈150 nm) and outstanding electron transport properties (≈12 $cm^2\ V^{-1}\ S^{-1}$) [23,25]. (3) it has an adequate valence band edge for water oxidation [26]. (4) it has good chemical stability in acidic electrolytes [23].

A variety of methods, including hydrothermal, electrodeposition, dip coating, sputtering, spray pyrolysis, and anodic oxidation, can be used to create WO_3 thin films [27–33]. Anodic oxidation has become one of the most widely used manufacturing processes for forming ordered nanostructures of metal oxides [34,35]. It can be utilized to prepare WO_3 nanostructures with a variety of morphologies, such as nanopores [36,37], nanotubes [38], nanowires [39], and nanoplates [40], and compact films [37]. Among the many benefits of anodic oxidation are its

affordability, ease of use, and scalability [34]. Additionally, the generated anodic oxide layer adheres strongly to the conductive metallic substrate, which is essential for PEC applications [37]. Niloy Mukherjee et al. utilized the galvanostatic anodization of W to form WO_3 nanoporous (NPor) with pore diameters of 50–100 nm [41]. As well as WO_3 NPor with a pore size of 70 nm was fabricated using NH_4F and $(NH_4)_2SO_4$ electrolytes during the anodization process of the W sheet [42].

Despite extensive studies using WO_3 photoelectrodes for PEC-WS, the photo-to-hydrogen conversion efficiency of bare WO_3 is poor [34,43,44]. This is because of its narrow light absorption range, sluggish charge transport at the semiconductor/electrolyte interface, and high rate of e^-/h^+ pairs recombination [45,46]. A lot of work has been done to address these problems and improve the PEC-WS efficiency, involving (i) metals and non-metals doping to ameliorate the e^-/h^+ pairs separation, (ii) cocatalyst loading to enhance the kinetics of surface reactions, and (iii) integrating with narrow bandgap semiconductor QDs to facilitate the e^-/h^+ transfer and mitigate their recombination rate [47–49]. Among these approaches, coupling with narrow bandgap semiconductor QDs can efficiently improve the transport of e^-/h^+ pairs and inhibit their recombination, leading to a high PEC efficiency [50,51]. Various MCs, such as PdS [52], CdS [53,54], Cu_2S [55], and Bi_2S_3 [56–58], have been examined as narrow bandgap semiconductor QDs. Bi_2S_3 QDs can be considered an excellent candidate among numerous MCs owing to its high optical absorption coefficient, narrow bandgap (1.3–1.7 eV), good band alignment with WBSs, and low toxicity [59–61]. Bi_2S_3 sensitized with many WBSs photoelectrodes, such as $WO_3/Cu/Bi_2S_3$ [56], Bi_2S_3/TiO_2 [62,63], $Bi_2S_3/ZnS/ZnO$ [64], Bi_2S_3 /Zr:Fe_2O_3 [65], and WO_3/Bi_2S_3 [61] improved Vis light absorption ability and boosted PEC-WS efficiency compared to bare WBSs. Although various studies have primarily concentrated on the PEC-WS activity of anodic WO_3 under UV light [39,66], its performance under the Vis response needs more investigation. This is because vis light makes up half of the solar energy spectrum [67].

In this study, anodic NPor (ANPor) WO_3 was sensitized with Bi_2S_3 QDs using the SILAR process for the first time, to ameliorate Vis light PEC-WS efficiency. The deposited quantity of Bi_2S_3 QDs is adjusted by changing the number of SILAR cycles to 6, 8, 10, and 12 cycles. The ANPor WO_3/Bi_2S_3 QDs (10) photoanode displayed the highest current density, which was around 19 folds higher than that of bare ANPor WO_3. It also demonstrated the highest applied bias photon-

to-current efficiency (ABPE) of 4.1%. This boosted PEC performance was attributed to improving light absorption ability, good energy band alignment, and improved e^-/h^+ pairs separation and transport.

2.2. Experimental

2.2.1. Preparation of anodic nanoporous WO_3/Bi_2S_3 quantum dots photoanode

Firstly, ANPor WO_3 was prepared on a W sheet (99.95%, 0.2 mm thick) using a single-step anodization process [37]. The anodization technique was carried out using a two-electrode setup, a cleaned piece of W sheet as an anode, and a platinum rod as the cathode. The consistent distance between the two electrodes was 2 cm. W sheet (2×3 cm^2) was sonicated and cleaned with acetone before the anodization process. Then, it was anodized at 50 V in an electrolyte consisting of 0.075 M ammonium fluoride and 1 M ammonium sulfate at 20°C for 4 h. Following anodization, the anodized W sample was sonicated for 10 s in 20 wt% HF aqueous solution and for 5 s in ethanol. Finally, the anodized sample was annealed for 2 h at 500°C (2°C/min) in the air.

Secondly, ANPor WO_3/Bi_2S_3 QDs photoanode with various deposited quantities of Bi_2S_3 QDs was fabricated using the SILAR technique [68]. The prepared ANPor WO_3 sheet was successively submerged in four solutions for 1 min: (1) 0.05 M bismuth (III) nitrate pentahydrate in water/methanol ((1:1), 30 mL) with glycerol (3 mL), (2) water/methanol ((1:1), 30 mL), (3) 0.05 M Na_2S in water/methanol ((1:1), 30 mL), and (4) water/methanol ((1:1), 30 mL). These four steps deposited one cycle of Bi_2S_3 QDs on the surface of ANPor WO_3. We deposited various 6, 8, 10, and 12 cycles. Afterward, the fabricated ANPor WO_3/Bi_2S_3 QDs samples were annealed at 200°C for 30 min in air.

2.2.2. Characterization

The crystal structure of the fabricated samples was investigated by an X-ray diffractometer (XRD) analysis (Rigaku, RINT 2500, Japan) and CuKα radiation. The elemental composition and valence states were examined by X-ray photoelectron spectroscopy (XPS) device (ULVAC-Phi, QuanteraSXM, Al Kα, Japan). The surface morphology and elemental structure were studied by a scanning electron microscope (SEM) device (HITACHI high technologies, S-4800, Japan) linked to an energy-dispersive X-ray spectroscopy (EDX) system. The electron diffraction images and the crystal size were investigated by the transmission electron microscope (TEM) device (JEOL,

JEM-2100F, Japan). Finally, the optical characteristics were measured by UV–Vis diffuse reflectance spectroscopy (DRS) (JASCO, V-670 spectrophotometer, Japan).

2.2.3. Photoelectrochemical water splitting evaluation

The PEC performance of the fabricated photoanodes was assessed using a three-electrode PEC cell that has a quartz window. Bare ANPor WO_3 and samples modified with Bi_2S_3 QDs were used as working electrodes(1 cm^2 illuminated area), a Pt coil served as a counter electrode, and Hg/HgO (1 M NaOH) served as a reference electrode. All three electrodes were immersed in 0.1 M Na_2S/Na_2SO_3 (pH = 12.49) as an electrolyte. A compact 300 W xenon lamp with an AM 1.5 G filter was employed as the light source controlling the light intensity to 1 Sun (100 mW/cm^2). The electrolyte was flushed with argon gas before each measurement to eliminate any dissolved oxygen. The linear sweep voltammetry (LSV) curve was recorded with a scan rate of 10 mV/s. The electrochemical impedance spectroscopy (EIS) was measured with a frequency range of 100 kHz-0.01 Hz and with an amplitude of 10 mV under illumination. The Mott−Schottky (M-S) analysis was measured under dark conditions at 1000 Hz in 0.25 M Na_2SO_4 (pH = 6.24) using Ag/AgCl (3 M KCl) as a reference electrode. The quantity of produced H_2 was determined using gas chromatography (Shimadzu, GC-8A, Japan) linked to a gas circulation system (Makuhari Rikagaku Garasu Seisakujo, Japan), where argon was utilized as a carrier gas.

The potential versus the reversible hydrogen electrode (vs. RHE) was estimated by transforming the applied potential vs. Hg/HgO as indicated in equation 2-1 [69]:

$$E_{RHE} = E_{Hg/HgO} + 0.0592 \times pH + E^{o}_{Hg/HgO} \quad \text{(Eq. 2-1)}$$

where E_{RHE} and $E_{Hg/HgO}$ are the potential vs. RHE and applied potential versus the Hg/HgO, respectively. $E^{o}_{Hg/HgO}$ equals 0.118 V at 25°C.

The potential vs. RHE was estimated from the applied potential vs. Ag/AgCl utilizing the Nernst equation (equation (2)) [35];

$$E_{RHE} = E_{Ag/AgCl} + 0.059 \times pH + E^{o}_{Ag/AgCl} \quad \text{(Eq. 2-2)}$$

where E_{RHE} and $E_{Ag/AgCl}$ are the potential vs. RHE and applied potential versus the Ag/AgCl, respectively. $E^{o}_{Ag/AgCl}$ equal 0.210 V at 25°C at 25°C.

2.3. Results and discussion

2.3.1. Characterization results

ANPor WO_3 and ANPor WO_3/Bi_2S_3 QDs samples were investigated using XRD analysis to study the phase and crystal structure (**Figure 2-1**). The XRD analysis of the fabricated WO_3 before the annealing process disclosed only the distinctive peaks of cubic W with planes at (110), (200), and (211) (JCPDS No.00-001-1203) [34] verifying the amorphous structure of formed WO_3. While, after the annealing process, the crystalline structure was generated. WO_3 showed a monoclinic structure with characteristic planes at (002), (020), (200), (120), (112), (022), (202), (040), (114), and (042) (JCPDS 43–1035) [44,70,71]. Regarding, ANPor WO_3/Bi_2S_3 QDs (10), the XRD pattern displayed similar peaks of WO_3. There were no distinctive peaks for the Bi_2S_3 QDs, which could be attributed to the low crystallinity and/or low loaded amount of Bi_2S_3 QDs. According to the data, the crystalline structure of the nanoporous WO_3 was unaffected by the SILAR approach. After a five-hour chronoamperometry measurement (5 h) of the ANPor WO_3 and ANPor WO_3/Bi_2S_3 QDs photoanodes, the XRD patterns displayed the distinctive peaks of W metal, indicating that the ANPor WO_3 and ANPor WO_3/Bi_2S_3 QDs have entirely collapsed.

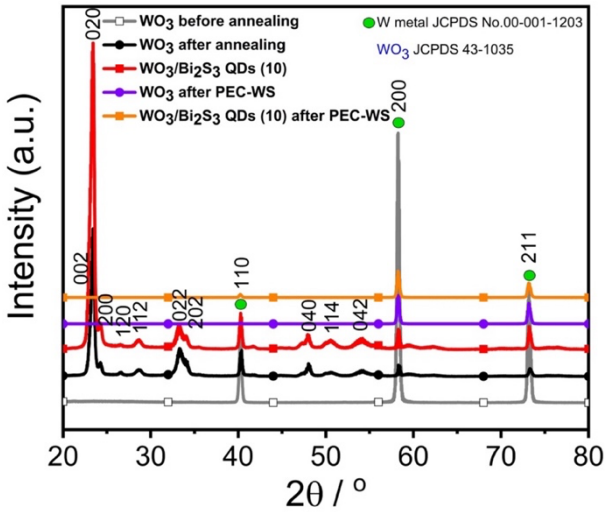

Figure 2-1. XRD patterns of bare ANPor WO_3 before and after the annealing process at 500°C, ANPor WO_3/Bi_2S_3 QDs (10) photoanodes, and used samples after a five-hour chronoamperometry measurement.

The morphology of bare ANPor WO_3 and ANPor WO_3/Bi_2S_3 QDs photoanodes are studied using FE-SEM analysis as indicated in **Figure 2-2**. As shown, the anodic WO_3 before the annealing process (**Figure 2-2a**) presented an irregular porous structure [72]. After annealing at 500°C for 2

h, the morphology of anodic WO_3 slightly changed (**Figure 2-2b**). Comparatively transformation of smooth nanopores into granular morphology was observed. This was ascribed to the formation of the crystallite and the change in oxide density during the conversion from amorphous to monoclinic phase [73]. The cross-sectional image shown in **Figure 2-2c** disclosed that the thickness of the produced oxide layer was 600–700 nm. Following the deposition of 10 cycles of Bi_2S_3 QDs, the ANPor WO_3 surface got rougher, and a lot of spherical particles that were identified as Bi_2S_3 QDs were visible (**Figure 2-2d**). As a result of Bi_2S_3 QDs deposition, the thickness of the oxide layer rose to 800–900 nm (**Figure 2-2e**). The elemental mapping was carried out to examine the Bi_2S_3 QDs distribution over the surface of ANPor WO_3, The EDS images (**Figure 2-2f–k**) manifested that the Bi_2S_3 QDs were effectively and uniformly dispersed on the surface of WO_3.

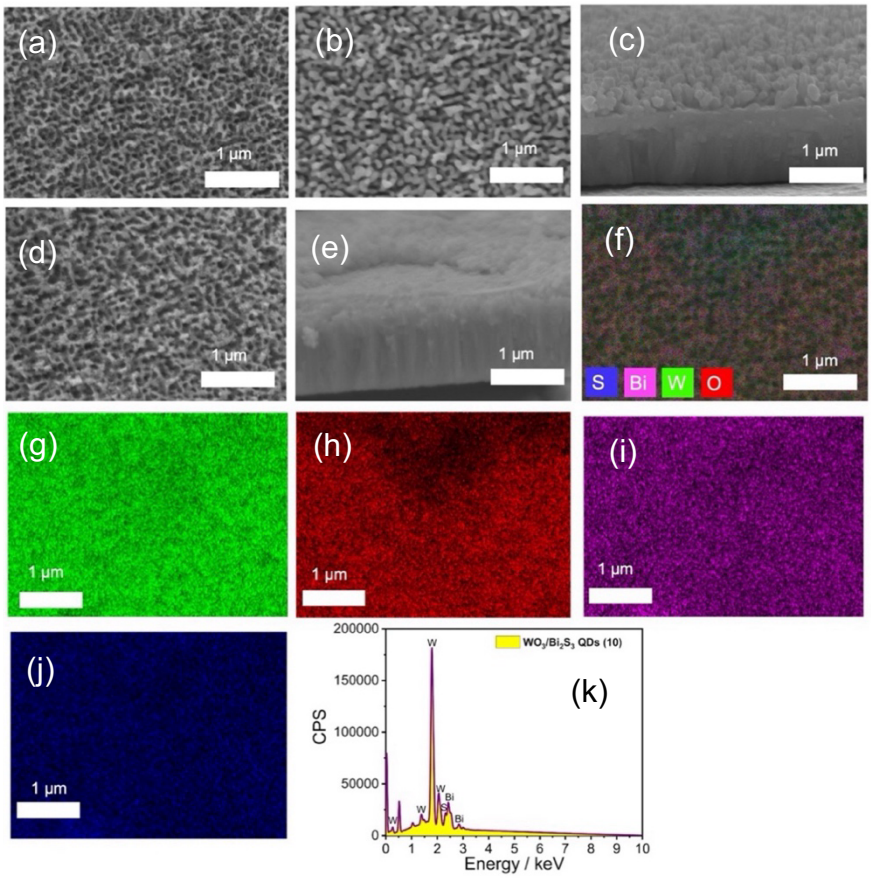

Figure 2-2. SEM images of (a) WO_3 before annealing, (b) Top, (c) Cross-section views of ANPor WO_3 after annealing, (d) Top, and (e) Cross-section views of ANPor WO_3/Bi_2S_3 QDs (10). (f) EDS element mapping image of ANPor WO_3/Bi_2S_3 QDs (10) all the elements included, (g)

Tungsten, (h) Oxygen, (i) Bismuth, and (j) Sulfur. (K) The EDS spectrum of ANPor WO_3/Bi_2S_3 QDs (10) demonstrated the appearance of its fundamental elements.

Figure 2-3a,b depicts the TEM and HRTEM images of ANPor WO_3. The results illustrated that WO_3 nanocrystals with crystal size around 50 nm were formed, which is consistent with the nanoporous walls seen in SEM images **(Figure 2-2b,c).** The TEM image of ANPor WO_3/Bi_2S_3 QDs (10) (**Figure 2-3c**) resembled that of the WO_3 image (**Figure 2-3a**), while the HRTEM image (**Figure 2-3d**) disclosed the homogeneous dispersion of Bi_2S_3 QDs over the WO_3 surface. Because of the homogeneous covering of ANPor WO_3 with Bi_2S_3 QDs, a core-shell-like structure was generated in the ANPor WO_3/Bi_2S_3 QDs (10), as noticed in the STEM-EDS mappings (**Figure 2-3e,f**). The microscopic observations illustrated in **Figures 2-2** and **2-3** clarified that ANPor WO_3 was successfully prepared on the surface of the W sheet after 4 h of the anodization technique and Bi_2S_3 QDs uniformly coated the surface of WO_3 through the application of 10 cycles of SILAR procedure (**Figure 2-3g**).

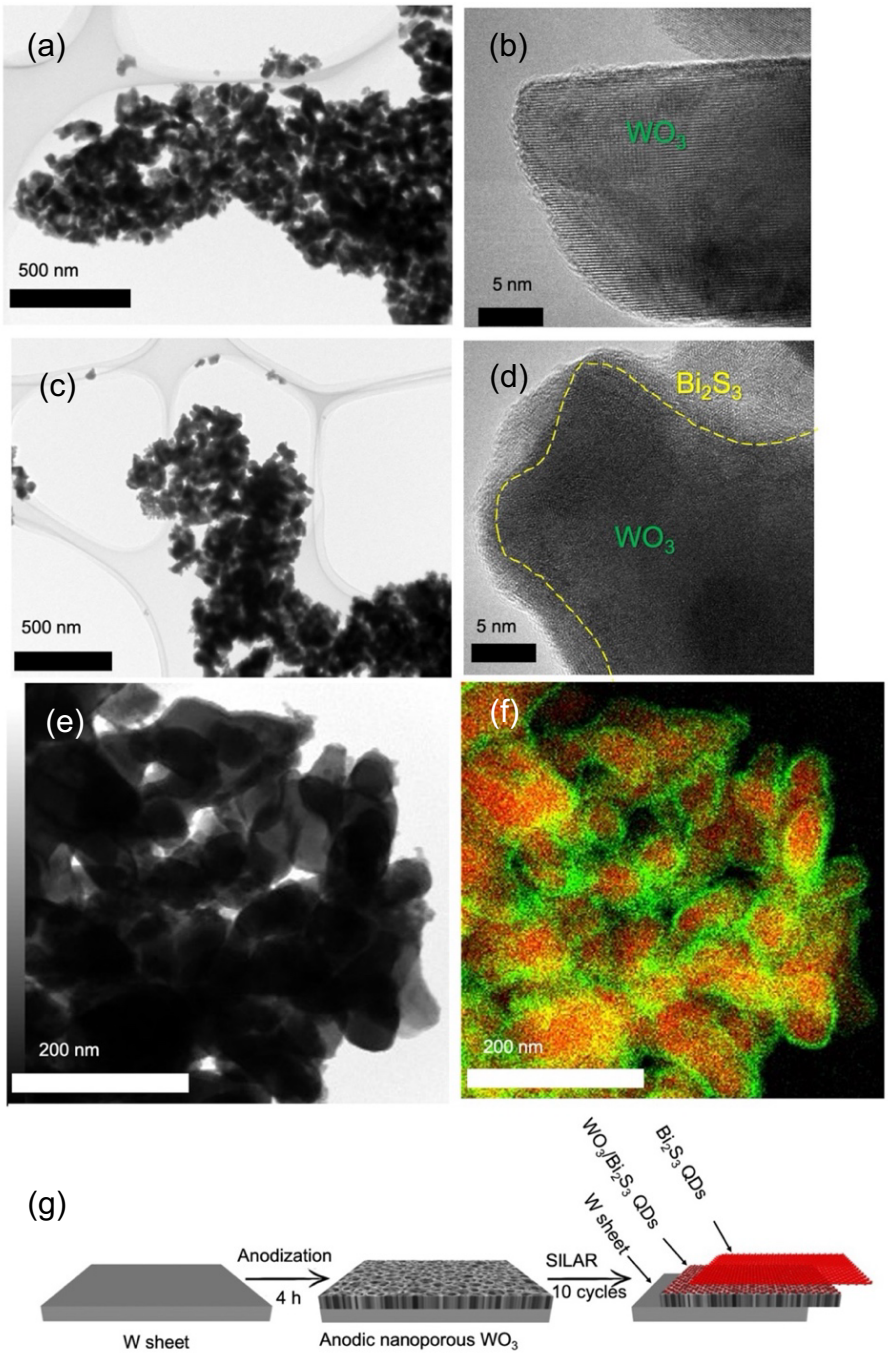

Figure 2-3. (a) TEM and (b) HRTEM images of annealed ANPor WO_3. (c) TEM and (d) HRTEM images of ANPor WO_3/Bi_2S_3 QDs (10). (e) STEM and (f) EDS mappings of ANPor WO_3/Bi_2S_3 QDs (10). W and Bi are represented in red and green colors, respectively, in panel f. (g) Graphic representation of the fabricated ANPor WO_3/Bi_2S_3 QDs photoanode.

The elemental composition and valence states of as prepared ANPor WO_3 and ANPor WO_3/Bi_2S_3 QDs were examined using XPS analysis. The WO_3 survey spectrum, as shown in **Figure 2-4a**, indicates the existence of W and O elements together with adventitious C contamination [74]. **Figure 2-4b** shows the narrow spectrum of W 4f with a curve fitting to two spin-orbit doublets at 35.7 and 37.9 eV, matching $4f_{7/2}$ and W $4f_{5/2,}$ respectively, clarifying the W^{6+} oxidation state in ANPor WO_3 [61,74,75]. The 2.2 eV splitting between the two core levels is consistent with previous measurements [76]. **Figure 2-4c** illustrates the O 1s narrow spectrum with the main peak at 530.5 eV, related to O^{2-} bonded with W in WO_3 [77]. The ANPor WO_3/Bi_2S_3 QDs survey spectrum clarifies the existence of W, O, Bi, S, elements, and adventitious C (**Figure 2-4d**). The narrow spectrum of W4f in ANPor WO_3/Bi_2S_3 QDs (**Figure 2-4e**) indicates the unchanged doublet of W $4f_{5/2}$ and W $4f_{7/2}$ at 38.1 eV and 36 eV respectively, corresponding to the W^{6+} as in WO_3. **Figure 2-4f** shows three peaks at 530.8, 531.8, and 532.9 eV, which are ascribed to O bonded to W, O defect sites that verify the formation of O vacancies, and OH of the adsorbed H_2O on the surface, respectively [78,79]. **Figure 2-4g** discloses two large peaks at 164.5 and 159.2 eV, related to Bi $4f_{5/2}$ and Bi $4f_{7/2}$, verifying the existence of Bi^{3+} [80,81]. A small peak at 161.5 eV is related to S 2p, and the entire spectrum in this energy zone confirmed the formation of Bi_2S_3 [82].

The XPS analysis of the used ANPor WO_3 (**Figure 2-5a–c**) and ANPor WO_3/Bi_2S_3 QDs (**Figure 2-5d–f**) samples proved the dissolution of the WO_3 layer from the W sheet as well as the existence of two peaks at 33.8 and 31 eV, are attributed to W metal $4f_{5/2}$ and W metal $4f_{7/2}$ respectively [83]. Additionally, it was observed that the distinctive peaks of Bi 4f and S 2p disappeared.

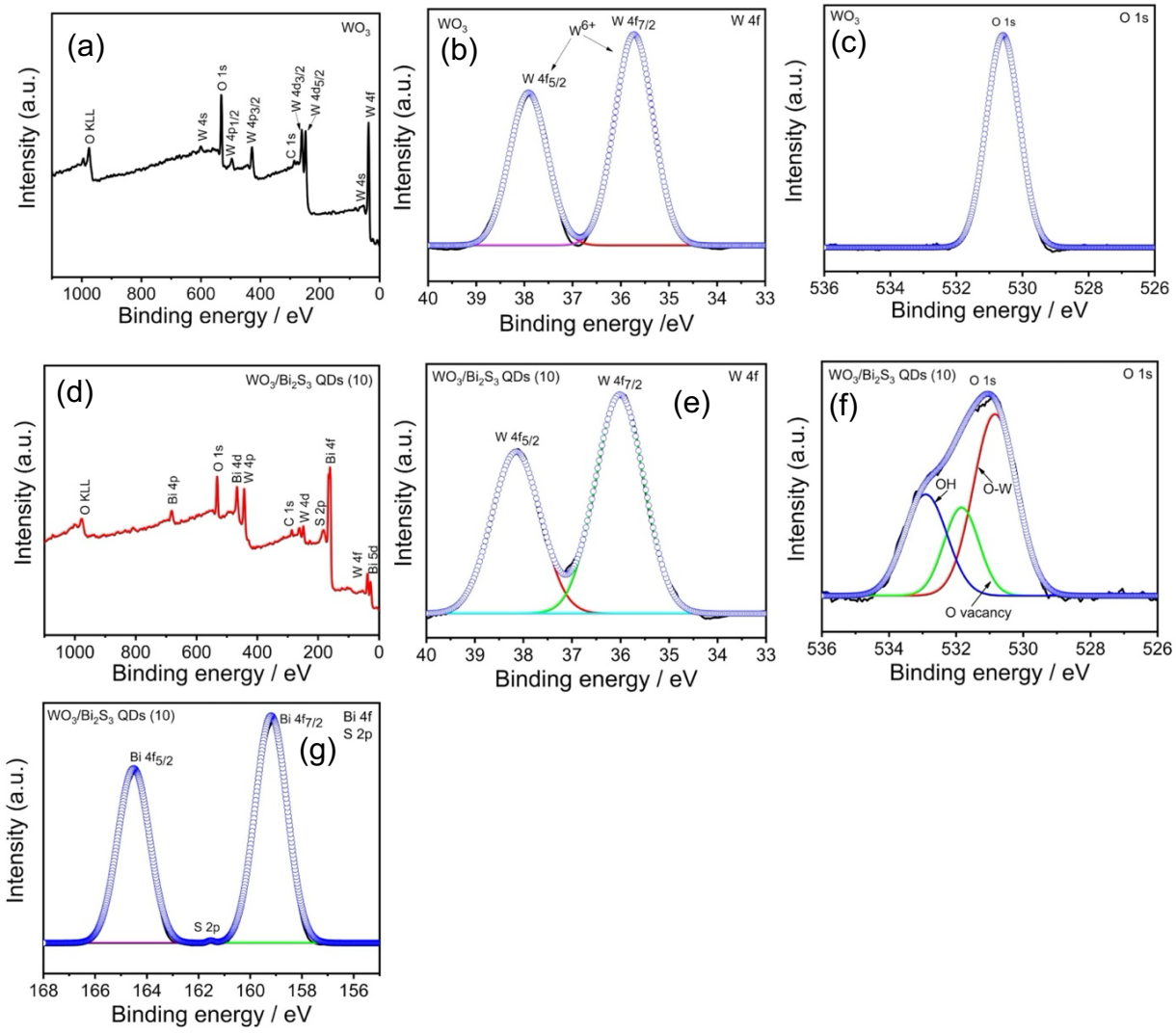

Figure 2-4. (a) XPS survey scan of ANPor WO_3, and related narrow scan of (b) W 4f, (c) O 1s. (d) survey scan of ANPor WO_3/Bi_2S_3 QDs, and related narrow scan of (e) W 4f, (f) O 1s, (g) Bi 4f, and S 2p.

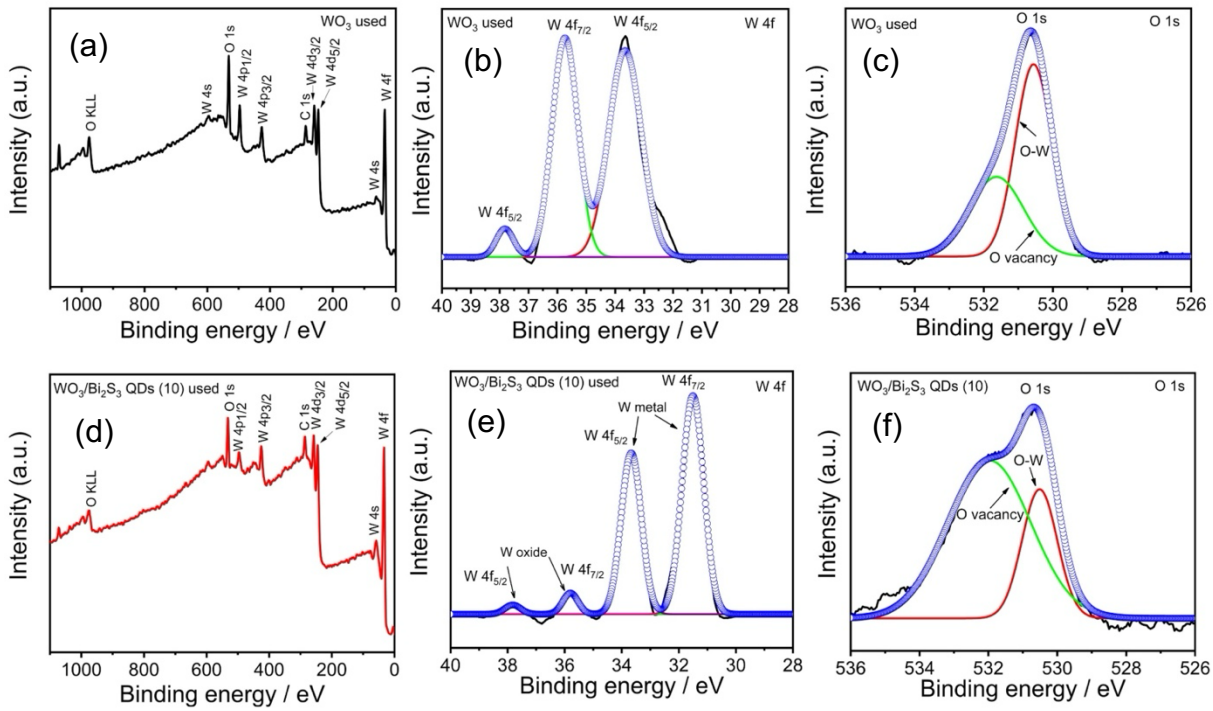

Figure 2-5. (a) XPS survey scan of used ANPor WO_3, and related narrow scan of (b) W 4f, (c) O 1s. (d) survey scan of used ANPor WO_3/Bi_2S_3 QDs, and related narrow scan of (e) W 4f, (f) O 1s.

The UV–Vis DRS was utilized to study the influence of the Bi_2S_3 QDs deposition on the light absorption ability and bandgap energy. **Figure 2-6a** demonstrates that ANPor WO_3 absorbs light in the UV zone. following the deposition of Bi_2S_3 QDs (10), ANPor WO_3/Bi_2S_3 QDs manifest a redshift and strong light absorption in the UV–Vis zone (200-700 nm). The bandgap energy of ANPor WO_3 and ANPor WO_3/Bi_2S_3 QDs was estimated utilizing the Kubelka−Munk function [84]. **Figure 2-6b** depicts that the bandgap energy was remarkably decreased after the deposition of Bi_2S_3 QDs on the surface of WO_3, from 3.13 to 1.31 eV, thus significantly enhanced Vis light absorption.

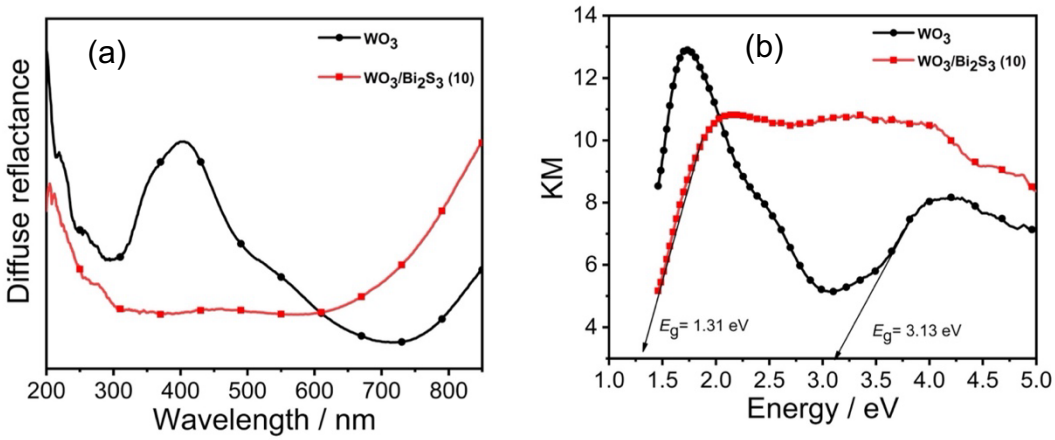

Figure 2-6. (a) UV–Vis DRS, (b) bandgap energy of ANPor WO_3, and ANPor WO_3/Bi_2S_3 QDs samples.

2.3.2. Photoelectrochemical water splitting results

2.3.2.1. Chronoamperometry measurement

Chronoamperometry study was carried out at 0.95 V vs. RHE in 0.1 M Na_2S/Na_2SO_3 electrolyte for 5 h to examine the chemical and structural stabilities of ANPor WO_3 and ANPor WO_3/Bi_2S_3 QDs (10) photoanodes during PEC-WS (**Figure 2-7a**). it was observed that the generated photocurrent by ANPor WO_3 photoanode rose over time, eventually stabilizing after 100 min. Meanwhile, ANPor WO_3/Bi_2S_3 QDs (10) achieved a much higher initial photocurrent than WO_3 before dropping and increasing over time, they later manifested a little decline before stabilizing. After 5 h of chronoamperometry measurement, the current densities were similar. This was attributed to the corrosion of the ANPor WO_3 and ANPor WO_3/Bi_2S_3 QDs (10) photoanodes, and the dissolution of the WO_3 and Bi_2S_3 QDs layers in the 0.1 M Na_2S/Na_2SO_3 electrolyte. This presumption was verified by XRD (**Figure 2-1**) and XPS (**Figure 2-5**) of both samples following 5 h of chronoamperometry measurement. After getting this result, we studied the chronoamperometry of the pure W sheet, which displayed high stability and current density similar to the other investigated samples. This proved that the observed continuous activity of ANPor WO_3 and ANPor WO_3/Bi_2S_3 QDs (10) photoanodes after extreme corrosion was owing to the electrochemical activity of W metal.

2.3.2.2. Hydrogen generation

The PEC H_2 production was performed at 0.95 V vs. RHE and utilized 0.1 M Na_2S/Na_2SO_3 as a sacrificial agent during the chronoamperometry measurement. The quantity of H_2 produced utilizing W sheet, ANPor WO_3, and ANPor WO_3/Bi_2S_3 QDs (10) photoanodes were plotted in **Figure 2-7b**. It can be noticed that the H_2 quantity for the photoanodes rose over time. The maximum H_2 quantities achieved after 5 h, were 4.78, 3.59, and 2.64 mmol for the W sheet, ANPor WO_3/Bi_2S_3 QDs (10), and ANPor WO_3 photoanodes, respectively.

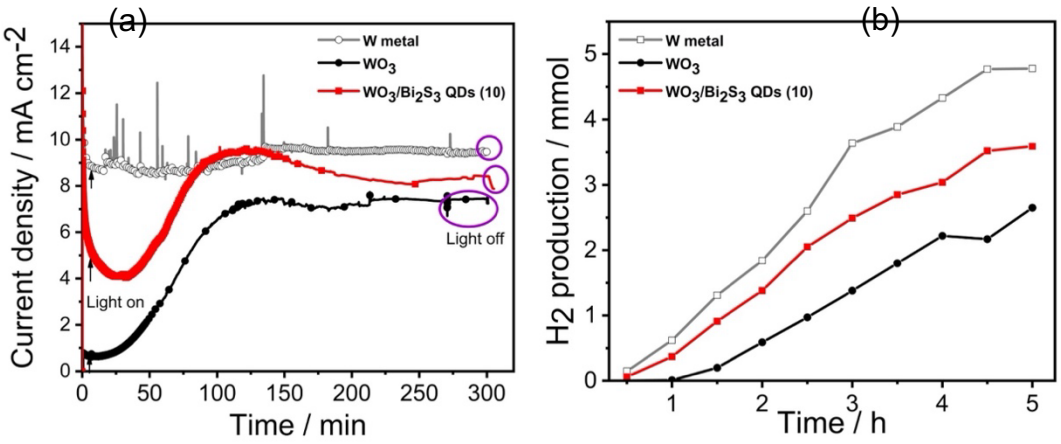

Figure 2-7. (a) Chronoamperometry measurement and (b) H_2 generation quantity over time in 0.1 M Nas_2S/Na_2SO_3 at 0.95 V vs. RHE of pure W sheet, ANPor WO_3, and ANPor WO_3/Bi_2S_3 QDs (10) photoanodes.

2.3.2.3. Linear sweep voltammetry

The LSV determination of bare ANPor WO_3 and ANPor WO_3/Bi_2S_3 QDs photoanodes are shown in **Figure 2-8a**. Under light irradiation, the pure ANPor WO_3 showed a low photocurrent density of 0.85 mA cm^{-2} at 0.95 V vs. RHE, While Bi_2S_3 QDs deposition remarkably improved the photocurrent density and reduced the onset potential. ANPor WO_3/Bi_2S_3 QDs (10) achieved the highest photocurrent density of 16.28 mA cm^{-2} at 0.95 V vs. RHE. This can be ascribed to the adequate quantity of Bi_2S_3 QDs deposited through 10 cycles of the SILAR procedure. The deposition of Bi_2S_3 QDs enhanced the PEC-WS performance owing to the developed visible light absorption ability and improved e^-/h^+ pairs separation and transmission. On the other hand, when the quantity of Bi_2S_3 QDs was excessively high, a compact layer of Bi_2S_3 QDs was formed which impeded the activity of WO_3 and significantly reduced the photocurrent density.

The boosted PEC-WS activity was in agreement with the UV–Vis DRS result (**Figure 2-6**). **Table 2-1** illustrates the values of current density under dark/illumination conditions of pure ANPor WO_3 and ANPor WO_3/Bi_2S_3 QDs with various cycles of Bi_2S_3 QDs deposition (6, 8, 10, and 12 cycles) at 0.95 V vs. RHE. The current density attained in this study is the highest compared to the previously published anodic WO_3-based studies. This can be attributed to the suitable absorption band edge of Bi_2S_3 QDs and the superb use of photogenerated electrons through the ANPor WO_3 structure. **Table 2-2** displays the PEC-WS performance of a variety of modified anodic WO_3 photoanodes reported in the literature from 2010 to 2021 in comparison to this study. The data disclosed that the ANPor WO_3/Bi_2S_3 QDs (10) photoanode attained the best efficiency.

The transient photocurrent response explains the relation between the photoresponse and the photocurrent. **Figure 2-8b** shows the on-off transient photocurrent responses of pristine ANPor WO_3 and ANPor WO_3/Bi_2S_3 QDs (10) photoanodes at 0.95 V vs. RHE and 100 mW/cm^2. Both pristine ANPor WO_3 and ANPor WO_3/Bi_2S_3 QDs (10) photoanodes demonstrated a quick rise under light irradiation and a quick decline under dark conditions, clarifying that both photoanodes show photoresponse during the PEC-WS. Bare ANPor WO_3 manifested very low photocurrent under light illumination, owing to light absorption, particularly in the UV zone, as verified by UV–Vis DRS spectra (**Figure 2-6**) and a very high rate of e^-/h^+ pairs recombination. whereas, ANPor WO_3/Bi_2S_3 QDs (10) demonstrated a higher photocurrent density than bare ANPor WO_3, which was in agreement with the LSV result. This is owing to the type-II band alignment formation between Bi_2S_3 QDs and WO_3, and the enhanced light absorption supported by Bi_2S_3 QDs deposition [61]. As a result, it significantly ameliorated the interfacial e^-/h^+ pairs separation and transport. This experimental result indicates that the PEC-WS performance of the ANPor WO_3/Bi_2S_3 QDs (10) photoanode is much higher than that of pristine ANPor WO_3.

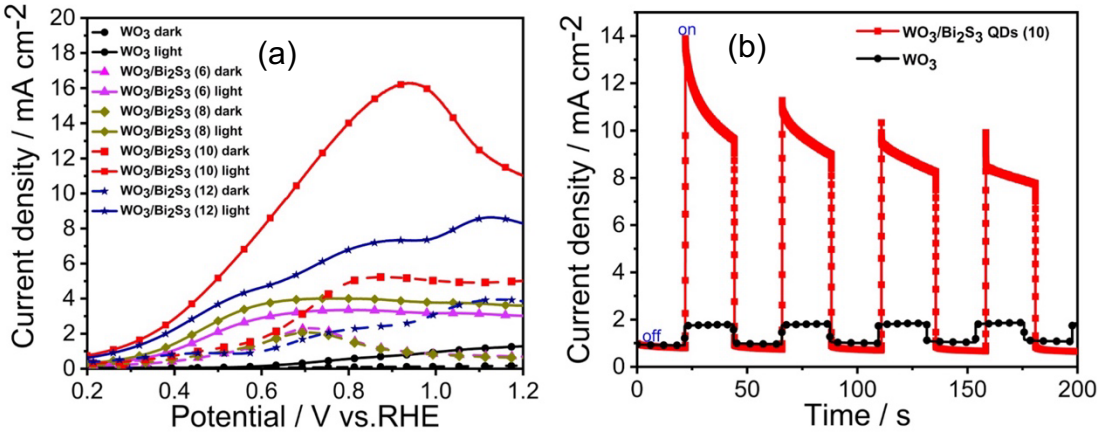

Figure 2-8. (a) LSV curves of bare ANPor WO_3 and ANPor WO_3/Bi_2S_3 QDs with various cycles of Bi_2S_3 QDs deposition (6, 8, 10, and 12), at a scan rate of 10 mV s^{-1}. (b) Current density-time curves at 0.95 V vs. RHE under light illumination with 20 s light on/off cycles of ANPor WO_3 and ANPor WO_3/Bi_2S_3 QDs (10) photoanodes.

2.3.2.4. Electrochemical impedance spectroscopy

Figure 2-9a displays the Nyquist plots of bare ANPor WO_3 and ANPor WO_3/Bi_2S_3QDs (10) photoanodes. The semicircle in the plots shows the e^-/h^+ pairs transfer procedure at the interface between the photoelectrode and electrolyte. In general, the smaller the semicircle radius, the lower the e^-/h^+ pairs migration impedance [85,86]. Pure ANPor WO_3 demonstrated a higher impedance than ANPor WO_3/Bi_2S_3 QDs (10), owing to the delayed mobility of e^-/h^+ pairs and high recombination rate at the interface between ANPor WO_3 and electrolyte.

The interfacial charge transfer resistances (R_{ct}) of the ANPor WO_3 and ANPor WO_3/Bi_2S_3 QDs (10) photoanodes were 865 Ω and 62 Ω, respectively. The small R_{ct} value of the ANPor WO_3/Bi_2S_3 QDs (10) photoanode exhibited lower charge transfer resistance and higher photocurrent, which is in agreement with the LSV data depicted in **Figure 2-8a**. The generated type-II heterojunction among ANPor WO_3 and Bi_2S_3 QDs ameliorated e^-/h^+ pairs separation and mobility, resulting in the mitigation of charge recombination and reduction of charge transfer resistance.

2.3.2.5. Mott–Schottky

The M-S curves of bare ANPor WO_3 and ANPor WO_3/Bi_2S_3 QDs (10) are represented in **Figure 2-9b**. The observed positive slope of the two photoanodes proved that ANPor WO_3 and ANPor WO_3/Bi_2S_3 QDs (10) are n-type semiconductors. The flat band potentials (E_{fb}) of ANPor WO_3 and ANPor WO_3/Bi_2S_3 QDs (10) were 0.36 V and 0.30 V vs. RHE, respectively. This reduction in E_{fb} also confirmed the efficient mobility of e^-/h^+ pairs in the ANPor WO_3/Bi_2S_3 QDs photoanode [61].

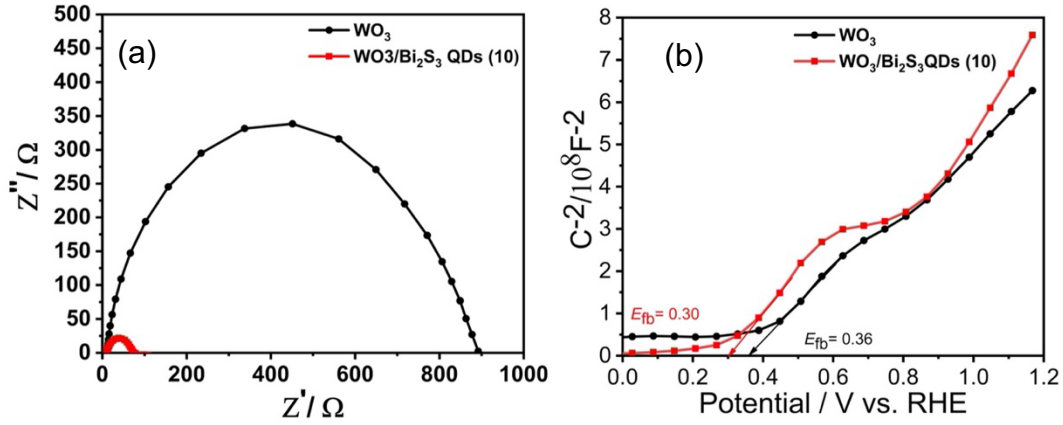

Figure 2-9. (a) EIS, and (b) M-S curves of ANPor WO_3 and ANPor WO_3/Bi_2S_3 QDs (10) photoanodes.

2.3.2.6. Photoconversion efficiency

To further study the PEC-WS performance of pure ANPor WO_3 and samples modified with Bi_2S_3 QDs, the photoconversion efficiency was estimated using the ABPE as illustrated in equation (3) [87]:

$$\eta\ (\%) = j_p\ \frac{(1.23-V)}{I_o}\ \text{X100} \qquad \text{(Eq. 2-3)}$$

where j_p , V, and I_o are the photocurrent density (mA cm^{-2}), the applied voltage vs. RHE, and the light intensity (100 mW cm^{-2} for AM 1.5G), respectively.

The ANPor WO_3/Bi_2S_3 QDs (10) photoanode achieved the highest photoconversion efficiency of 4.1% at 0.66 V vs. RHE, while bare ANPor WO_3 photoanode achieved 0.3% at 0.85 V vs. RHE (**Figure 2-10**).

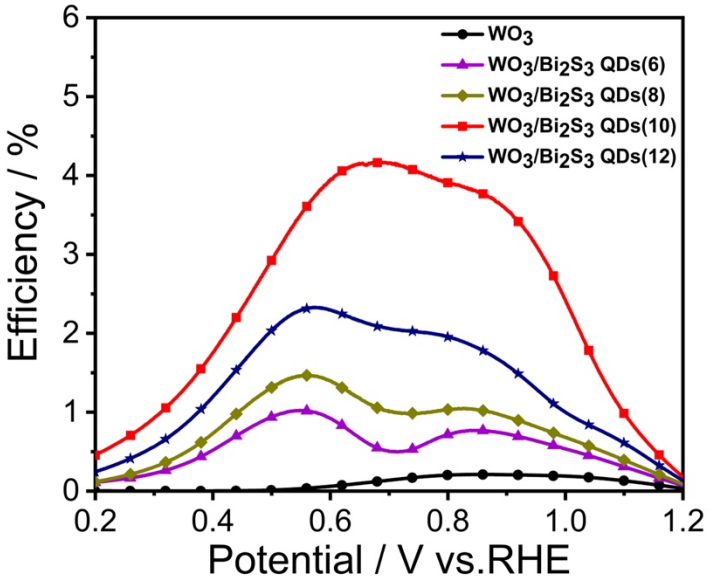

Figure 2-10. Photoconversion efficiency as a function of the applied potential of bare ANPor WO_3 and samples modified with various cycles of Bi_2S_3 QDs.

Table 2-1. Values of the current density of bare ANPor WO_3 and ANPor WO_3/Bi_2S_3 QDs photoanodes under dark and light illumination conditions at 0.95 V vs. RHE.

Photoanode	**I (mA cm^{-2}) under dark**	**I (mA cm^{-2}) under illumination**
ANPor WO_3	0.13	0.85
ANPor WO_3/Bi_2S_3 QDs (6)	0.90	3.23
ANPor WO_3/Bi_2S_3 QDs (8)	0.90	3.88
ANPor WO_3/Bi_2S_3 QDs (10)	5.16	16.28
ANPor WO_3/Bi_2S_3 QDs (12)	2.68	7.30

Table 2-2. PEC-WS performance of various modified anodic WO_3 photoanodes in the literature (2010–2021). The data implied that our ANPor WO_3/Bi_2S_3 QDs (10) photoanode attained the best efficiency.

Photoanode	Morphology	Light source/intensity	Electrolyte	PEC-WS efficiency	Ref.
WO_3/W	Nanotubes	LED irradiation (λ = 420 nm, 15 mW/cm^2, active area = 5 cm^2	0.5 M Na_2SO_4/25 vol % methanol	I = 0.6 mA cm^{-2} at 1 V vs. SCE, QE = ~5.23%, H_2 = ~27 μmol/cm^2 after 10 h	[70]
WO_3	Nanoporous	300 W Xe lamp with an AM 1.5 G filter,100 mW/cm^2	0.5 M Na_2SO_4	1.1 mA cm^{-2} at 1.6 V vs. Ag/Agcl IPCE = 4% at 400 nm, (~20% at UV region)	[34]
$CuWO_4$–WO_3	Nanoporous	150 W xenon arc lamp	0.1 M KNO_3	I = 53 μA cm^{-2} at 1 V vs. SCE	[44]
WO_3	Nanoporous	150 W xenon lamp (800 W/m^2)	1 M H_2SO_4/~1 wt% $C_2H_6O_2$	I = 0.18 mA cm^{-2} at 0.7 V vs. SCE	[88]
WO_3	Nanoporous	500 W Xe lamp, 100 mW/cm^2	0.5 M H_2SO_4	I = 3.45 mA cm^{-2} at 1.6 V vs. Ag/AgCl, ABPE = 0.91%, IPCE = 92% at 340 nm at 1.2 V vs. Ag/AgCl,	[89]
NH_4-doped WO_3	Nanoporous	AM 1.5 G illumination	0.33 M H_3PO_4	I = ~0.6 mA cm^{-2} at 1.8 V vs. Ag/AgCl	[90]
WO_3	Nanotubes	150 W Xe lamp with AM1.5 G filter	1 M H_2SO_4	3.5 mA cm^{-2} at 1.5 V vs. SCE	[91]
ANPor WO_3/Bi_2S_3 QDs	Nanoporous, Quantum dots	300 W Xenon lamp, AM 1.5G filter	0.1 M Na_2S/Na_2SO_3	16.28 mA cm^{-2} at 0.95 V vs. RHE, ABPE = 4.1% at 0.66 V vs. RHE, H_2 after 5 h = 3.59 mmol	This study

2.3.3. Photoelectrochemical mechanism

The proposed charge flow mechanism in the ANPor WO_3/Bi_2S_3 QDs photoanode is depicted in **Figure 2-11**. The potential energy chart was suggested depending on the measured bandgap energy by the XPS valence band edge of ANPor WO_3 and Bi_2S_3 QDs (**Figure 2-11a,b**). The XPS valence band edge shows the energy difference between the valence band and the Fermi level [92]. Upon light illumination on the ANPor WO_3/Bi_2S_3 QDs photoanode, the photons with energies equal to or greater than the semiconductor's bandgap energy (WO_3: 3.13 eV, Bi_2S_3 QDs: 1.31 eV) could be absorbed. Electrons were excited to the CB and generated positive holes in the VB. Because the CB of Bi_2S_3 QDs is more negative than the CB of WO_3 [93], the excited electrons transferred from the CB of Bi_2S_3 QDs to the CB of WO_3 via the core-shell-like structure displayed in **Figure 2-3f**, then migrated to the Pt electrode to reduce H_2O to H_2. Conversely, the holes in the VB of WO_3 were transported to the VB of Bi_2S_3 QDs and then reacted with the scavenger electrolyte (0.1 M Na_2S/Na_2SO_3) (**Figure 2-11c)**. This inverse charge flow pathway inhibited the e^-/h^+ pairs recombination, leading to high photocurrent generation. Thus, the improved PEC-WS efficiency on ANPor WO_3/Bi_2S_3 QDs photoanodes was attributed to (1) the superb Vis light absorption ability of Bi_2S_3 QDs. (2) The uniform distribution and superb contact of Bi_2S_3 QDs with WO_3 ameliorated the e^-/h^+ pairs separation and mobility. (3) The constructed type-II heterojunction enhanced charge separation and inhibited the recombination rate.

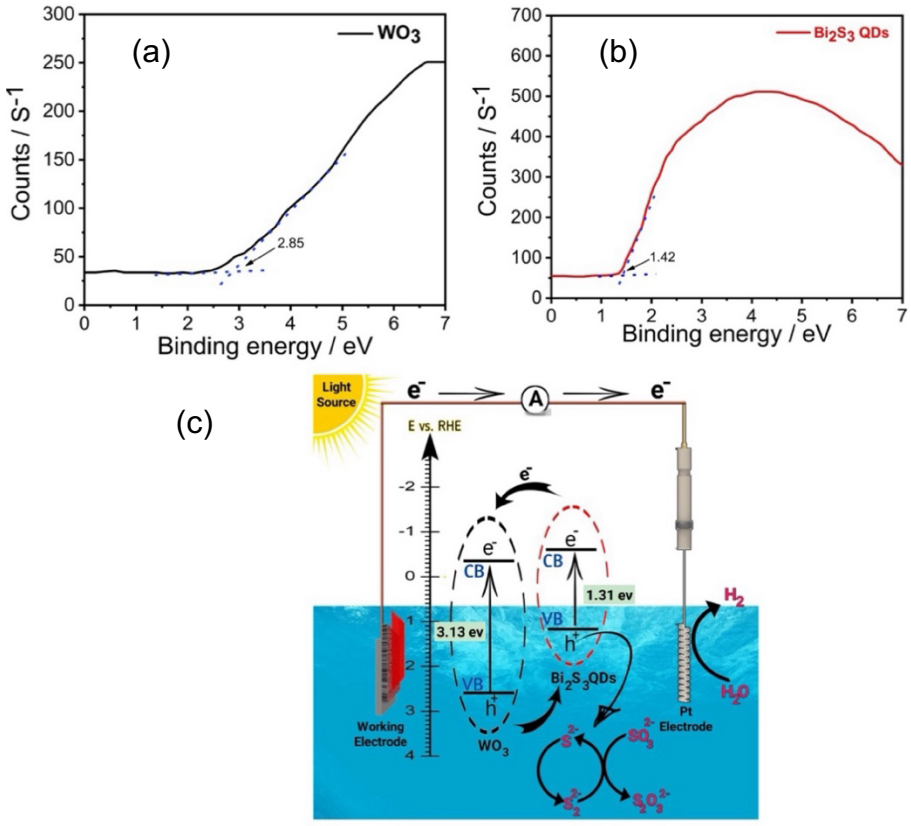

Figure 2-11. Valence band XPS spectra of (a) ANPor WO_3 and (b) Bi_2S_3 QDs (c) Charge transfer mechanism in the ANPor WO_3/Bi_2S_3 QDs photoanode.

2.4. Conclusions

The ANPor WO_3/Bi_2S_3 QDs heterojunction was successfully fabricated utilizing anodization and SILAR procedures. The ANPor WO_3/Bi_2S_3 QDs (10) photoanode attained the highest photocurrent density of 16.28 mA cm^{-2} at 0.95 V vs. RHE, which is nearly 19 folds higher than that of pristine ANPor WO_3 (0.85 mA cm^{-2}). Furthermore, it demonstrated a maximum photoconversion efficiency of 4.1% at 0.66 V vs. RHE and formed 3.59 mmol of H_2 after 5 h. This can be attributed to the adequate quantity and uniform distribution of Bi_2S_3QDs on the surface of WO_3. Moreover, the ANPor WO_3/Bi_2S_3 QDs (10) heterojunction displayed higher Vis light absorption ability, higher charge density, and lower charge transfer resistance than pristine ANPor WO_3 proved by UV–Vis DRS, M-S, and EIS results respectively. This remarkably boosted PEC-WS performance was also owing to the generation of type-II heterojunction between ANPor WO_3 and Bi_2S_3 QDs, which ameliorated the separation and mobility of e^-/h^+ pairs.

References

[1] I. Roger, M.A. Shipman, M.D. Symes, Earth-abundant catalysts for electrochemical and photoelectrochemical water splitting, Nat Rev Chem 1 (2017) 0003. https://doi.org/10.1038/s41570-016-0003.

[2] Z. Wei, M. Janczarek, K. Wang, S. Zheng, E. Kowalska, Morphology-Governed Performance of Plasmonic Photocatalysts, Catalysts 10 (2020) 1070. https://doi.org/10.3390/catal10091070.

[3] G. Dong, H. Hu, X. Huang, Y. Zhang, Y. Bi, Rapid activation of Co_3O_4 cocatalysts with oxygen vacancies on TiO_2 photoanodes for efficient water splitting, J Mater Chem A Mater 6 (2018) 21003–21009. https://doi.org/10.1039/C8TA08342H.

[4] A. FUJISHIMA, K. HONDA, Electrochemical Photolysis of Water at a Semiconductor Electrode, Nature 238 (1972) 37–38. https://doi.org/10.1038/238037a0.

[5] R. Jia, Y. Wang, A. Li, C. Cheng, Recent advances on three-dimensional ordered macroporous metal oxide-based photoelectrodes for photoelectrochemical water splitting, Mater Chem Front 8 (2024) 1230–1249. https://doi.org/10.1039/D3QM00990D.

[6] Q. Wang, J. Lian, Q. Ma, S. Zhang, J. He, J. Zhong, J. Li, H. Huang, B. Su, Preparation of carbon spheres supported CdS photocatalyst for enhancement its photocatalytic H 2 evolution, Catal Today 281 (2017) 662–668. https://doi.org/10.1016/j.cattod.2016.05.013.

[7] C. Ding, J. Shi, Z. Wang, C. Li, Photoelectrocatalytic Water Splitting: Significance of Cocatalysts, Electrolyte, and Interfaces, ACS Catal 7 (2017) 675–688. https://doi.org/10.1021/acscatal.6b03107.

[8] J. Hou, C. Yang, H. Cheng, S. Jiao, O. Takeda, H. Zhu, High-performance p-Cu_2O/n-TaON heterojunction nanorod photoanodes passivated with an ultrathin carbon sheath for photoelectrochemical water splitting, Energy Environ. Sci. 7 (2014) 3758–3768. https://doi.org/10.1039/C4EE02403F.

[9] M. El ouardi, A. Idrissi, H. Ahsaine, A. BaQais, M. Saadi, M. Arab, Current advances on nanostructured oxide photoelectrocatalysts for water splitting: A comprehensive review, Surfaces and Interfaces 45 (2024) 103850. https://doi.org/10.1016/j.surfin.2024.103850.

[10] W. Tian, C. Chen, L. Meng, W. Xu, F. Cao, L. Li, PVP Treatment Induced Gradient Oxygen Doping in In_2S_3 Nanosheet to Boost Solar Water Oxidation of WO_3 Nanoarray Photoanode, Adv Energy Mater 10 (2020) 1903951. https://doi.org/10.1002/aenm.201903951.

[11] F. Zhao, H. Sheng, Q. Sun, J. Wang, Q. Liu, Z. Hu, B. He, Y. Wang, Z. Li, X. Liu, Harvesting the infrared part of solar light to promote charge transfer in Bi_2S_3/WO_3 photoanode for enhanced photoelectrochemical water splitting, J Colloid Interface Sci 621 (2022) 267–274. https://doi.org/10.1016/j.jcis.2022.04.052.

[12] M. Okazaki, Y. Suganami, N. Hirayama, H. Nakata, T. Oshikiri, T. Yokoi, H. Misawa, K. Maeda, Site-Selective Deposition of a Cobalt Cocatalyst onto a Plasmonic Au/TiO_2 Photoanode for Improved Water Oxidation, ACS Appl Energy Mater 3 (2020) 5142–5146. https://doi.org/10.1021/acsaem.0c00857.

[13] F. Liao, Y. Shi, Q. Dang, H. Yang, H. Huang, Z. Kang, M. Shao, Carbon dots dominated photoelectric surface in titanium dioxide nanotube/nitrogen-doped carbon dot/gold nanocomposites for improved photoelectrochemical water splitting, J Colloid Interface Sci 606 (2022) 1274–1283. https://doi.org/10.1016/j.jcis.2021.08.131.

[14] L. Li, Y. Chen, X. Liu, Q. Wang, L. Du, X. Chen, G. Tian, Cu_2O decorated α-Fe_2O_3/SnS_2 core/shell heterostructured nanoarray photoanodes for water splitting, Solar Energy 220 (2021) 843–851. https://doi.org/10.1016/j.solener.2021.04.022.

[15] M.-H. Ji, Y.-X. Chen, R. Chen, K.-X. Li, H.-P. Zhao, H.-Y. Shi, H.-L. Wang, X. Jiang, C.-Z. Lu, A novel α-Fe_2O_3 photoanode with multilayered In_2O_3/Co–Mn nanostructure for efficient photoelectrochemical water splitting, Int J Hydrogen Energy 51 (2024) 66–77. https://doi.org/10.1016/j.ijhydene.2023.08.061.
[16] W. Xia, R. Zhang, Z. Chai, J. Pu, R. Kang, G. Wu, X. Zeng, Synergies of Zn/P-co-doped α-Fe_2O_3 photoanode for improving photoelectrochemical water splitting performance, Int J Hydrogen Energy 59 (2024) 22–29. https://doi.org/10.1016/j.ijhydene.2024.01.311.
[17] T.W. Kim, Y. Ping, G.A. Galli, K.-S. Choi, Simultaneous enhancements in photon absorption and charge transport of bismuth vanadate photoanodes for solar water splitting, Nat Commun 6 (2015) 8769. https://doi.org/10.1038/ncomms9769.
[18] Z. Tian, P. Zhang, P. Qin, D. Sun, S. Zhang, X. Guo, W. Zhao, D. Zhao, F. Huang, Novel Black $BiVO_4$/TiO_{2-x} Photoanode with Enhanced Photon Absorption and Charge Separation for Efficient and Stable Solar Water Splitting, Adv Energy Mater 9 (2019) 1901287. https://doi.org/10.1002/aenm.201901287.
[19] Y. Wang, W. Wang, J. Fu, Y. Liang, L. Yao, T. Zhu, Integrating the plasmonic sensitizer and electron relay into ZnO/Au/CdS sandwich nanotube array photoanode for efficient solar-to-hydrogen conversion with 3.2% efficiency, Renew Energy 168 (2021) 647–658. https://doi.org/10.1016/j.renene.2020.12.076.
[20] L. Sun, J. Sun, X. Sun, S. Bai, Y. Zhao, R. Luo, D. Li, A. Chen, rGO decorated ZnO/CdO heterojunction as a photoanode for photoelectrochemical water splitting, J Colloid Interface Sci 608 (2022) 2377–2386. https://doi.org/10.1016/j.jcis.2021.10.140.
[21] P.A. Koyale, S.P. Kulkarni, J.L. Gunjakar, T.D. Dongale, S.S. Sutar, S.S. Soni, Y.G. Kapdi, R.N. R, S. V. Mulik, S.D. Delekar, ZnO Nanorod/Multiwalled Carbon Nanotube Composites Sensitized with Cu-Based Metal–Organic Frameworks as Photoanodes for Solar-Driven Water Splitting, ACS Appl Nano Mater 7 (2024) 2662–2674. https://doi.org/10.1021/acsanm.3c04694.
[22] R. Bashiri, M.S. Irfan, N.M. Mohamed, S. Sufian, L.Y. Ling, N.A. Suhaimi, M.F.R. Samsudin, Hierarchically $SrTiO_3$@TiO_2@Fe_2O_3 nanorod heterostructures for enhanced photoelectrochemical water splitting, Int J Hydrogen Energy 46 (2021) 24607–24619. https://doi.org/10.1016/j.ijhydene.2020.02.106.
[23] X. Liu, F. Wang, Q. Wang, Nanostructure-based WO_3 photoanodes for photoelectrochemical water splitting, Physical Chemistry Chemical Physics 14 (2012) 7894. https://doi.org/10.1039/c2cp40976c.
[24] J. Song, Z.-F. Huang, L. Pan, J.-J. Zou, X. Zhang, L. Wang, Oxygen-Deficient Tungsten Oxide as Versatile and Efficient Hydrogenation Catalyst, ACS Catal 5 (2015) 6594–6599. https://doi.org/10.1021/acscatal.5b01522.
[25] W. Li, P. Da, Y. Zhang, Y. Wang, X. Lin, X. Gong, G. Zheng, WO_3 Nanoflakes for Enhanced Photoelectrochemical Conversion, ACS Nano 8 (2014) 11770–11777. https://doi.org/10.1021/nn5053684.
[26] T. Jin, P. Diao, Q. Wu, D. Xu, D. Hu, Y. Xie, M. Zhang, WO_3 nanoneedles/α-Fe_2O_3/cobalt phosphate composite photoanode for efficient photoelectrochemical water splitting, Appl Catal B 148–149 (2014) 304–310. https://doi.org/10.1016/j.apcatb.2013.10.052.
[27] N.B.D. da Costa, J.C.O. Pazinato, G. Sombrio, M.B. Pereira, H. Boudinov, A. Gündel, E.C. Moreira, I.T.S. Garcia, Controlling the structural and optical properties of tungsten oxide films synthesized under environmentally friendly conditions, Mater Sci Semicond Process 122 (2021) 105476. https://doi.org/10.1016/j.mssp.2020.105476.

[28] M. Qamar, Q. Drmosh, M.I. Ahmed, M. Qamaruddin, Z.H. Yamani, Enhanced photoelectrochemical and photocatalytic activity of WO_3-surface modified TiO_2 thin film, Nanoscale Res Lett 10 (2015) 54. https://doi.org/10.1186/s11671-015-0745-2.

[29] J. Olejníček, M. Brunclíková, Š. Kment, Z. Hubička, H. Kmentová, P. Kšírová, M. Čada, M. Zlámal, J. Krýsa, WO_3 thin films prepared by sedimentation and plasma sputtering, Chemical Engineering Journal 318 (2017) 281–288. https://doi.org/10.1016/j.cej.2016.09.083.

[30] J. Han, K. Ko, S. Sarwar, M. Lee, S. Park, S. Hong, C. Han, Enhanced electrochromic properties of TiO_2 nanocrystal embedded amorphous WO_3 films, Electrochim Acta 278 (2018) 396–404. https://doi.org/10.1016/j.electacta.2018.05.026.

[31] L.M. Bertus, A. Duta, Synthesis of WO_3 thin films by surfactant mediated spray pyrolysis, Ceram Int 38 (2012) 2873–2882. https://doi.org/10.1016/j.ceramint.2011.11.060.

[32] G. Yun, M. Balamurugan, H.-S. Kim, K.-S. Ahn, S.H. Kang, Role of WO_3 Layers Electrodeposited on SnO_2 Inverse Opal Skeletons in Photoelectrochemical Water Splitting, The Journal of Physical Chemistry C 120 (2016) 5906–5915. https://doi.org/10.1021/acs.jpcc.6b00044.

[33] Y. Gu, W. Zheng, Y. Bu, Facile preparation of nanoflower structured WO_3 thin film on etched titanium substrate with high photoelectrochemical performance, Journal of Electroanalytical Chemistry 833 (2019) 54–62. https://doi.org/10.1016/j.jelechem.2018.11.001.

[34] T. Zhang, M. Paulose, R. Neupane, L.A. Schaffer, D.B. Rana, J. Su, L. Guo, O.K. Varghese, Nanoporous WO_3 films synthesized by tuning anodization conditions for photoelectrochemical water oxidation, Solar Energy Materials and Solar Cells 209 (2020) 110472. https://doi.org/10.1016/j.solmat.2020.110472.

[35] L. Cao, K. Xu, M. Fan, $Zn_{0.5}Cd_{0.5}S$ nanoparticles modified TiO_2 nanotube arrays with efficient charge separation and enhanced light harvesting for boosting visible-light-driven photoelectrochemical performance, J Power Sources 482 (2021) 228956. https://doi.org/10.1016/j.jpowsour.2020.228956.

[36] E. Ahmadi, C.Y. Ng, K.A. Razak, Z. Lockman, Preparation of anodic nanoporous WO_3 film using oxalic acid as electrolyte, J Alloys Compd 704 (2017) 518–527. https://doi.org/10.1016/j.jallcom.2017.02.123.

[37] K. Syrek, L. Zaraska, M. Zych, G.D. Sulka, The effect of anodization conditions on the morphology of porous tungsten oxide layers formed in aqueous solution, Journal of Electroanalytical Chemistry 829 (2018) 106–115. https://doi.org/10.1016/j.jelechem.2018.09.054.

[38] C.W. Lai, S.B. Abd Hamid, S. Sreekantan, A Novel Solar Driven Photocatalyst: Well-Aligned Anodic WO_3 Nanotubes, International Journal of Photoenergy 2013 (2013) 1–6. https://doi.org/10.1155/2013/745301.

[39] N.R. de Tacconi, C.R. Chenthamarakshan, G. Yogeeswaran, A. Watcharenwong, R.S. de Zoysa, N.A. Basit, K. Rajeshwar, Nanoporous TiO_2 and WO_3 Films by Anodization of Titanium and Tungsten Substrates: Influence of Process Variables on Morphology and Photoelectrochemical Response, J Phys Chem B 110 (2006) 25347–25355. https://doi.org/10.1021/jp064527v.

[40] R.M. Fernández-Domene, R. Sánchez-Tovar, B. Lucas-Granados, G. Roselló-Márquez, J. García-Antón, A simple method to fabricate high-performance nanostructured WO_3

photocatalysts with adjusted morphology in the presence of complexing agents, Mater Des 116 (2017) 160–170. https://doi.org/10.1016/j.matdes.2016.12.016.
[41] N. Mukherjee, M. Paulose, O.K. Varghese, G.K. Mor, C.A. Grimes, Fabrication of nanoporous tungsten oxide by galvanostatic anodization, J Mater Res 18 (2003) 2296–2299. https://doi.org/10.1557/JMR.2003.0321.
[42] Y. Liu, Y. Li, W. Li, S. Han, C. Liu, Photoelectrochemical properties and photocatalytic activity of nitrogen-doped nanoporous WO_3 photoelectrodes under visible light, Appl Surf Sci 258 (2012) 5038–5045. https://doi.org/10.1016/j.apsusc.2012.01.080.
[43] Y. Wang, W. Tian, C. Chen, W. Xu, L. Li, Tungsten Trioxide Nanostructures for Photoelectrochemical Water Splitting: Material Engineering and Charge Carrier Dynamic Manipulation, Adv Funct Mater 29 (2019) 1809036. https://doi.org/10.1002/adfm.201809036.
[44] M. Zych, K. Syrek, E. Wiercigroch, K. Malek, M. Kozieł, G.D. Sulka, Visible-light sensitization of anodic tungsten oxide layers with $CuWO_4$, Electrochim Acta 368 (2021) 137591. https://doi.org/10.1016/j.electacta.2020.137591.
[45] S. Han, J. Li, X. Chen, Y. Huang, C. Liu, Y. Yang, W. Li, Enhancing photoelectrochemical activity of nanocrystalline WO_3 electrodes by surface tuning with Fe(III), Int J Hydrogen Energy 37 (2012) 16810–16816. https://doi.org/10.1016/j.ijhydene.2012.08.145.
[46] C.A. Bignozzi, S. Caramori, V. Cristino, R. Argazzi, L. Meda, A. Tacca, Nanostructured photoelectrodes based on WO_3 : applications to photooxidation of aqueous electrolytes, Chem. Soc. Rev. 42 (2013) 2228–2246. https://doi.org/10.1039/C2CS35373C.
[47] W.A. Smith, I.D. Sharp, N.C. Strandwitz, J. Bisquert, Interfacial band-edge energetics for solar fuels production, Energy Environ Sci 8 (2015) 2851–2862. https://doi.org/10.1039/C5EE01822F.
[48] K. Maeda, K. Domen, Photocatalytic Water Splitting: Recent Progress and Future Challenges, J Phys Chem Lett 1 (2010) 2655–2661. https://doi.org/10.1021/jz1007966.
[49] B.M. Klepser, B.M. Bartlett, Anchoring a Molecular Iron Catalyst to Solar-Responsive WO_3 Improves the Rate and Selectivity of Photoelectrochemical Water Oxidation, J Am Chem Soc 136 (2014) 1694–1697. https://doi.org/10.1021/ja4086808.
[50] L. Jin, H. Zhao, Z.M. Wang, F. Rosei, Quantum Dots-Based Photoelectrochemical Hydrogen Evolution from Water Splitting, Adv Energy Mater 11 (2021) 2003233. https://doi.org/10.1002/aenm.202003233.
[51] Z. Liu, J. Wu, J. Zhang, Quantum dots and plasmonic Ag decorated WO_3 nanorod photoanodes with enhanced photoelectrochemical performances, Int J Hydrogen Energy 41 (2016) 20529–20535. https://doi.org/10.1016/j.ijhydene.2016.09.055.
[52] X. Zhang, Y. Tang, Y. Li, Y. Wang, X. Liu, C. Liu, S. Luo, Reduced graphene oxide and PbS nanoparticles co-modified TiO_2 nanotube arrays as a recyclable and stable photocatalyst for efficient degradation of pentachlorophenol, Appl Catal A Gen 457 (2013) 78–84. https://doi.org/10.1016/j.apcata.2013.03.011.
[53] P. Sheng, L. Yao, P. Yang, D. Yang, C. Lu, K. Cao, W. Li, The origin of enhanced photoelectrochemical activity in metal-ion-doped ZnO/CdS quantum dots, J Alloys Compd 822 (2020) 153700. https://doi.org/10.1016/j.jallcom.2020.153700.
[54] M. Mohamed Abouelela, G. Kawamura, A. Matsuda, Metal chalcogenide-based photoelectrodes for photoelectrochemical water splitting, Journal of Energy Chemistry 73 (2022) 189–213. https://doi.org/10.1016/j.jechem.2022.05.022.

[55] Y. Liu, Y. Deng, Z. Sun, J. Wei, G. Zheng, A.M. Asiri, S.B. Khan, M.M. Rahman, D. Zhao, Hierarchical Cu_2S Microsponges Constructed from Nanosheets for Efficient Photocatalysis, Small 9 (2013) 2702–2708. https://doi.org/10.1002/smll.201300197.

[56] P. Subramanyam, B. Meena, G.N. Sinha, M. Deepa, C. Subrahmanyam, Decoration of plasmonic Cu nanoparticles on WO_3/Bi_2S_3 QDs heterojunction for enhanced photoelectrochemical water splitting, Int J Hydrogen Energy 45 (2020) 7706–7715. https://doi.org/10.1016/j.ijhydene.2019.05.168.

[57] S. Majumder, N.D. Quang, C. Kim, D. Kim, Anion exchange and successive ionic layer adsorption and reaction-assisted coating of $BiVO_4$ with Bi_2S_3 to produce nanostructured photoanode for enhanced photoelectrochemical water splitting, J Colloid Interface Sci 585 (2021) 72–84. https://doi.org/10.1016/j.jcis.2020.11.081.

[58] M. Wang, Q. Wang, P. Guo, Z. Jiao, In situ fabrication of nanoporous $BiVO_4/Bi_2S_3$ nanosheets for enhanced photoelectrochemical water splitting, J Colloid Interface Sci 534 (2019) 338–342. https://doi.org/10.1016/j.jcis.2018.09.056.

[59] S. Sharma, N. Khare, Sensitization of narrow band gap Bi_2S_3 hierarchical nanostructures with polyaniline for its enhanced visible-light photocatalytic performance, Colloid Polym Sci 296 (2018) 1479–1489. https://doi.org/10.1007/s00396-018-4362-3.

[60] P. Subramanyam, B. Meena, D. Suryakala, M. Deepa, C. Subrahmanyam, Plasmonic nanometal decorated photoanodes for efficient photoelectrochemical water splitting, Catal Today 379 (2021) 1–6. https://doi.org/10.1016/j.cattod.2020.01.041.

[61] Y. Wang, W. Tian, L. Chen, F. Cao, J. Guo, L. Li, Three-Dimensional WO_3 Nanoplate/Bi_2S_3 Nanorod Heterojunction as a Highly Efficient Photoanode for Improved Photoelectrochemical Water Splitting, ACS Appl Mater Interfaces 9 (2017) 40235–40243. https://doi.org/10.1021/acsami.7b11510.

[62] A. Ahmad, F. Tezcan, G. Yerlikaya, Zia-ur-Rehman, H. Paksoy, G. Kardaş, Three dimensional rosette-rod TiO_2/Bi_2S_3 heterojunction for enhanced photoelectrochemical water splitting, J Alloys Compd 868 (2021) 159133. https://doi.org/10.1016/j.jallcom.2021.159133.

[63] G. Huang, J. Zhang, F. Jiang, Z. Zhang, J. Zeng, X. Qi, Z. Shen, H. Wang, Z. Kong, J. Xi, Z. Ji, Excellent photoelectrochemical activity of Bi_2S_3 nanorod/TiO_2 nanoplate composites with dominant {001} facets, J Solid State Chem 281 (2020) 121041. https://doi.org/10.1016/j.jssc.2019.121041.

[64] S. Sadhasivam, N. Anbarasan, M. Mukilan, P. Manivel, K. Jeganathan, Bi2S3 anchored ZnS/ZnO nanorod arrays photoanode for enhanced visible light driven photo electrochemical properties, Int J Hydrogen Energy 45 (2020) 30080–30090. https://doi.org/10.1016/j.ijhydene.2020.08.026.

[65] M.A. Mahadik, J.W. Park, W.-S. Chae, S.H. Choi, H.-S. Chung, M. Cho, J.S. Jang, Facile synthesis of Bi_2S_3 nanosheet/Zr:Fe_2O_3 nanorod heterojunction: Effect of Ag interlayer on the change transport and photoelectrochemical stability, Journal of Industrial and Engineering Chemistry 70 (2019) 311–321. https://doi.org/10.1016/j.jiec.2018.10.031.

[66] S. Berger, H. Tsuchiya, A. Ghicov, P. Schmuki, High photocurrent conversion efficiency in self-organized porous WO_3, Appl Phys Lett 88 (2006) 203119. https://doi.org/10.1063/1.2206696.

[67] A. Hellman, B. Wang, First-Principles View on Photoelectrochemistry: Water-Splitting as Case Study, Inorganics (Basel) 5 (2017) 37. https://doi.org/10.3390/inorganics5020037.

[68] C. Rosiles-Perez, S. Sidhik, L. Ixtilico-Cortés, F. Robles-Montes, T. López-Luke, A.E. Jiménez-González, High short-circuit current density in a non-toxic Bi2S3 quantum dot sensitized solar cell, Mater Today Energy 21 (2021) 100783. https://doi.org/10.1016/j.mtener.2021.100783.

[69] J.M. Yu, J. Lee, Y.S. Kim, J. Song, J. Oh, S.M. Lee, M. Jeong, Y. Kim, J.H. Kwak, S. Cho, C. Yang, J.-W. Jang, High-performance and stable photoelectrochemical water splitting cell with organic-photoactive-layer-based photoanode, Nat Commun 11 (2020) 5509. https://doi.org/10.1038/s41467-020-19329-0.

[70] L. Li, X. Zhao, D. Pan, G. Li, Nanotube array-like WO_3/W photoanode fabricated by electrochemical anodization for photoelectrocatalytic overall water splitting, Chinese Journal of Catalysis 38 (2017) 2132–2140. https://doi.org/10.1016/S1872-2067(17)62948-6.

[71] M. Sadakane, K. Sasaki, H. Kunioku, B. Ohtani, W. Ueda, R. Abe, Preparation of nano-structured crystalline tungsten(vi) oxide and enhanced photocatalytic activity for decomposition of organic compounds under visible light irradiation, Chemical Communications (2008) 6552. https://doi.org/10.1039/b815214d.

[72] K. Syrek, M. Zych, L. Zaraska, G.D. Sulka, Influence of annealing conditions on anodic tungsten oxide layers and their photoelectrochemical activity, Electrochim Acta 231 (2017) 61–68. https://doi.org/10.1016/j.electacta.2017.02.039.

[73] Z.S. Houweling, J.W. Geus, R.E.I. Schropp, Synthesis of WO_3 Nanogranular Thin Films by Hot-Wire CVD, Chemical Vapor Deposition 16 (2010) 179–184. https://doi.org/10.1002/cvde.200906838.

[74] M. Pudukudy, Q. Jia, Facile chemical synthesis of nanosheets self-assembled hierarchical H_2WO_4 microspheres and their morphology-controlled thermal decomposition into WO_3 microspheres, J Mater Sci 54 (2019) 13914–13937. https://doi.org/10.1007/s10853-019-03874-1.

[75] M.A. Borik, T. v. Volkova, I.E. Kuritsyna, E.E. Lomonova, V.A. Myzina, P.A. Ryabochkina, N.Yu. Tabachkova, Features of the local structure and transport properties of ZrO_2-Y_2O_3-Eu_2O_3 solid solutions, J Alloys Compd 770 (2019) 320–326. https://doi.org/10.1016/j.jallcom.2018.08.117.

[76] Y. Shen, X. Chen, W. Wang, Y. Gong, S. Chen, J. Liu, D. Wei, D. Meng, X. San, Complexing surfactants-mediated hydrothermal synthesis of WO_3 microspheres for gas sensing applications, Mater Lett 163 (2016) 150–153. https://doi.org/10.1016/j.matlet.2015.10.067.

[77] F. Zheng, C. Xi, J. Xu, Y. Yu, W. Yang, P. Hu, Y. Li, Q. Zhen, S. Bashir, J.L. Liu, Facile preparation of WO_3 nano-fibers with super large aspect ratio for high performance supercapacitor, J Alloys Compd 772 (2019) 933–942. https://doi.org/10.1016/j.jallcom.2018.09.085.

[78] D. Liu, C. Zhang, Y. Yu, Y. Shi, Y. Yu, Z. Niu, B. Zhang, Hydrogen evolution activity enhancement by tuning the oxygen vacancies in self-supported mesoporous spinel oxide nanowire arrays, Nano Res 11 (2018) 603–613. https://doi.org/10.1007/s12274-017-1670-8.

[79] D. Liu, C. Wang, Y. Yu, B.-H. Zhao, W. Wang, Y. Du, B. Zhang, Understanding the Nature of Ammonia Treatment to Synthesize Oxygen Vacancy-Enriched Transition Metal Oxides, Chem 5 (2019) 376–389. https://doi.org/10.1016/j.chempr.2018.11.001.

[80] S. Wang, X. Li, Y. Chen, X. Cai, H. Yao, W. Gao, Y. Zheng, X. An, J. Shi, H. Chen, A Facile One-Pot Synthesis of a Two-Dimensional MoS_2/Bi_2S_3 Composite Theranostic Nanosystem for Multi-Modality Tumor Imaging and Therapy, Advanced Materials 27 (2015) 2775–2782. https://doi.org/10.1002/adma.201500870.

[81] C. Liu, Y. Yang, W. Li, J. Li, Y. Li, Q. Shi, Q. Chen, Highly Efficient Photoelectrochemical Hydrogen Generation Using $Zn_xBi_2S_{3+x}$ Sensitized Platelike WO_3 Photoelectrodes, ACS Appl Mater Interfaces 7 (2015) 10763–10770. https://doi.org/10.1021/acsami.5b00830.

[82] A.A. AL-Zahrani, Z. Zainal, Z.A. Talib, H.N. Lim, A.M. Holi, Bismuth sulphide decorated ZnO nanorods heterostructure assembly via controlled SILAR cationic concentration for enhanced photoelectrochemical cells, Mater Res Express 7 (2020) 025510. https://doi.org/10.1088/2053-1591/ab6e2e.

[83] Z. Wang, Z. Liu, Z. Yang, S. Shingubara, Characterization of sputtered tungsten nitride film and its application to Cu electroless plating, Microelectron Eng 85 (2008) 395–400. https://doi.org/10.1016/j.mee.2007.07.017.

[84] P. Makuła, M. Pacia, W. Macyk, How To Correctly Determine the Band Gap Energy of Modified Semiconductor Photocatalysts Based on UV–Vis Spectra, J Phys Chem Lett 9 (2018) 6814–6817. https://doi.org/10.1021/acs.jpclett.8b02892.

[85] W. Wang, J. Dong, X. Ye, Y. Li, Y. Ma, L. Qi, Heterostructured TiO_2 Nanorod@Nanobowl Arrays for Efficient Photoelectrochemical Water Splitting, Small 12 (2016) 1469–1478. https://doi.org/10.1002/smll.201503553.

[86] F. Wu, Q. Liao, F. Cao, L. Li, Y. Zhang, Non-noble bimetallic $NiMoO_4$ nanosheets integrated Si photoanodes for highly efficient and stable solar water splitting, Nano Energy 34 (2017) 8–14. https://doi.org/10.1016/j.nanoen.2017.02.004.

[87] M.A. Rahman, S. Bazargan, S. Srivastava, X. Wang, M. Abd-Ellah, J.P. Thomas, N.F. Heinig, D. Pradhan, K.T. Leung, Defect-rich decorated TiO_2 nanowires for super-efficient photoelectrochemical water splitting driven by visible light, Energy Environ Sci 8 (2015) 3363–3373. https://doi.org/10.1039/C5EE01615K.

[88] C.W. Lai, S. Sreekantan, Fabrication of WO_3 nanostructures by anodization method for visible-light driven water splitting and photodegradation of methyl orange, Mater Sci Semicond Process 16 (2013) 303–310. https://doi.org/10.1016/j.mssp.2012.10.007.

[89] W. Li, J. Li, X. Wang, S. Luo, J. Xiao, Q. Chen, Visible light photoelectrochemical responsiveness of self-organized nanoporous WO_3 films, Electrochim Acta 56 (2010) 620–625. https://doi.org/10.1016/j.electacta.2010.06.025.

[90] Y.-W. Choi, S. Kim, M. Seong, H. Yoo, J. Choi, NH4-doped anodic WO_3 prepared through anodization and subsequent NH_4OH treatment for water splitting, Appl Surf Sci 324 (2015) 414–418. https://doi.org/10.1016/j.apsusc.2014.10.059.

[91] V. Cristino, S. Caramori, R. Argazzi, L. Meda, G.L. Marra, C.A. Bignozzi, Efficient Photoelectrochemical Water Splitting by Anodically Grown WO_3 Electrodes, Langmuir 27 (2011) 7276–7284. https://doi.org/10.1021/la200595x.

[92] S.S. Kalanur, Structural, Optical, Band Edge and Enhanced Photoelectrochemical Water Splitting Properties of Tin-Doped WO_3, Catalysts 9 (2019) 456. https://doi.org/10.3390/catal9050456.

[93] H. He, S.P. Berglund, P. Xiao, W.D. Chemelewski, Y. Zhang, C.B. Mullins, Nanostructured Bi_2S_3/WO_3 heterojunction films exhibiting enhanced photoelectrochemical performance, J Mater Chem A Mater 1 (2013) 12826. https://doi.org/10.1039/c3ta13239k.

Chapter 3. ZnO nanopagoda arrays decorated with Ag nanoparticles for photoelectrochemical application

3.1. Introduction

It is vital for the world to effectively use solar energy by turning it into chemical and electrical energy [1,2]. PEC-WS technique is an appealing approach for H_2 production as a clean alternative fuel utilizing clean and sustainable resources [3–7]. The semiconductor photoelectrode is an essential component of the photoelectrochemical cell because it can absorb solar energy and use it to produce photogenerated electrons and holes, facilitating their transfer to the interface between the semiconductor and electrolyte to take part in redox reactions [8,9]. Thus, developing and producing semiconductor photoelectrodes with appropriate light absorption capability, efficient e^-/h^+ pairs separation, robust surface reactivity, and high stability are essential [10,11]. Among a variety of investigated semiconductor metal oxides, ZnO has received superb attentiveness because of its distinctive properties. ZnO is a cheap, widely available, readily synthesized, non-toxic material with an anisotropic crystal structure and a wide bandgap of 3.37 eV [12–16]. Additionally, it has proven to be able to mold into a range of morphologies, resulting in the creation of an enormous diversity of different superstructures [17–20]. The term "superstructures" represents 3D micro/nanostructures, which grow at the expense of regulated one-dimensional and two-dimensional (1D, 2D) nanostructures [21]. ZnO superstructures are advantageous to 1D and 2D nanostructures owing to their frequently larger surface areas, higher conductivity, combined stacked arrays, better crystallinity, and developed scattering with increased light absorption ability. Therefore, ZnO superstructures demonstrate superb performance for H_2 production using the PEC-WS procedure [12]. ZnO superstructures have numerous morphologies, involving worm-like [22], wool ball [23], mulberry-like [24], firecracker [25], nanopagoda [26], birdcage-like [27], nanoforest [28], nanodendrite [29], jack [30], nanocomb [31], nanoflower [32], nanopinecone [33], and branched nanorods [34,35]. Among a variety of superstructure morphologies, ZnO nanopagoda arrays (NPGs) have displayed much interest in being used for light-emitting systems due to their unique electronic and optical features alongside their adjustable surface morphology and defect density. The challenge of reproducibly fabricating ZnO NPGs is a concomitant problem with their use, one that would have prevented a rise in publications.

Recently, plasmonic metal NPs decorated with semiconductor nanostructures have attracted more attention because of their unique interfacial electronic properties, which can enhance the PC and PEC performance [36–45]. Among studied plasmonic noble metals, Ag is preferable due to its powerful LSPR and freaked physicochemical prosperities [46–51]. As well as Ag is less costly than Pt, Au, and Pd [52,53]. Several studies have been focused on the utilization of Ag-decorated metal oxide semiconductor nanocomposites for PEC-WS technology [54–57]. It's proven that the incorporation of Ag NPs is a successful strategy for expanding the photoresponse of ZnO to the Vis light zone due to the LSPR effect and inhibition of e^-/h^+ pairs recombination [58–60]. The Schottky barrier created between ZnO and Ag can increase the lifetime of e^-/h^+ pairs via the junction and accelerate their mobility [61]. Additionally, Ag acts as a trapping center that can capture the excited electrons, which substantially decreases the e^-/h^+ pairs recombination rate [62]. Recent research has demonstrated that well-constructed Ag–ZnO nanocomposites can extend Vis light absorption from 400 to 520 nm and prolong the lifetime of the photogenerated charge carriers [58,63]. The excited Ag electrons can migrate to the CB of ZnO mainly through the HEI mechanism [64,65].

In this study, the aqueous chemical downward technique was applied to fabricate ZnO nanorods (NRs) and ZnO NPGs on a fluorine-doped tin oxide (FTO) substrate with reproducibility. ZnO NPGs displayed better PEC performance than ZnO NRs, which was mostly ascribed to the higher light absorption capability and lower e^-/h^+ pairs recombination rate of ZnO NPGs. Ag NPs were thereafter deposited on ZnO NPGs films using the SILAR procedure. The quantity of Ag NPs was tuned by controlling the number of SILAR cycles. A variety of ZnO NPGs/Ag NPs samples were fabricated with various cycles (2,4,6,8, and 10 cycles). All the decorated films with Ag NPs manifested higher photocurrent density compared to bare ZnO NRs and ZnO NPGs photoanodes. The highest PEC conversion efficiency was achieved after depositing Ag NPs on ZnO NPGs for eight cycles, owing to the improved light scattering with increased light absorption and mitigated charge recombination.

3.2. Experimental

3.2.1. Materials synthesis

3.2.1.1. Synthesis of ZnO nanorods

ZnO NRs were fabricated on an FTO substrate through two steps; (1) deposition of ZnO seed layer on FTO utilizing spin coating procedure and (2) growth of ZnO NRs utilizing downward

growth procedure in an aqueous solution. Firstly, The ZnO seed layer was deposited on a cleaned FTO substrate as follows: 0.05 M zinc acetate dehydrate and 0.06 M of diethanolamine were dissolved in 10 ml of ethanolic solution and stirred for 20 min at 65°C. After cooling, the clear solution was spin-coated on an FTO and oven-dried for ten minutes at 180°C. This process was repeated six times. Subsequently, the synthesized film was annealed at 450°C for 1 hour.

Secondly, ZnO NRs were produced using the downward growth procedure in an aqueous solution (100 mL) comprising 50 mM $Zn(NO_3)_2 \bullet 6H_2O$ and 50 mM hexamethylenetetramine [66,67]. Subsequently, the solution was moved into a 120 mL closed bottle. The ZnO seed layer containing FTO substrate was positioned near the surface of the solution and maintained at 90°C for 3 h. Following the complete reaction, the bottle was removed from the water bath and allowed to cool down at room temperature. Then, the prepared ZnO NRs film was rinsed with deionized water and air-dried.

3.2.1.2. Synthesis of ZnO nanopagoda arrays

ZnO NPGs were prepared using the downward growth procedure in an aqueous solution (100 mL) comprising 10 mM $Zn(NO_3)_2 \bullet 6H_2O$, 10 mM hexamethylenetetramine, and 0.275 mM ascorbic acid [67]. This solution was moved into a 120 mL closed bottle. The FTO thin film of ZnO NRs was positioned near the surface of the solution and maintained at 90°C for 4 h. Following the complete reaction, the bottle was removed from the water bath and allowed to cool down at room temperature. Then, the prepared ZnO NPGs film was rinsed with deionized water and air-dried.

3.2.1.3. Synthesis of ZnO nanopagoda arrays /Ag nanoparticles

The SILAR process was utilized to deposit Ag NPs over ZnO NPGs films. The ZnO NPGs film was immersed in two an aqueous solution, (1) 50 mM $AgNO_3$ for 10 s. (2) 50 mM $NaBH_4$ for 10 s. Following each immersion, the film should be rinsed with deionized water. The SILAR technique was applied for various cycles (2, 4, 6, 8, and 10 cycles) to control the deposited quantity of Ag NPs over ZnO NPGs. **Scheme 3-1** explains the preparation steps of ZnO NRs, ZnO NPGs, and ZnO NPGs/Ag NPs photoanodes.

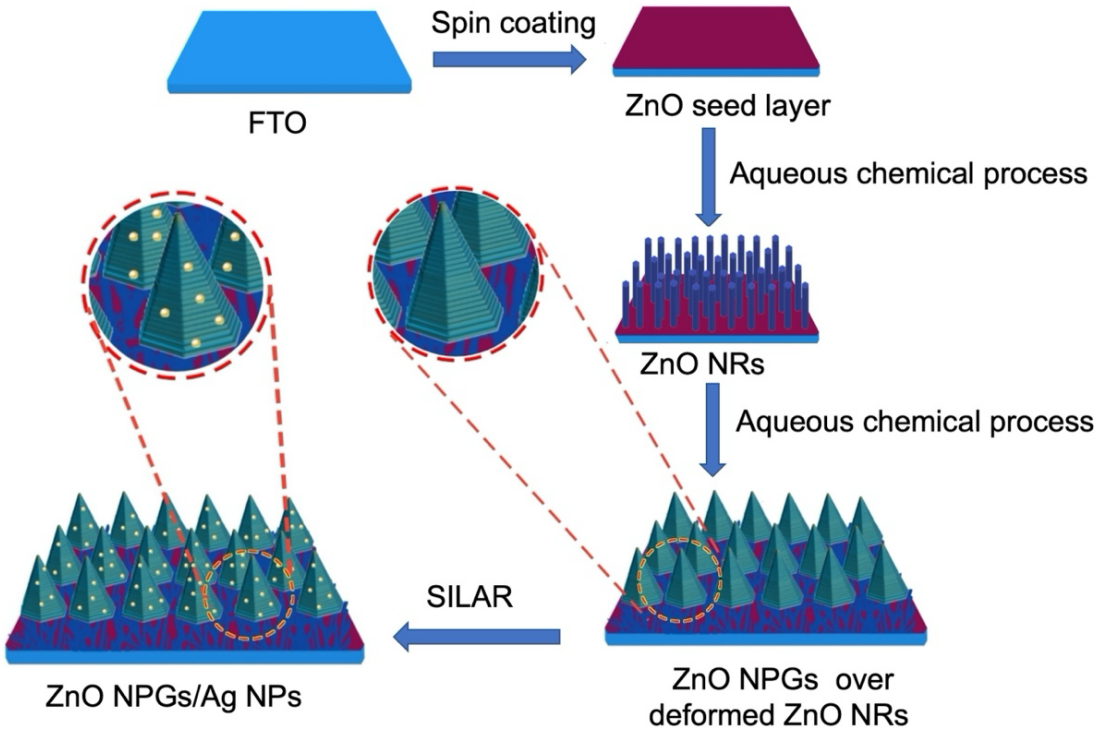

Scheme 3-1. Preparation steps of ZnO NRs, ZnO NPGs, and ZnO NPGs/Ag NPs photoanodes.

3.2.2. Materials characterization

The crystal structure, microscopic and elemental observations, and optical characteristics of all synthesized samples were analyzed as indicated previously in Chapter 2 in section 2.2.2. However, for SEM analysis, HITACHI, SU8000 Type II, Japan was used. The photoluminescence (PL) properties were investigated using a He-Cd laser (KIMMON KOHA, Tokyo, Japan, excitation wavelength, λ = 325 nm) as an excitation source, and a monochromator (Nikon G250, Japan) was utilized to record the spectra. 3D finite-difference time-domain (FDTD) simulation was recorded using a commercial software package (Lumerical FDTD Solution, Ansys, USA). The ZnO nanostructures and deposited Ag NPs were modeled according to SEM and TEM images. Concretely, the diameter and length of ZnO NRs were set to 110 and 1400 nm, respectively. The width and height of ZnO NPGs were both 400 nm. Two sorts of Ag NPs that had diameters of 20 and 100 nm, were placed over ZnO NPGs surface. The boundary conditions were adjusted as periodic for the x- and y-directions and as perfectly matched layer conditions for the z-direction. A plane wave source with x-polarization in 350–800 nm range was incident to the structures from the top side of the model.

3.2.3. Photoelectrochemical measurements

The PEC performance of the prepared photoanodes (1 cm^2 illuminated area) as working electrodes was measured with a biologic potentiostat (VSP-300) connected to the PEC cell having three electrodes. Pt coil and Ag/AgCl (3 M KCl) electrodes were used as counter and reference electrodes, respectively, in 0.2 M Na_2SO_4/10% methanol electrolyte (pH = 6.5). A xenon lamp (300 W) was applied to simulate solar irradiation through an air mass 1.5 global filter. The intensity of the light was set to 1 Sun (100 mW cm^{-2}). The LSV plot was recorded at a scan rate of 10 mV/s. before each measurement, the electrolyte present in the PEC cell was flushed utilizing argon gas to eliminate the dissolved oxygen. EIS was studied at open circuit potential in 0.2 M Na_2SO_4 at 10^5 Hz to 0.01 Hz under illumination. The M-S was recorded in 0.2 M Na_2SO_4 at 1000 Hz under dark conditions. The ABPE was calculated from the LSV results as previously explained in Chapter 2 in section 2.3.2.6. The incident photon-to-current efficiency (IPCE) was obtained from the measurement of photocurrent density at the wavelength range of 325-850 nm using a monochromator light source at 0.6 V vs. Ag/AgCl as follows (equation 3-1) [68]:

$$IPCE\ (\%) = \frac{J\ X1240}{\lambda\ X P_{light}} \times\ 100 \qquad \text{(Eq. 3-1)}$$

where J is the photocurrent density at λ is the incident wavelength, and P_{light} is the light power density. The Potential versus RHE was calculated by transforming the applied potential versus Ag/AgCl as illustrated in Chapter 2 in section 2.2.3.

3.3. Results and discussion

3.3.1. Characterization results

The XRD analysis was performed to study the crystalline structure and composition of ZnO NRs, ZnO NPGs, and ZnO NPGs/Ag NPs samples. **Figure 3-1** illustrates the XRD pattern of the clean FTO substrate, ZnO NRs, ZnO NPGs, and ZnO NPGs/Ag NPs (8). The diffraction peaks of the pure FTO showed the tetragonal structure of SnO_2 [69]. The XRD patterns of ZnO NRs and NPGs displayed the creation of a wurtzite hexagonal crystal structure that is matched with (JCPDS, 36–1451) [70,71]. The strong and sharp peak corresponding to the (002) crystal plane disclosed that the favorable growth direction of ZnO NRs and NPGs was [001] direction

[72,73]. The XRD spectra of ZnO NPGs/Ag NPs (8) showed similar diffraction peaks of ZnO NPGs with no characteristic peaks of Ag NPs. This may be owing to the low deposited quantity of Ag NPs, confirming that the ZnO NPGs crystal structure was unaffected by the SILAR growing solutions.

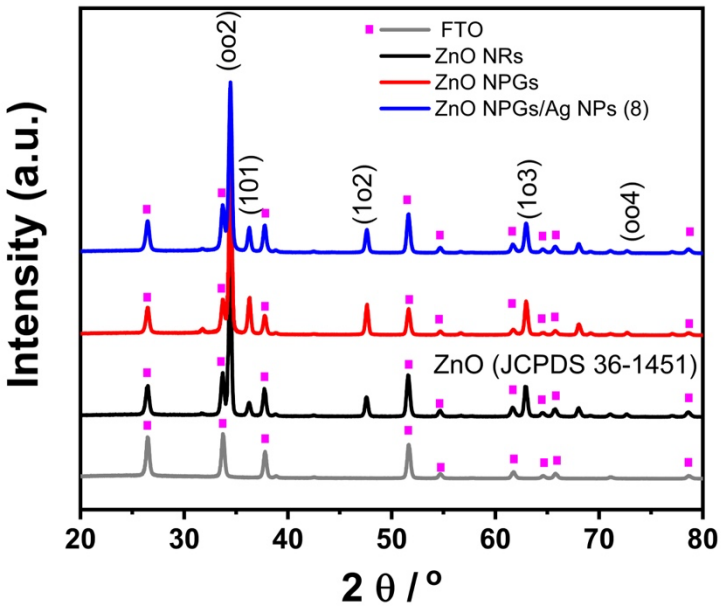

Figure 3-1. XRD patterns of clean FTO, ZnO NRs, ZnO NPGs, and ZnO NPGs/Ag NPs (8) samples.

The morphological structure of the as-prepared samples was examined using SEM analysis. **Figure 3-2a** displays the well-ordered hexagonal ZnO NRs with a smooth top surface. The cross-sectional view (**Figure 3-2b**) manifested that ZnO NRs were formed with lengths and diameters of ~1.5 µm and ~115 nm, respectively. The 30° tilt (**Figure 3-2c**) SEM image of ZnO NPGs clarified that ZnO NPGs were successfully generated in a hexagonal shape. The cross-sectional view (**Figure 3-2d**) of ZnO NPGs revealed that they have grown over some distorted ZnO NRs with lengths and base diameters of ~340 nm and ~385 nm, respectively. The 30° tilt SEM images of ZnO NPGs/Ag NPs (8) disclosed that Ag NPs of different sizes were deposited on the surface of ZnO NPGs (**Figure 3-2e**). Moreover, the cross-section view (**Figure 3-2f**) displayed that the deposition of Ag NPs did not damage ZnO NPGs that have formed over distorted ZnO NRs. **Figure 3-3a-d** displays the 30° tilt SEM images of different deposited cycles (2, 4, 6, and 10

cycles) of Ag over ZnO NPGs. It is obvious that the deposited amount of Ag NPs raised as the count of cycles increased.

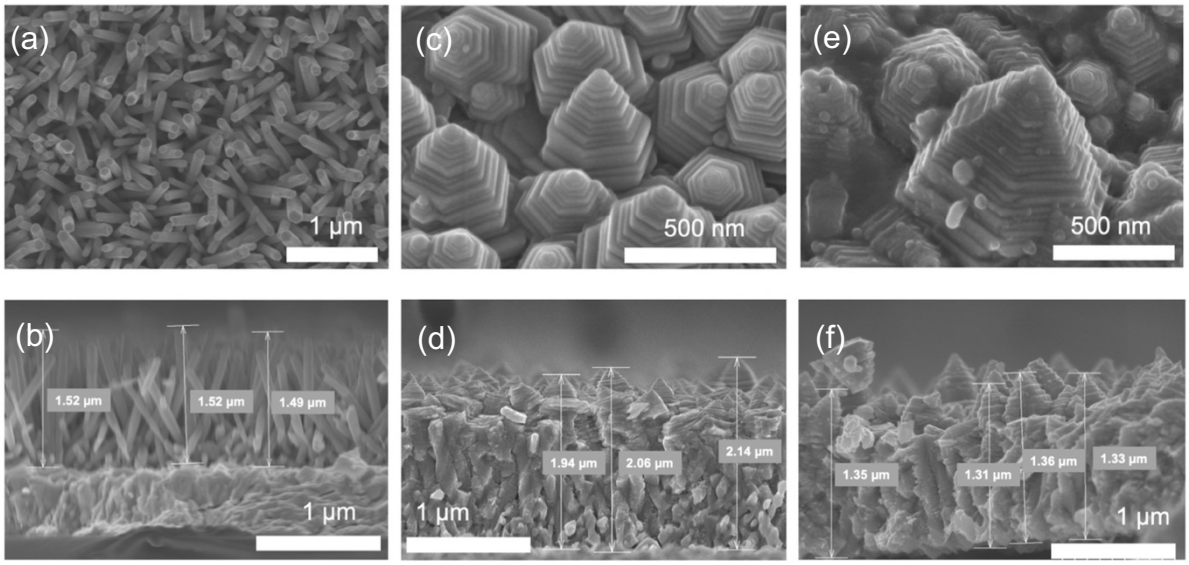

Figure 3-2. (a) Top view and (b) cross-sectional SEM images of ZnO NRs (c) 30° tilt view and (d) cross-sectional SEM images of ZnO NPGs. (e) 30° tilt view and (f) cross-sectional SEM images of ZnO NPGs/Ag NPs (8).

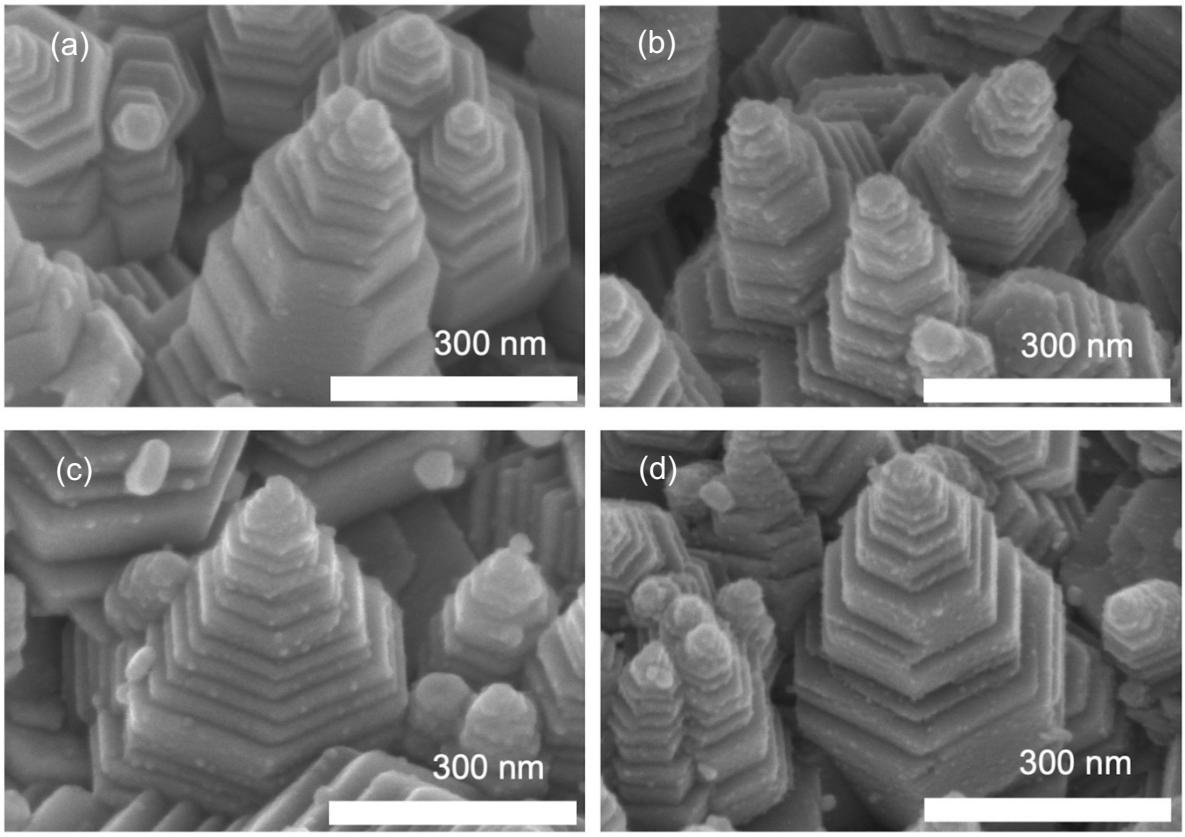

Figure 3-3. 30° tilt-view SEM images of (a) ZnO NPGs/Ag NPs (2), (b) ZnO NPGs/Ag NPs (4), (c) ZnO NPGs/Ag NPs (6), and (d) ZnO NPGs/Ag NPs (10).

The crystal structure of as prepared ZnO NPGs and the deposition status of Ag were investigated using HRTEM and scanning TEM-EDX (STEM-EDX). **Figure 3-4a** presents the HRTEM image of ZnO NPGs. The inset image is the low magnification TEM image, which clarifies the region where the HRTEM image was taken by a red square. The HRTEM image verified the high crystallinity of ZnO NPGs, having nearly no significant structural defects, such as grain borders. The measured fringe spacing was 0.27 nm, which was consistent with the d-spacing of $(\bar{1}100)$ planes of the ZnO wurtzite structure [74]. The inset illustration demonstrated the ZnO NPGs crystal structure which was assumed by the XRD pattern and the microscopic investigation. **Figure 3-4b,c** display the STEM image and the corresponding Ag elemental mapping, respectively. It can be noticed that Ag NPs didn't coat the whole surface of ZnO NPGs but was separately deposited with particle size 5–100 nm.

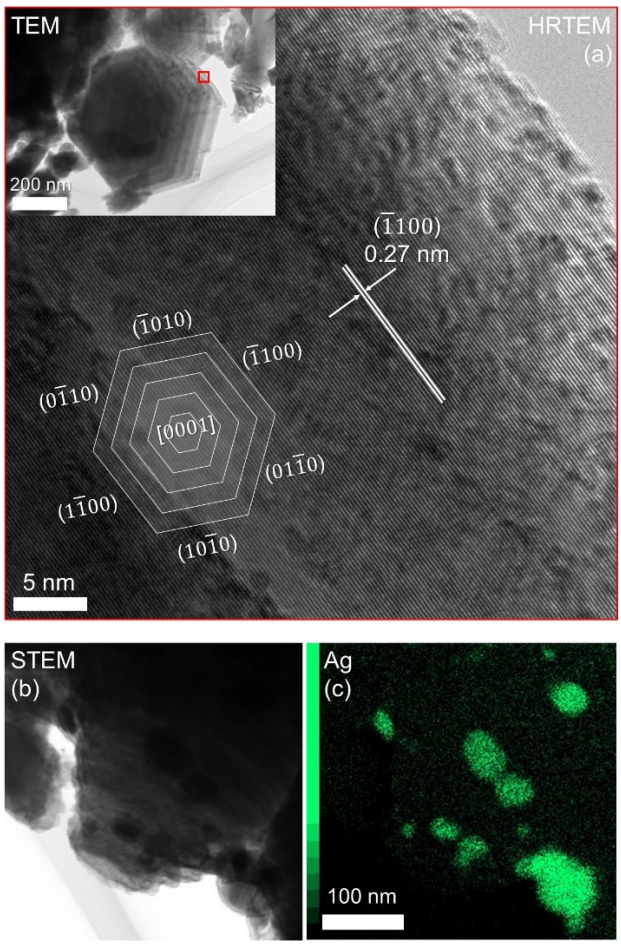

Figure 3-4. (a) HRTEM image of ZnO NPGs. The insets are the corresponding low magnification TEM image and the crystal structure illustration of NPGs, respectively. (b) STEM image of ZnO NPGs/Ag NPs (8) and (c) the corresponding EDX mapping for Ag.

The XPS was investigated to analyze the composition and chemical states of bare ZnO NPGs and samples modified with various quantities of Ag NPs. The ZnO NPGs survey spectrum (**Figure 3-5a**) displays the distinctive peaks of Zn, O, and C elements. The high-resolution spectrum of Zn 2p **(Figure 3-5b**) shows two characteristic peaks of Zn $2p_{1/2}$ at 1045 eV and Zn $2p_{3/2}$ at 1022 eV, verifying that Zn formed Zn^{2+} chemical state [75,76]. **Figure 3-5c** illustrates the distinctive peak of O 1s that was split into two peaks at 531.1 eV, which is related to the crystal lattice of O in Zn, and at 532.7 eV, which corresponded to surface hydroxyl oxygen [77]. As seen in **Figure 3-5d**, the survey spectrum of ZnO NPGs/Ag NPs (8) reveals all distinctive peaks of Zn, O, Ag, and C elements. Moreover, the high-resolution spectra of Zn 2p and O 1s (**Figure 3-5e,f**) demonstrate the distinctive peaks of Zn and O at the same binding energies as ZnO NPGs,

meanwhile the intensity of the surface hydroxyl oxygen peak reduced. The high-resolution spectrum of Ag 3d (**Figure 3-5g**) displays two characteristic peaks at 374.4 eV and 368.4 eV, which are related to Ag $3d_{3/2}$ and Ag $3d_{5/2}$ respectively. The two peaks are separated by 6.0 eV, proving the presence of metallic Ag [78]. These results manifested that the SILAR method reduced the hydroxyl group from the surface of ZnO NPGs surface in addition to depositing metallic Ag NPs. **Figure 3-6** shows the XPS spectra of ZnO NPGs modified with various cycles (2,4,6,8, and 10, cycles). **Table 3-1** shows the weight percentage of decorated Ag NPs for different SILAR cycles. As can be noticed, increasing the number of cycles causes the Ag 3d peak's intensity to rise in the XPS spectrum, consistent with the SEM data shown in **Figure 3-3**.

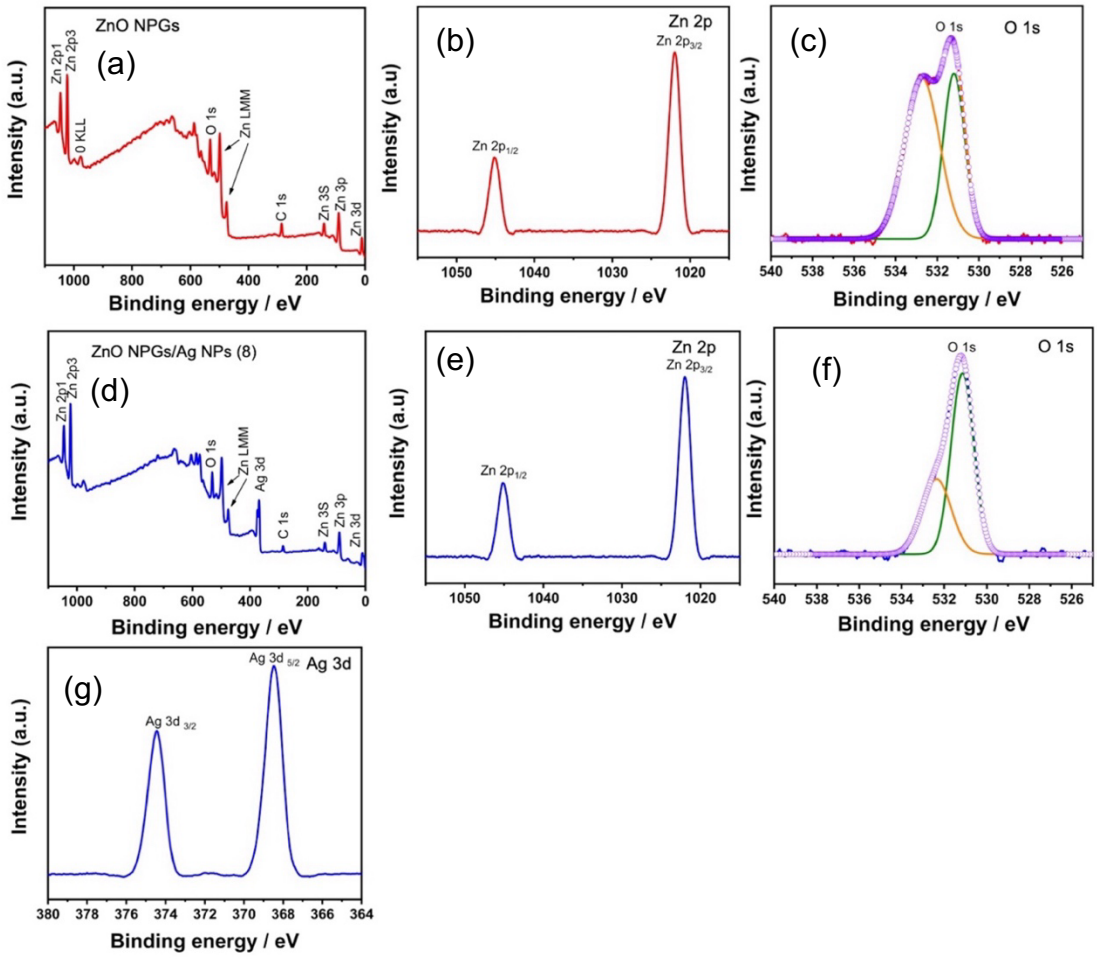

Figure 3-5. (a) Survey, (b) Zn 2p, and (c) O 1s high-resolution XPS spectra of ZnO NPGs. (d) Survey, (e) Zn 2p, (f) O 1s, and (g) Ag 3d high-resolution XPS spectra of ZnO NPGs/Ag NPs (8).

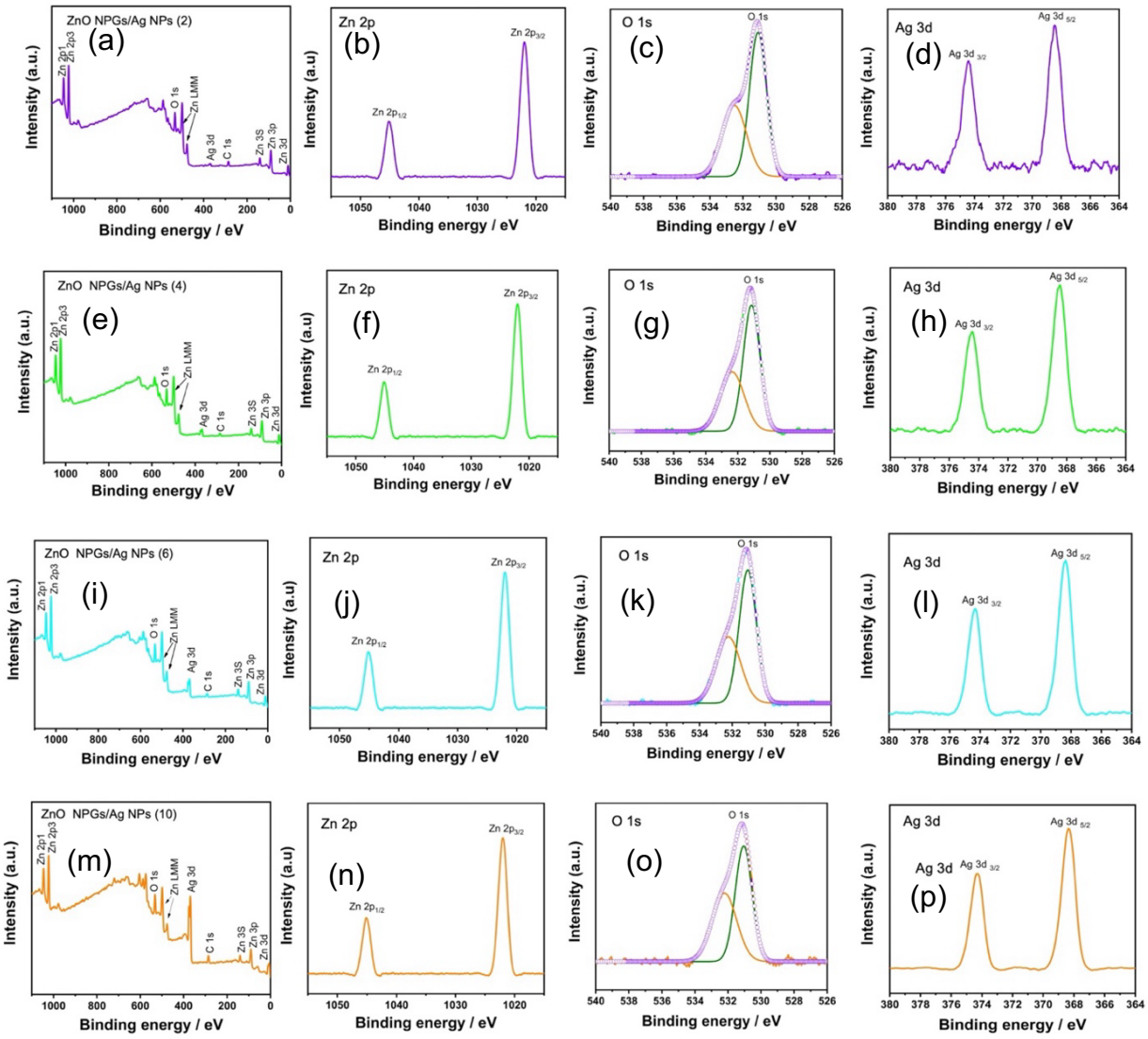

Figure 3-6. XPS spectra including survey and high-resolution spectrums of all elements in (a-d) ZnO NPGs/Ag NPs (2), (e-h) ZnO NPGs/Ag NPs (4), (i-l) ZnO NPGs/Ag NPs (6), and (m-p) ZnO NPGs/Ag NPs (10).

Table 3-1. XPS elemental analysis.

Photoelectrodes	Zn/wt%	O/wt%	Ag/wt%
ZnO NPGs	0.34	0.62	-
ZnO NPGs/Ag NPs (2)	0.41	0.67	0.02
ZnO NPGs/Ag NPs (4)	0.51	0.80	0.05
ZnO NPGs/Ag NPs (6)	0.41	0.65	0.10
ZnO NPGs/Ag NPs (8)	0.33	0.56	0.18
ZnO NPGs/Ag NPs (10)	0.24	0.36	0.24

Additionally, the light absorption capability of the as prepared samples, the UV–Vis extinction spectra were determined, as shown in **Figure 3-7a**. ZnO NRs attained high optical absorption in the UV zone owing to its intrinsic wide bandgap and moderate optical absorption in the Vis zone owing to its structural defects. ZnO NPGs attained similar absorption in the UV zone due to its wide bandgap, whereas they demonstrated much weaker absorption in the Vis zone, proving that ZnO NPGs have lower defects than ZnO NRs. It is obvious that the deposition of Ag NPs over ZnO NPGs improved the Vis light absorption due to the LSPR and scattering effects of Ag NPs [79]. **Figure 3-7b** shows the UV–Vis spectra of ZnO NPGs modified with various SILAR cycles (2,4,6, and 10). The extinction in the Vis zone initially rose with the cycle number and then reduced when it reached 10 cycles. This implied that excessive Ag deposition caused Ag NPs to aggregate and reduced the effectiveness of LSPR. The extinction rose over a wide wavelength range in the Vis zone. This is a result of the Ag NPs' varied sizes and shapes being deposited, as shown in the TEM and SEM images. The direct bandgap energies of the prepared samples were calculated utilizing Tauc's equation [80]. The bandgap was drawn using Tauc's curve by plotting $(ah\nu)^2$ versus energy ($h\nu$), as illustrated in **Figure 3-7c**. The bandgap energies of ZnO NRs, ZnO NPGs, and ZnO NPGs/Ag NPs (8) were 3.15 eV, 3.28 eV, and 3.24 eV, respectively. The smaller bandgap energies of ZnO NRs and ZnO NPGs/Ag NPs (8) than ZnO NPGs can be attributed to the enhanced Vis light absorption by defects and Ag NPs respectively.

The photoluminescence (PL) spectra were determined to study the e^-/h^+ pairs recombination properties of ZnO NRs, ZnO NPGs, and ZnO NPGs/Ag NPs (8). The emission peaks PL spectra are produced from the recombination of electrons and holes [81,82]. **Figure 3-7d** shows that all synthesized samples exhibited two peaks of emission: a narrow UV peak at ~380

nm, which is related to the emission of near-band edge exciton, and a broad Vis peak at ~600 nm, which corresponds to deep-level emission owing to intrinsic and external defects [74,83]. The intensity of the PL Vis peak of ZnO NPGs was weaker than ZnO NRs, indicating lower structural defects in ZnO NPGs. ZnO NPGs/Ag NPs (8) demonstrated similar PL intensity in the Vis zone to ZnO NPGs. Generally, the Ag NPs passivation effect which reduced the surface states and/or surface defects of ZnO film was expected [84]. The effect wasn't obviously seen in our case as there were few surface defects on ZnO NPGs. This presumption also agreed well with the UV–Vis result. Because the transformation from NRs to NPGs decreased the defects, which frequently acted as e^-/h^+ pairs recombination centers, and because the Ag NPs deposition improved the Vis light absorption, an enhancement of PEC activity was highly anticipated.

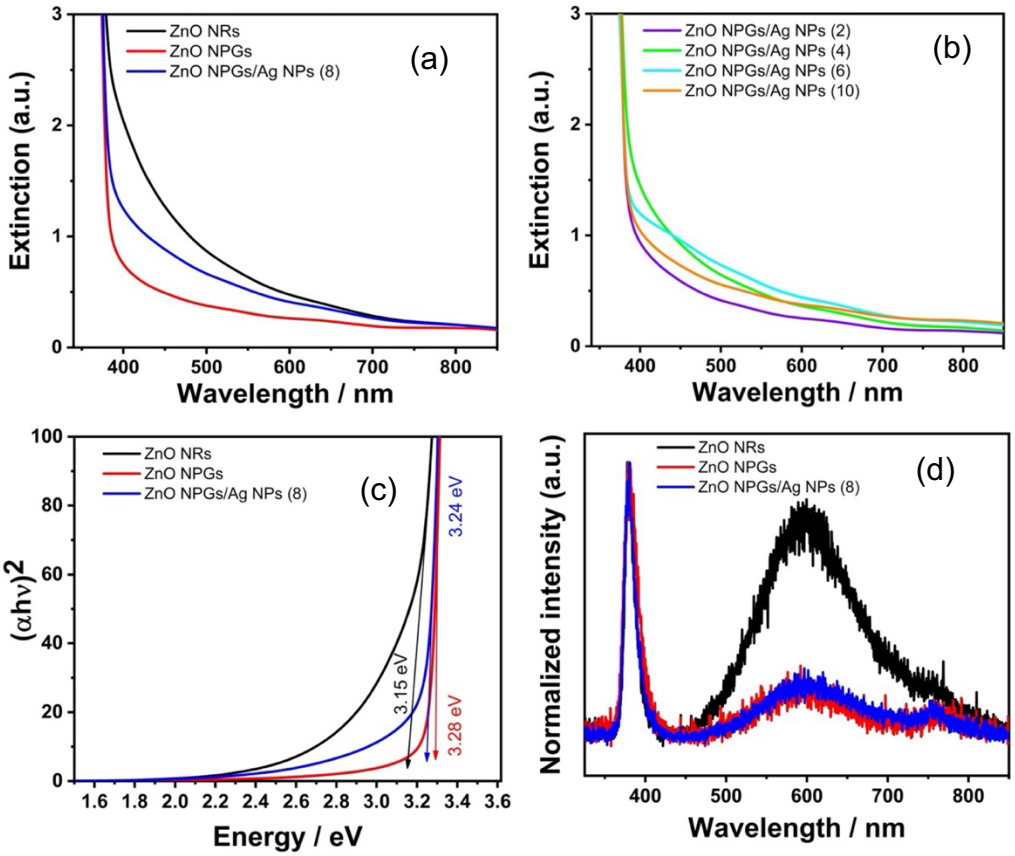

Figure 3-7. (a) UV–Vis extinction spectra of ZnO NRs, ZnO NPGs, and ZnO NPGs/Ag NPs (8). (b) The UV-Vis spectra of ZnO NPGs decorated with different SILAR cycles (2, 4, 6, and 10) of Ag NPs. (c) The corresponding Tauc plots. (d) PL spectra of ZnO NRs, ZnO NPGs, and ZnO NPGs/Ag NPs (8).

3.3.2. FDTD simulation

Figure 3-8a shows the 3D model of ZnO NPGs/Ag NPs for FDTD simulation, where one large (100 nm) and four small (20 nm) Ag NPs were deposited over ZnO NPGs. The morphology was established based on the data of microscopic investigations as depicted in **Figure 3-2**. **Figure 3-8b–d** illustrates the x–z cross-sectional images of ZnO NRs, ZnO NPGs, and ZnO NPGs/Ag NPs. **Figure 3-8e** presents the corresponding simulated absorption spectra. The large absorption in the UV range was observed in each sample, which was attributed to the strong direct bandgap absorption by ZnO. The growth of ZnO NPGs on ZnO NRs enhanced the absorption in the UV zone; although, it made nearly no change in the spectrum in the Vis zone. This was ascribed to the structural defects in ZnO, which influenced the actual UV–Vis absorption spectra displayed in **Figure 3-7a**, and were not considered in this simulation. Conversely, the Ag NPs deposition over ZnO NPGs surface provided optical absorption in the Vis zone owing to their LSPR effects. **Figure 3-8f–h** presents the matching x–z E-field profiles at 368 nm. The area Encircled by white dotted lines represents the place where ZnO NRs are present. The E-field generated inside ZnO NPGs, was stronger than ZnO NRs clarifying that ZnO NPGs can absorb incident UV radiation well. This is probably owing to the distinct superstructure of NPGs morphology. ZnO NPGs/Ag NPs manifested a strong E-field, particularly at the Ag–ZnO interface owing to the LSPR of Ag NPs. This suggests that the high E-field produced by Ag's LSPR amplified ZnO NPs' ability to absorb light. This represents the light scattering and light concentration effects [37]. **Figure 3-8i–k** explains the corresponding x–z E-field profiles at 445 nm. A very strong E-field ($E/E_0 = 26.8$) was detected near Ag NPs owing to LSPR in the ZnO NPGs/Ag NPs film. Since ZnO absorbed little light within this wavelength range, the excited electrons of Ag NPs would be migrated to ZnO NPGs and then consumed for H_2 production. This represents the HEI mechanism from Ag to ZnO under Vis light illumination [64]. The simulated absorption spectra and E-field profiles were consistent very well with the experimental results, where ZnO NPGs/Ag NPs achieved the highest IPCE in the UV zone and the strongest Vis light response (explained in the following section **Figure 3-10c,d**).

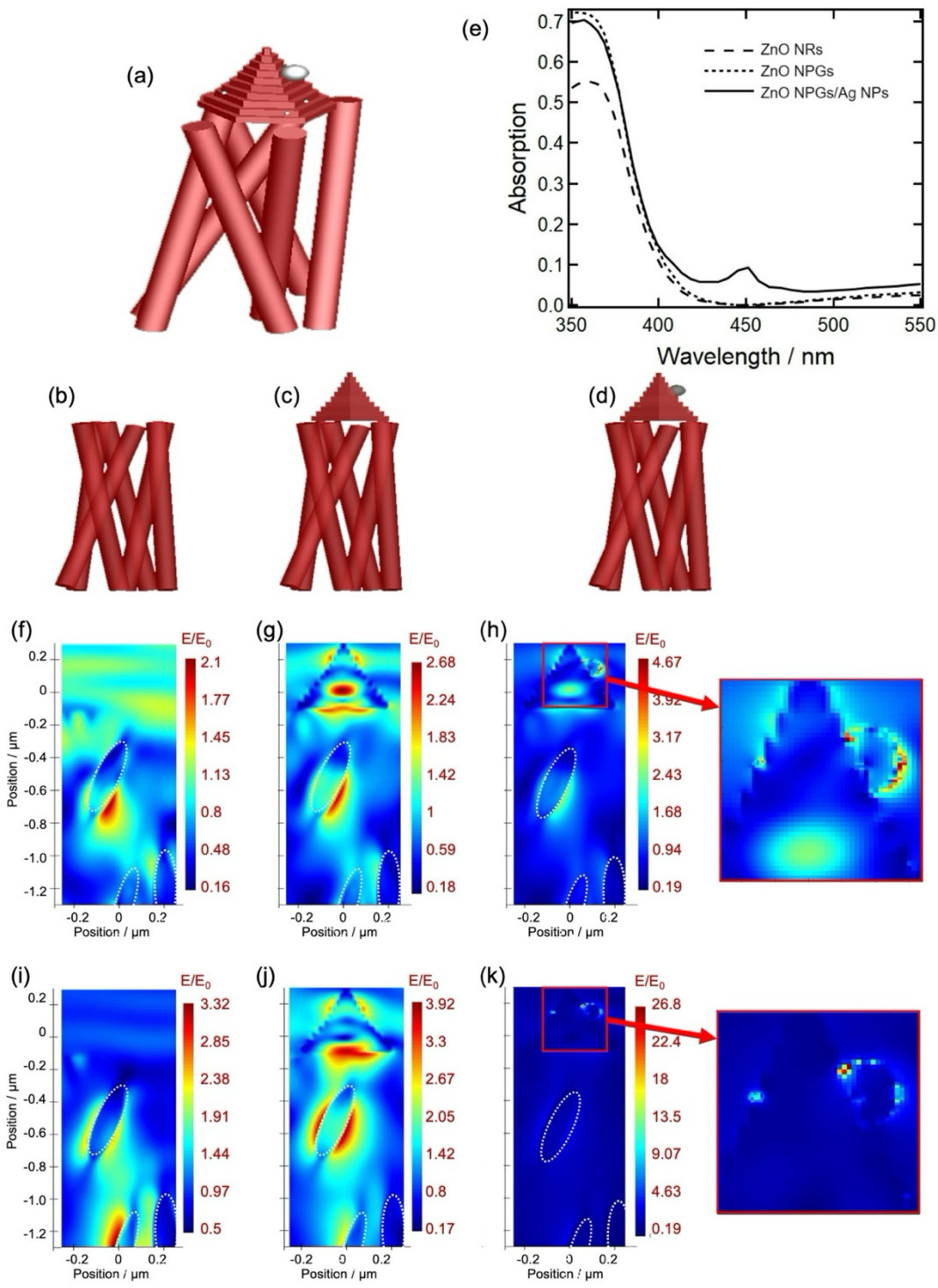

Figure 3-8. FDTD simulation involving (a) 3D model of ZnO NPGs with Ag NPs, (b–d) x–z cross-sectional images of ZnO NRs, ZnO NPGs, and ZnO NPGs with Ag NPs, (e) the simulated absorption spectra, (f–h) the corresponding x–z E-field profiles at 368 nm, and (i–k) the corresponding x–z E-field profiles at 445 nm.

3.3.3. Photoelectrochemical Measurements

3.3.3.1. Linear sweep voltammetry

The PEC measurements of the as-prepared samples were determined under the simulated solar irradiation. The PEC performance of bare ZnO NRs, bare ZnO NPGs, and ZnO NPGs decorated with various Ag NPs cycles was studied for comparison. All studied photoanodes demonstrated very small current density under dark conditions as depicted in **Figure 3-9a**. The LSV curves under light illumination (**Figure 3-9b**) illustrated that bare ZnO NRs attained a photocurrent of 0.94 mA cm^{-2} at 1.23 V vs. RHE, while ZnO NPGs boosted the photocurrent to 1.43 mA cm^{-2} at 1.23 V vs. RHE. This noticeable increase was due to improved light absorption in the UV zone and decreased structural defects, which act as e^-/h^+ pairs recombination centers. The deposition of Ag NPs over ZnO NPGs further increased the photocurrent owing to the LSPR effect of Ag NPs. The larger amount of Ag NPs resulted in higher photocurrent density and a maximum photocurrent of 2.15 mA cm^{-2} at 1.23 V vs. RHE was achieved after deposition of eight cycles. More increasing the amount of Ag NPs over eight deposition cycles led to the deterioration of photocurrent. This was attributed to the aggregation of photoexcited charge carriers into the overly deposited Ag NPs. So, the deposited quantity of Ag NPs should be tuned to attain high photocurrent. **Table 3-2** shows the photocurrent density under the light irradiation of all investigated samples.

Figure 3-9c illustrates the transient photocurrent response of ZnO NRs, ZnO NPGs, and ZnO NPGs/Ag NPs (8) photoanodes. The photocurrent response of the investigated photoanodes was determined under consecutive on/off cycles of light illumination at 1.1 V vs. RHE. A sharp rise in photocurrent was observed under light illumination, which dramatically reduced under dark. The transient photocurrent response of investigated photoanodes was agreed with LSV results.

Table 3-2. Photocurrent density of all investigated photoanodes at 1.23 V vs. RHE.

Photoelectrode	Photocurrent density / mA cm^{-2}
ZnO NRs	0.94
ZnO NPGs	1.43
ZnO NPGs/Ag NPs (2)	1.28
ZnO NPGs/Ag NPs (4)	1.80
ZnO NPGs/Ag NPs (6)	2.07
ZnO NPGs/Ag NPs (8)	2.15
ZnO NPGs/Ag NPs (10)	1.49

3.3.3.2. Electrochemical impedance spectroscopy

The EIS was measured to investigate the kinetics of charge carriers transfer at the interface of photoelectrode and electrolyte, as illustrated in **Figure 3-9d**. The ZnO NPGs had a smaller arc diameter than in the case of ZnO NRs. Conversely, ZnO NPGs/Ag NPs (8) had the smallest arc diameter, which verify the inhibition of charge transfer resistance. The data were fitted utilizing the ZView program (Scribner Associates, USA) with an equivalent circuit model inserted in **Figure 3-9d**. R_2 equals the R_{ct} which represents the interfacial charge transfer resistance between the photoelectrode and electrolyte. The obtained R_{ct} values were 1970 Ω, 387 Ω, and 176 Ω for ZnO NRs, ZnO NPGs, and ZnO NPGs/Ag NPs (8) photoanodes, respectively. The lowest R_{ct} value of ZnO NPGs/Ag NPs (8) photoanode proved the lowest charge transfer resistance and the highest photocurrent, well agreed with the LSV results exhibited in **Figure 3-9b**.

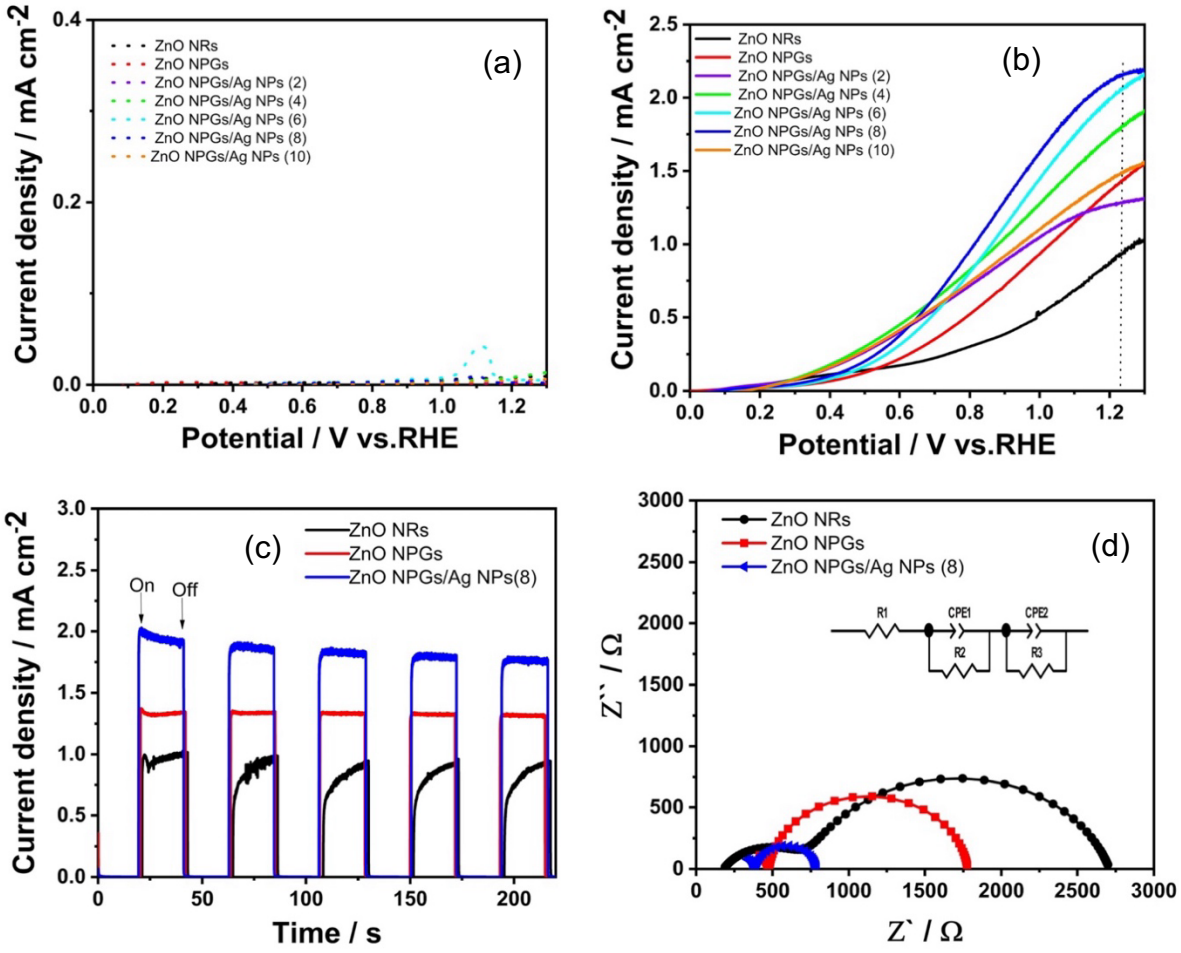

Figure 3-9. LSV curves under dark conditions (a), and under light illumination (b) of ZnO NRs, ZnO NPGs, and ZnO NPGs decorated with different cycles (2,4,6,8, and 10) of Ag NPs. (c) Transient photocurrent response of ZnO NRs, ZnO NPGs, and ZnO NPGs/Ag NPs (8) photoanodes that was determined at 1.1 V vs. RHE. (d) Nyquist plots were determined under the simulated solar irradiation. The inserted image is the corresponding equivalent circuit.

3.3.3.3. Mott–Schottky

The Mott–Schottky curves of ZnO NPGs and ZnO NPGs/Ag NPs (8) depicted a positive slope, which implied that both materials are n-type semiconductors (**Figure 3-10a**). The deposition of Ag NPs caused a small negative shift of the E_{fb}, which confirms the increase of the band bending at the interface of the semiconductor and the electrolyte, resulting in enhancing charge carriers' separation and mobility.

3.3.3.4. Photoelectrochemical conversion efficiency

The ABPE of ZnO NRs, ZnO NPGs and ZnO NPGs/Ag NPs (8) is depicted in **Figure 3-10b**. It is obvious that the ZnO NPGs/Ag NPs (8cycles) attained the maximum photoconversion efficiency of 0.43% at 0.88 V vs. RHE, meanwhile, ZnO NRs and ZnO NPGs demonstrated a photoconversion efficiency of 0.12% and 0.23% at the same potential, respectively. **Figure 3-10c** illustrates the IPCE spectra of the same samples. The ZnO NPGs photoanode achieved higher IPCE than ZnO NRs in the UV range, owing to the lower structural defects and electrical resistance. ZnO NPGs/Ag NPs (8) improved the IPCE in the visible range (420–550 nm) as depicted in **Figure 3-10d**. This remarkable improvement can be attributed to the enhanced visible light absorption, and the hot electron transfer from Ag to ZnO, due to the LSPR effect of Ag NPs [61].

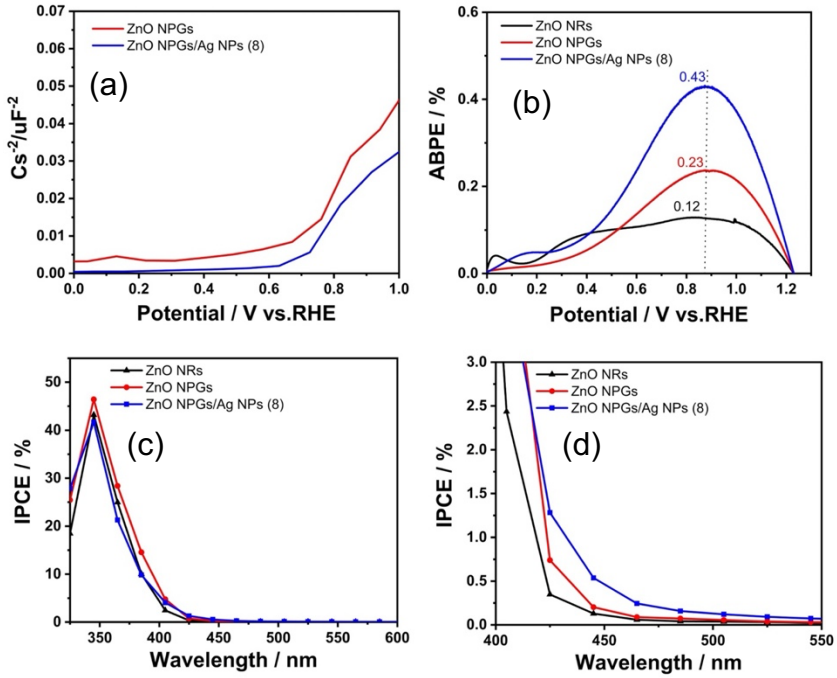

Figure 3-10. (a) Mott–Schottky plots were recorded at 1000 Hz under dark conditions. The photoconversion efficiency estimated utilizing ABPE (%) (b), and IPCE (%) at the wavelength range of 325-600 nm (c), and 400-550 nm (d) of ZnO NRs, ZnO NPGs, and ZnO NPGs/Ag NPs (8) photoanodes.

3.3.3.5. Proposed reaction mechanism

The suggested PEC reaction mechanism using ZnO NPGs/Ag NPs photoanode is shown in **Figure 3-11** depending on the obtained data. because the work functions of ZnO and Ag are almost 5.2 and 4.26 eV, respectively, an Ohmic junction should be generated at the contact between ZnO and Ag [85]. Owing to the application of the external bias, electrons have only flowed from Ag to ZnO with a small potential barrier. Under light irradiation, UV radiation excited electrons from VB to CB of ZnO. These excited electrons of ZnO migrated to the FTO substrate and then moved to the Pt electrode through the external circuit to reduce protons and produce H_2. The holes in the VB of ZnO would mostly be used to oxidize the sacrificial reagent (i.e., methanol, in the electrolyte) on the surface of ZnO.

Some of the holes can be migrated to Ag NPs but eventually react with methanol on Ag NPs' surface. Conversely, Vis light induced the LSPR of Ag NPs. The produced hot electrons were migrated to the CB of ZnO and then to the Pt electrode via FTO and the external circuit. The generated holes in Ag NPs are consumed to oxidize methanol in the electrolyte on the Ag NPs' surface. Therefore, the existence of methanol prevented the oxidation of Ag and guaranteed the continuous generation of hot electrons.

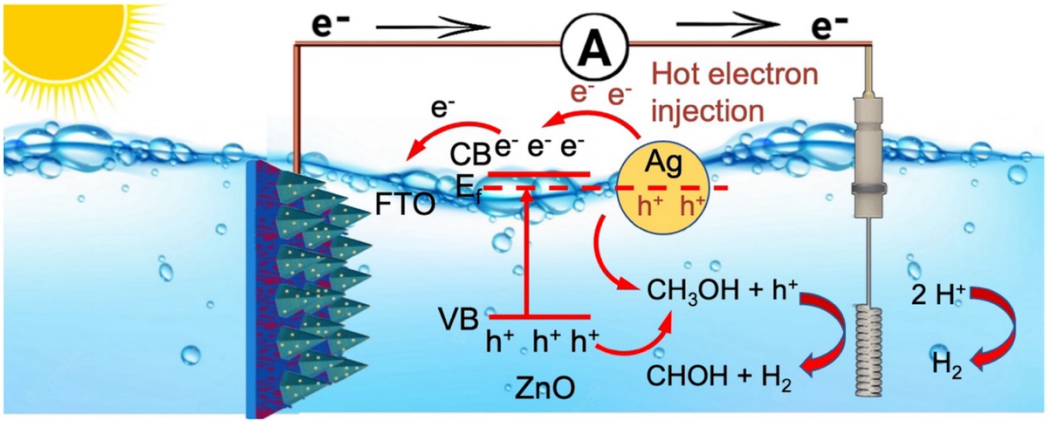

Figure 3-11. Suggested PEC mechanism over ZnO NPGs/Ag NPs photoanode under solar irradiation.

3.4. Conclusions

This study offered a simple and efficient approach to preparing distinct ZnO NPGs using an aqueous chemical downward method. Subsequently, ZnO NPGs were decorated with various

amounts of Ag NPs utilizing the SILAR technique. The quantity of Ag NPs was adjusted by controlling the number of SILAR cycles (2, 4, 6, 8, and 10). The quantity of Ag NPs deposited on the surface of ZnO NPGs had a substantial impact on the PEC performance. The ZnO NPGs/Ag NPs photoanode with an optimum eight cycles deposition of Ag NPs attained the highest photocurrent of 2.15 mA cm^{-2} at 1.23 V vs RHE and significantly boosted the photoconversion efficiency. The hot electrons transfer from Ag NPs to the CB of ZnO NPGs under Vis light happened owing to the LSPR effect. The enhanced PEC performance using ZnO NPGs/Ag NPs photoanode can be ascribed to the following: (1) the unique superstructure properties of ZnO NPGs that increased scattering, improved light absorption, and mitigated e^{-}/h^{+} pairs recombination. (2) The deposition of plasmonic Ag NPs ameliorated the interfacial mobility of charge carriers between photoelectrode and electrolyte, as well as enhanced the Vis light response owing to their LSPR effect.

References

[1] F. Meng, S.K. Cushing, J. Li, S. Hao, N. Wu, Enhancement of Solar Hydrogen Generation by Synergistic Interaction of $La_2Ti_2O_7$ Photocatalyst with Plasmonic Gold Nanoparticles and Reduced Graphene Oxide Nanosheets, ACS Catal 5 (2015) 1949–1955. https://doi.org/10.1021/cs5016194.

[2] G.U. Kamble, S.W. Shin, S.W. Park, M.A. Gaikwad, V.C. Karade, J.S. Jang, Y. Park, U. V. Ghorpade, M.P. Suryawanshi, J.H. Kim, Germanium Selenide: A Critical Review on Recent Advances in Material Development for Photovoltaic and Photoelectrochemical Water-Splitting Applications, Solar RRL (2023). https://doi.org/10.1002/solr.202300502.

[3] D. Lee, W. Wang, C. Zhou, X. Tong, M. Liu, G. Galli, K.-S. Choi, The impact of surface composition on the interfacial energetics and photoelectrochemical properties of $BiVO_4$, Nat Energy 6 (2021) 287–294. https://doi.org/10.1038/s41560-021-00777-x.

[4] M.M. Abouelela, G. Kawamura, W.K. Tan, A. Matsuda, Anodic nanoporous WO_3 modified with Bi_2S_3 quantum dots as a photoanode for photoelectrochemical water splitting, J Colloid Interface Sci 629 (2023) 958–970. https://doi.org/10.1016/j.jcis.2022.09.041.

[5] Q. Chen, J. Li, B. Zhou, M. Long, H. Chen, Y. Liu, W. Cai, W. Shangguan, Preparation of well-aligned WO_3 nanoflake arrays vertically grown on tungsten substrate as photoanode for photoelectrochemical water splitting, Electrochem Commun 20 (2012) 153–156. https://doi.org/10.1016/j.elecom.2012.03.043.

[6] S. Grigorescu, B. Bärhausen, L. Wang, A. Mazare, J.E. Yoo, R. Hahn, P. Schmuki, Tungsten doping of Ta_3N_5-nanotubes for band gap narrowing and enhanced photoelectrochemical water splitting efficiency, Electrochem Commun 51 (2015) 85–88. https://doi.org/10.1016/j.elecom.2014.12.019.

[7] M.M. Abouelela, K. Inoue, G. Kawamura, W.K. Tan, A. Matsuda, Heterojunction of TiO_2 nanotubes arrays/Bi_2Se_3 quantum dots as an effective and stable photoanode for photoelectrochemical H2 generation, Sustainable Materials and Technologies 38 (2023) e00718. https://doi.org/10.1016/j.susmat.2023.e00718.

[8] K. Sivula, R. van de Krol, Semiconducting materials for photoelectrochemical energy conversion, Nat Rev Mater 1 (2016) 15010. https://doi.org/10.1038/natrevmats.2015.10.

[9] P. Lianos, Review of recent trends in photoelectrocatalytic conversion of solar energy to electricity and hydrogen, Appl Catal B 210 (2017) 235–254. https://doi.org/10.1016/j.apcatb.2017.03.067.

[10] B. Zhang, S. Yu, Y. Dai, X. Huang, L. Chou, G. Lu, G. Dong, Y. Bi, Nitrogen-incorporation activates NiFeOx catalysts for efficiently boosting oxygen evolution activity and stability of $BiVO_4$ photoanodes, Nat Commun 12 (2021) 6969. https://doi.org/10.1038/s41467-021-27299-0.

[11] M. Mohamed Abouelela, G. Kawamura, A. Matsuda, Metal chalcogenide-based photoelectrodes for photoelectrochemical water splitting, Journal of Energy Chemistry 73 (2022) 189–213. https://doi.org/10.1016/j.jechem.2022.05.022.

[12] M.A. Desai, A.N. Vyas, G.D. Saratale, S.D. Sartale, Zinc oxide superstructures: Recent synthesis approaches and application for hydrogen production via photoelectrochemical water splitting, Int J Hydrogen Energy 44 (2019) 2091–2127. https://doi.org/10.1016/j.ijhydene.2018.08.042.

[13] L. Liccardo, E. Lushaj, L. Dal Compare, E. Moretti, A. Vomiero, Nanoscale ZnO/α-Fe_2O_3 Heterostructures: Toward Efficient and Low-Cost Photoanodes for Water Splitting, Small Science 2 (2022) 2100104. https://doi.org/10.1002/smsc.202100104.

[14] W.K. Tan, K. Abdul Razak, Z. Lockman, G. Kawamura, H. Muto, A. Matsuda, Photoluminescence properties of rod-like Ce-doped ZnO nanostructured films formed by hot-water treatment of sol–gel derived coating, Opt Mater (Amst) 35 (2013) 1902–1907. https://doi.org/10.1016/j.optmat.2013.01.011.
[15] W.K. Tan, K.A. Razak, K. Ibrahim, Z. Lockman, Oxidation of etched Zn foil for the formation of ZnO nanostructure, J Alloys Compd 509 (2011) 6806–6811. https://doi.org/10.1016/j.jallcom.2011.03.055.
[16] Y.-K. Hsu, Y.-G. Lin, Y.-C. Chen, Polarity-dependent photoelectrochemical activity in ZnO nanostructures for solar water splitting, Electrochem Commun 13 (2011) 1383–1386. https://doi.org/10.1016/j.elecom.2011.08.016.
[17] M.A. Desai, S.D. Sartale, Facile Soft Solution Route To Engineer Hierarchical Morphologies of ZnO Nanostructures, Cryst Growth Des 15 (2015) 4813–4820. https://doi.org/10.1021/acs.cgd.5b00561.
[18] T. Zhou, J. Wang, S. Chen, J. Bai, J. Li, Y. Zhang, L. Li, L. Xia, M. Rahim, Q. Xu, B. Zhou, Bird-nest structured ZnO/TiO_2 as a direct Z-scheme photoanode with enhanced light harvesting and carriers kinetics for highly efficient and stable photoelectrochemical water splitting, Appl Catal B 267 (2020) 118599. https://doi.org/10.1016/j.apcatb.2020.118599.
[19] P. Madhusudan, Y. Wang, B.N. Chandrashekar, W. Wang, J. Wang, J. Miao, R. Shi, Y. Liang, G. Mi, C. Cheng, Nature inspired ZnO/ZnS nanobranch-like composites, decorated with $Cu(OH)_2$ clusters for enhanced visible-light photocatalytic hydrogen evolution, Appl Catal B 253 (2019) 379–390. https://doi.org/10.1016/j.apcatb.2019.04.008.
[20] A. Ali, X. Li, J. Song, S. Yang, W. Zhang, Z. Zhang, R. Xia, L. Zhu, X. Xu, Nature-Mimic ZnO Nanoflowers Architecture: Chalcogenide Quantum Dots Coupling with ZnO/$ZnTiO_3$ Nanoheterostructures for Efficient Photoelectrochemical Water Splitting, The Journal of Physical Chemistry C 121 (2017) 21096–21104. https://doi.org/10.1021/acs.jpcc.7b04701.
[21] T.L. Sounart, J. Liu, J.A. Voigt, J.W.P. Hsu, E.D. Spoerke, Z. Tian, Y.B. Jiang, Sequential Nucleation and Growth of Complex Nanostructured Films, Adv Funct Mater 16 (2006) 335–344. https://doi.org/10.1002/adfm.200500468.
[22] H.R. Liu, G.X. Shao, J.F. Zhao, Z.X. Zhang, Y. Zhang, J. Liang, X.G. Liu, H.S. Jia, B.S. Xu, Worm-Like Ag/ZnO Core–Shell Heterostructural Composites: Fabrication, Characterization, and Photocatalysis, The Journal of Physical Chemistry C 116 (2012) 16182–16190. https://doi.org/10.1021/jp2115143.
[23] S. Singh, V.C. Srivastava, S.L. Lo, T.K. Mandal, G. Naresh, Morphology-controlled green approach for synthesizing the hierarchical self-assembled 3D porous ZnO superstructure with excellent catalytic activity, Microporous and Mesoporous Materials 239 (2017) 296–309. https://doi.org/10.1016/j.micromeso.2016.10.016.
[24] J. Ma, J. Liu, Y. Bao, Z. Zhu, X. Wang, J. Zhang, Synthesis of large-scale uniform mulberry-like ZnO particles with microwave hydrothermal method and its antibacterial property, Ceram Int 39 (2013) 2803–2810. https://doi.org/10.1016/j.ceramint.2012.09.049.
[25] W. Ma, Z. Gu, H. Nan, B. Geng, X. Zhang, Morphology-controllable synthesis of 3D firecracker-like ZnO nanoarchitectures for high catalytic performance, CrystEngComm 17 (2015) 1121–1128. https://doi.org/10.1039/C4CE02151G.
[26] Y.-C. Chang, W.-C. Yang, C.-M. Chang, P.-C. Hsu, L.-J. Chen, Controlled Growth of ZnO Nanopagoda Arrays with Varied Lamination and Apex Angles, Cryst Growth Des 9 (2009) 3161–3167. https://doi.org/10.1021/cg801172h.

[27] S. Yang, J. Wang, X. Li, H. Zhai, D. Han, B. Wei, D. Wang, J. Yang, One-step synthesis of bird cage-like ZnO and other controlled morphologies: Structural, growth mechanism and photocatalytic properties, Appl Surf Sci 319 (2014) 211–215. https://doi.org/10.1016/j.apsusc.2014.07.165.
[28] S.H. Ko, D. Lee, H.W. Kang, K.H. Nam, J.Y. Yeo, S.J. Hong, C.P. Grigoropoulos, H.J. Sung, Nanoforest of Hydrothermally Grown Hierarchical ZnO Nanowires for a High Efficiency Dye-Sensitized Solar Cell, Nano Lett 11 (2011) 666–671. https://doi.org/10.1021/nl1037962.
[29] C.-T. Wu, W.-P. Liao, J.-J. Wu, Three-dimensional ZnO nanodendrite/nanoparticle composite solar cells, J Mater Chem 21 (2011) 2871. https://doi.org/10.1039/c0jm03481a.
[30] P. Sudhagar, R.S. Kumar, J.H. Jung, W. Cho, R. Sathyamoorthy, J. Won, Y.S. Kang, Facile synthesis of highly branched jacks-like ZnO nanorods and their applications in dye-sensitized solar cells, Mater Res Bull 46 (2011) 1473–1479. https://doi.org/10.1016/j.materresbull.2011.04.027.
[31] X. Pan, X. Liu, A. Bermak, Z. Fan, Self-Gating Effect Induced Large Performance Improvement of ZnO Nanocomb Gas Sensors, ACS Nano 7 (2013) 9318–9324. https://doi.org/10.1021/nn4040074.
[32] X. Wang, W. Wang, Y.-L. Liu, Enhanced acetone sensing performance of Au nanoparticles functionalized flower-like ZnO, Sens Actuators B Chem 168 (2012) 39–45. https://doi.org/10.1016/j.snb.2012.01.006.
[33] Y.-C. Chang, ZnO nanopinecone arrays with enhanced photocatalytic performance in sunlight, RSC Adv. 4 (2014) 20273–20280. https://doi.org/10.1039/C4RA02044H.
[34] M.A. Desai, S.D. Sartale, Facile Soft Solution Route To Engineer Hierarchical Morphologies of ZnO Nanostructures, Cryst Growth Des 15 (2015) 4813–4820. https://doi.org/10.1021/acs.cgd.5b00561.
[35] A. Matsuda, W.K. Tan, S. Furukawa, H. Muto, Morphology-control of crystallites precipitated from ZnO gel films by applying electric field during hot-water treatment, Mater Sci Semicond Process 16 (2013) 1232–1239. https://doi.org/10.1016/j.mssp.2012.12.018.
[36] C. Mahala, M.D. Sharma, M. Basu, Near-Field and Far-Field Plasmonic Effects of Gold Nanoparticles Decorated on ZnO Nanosheets for Enhanced Solar Water Splitting, ACS Appl Nano Mater 3 (2020) 1153–1165. https://doi.org/10.1021/acsanm.9b01678.
[37] M.M. Abouelela, G. Kawamura, A. Matsuda, A review on plasmonic nanoparticle-semiconductor photocatalysts for water splitting, J Clean Prod 294 (2021) 126200. https://doi.org/10.1016/j.jclepro.2021.126200.
[38] G. Kawamura, A. Matsuda, Synthesis of Plasmonic Photocatalysts for Water Splitting, Catalysts 9 (2019) 982. https://doi.org/10.3390/catal9120982.
[39] P. Subramanyam, B. Meena, G.N. Sinha, M. Deepa, C. Subrahmanyam, Decoration of plasmonic Cu nanoparticles on WO_3/Bi_2S_3 QDs heterojunction for enhanced photoelectrochemical water splitting, Int J Hydrogen Energy 45 (2020) 7706–7715. https://doi.org/10.1016/j.ijhydene.2019.05.168.
[40] S. Hou, M.-H. Huang, F.-X. Xiao, Stabilizing atomically precise metal nanoclusters as simultaneous charge relay mediators and photosensitizers, J Mater Chem A Mater 10 (2022) 7006–7012. https://doi.org/10.1039/D2TA00572G.
[41] F.-X. Xiao, B. Liu, Plasmon-Dictated Photo-Electrochemical Water Splitting for Solar-to-Chemical Energy Conversion: Current Status and Future Perspectives, Adv Mater Interfaces 5 (2018) 1701098. https://doi.org/10.1002/admi.201701098.

[42] X. He, W. Tian, L. Yang, Z. Bai, L. Li, Optical and Electrical Modulation Strategies of Photoelectrodes for Photoelectrochemical Water Splitting, Small Methods (2023). https://doi.org/10.1002/smtd.202300350.
[43] X. Du, L. Liu, J. Ye, Plasmonic Metal Nanoparticles for Artificial Photosynthesis: Advancements, Mechanisms, and Perspectives, Solar RRL 5 (2021). https://doi.org/10.1002/solr.202100611.
[44] H. Tada, S. Naya, M. Fujishima, Water splitting by plasmonic photocatalysts with a gold nanoparticle/cadmium sulfide heteroepitaxial junction: A mini review, Electrochem Commun 97 (2018) 22–26. https://doi.org/10.1016/j.elecom.2018.10.005.
[45] W.-H. Tu, Y.-K. Hsu, C.-H. Yen, C.-I. Wu, J.-S. Hwang, L.-C. Chen, K.-H. Chen, Au nanoparticle modified GaN photoelectrode for photoelectrochemical hydrogen generation, Electrochem Commun 13 (2011) 530–533. https://doi.org/10.1016/j.elecom.2011.02.036.
[46] W.K. Tan, H. Muto, T. Ito, G. Kawamura, Z. Lockman, A. Matsuda, Facile Fabrication of Plasmonic Enhanced Noble-Metal-Decorated ZnO Nanowire Arrays for Dye-Sensitized Solar Cells, J Nanosci Nanotechnol 20 (2020) 359–366. https://doi.org/10.1166/jnn.2020.17223.
[47] J. Yu, L. Zhang, J. Qian, Z. Zhu, S. Ni, G. Liu, X. Xu, In situ exsolution of silver nanoparticles on $AgTaO_3$-$SrTiO_3$ solid solutions as efficient plasmonic photocatalysts for water splitting, Appl Catal B 256 (2019) 117818. https://doi.org/10.1016/j.apcatb.2019.117818.
[48] S.W. Verbruggen, M. Keulemans, M. Filippousi, D. Flahaut, G. van Tendeloo, S. Lacombe, J.A. Martens, S. Lenaerts, Plasmonic gold–silver alloy on TiO_2 photocatalysts with tunable visible light activity, Appl Catal B 156–157 (2014) 116–121. https://doi.org/10.1016/j.apcatb.2014.03.027.
[49] F.S. Lim, S.T. Tan, Y. Zhu, J.-W. Chen, B. Wu, H. Yu, J.-M. Kim, R.T. Ginting, K.S. Lau, C.H. Chia, H. Wu, M. Gu, W.S. Chang, Tunable Plasmon-Induced Charge Transport and Photon Absorption of Bimetallic Au–Ag Nanoparticles on ZnO Photoanode for Photoelectrochemical Enhancement under Visible Light, The Journal of Physical Chemistry C 124 (2020) 14105–14117. https://doi.org/10.1021/acs.jpcc.0c03967.
[50] B. Tang, S.-C. Zhu, H. Liang, S. Li, B.-J. Liu, F.-X. Xiao, Tuning atomically precise metal nanocluster mediated photoelectrocatalysis *via* a non-conjugated polymer, J Mater Chem A Mater 10 (2022) 4032–4042. https://doi.org/10.1039/D1TA10284B.
[51] F. Amano, S. Nakayama, Improvement of water splitting activity of silver-excess $AgTaO_3$ photocatalysts via nitric acid washing treatment, J Environ Chem Eng 10 (2022) 108089. https://doi.org/10.1016/j.jece.2022.108089.
[52] P. Peerakiatkhajohn, J.-H. Yun, T. Butburee, W. Nisspa, S. Thaweesak, Surface plasmon-driven photoelectrochemical water splitting of a Ag/TiO_2 nanoplate photoanode, RSC Adv 12 (2022) 2652–2661. https://doi.org/10.1039/D1RA09070D.
[53] S. Saeed, H. Siddique, R. Dai, J. Wang, A. Ali, C. Gao, X. Tao, Z. Wang, Z. Ding, Z. Zhang, Enhanced PEC Water Splitting Performance of Silver Nanoparticle-Coated CdS Nanowire Photoanodes: The Role of Silver Deposition, The Journal of Physical Chemistry C 125 (2021) 7542–7551. https://doi.org/10.1021/acs.jpcc.0c11332.
[54] L. Lei, L. Sang, Y. Gao, Pulse electrodeposition of Ag, Cu nanoparticles on TiO_2 nanoring/nanotube arrays for enhanced photoelectrochemical water splitting, Advanced Powder Technology 33 (2022) 103511. https://doi.org/10.1016/j.apt.2022.103511.

[55] C. Yang, H. Xu, Dual modification with plasmonic Ag and Co–Pi significantly promoted photoelectrochemical performances of CdS photoanodes, Journal of Materials Science: Materials in Electronics 33 (2022) 10551–10560. https://doi.org/10.1007/s10854-022-08041-y.

[56] Y. Li, Z. Liu, Z. Guo, M. Ruan, X. Li, Y. Liu, Efficient WO_3 Photoanode Modified by Pt Layer and Plasmonic Ag for Enhanced Charge Separation and Transfer To Promote Photoelectrochemical Performances, ACS Sustain Chem Eng (2019) acssuschemeng.9b02450. https://doi.org/10.1021/acssuschemeng.9b02450.

[57] Z. Zeng, T. Li, Y.-B. Li, X.-C. Dai, M.-H. Huang, Y. He, G. Xiao, F.-X. Xiao, Plasmon-induced photoelectrochemical water oxidation enabled by *in situ* layer-by-layer construction of cascade charge transfer channel in multilayered photoanode, J Mater Chem A Mater 6 (2018) 24686–24692. https://doi.org/10.1039/C8TA08841A.

[58] A. Das, T. Deka, P.M. Kumar, M. Bhagavathiachari, R.G. Nair, Ag-modified ZnO nanorods and its dual application in visible light-driven photoelectrochemical water oxidation and photocatalytic dye degradation: A correlation between optical and electrochemical properties, Advanced Powder Technology 33 (2022) 103434. https://doi.org/10.1016/j.apt.2022.103434.

[59] G. v. Belessiotis, A.G. Kontos, Plasmonic silver (Ag)-based photocatalysts for H_2 production and CO_2 conversion: Review, analysis and perspectives, Renew Energy 195 (2022) 497–515. https://doi.org/10.1016/j.renene.2022.06.044.

[60] B. Kumari, S. Sharma, N. Singh, A. Verma, V.R. Satsangi, S. Dass, R. Shrivastav, ZnO thin films, surface embedded with biologically derived Ag/Au nanoparticles, for efficient photoelectrochemical splitting of water, Int J Hydrogen Energy 39 (2014) 18216–18229. https://doi.org/10.1016/j.ijhydene.2014.09.025.

[61] N.P. Klochko, K.S. Klepikova, I.V. Khrypunova, V.R. Kopach, I.I. Tyukhov, S.I. Petrushenko, S.V. Dukarov, V.M. Sukhov, M.V. Kirichenko, A.L. Khrypunova, Solution-processed flexible broadband ZnO photodetector modified by Ag nanoparticles, Solar Energy 232 (2022) 1–11. https://doi.org/10.1016/j.solener.2021.12.051.

[62] S.A. Ansari, M.M. Khan, M.O. Ansari, J. Lee, M.H. Cho, Biogenic Synthesis, Photocatalytic, and Photoelectrochemical Performance of Ag–ZnO Nanocomposite, The Journal of Physical Chemistry C 117 (2013) 27023–27030. https://doi.org/10.1021/jp410063p.

[63] Q. Zhang, G. Xie, M. Xu, Y. Su, H. Tai, H. Du, Y. Jiang, Visible light-assisted room temperature gas sensing with ZnO-Ag heterostructure nanoparticles, Sens Actuators B Chem 259 (2018) 269–281. https://doi.org/10.1016/j.snb.2017.12.052.

[64] T.N.Q. Trang, T.B. Phan, N.D. Nam, V.T.H. Thu, In Situ Charge Transfer at the Ag@ZnO Photoelectrochemical Interface toward the High Photocatalytic Performance of H_2 Evolution and RhB Degradation, ACS Appl Mater Interfaces 12 (2020) 12195–12206. https://doi.org/10.1021/acsami.9b15578.

[65] S.K. Cushing, J. Li, J. Bright, B.T. Yost, P. Zheng, A.D. Bristow, N. Wu, Controlling Plasmon-Induced Resonance Energy Transfer and Hot Electron Injection Processes in Metal@TiO_2 Core–Shell Nanoparticles, The Journal of Physical Chemistry C 119 (2015) 16239–16244. https://doi.org/10.1021/acs.jpcc.5b03955.

[66] Y.-C. Chang, W.-C. Yang, C.-M. Chang, P.-C. Hsu, L.-J. Chen, Controlled Growth of ZnO Nanopagoda Arrays with Varied Lamination and Apex Angles, Cryst Growth Des 9 (2009) 3161–3167. https://doi.org/10.1021/cg801172h.

[67] M.M. Abouelela, M.S. Sayed, G. Kawamura, W.K. Tan, A. Matsuda, Enhancing the photoelectrochemical performance of ZnO nanopagoda photoanode through sensitization with Ag and Ag_2S NPs co-deposition, Mater Chem Phys 305 (2023) 127984. https://doi.org/10.1016/j.matchemphys.2023.127984.
[68] W. Bai, Y. Zhou, G. Peng, J. Wang, A. Li, P.F.-X. Corvini, Engineering efficient hole transport layer Ferrihydrite-MXene on $BiVO_4$ photoanodes for photoelectrochemical water splitting: Work function and conductivity regulated, Appl Catal B 315 (2022) 121606. https://doi.org/10.1016/j.apcatb.2022.121606.
[69] Y. Kong, H. Sun, W. Fan, L. Wang, H. Zhao, X. Zhao, S. Yuan, Enhanced photoelectrochemical performance of tungsten oxide film by bifunctional Au nanoparticles, RSC Adv 7 (2017) 15201–15210. https://doi.org/10.1039/C7RA01426K.
[70] I.-C. Yao, P. Lin, T.-Y. Tseng, Field Emission Properties and Reliability of ZnO Nanorod, Nanopagoda, and Nanotip Current Emitters, IEEE Trans Nanotechnol 11 (2012) 746–750. https://doi.org/10.1109/TNANO.2012.2195502.
[71] A. Azam, S. Babkair, Low-temperature growth of well-aligned zinc oxide nanorod arrays on silicon substrate and their photocatalytic application, Int J Nanomedicine (2014) 2109. https://doi.org/10.2147/IJN.S60839.
[72] Y.-C. Chang, W.-C. Yang, C.-M. Chang, P.-C. Hsu, L.-J. Chen, Controlled Growth of ZnO Nanopagoda Arrays with Varied Lamination and Apex Angles, Cryst Growth Des 9 (2009) 3161–3167. https://doi.org/10.1021/cg801172h.
[73] W.K. Tan, Z. Lockman, K. Abdul Razak, G. Kawamura, H. Muto, A. Matsuda, Enhanced dye-sensitized solar cells performance of ZnO nanorod arrays grown by low-temperature hydrothermal reaction, Int J Energy Res (2013) n/a-n/a. https://doi.org/10.1002/er.3026.
[74] W.K. Tan, K. Abdul Razak, Z. Lockman, G. Kawamura, H. Muto, A. Matsuda, Formation of highly crystallized ZnO nanostructures by hot-water treatment of etched Zn foils, Mater Lett 91 (2013) 111–114. https://doi.org/10.1016/j.matlet.2012.08.103.
[75] Z. Wu, C. Xu, Y. Wu, H. Yu, Y. Tao, H. Wan, F. Gao, ZnO nanorods/Ag nanoparticles heterostructures with tunable Ag contents: A facile solution-phase synthesis and applications in photocatalysis, CrystEngComm 15 (2013) 5994. https://doi.org/10.1039/c3ce40753e.
[76] K. Kim, P. gyu Choi, T. Itoh, Y. Masuda, Atomic step formation on porous ZnO nanobelts: remarkable promotion of acetone gas detection up to the parts per trillion level, J Mater Chem A Mater 10 (2022) 13839–13847. https://doi.org/10.1039/D2TA02789E.
[77] Md. Molla, M. Furukawa, I. Tateishi, H. Katsumata, S. Kaneco, Studies of Effects of Calcination Temperature on the Crystallinity and Optical Properties of Ag-Doped ZnO Nanocomposites, Journal of Composites Science 3 (2019) 18. https://doi.org/10.3390/jcs3010018.
[78] S. Khosravi-Gandomani, R. Yousefi, F. Jamali-Sheini, N.M. Huang, Optical and electrical properties of p-type Ag-doped ZnO nanostructures, Ceram Int 40 (2014) 7957–7963. https://doi.org/10.1016/j.ceramint.2013.12.145.
[79] P. Tuersun, Simulated localized surface plasmon spectra of single gold and silver nanobars, Optik (Stuttg) 127 (2016) 3466–3470. https://doi.org/10.1016/j.ijleo.2015.12.074.
[80] M. Karyaoui, D. ben Jemia, M. Daoudi, A. Bardaoui, A. Boukhachem, M. Amlouk, R. Chtourou, Physical properties of graphene oxide GO-doped ZnO thin films for optoelectronic application, Applied Physics A 127 (2021) 134. https://doi.org/10.1007/s00339-020-04269-9.

[81] G. Zhu, H. Yin, C. Yang, H. Cui, Z. Wang, J. Xu, T. Lin, F. Huang, Black Titania for Superior Photocatalytic Hydrogen Production and Photoelectrochemical Water Splitting, ChemCatChem 7 (2015) 2614–2619. https://doi.org/10.1002/cctc.201500488.
[82] W.K. Tan, G. Kawamura, H. Muto, K. Abdul Razak, Z. Lockman, A. Matsuda, Blue-emitting photoluminescence of rod-like and needle-like ZnO nanostructures formed by hot-water treatment of sol–gel derived coatings, J Lumin 158 (2015) 44–49. https://doi.org/10.1016/j.jlumin.2014.09.028.
[83] S. Dellis, N. Kalfagiannis, S. Kassavetis, C. Bazioti, G.P. Dimitrakopulos, D.C. Koutsogeorgis, P. Patsalas, Photoluminescence enhancement of ZnO via coupling with surface plasmons on Al thin films, J Appl Phys 121 (2017) 103104. https://doi.org/10.1063/1.4977954.
[84] L. Cai, Y. Du, X. Guan, S. Shen, CdS nanocrystallites sensitized ZnO nanorods with plasmon enhanced photoelectrochemical performance, Chinese Chemical Letters 30 (2019) 2363–2367. https://doi.org/10.1016/j.cclet.2019.07.020.
[85] F. Yan, Y. Wang, J. Zhang, Z. Lin, J. Zheng, F. Huang, Schottky or Ohmic Metal-Semiconductor Contact: Influence on Photocatalytic Efficiency of Ag/ZnO and Pt/ZnO Model Systems, ChemSusChem 7 (2014) 101–104. https://doi.org/10.1002/cssc.201300818.

Chapter 4. Improving the photoelectrochemical performance of ZnO nanopagoda arrays through co-deposition of Ag and Ag_2S nanoparticles

4.1. Introduction

H_2 is the cleanest solar fuel that can address the problems of energy shortage and environmental pollution, as it emits no CO_2 during its oxidation in fuel cell devices [1,2]. PEC-WS is a promising approach that uses solar photons to produce chemical fuels, such as H_2 [3–7]. Developing a PEC system that is affordable and has high solar to H_2 conversion efficiency is essential [8]. The significant component of PEC systems is semiconductor photoelectrodes, which provide a route for producing H_2 through consuming solar energy [9]. Photoanode, where oxidation reaction takes place, can absorb photon energy and produce e^-/h^+ pairs. The photogenerated electrons are captured by photoanode and then transferred through the external circuit to the counter electrode where they are consumed in the reduction reaction. Whereas photogenerated holes participate in oxidation reactions [10,11]. Numerous metal oxide semiconductors have been applied as photoanodes for PEC-WS, e.g., ZnO [12,13], $BiVO_4$ [14–16], Fe_2O_3 [17], TiO_2 [18,19], and WO_3 [20–22]. Among the aforementioned photoelectrode semiconductors, ZnO has garnered significant scientific interest due to its eco-friendliness, availability on earth, affordability, and superior electron mobility [23–25]. However, ZnO absorbs light UV zone owing to its wide bandgap energy (about 3.3 eV) [26] and its inefficient e^-/h^+ pairs separation, slow reaction kinetics, and instability caused by photochemical corrosion limit its PEC performance [27]. To overcome these limitations, significant research has been done to select appropriate light-harvesting materials to create interface junctions with ZnO [28–30]. Selecting an adequate semiconductor material to create a heterojunction with ZnO is a good way to increase ZnO's PEC efficiency because it may increase the light absorption ability and facilitate e^-/h^+ pairs mobility [31]. Ag_2S is a nontoxic substance having a narrow direct bandgap (about 1.0 eV) [32], and it can be deposited over a variety of materials using chemical and physical procedures [9,33,34]. Additionally, Ag_2S has a superb ability to absorb light in Vis and NIR zones, and an efficient separation efficiency of e^-/h^+ pairs at heterojunction interfaces [35]. Therefore, it is widely applied in PEC systems as a photosensitizer in heterojunction with metal oxide semiconductors [9].

Recently, the heterojunction of ZnO with Ag_2S has greatly enhanced ZnO's PEC performance because Ag_2S can dramatically increase light absorption capability and boost the photogeneration and mobility of e^-/h^+ pairs, mitigating the rate of charge recombination [36–38]. Furthermore, the plasmonic metal deposited over the surface of the semiconductor can greatly enhance the PEC performance owing to its LSPR [39–42]. Recent research studies have demonstrated that plasmonic metal-semiconductor nanocomposites provide a notable improvement in PEC performance [43,44]. Ag is an excellent choice among many other plasmonic metal types due to its exceptional optical and PEC features; moreover, compared to other noble metals, Ag is less costly [45,46]. Recently, it has been reported that Ag–Ag_2S semiconductor nanocomposites have boosted the PEC performance [39,47]. To enhance the PEC performance, new ZnO morphologies can also be employed. Numerous research teams are putting a lot of effort into creating novel photoelectrode nanostructures [48–50]. ZnO superstructures showed better PEC performance than simple nanostructures [51], even though the preparation of such superstructures occasionally requires intricate, multi-step processes. Therefore, the direct fabrication of such superstructures is highly attractive but remains challenging. Furthermore, some ZnO superstructures, like NPGs and nanocomb arrays, have not been studied for PEC-WS application yet.

In this study, We synthesized ZnO NPGs decorated with various quantities of Ag–Ag_2S NPs and investigated their PEC performance. The preparation procedure includes two steps: (i) fabrication of ZnO NPGs by an aqueous chemical downward growth process, (ii) deposition of Ag-Ag_2S NPs on the ZnO NPGs by SILAR process. The coupling of Ag and Ag_2S NPs with ZnO NPGs remarkably enhanced the PEC performance as a result of the synergistic effect of increased visible light absorption capacity and e^-/h^+ pairs separation efficiency.

4.2. Experimental

4.2.1. Synthesis of photoanodes

4.2.1.1. Synthesis of ZnO nanopagoda arrays

The unique ZnO NPGs were synthesized chemical downward growth procedure as previously explained in detail in Chapter 3, section 3.2.1.2.

4.2.1.2. Synthesis of ZnO nanopagoda arrays/Ag-Ag_2S nanoparticles

Ag-Ag_2S NPs were deposited on the surface of ZnO NPGs utilizing the SILAR procedure. ZnO NPGs thin film was submerged in four aqueous solutions for 30 s: (1) cationic solution of 20 mM $AgNO_3$, (2) DI H_2O to remove the extra ions existing on the surface, (3) anionic aqueous solution of 20 mM Na_2S, and (4) DI H_2O to remove the extra ions existing on the surface. This procedure forms one cycle of Ag-Ag_2S NPs. The SILAR process was repeated for different cycles (2, 4, 6, 8, and 10 cycles) to control the deposited quantity of Ag-Ag_2S NPs on the surface of ZnO NPGs. Finally, the prepared ZnO NPGs/Ag-Ag_2S NPs thin film was dried in an oven at 60 ^oC for 1 h. The prepared samples with 2, 4, 6, 8, and 10 cycles of the SILAR procedure were defined as ZnO NPGs/Ag-Ag_2S NPs (2), ZnO NPGs/Ag-Ag_2S NPs (4), ZnO NPGs/Ag-Ag_2S NPs (6), ZnO NPGs/Ag-Ag_2S NPs (8), and ZnO NPGs/Ag-Ag_2S NPs (10), respectively. **Scheme 4-1** presents the synthesis procedures of pristine ZnO NRs as well as pristine and modified ZnO NPGs with Ag-Ag_2S NPs.

4.2.2. Characterization of prepared samples

The crystal structure, microscopic and elemental investigations, and optical characteristics of all prepared samples were analyzed as illustrated previously in Chapter 2, section 2.2.2. SEM analysis was studied as explained previously in Chapter 3, section 3.2.2.

4.2.3. Photoelectrochemical measurements

The PEC performance of the prepared samples was evaluated using a biologic potentiostat (VSP-300) connected to a three-electrode PEC cell. A 300 W xenon lamp was applied as a simulated solar illumination with an air mass 1.5 global filter (AM 1.5G). The light intensity was adjusted to 1 Sun (100 mW cm^{-2}) before the PEC determinations. The three electrodes were the prepared sample (1 cm^2 illuminated area), Pt coil, Hg/HgO (1 M NaOH) as the working, the counter, and the reference electrodes, respectively submerged in 0.1 M Na_2SO_3/Na_2S electrolyte (pH = 12.49). The LSV curve was recorded with a 0.01 V/s scan rate. The electrolyte was purged with argon before each determination. The M-S curve was determined at 1000 Hz under the dark condition in 0.25 M Na_2SO_4 (pH = 6.24) using the Ag/AgCl (3 M KCl) as the reference electrode. The EIS was recorded at 10^5–10^{-2} Hz under irradiation. The ABPE was calculated from the LSV results as previously explained in Chapter 2, section 2.3.2.6. The Potential versus RHE was calculated by transforming the applied potential versus Hg/HgO and the applied potential versus Ag/AgCl as illustrated in Chapter 2, section 2.2.3.

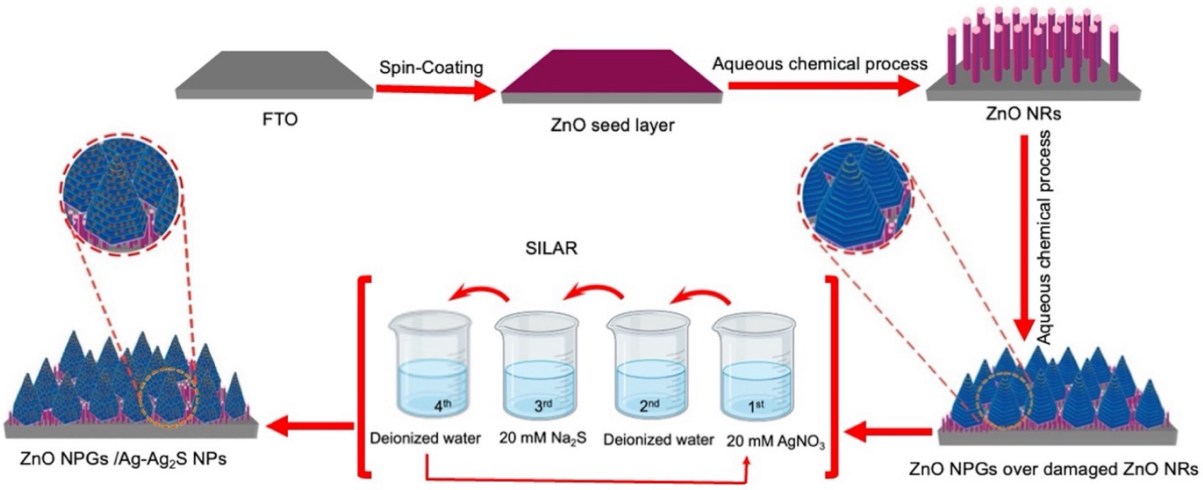

Scheme 4.1. The synthesis process of pristine ZnO NRs, pristine ZnO NPGs, and ZnO NPGs/Ag-Ag_2S NPs photoanodes.

4.3. Results and discussion

4.3.1. Characterization of pristine and modified ZnO nanopagoda arrays

The deposited amount of Ag-Ag_2S NPs on ZnO NPGs was optimized through the deposition of different SILAR cycles of Ag-Ag_2S NPs. Generally, the number of SILAR cycles influences the prepared thin films. **Figure 4-1** shows the morphology of pristine ZnO NRs, pristine ZnO NPGs, and ZnO NPGs decorated with different SILAR cycles of Ag-Ag_2S NPs. **Figure 4-1a** depicts the successful preparation of hexagonal ZnO NRs on the FTO substrate. The cross-sectional view manifested that ZnO NRs were prepared with a diameter and a length of ~ 110 nm and ~ 1.5 µm respectively (**Figure 4-1b**). The SEM image with a 30° tilt of ZnO NPGs clarified the successful preparation of ZnO NPGs in a hexagonal form (**Figure 4-1c**), with a diameter and length of ~ 470 and ~ 465 nm, respectively. Additionally, the cross-section view displayed that ZnO NPGs were grown over deformed ZnO NRs with a film thickness of ~ 1.76 µm (**Figure 4-1d**). **Figure 4-1e-n** illustrate the 30° tilt and cross-section of ZnO NPGs covered with different cycles of Ag-Ag_2S NPs. For two SILAR cycles of Ag-Ag_2S NPs, a few Ag-Ag_2S NPs were deposited on the ZnO NPGs' edges. From 4 to 8 SILAR cycles, the Ag-Ag_2S NPs coated the entire surface and edges of ZnO NPGs, making them grainy and rough. For 10 SILAR cycles, Ag-Ag_2S NPs agglomerated and coated the whole surface of ZnO NPGs. The deposited Ag-Ag_2S NPs were

in size of 20–30 nm, and the particle size raised with increasing SILAR cycles. The morphology of ZnO NPGs did not change after the deposition of Ag-Ag_2S NPs, which verifies that Ag-Ag_2S NPs can be efficiently deposited on ZnO NPGs and their edges with excellent uniformity. **Figure 4-1o** displays the EDS mapping of ZnO NPGs decorated with eight SILAR cycles of Ag-Ag_2S NPs. It also shows the EDS spectra of the Zn, O, Ag, and S peaks, manifesting the high purity of the prepared samples and confirming the existence of Ag and S elements.

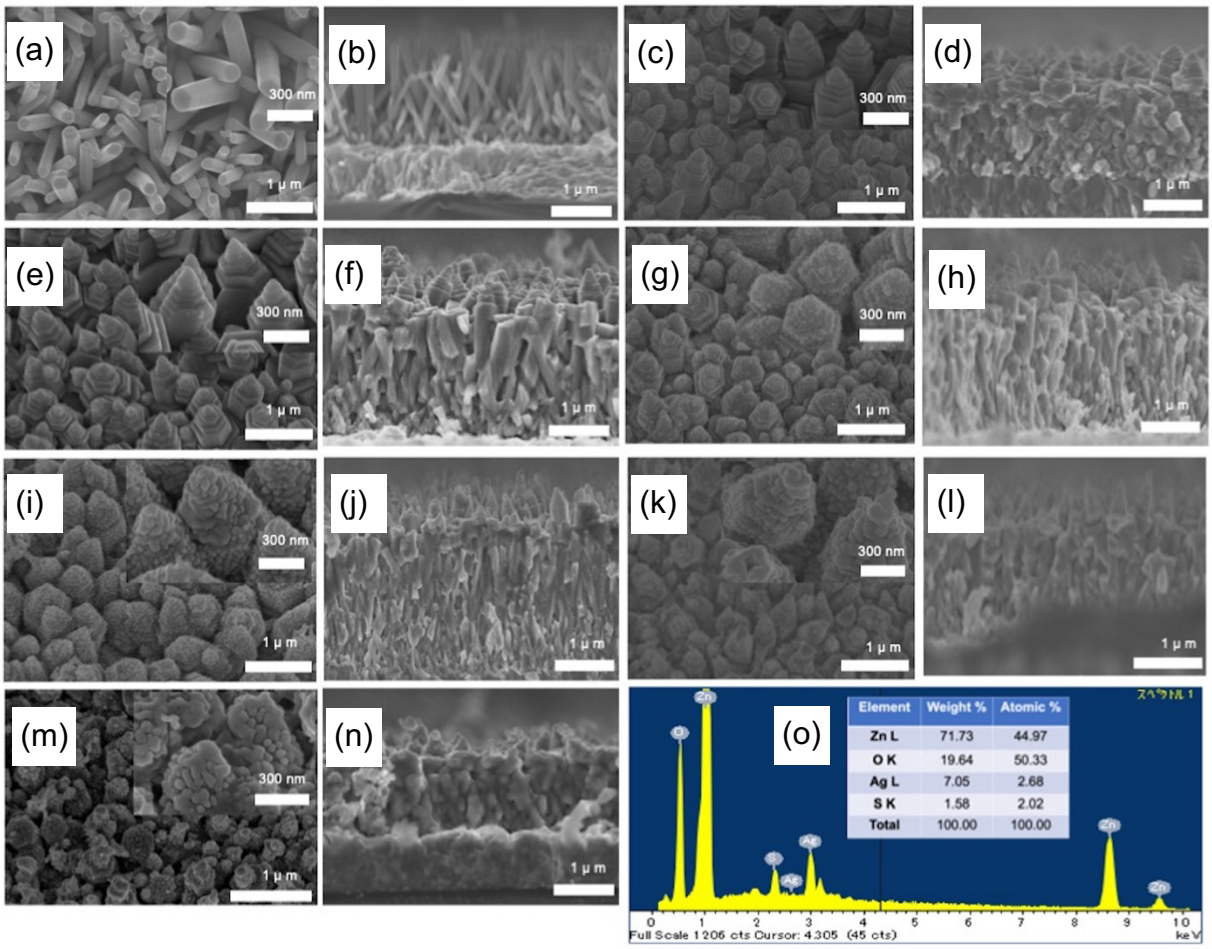

Figure 4-1. SEM images of (a) top view and (b) cross-section of ZnO NRs; 30° tilt and cross-section SEM images of (c, d) ZnO NPGs, (e, f) ZnO NPGs/Ag-Ag_2S NPs (2), (g, h) ZnO NPGs/Ag-Ag_2S NPs (4), (i, j) ZnO NPGs/Ag-Ag_2S NPs (6), (k, l) ZnO NPGs/Ag-Ag_2S NPs (8), and (m, n) ZnO NPGs/Ag-Ag_2S NPs (10) respectively, and (o) EDX mapping of ZnO NPGs/Ag-Ag_2S NPs (8).

The XRD patterns of the FTO substrate, pristine ZnO NRs, pristine ZnO NPGs, and ZnO NPGs modified with Ag-Ag_2S NPs are shown in **Figure 4-2**. The FTO substrate demonstrated characteristic peaks of the SnO_2 tetragonal structure (JCPDS no. 41-1445) [52]. The peaks of the pristine ZnO NRs and ZnO NPGs are assigned to the hexagonal wurtzite crystal structure (JCPDS, 36–1451) [48,53] in addition to SnO_2. Regarding ZnO NPGs modified with Ag-Ag_2S NPs, there were no distinctive diffraction peaks associated with Ag and S, which may be owing to the low loaded amount or small crystal size of Ag-Ag_2S NPs [54].

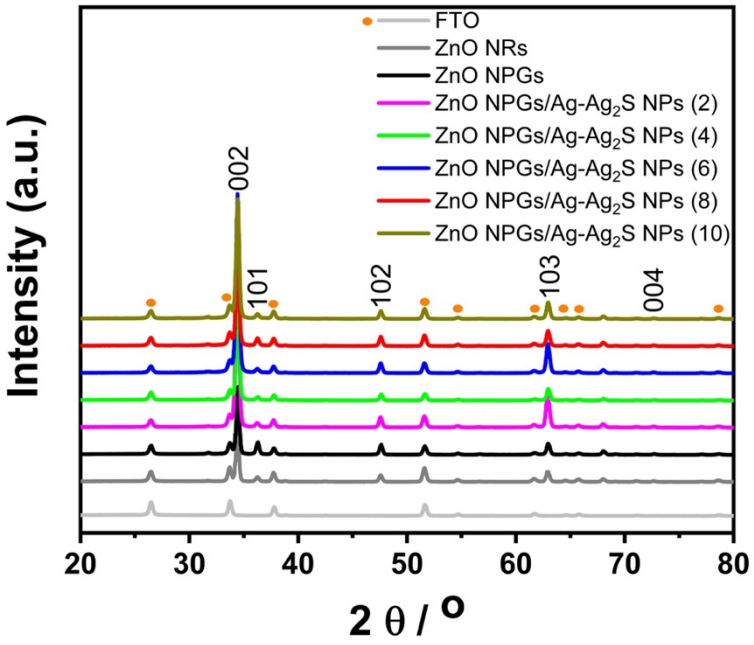

Figure 4-2. XRD patterns of FTO, pristine ZnO NRs, pristine ZnO NPGs, and ZnO NPGs modified with Ag-Ag_2S NPs.

The ZnO NPGs/Ag-Ag_2S NPs (8) was analyzed using STEM-EDX (**Figure 4-3a–d**). it was noted that there are two ZnO NPGs whose surfaces are modified by the SILAR procedure (**Figure 4-1k**). The NPs with diameters of 20 nm or larger deposited on the ZnO NPGs surface include almost only Ag element (see white arrows in panel **Figure 4-3 d**), while various smaller NPs include Ag and S elements (see black arrows in panel **Figure 4-3 d**). This verified that Ag and Ag_2S NPs were both deposited on the ZnO NPGs surface using the SILAR process. To approve the formation of Ag and Ag_2S crystals, HR-TEM was used. The HR-TEM images in **Figure 4-3 e,f** depicts two sorts of fringes with d-spacings of 0.31 and 0.28 nm, assigned to the (111) and (-112) facets of Ag_2S [55,56]. This confirmed the crystal formation of Ag_2S. Whereas, no clear

fringes of Ag crystal were noted, probably because Ag_2S is formed on the surface of Ag NPs in the final SILAR procedure, which involves immersion of the sample into the Na_2S solution; therefore, only unidentifiable blurry images were gained from large NPs.

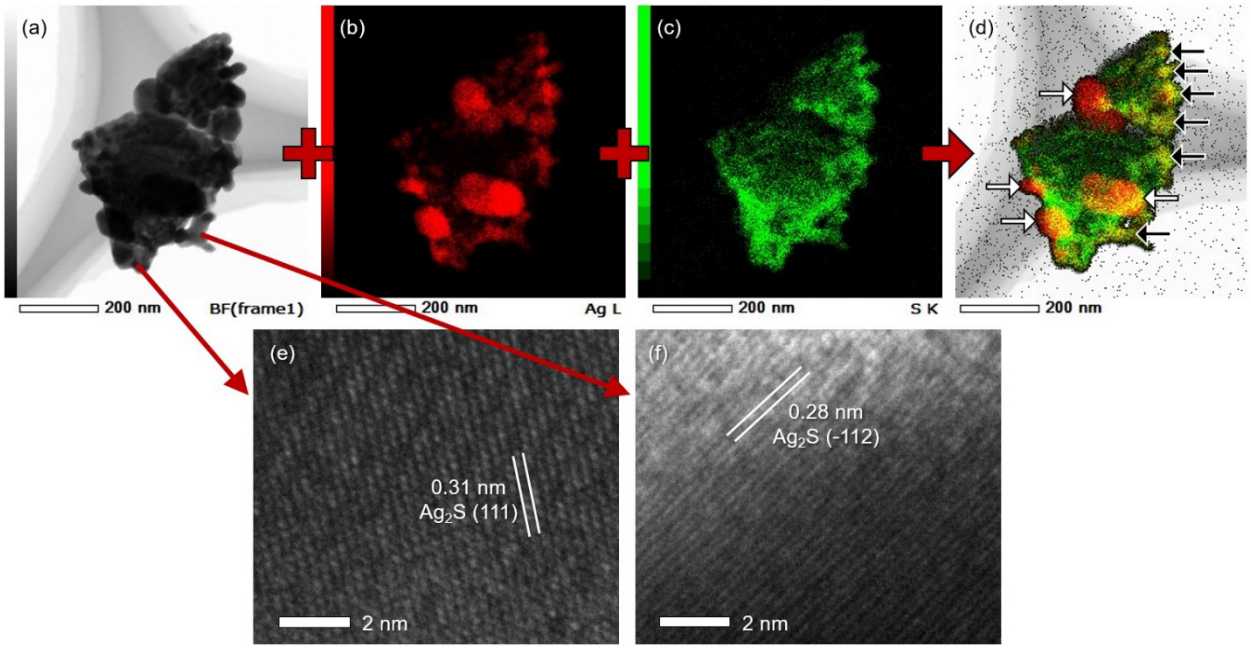

Figure 4-3. (a–c) STEM-EDX images of ZnO NPGs modified with 8 SILAR cycles. (d) Overlapped image created using (a–c). (e and f) HR-TEM images of areas including both Ag and S elements.

The comprehensive elemental examination of ZnO NPGs/Ag-Ag_2S NPs (8) was performed by XPS to investigate the surface chemical composition and electronic states. The characteristic peaks of Zn, O, Ag, and S elements were noted without any impurities (**Figure 4-4a**). The high-resolution XPS spectrum of Zn 2p is depicted in **Figure 4-4b**, indicating that the binding energy of Zn 2p was split into $2p_{½}$ and $2p_{3/2}$ peaks at 1,045 eV and 1,022 eV, respectively. The two split peaks were separated with 23 eV, verifying that the Zn (II) oxidation state exists in the hexagonal wurtzite structure [57,58]. The narrow XPS spectrum of O1s is shown in **Figure 4-4c**. The O1s peak split into two peaks at 531.0 eV and 530.4 eV, assigned to the OH group and lattice oxygen existent in ZnO, respectively [59]. **Figure 4-4d** illustrates that Ag 3d manifested four peaks at 374.7 eV, 374.3 eV, 368.7 eV, and 368.3 eV. Peaks at 368.3 eV and 374.3 eV are assigned to the metallic Ag, while peaks at 368.7 eV and 374.7 eV correspond to the monovalent oxidation state

of Ag in Ag_2S [60]. **Figure 4-4e** shows that S 2p exhibited two peaks of S $2p_{1/2}$ and $2p_{3/2}$ at 161.97 eV and 160.98 eV, respectively, which attributed to the S ions in Ag_2S [59]. Hence, the XPS results approved the deposition of both Ag and Ag_2S NPs on ZnO NPGs.

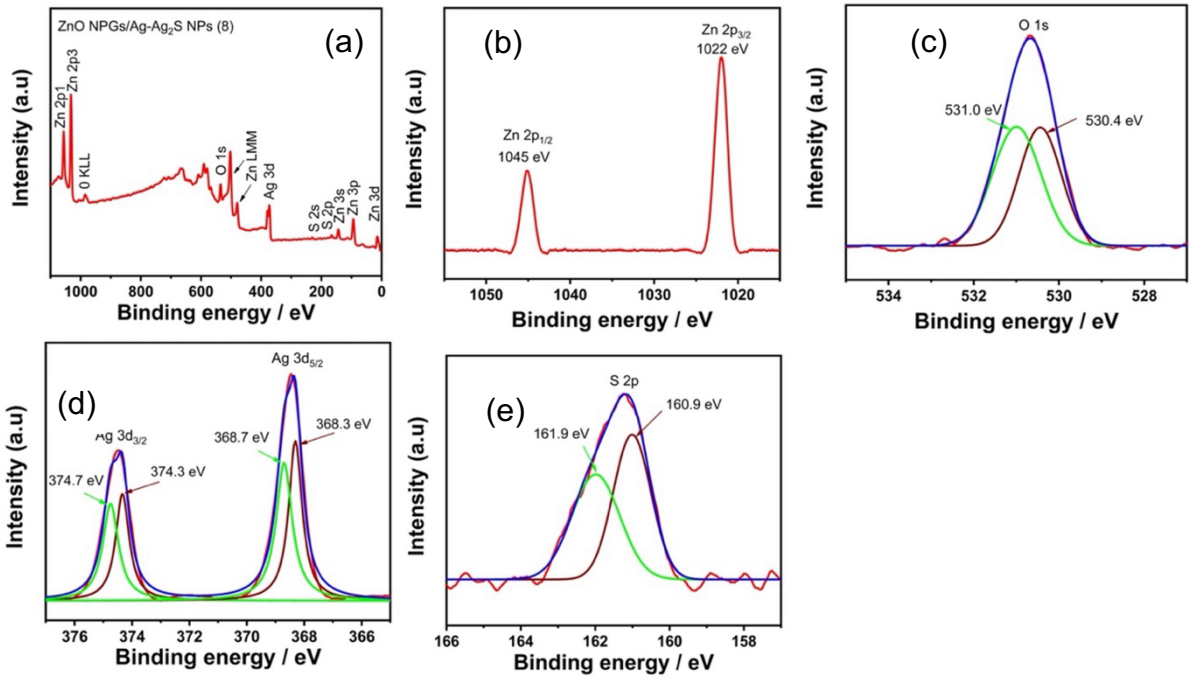

Figure 4-4. The XPS spectra of ZnO NPGs/Ag-Ag_2S NPs (8): (a) survey, (b) Zn 2p, (c) O 1s, (d) Ag 3d, and (e) S 2p.

The determined UV–Vis spectra and estimated bandgap energy of pristine ZnO NPGs and ZnO NPGs/Ag-Ag_2S NPs are depicted in **Figure 4-5**. The pristine ZnO NPGs have UV absorbance owing to their wide bandgap energy. Additionally, all samples of ZnO NPGs decorated with different SILAR cycles of Ag-Ag_2S NPs boosted Vis light absorption, probably because of the LSPR of Ag NPs [61,62] and the narrow bandgap energy of Ag_2S [63,64] (**Figure 4-5a**). This revealed that the heterojunction between ZnO NPGs and Ag-Ag_2S NPs improved the Vis light absorption ability. The bandgap energies of as-prepared samples were calculated utilizing Tauc's equation [65]:

$$(\alpha h\nu) = B(h\nu - E_g)^{1/2}, \qquad \text{(Eq. 4-1)}$$

where α is the absorption coefficient, $h\nu$ is the photon energy, B is a constant, and E_g is the bandgap energy. Pristine ZnO NPGs displayed bandgap energy of 3.30 eV, and after the deposition of 8 SILAR cycles of Ag-Ag_2S NPs, this value was reduced (**Figure 4-5b**). This reduction proved that

the deposition of Ag-Ag_2S NPs contributes significantly to increasing optical absorption in the longer wavelength range.

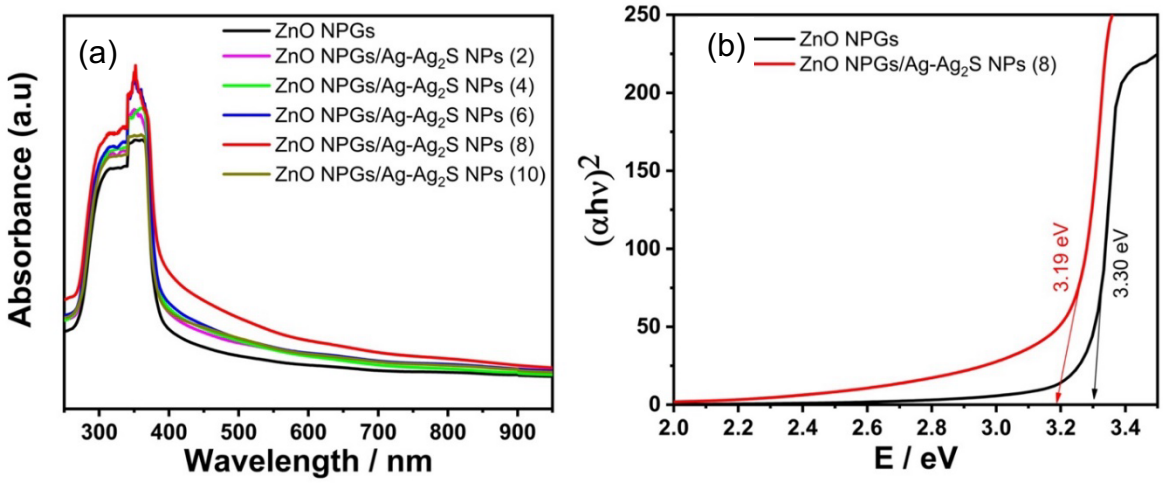

Figure 4-5. (a) UV–Vis optical absorption spectra of pristine ZnO NPGs and modified samples with different SILAR cycles of Ag-Ag_2S NPs. (b) The Tauc plots of pristine ZnO NPGs and ZnO NPGs/Ag-Ag_2S NPs (8).

4.3.2. Photoelectrochemical performance

4.3.2.1. Linear sweep voltammetry

The LSV curves (**Figure 4-6a**) show the current density of all the studied photoanodes under dark (dotted line) and light irradiation (solid lines). Pristine ZnO NRs and ZnO NPGs demonstrated small photocurrent densities of 0.38 and 0.57 mA cm^{-2}, respectively, at 1.23 V vs. RHE, while the deposition of Ag-Ag_2S NPs on ZnO NPGs remarkably boosted the photocurrent density. ZnO NPGs/Ag-Ag_2S NPs (8) demonstrated the maximum photocurrent density of 2.91 mA cm^{-2} at 1.23 V vs. RHE. This remarkably developed photocurrent can be ascribed to the LSPR effect of Ag NPs, improved Vis light absorption via sensitization with Ag_2S NPs, and ameliorated e^-/h^+ pairs separation that inhibited the rate of charge recombination [64]. SILAR cycles more than eight cycles ((e.g., 10) exhibited a reduction in the photocurrent, ascribed to the deposition of a thick layer of Ag-Ag_2S NPs on the surface of ZnO NPGs causing the increased charge carrier recombination [66]. **Table 4-1** presents the current densities of all photoanodes under dark/irradiation conditions. The transient photocurrent response of bare ZnO NPGs (**Figure 4-6b**) and ZnO NPGs/Ag-Ag_2S NPs (8) (**Figure 4-6c**) was recorded during various on/off runs. As anticipated, ZnO NPGs/Ag-Ag_2S NPs (8) attained higher photocurrent response than pristine ZnO NPGs. It is also noted that the stability of ZnO NPGs/Ag-Ag_2S NPs (8) was decreased with

prolonged determination time. Therefore, it was obvious that the heterojunction of ZnO NPGs and Ag-Ag_2S NPs facilitated interfacial charge mobility and so remarkably inhibited charge recombination in the ZnO NPGs/Ag-Ag_2S NPs photoanode.

4.3.2.2. Electrochemical impedance spectroscopy

The EIS of pristine ZnO NPGs and ZnO NPGs/Ag-Ag_2S NPs (8) were determined in 0.1 M Na_2S/Na_2SO_3 electrolyte under light irradiation, as shown by the Nyquist plot (**Figure 4-6d**) involving the equivalent circuit models. The Nyquist plot can provide information about the conductivity and charge transfer resistance [67]. It can offer qualitative data about the charge transfer in bulk and at the interface of the photoanode. ZnO NPGs/Ag-Ag_2S NPs (8) displayed a smaller arc diameter than pristine ZnO NPGs, verifying the decrease in the charge transfer resistance (R_2 in the equivalent circuits). The values of R_2 were estimated as about 582 and 478 Ω for pristine ZnO NPGs and ZnO NPGs/Ag-Ag_2S NPs (8), respectively. The lower R_{ct} value of ZnO NPGs/Ag-Ag_2S NPs (8) affirmed higher conductivity and fast interfacial charge transfer, which improved the PEC performance. Additionally, this confirmed that the heterojunction construction among ZnO NPGs and Ag-Ag_2S NPs ameliorated charge mobility and reduced the rate of e^-/h^+ pairs recombination.

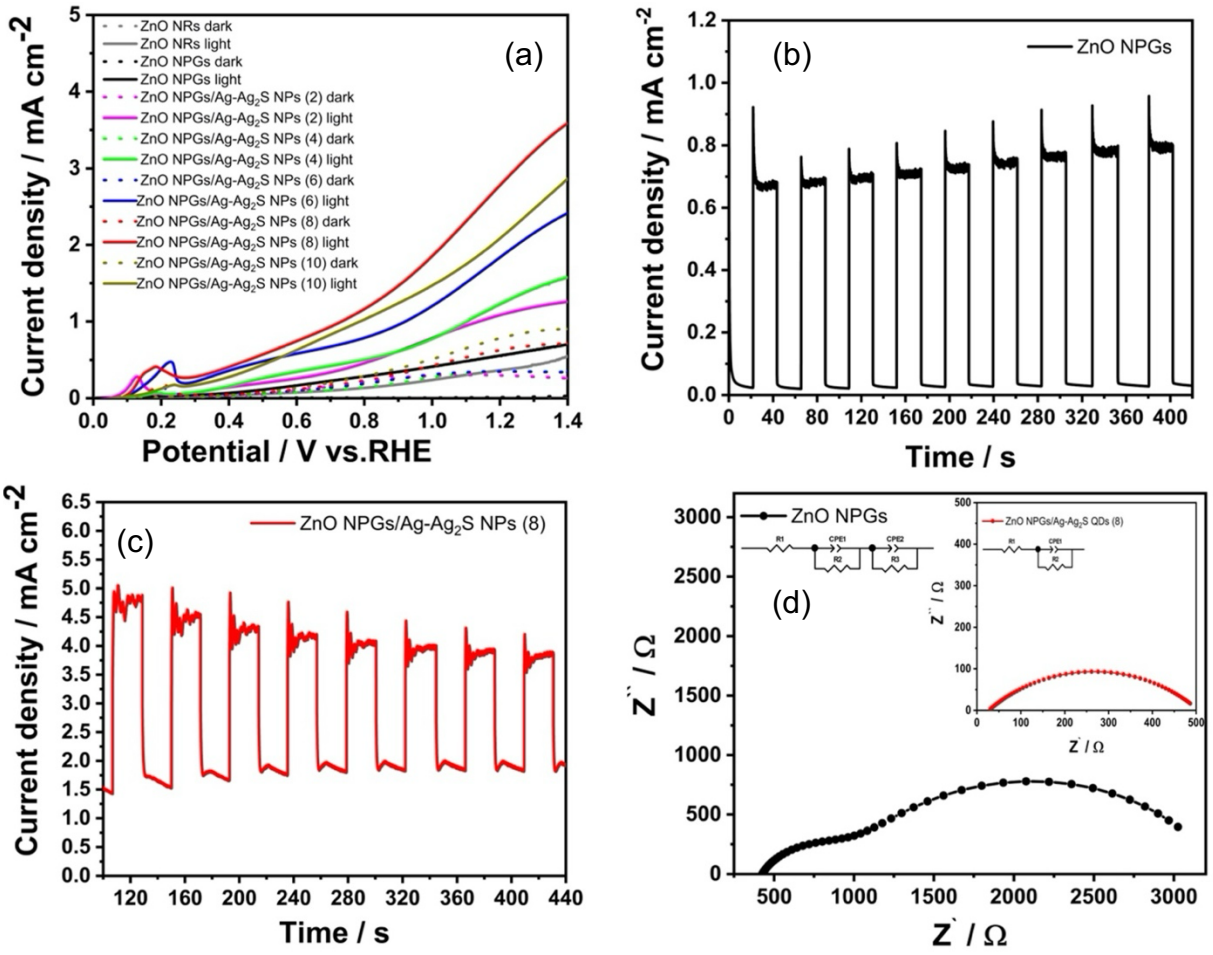

Figure 4-6. (a) LSV curves of all studied photoanodes under dark/irradiation conditions. Transient photocurrent responses of (b) pristine ZnO NPGs and (c) ZnO NPGs/Ag-Ag_2S NPs (8). (d) EIS curves of pristine ZnO NPGs and ZnO NPGs/Ag-Ag_2S NPs (8).

Table 4-1. The current density of all the studied photoanodes under dark/irradiation conditions at 1.23 V vs. RHE.

Photoanode	I / mA cm^{-2} (absence of light)	I / mA cm^{-2} (presence of light)
ZnO NRs	0.01	0.38
ZnO NPGs	0.01	0.57
ZnO NPGs/Ag-Ag_2S NPs (2)	0.34	1.11
ZnO NPGs/Ag-Ag_2S NPs (4)	0.34	1.28
ZnO NPGs/Ag-Ag_2S NPs (6)	0.34	1.93
ZnO NPGs/Ag-Ag_2S NPs (8)	0.64	2.91
ZnO NPGs/Ag-Ag_2S NPs (10)	0.81	2.20

4.3.2.3. Mott–Schottky

The M-S curves of pristine ZnO NPGs and ZnO NPGs/Ag-Ag_2S NPs (8) were determined to investigate their charge carrier density and E_{fb} (**Figure 4- 7a**). The two samples displayed positive slopes indicating n-type semiconductor photoelectrodes, which revealed that electrons were the major carriers. The E_{fb} displayed a negative shift after Ag-Ag_2S NPs deposition which confirmed the upward band bending at the semiconductor/electrolyte interface, resulting in improving the e^-/h^+ pairs separation and mobility, followed by inhibiting their recombination [9].

4.3.2.4. Photoconversion efficiency

The ABPE plots in **Figure 4-7b** depicted that ZnO NPGs exhibited 0.11% photoconversion efficiency at 0.7 V vs. RHE, while the decoration of ZnO NPGs with eight SILAR cycles of Ag-Ag_2S NPs enhanced the ABPE to 0.43% at 0.6 V vs. RHE. The boosted ABPE of ZnO NPGs/Ag-Ag_2S NPs (8) was ascribed to the enhanced Vis light absorption and the construction of type II heterojunction between ZnO NPGs and Ag-Ag_2S NPs resulting in facilitated e^-/h^+ pairs separation and mobility.

4.4. Photoelectrochemical reaction mechanism

To understand the mechanism of improved PEC performance using ZnO NPGs/Ag-Ag_2S NPs photoanode, it is important to study the charge transfer mechanism (**Figure 4-7c**). Under UV–

Vis irradiation, ZnO NPGs absorb UV light, while Ag_2S NPs absorb Vis light followed by the photogeneration of electrons and holes in ZnO NPGs and Ag_2S NPs. Ag NPs also absorb Vis light through the LSPR effect and photogenerate hot electrons, which migrate to the CB of ZnO NPGs [68]. The CB of Ag_2S is more negative than the CB of ZnO, while the VB of ZnO is more positive than the VB of Ag_2S [38]. When ZnO, Ag NPs, and Ag_2S NPs combine and form a heterojunction, under light irradiation, electrons transfer from Ag_2S's CB to Ag and then drift to ZnO's CB. Then, these electrons transport to the FTO substrate and finally to the counter electrode to make reduction of water and produce H_2. While the holes formed in ZnO NPGs' VB migrate to the Ag_2S's VB and then interact with Na_2SO_3/Na_2S electrolyte. This opposite-direction charge transfer mitigated the e^-/h^+ pairs recombination. Thus, the improved PEC performance of ZnO NPGs/Ag-Ag_2S NPs photoanodes can be attributed to; (1) the LSPR effect of Ag NPs, (2) the enhanced Vis light absorption after Ag_2S NPs deposition, and (3) the formation of type II heterojunction between ZnO NPGs and Ag-Ag_2S NPs that significantly ameliorated e^-/h^+ pairs separation and inhibited their recombination.

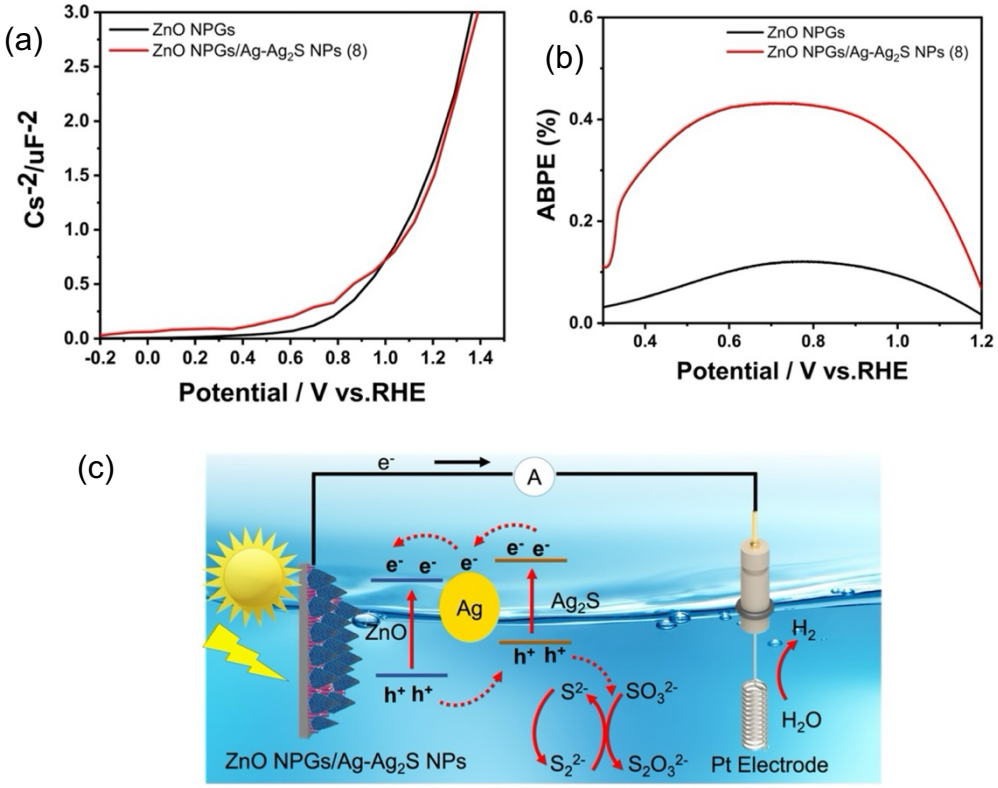

Figure 4-7. (a) Mott–Schottky curves and (b) ABPE of pristine ZnO NPGs and ZnO NPGs/Ag-Ag_2S NPs (8). (c) Charge transfer mechanism in ZnO NPGs/Ag-Ag_2S NPs photoanode.

4.5. Conclusions

The unique morphology of ZnO NPGs was successfully fabricated utilizing an aqueous chemical downward process. ZnO NPGs were decorated with different quantities of Ag-Ag_2S NPs utilizing the SILAR procedure. The morphological investigation revealed that the deposited quantity of Ag-Ag_2S NPs on the surface of ZnO NPGs raised with the number of SILAR cycles and covered the whole ZnO NPGs' surface and edges, keeping them grainy and rough. The deposited quantity of Ag-Ag_2S NPs on ZnO NPGs considerably affected the PEC performance. The deposition of 8 SILAR cycles of Ag-Ag_2S NPs on ZnO NPGs displayed the maximum photocurrent of 2.91 mA cm^{-2} at 1.23 V vs. RHE, five folds greater than pristine ZnO NPGs. Moreover, it attained the highest ABPE of 0.43% at 0.6 V vs. RHE. This remarkably improved PEC efficiency was attributed to the vital role of co-deposited Ag and Ag_2S NPs, which synergistically increased Vis light absorption and ameliorated e^-/h^+ pairs separation that inhibited their recombination.

References

[1] X. Wu, H. Fan, W. Wang, L. Lei, X. Chang, Ordered and Ultralong Graphitic Carbon Nitride Nanotubes Obtained via In-Air CVD for Enhanced Photocatalytic Hydrogen Evolution, ACS Appl Energy Mater 4 (2021) 13263–13271. https://doi.org/10.1021/acsaem.1c02846.

[2] Z. Masoumi, M. Tayebi, B.-K. Lee, The role of doping molybdenum (Mo) and back-front side illumination in enhancing the charge separation of α-Fe_2O_3 nanorod photoanode for solar water splitting, Solar Energy 205 (2020) 126–134. https://doi.org/10.1016/j.solener.2020.05.044.

[3] B. Zhang, L. Wang, Y. Zhang, Y. Ding, Y. Bi, Ultrathin FeOOH Nanolayers with Abundant Oxygen Vacancies on $BiVO_4$ Photoanodes for Efficient Water Oxidation, Angewandte Chemie International Edition 57 (2018) 2248–2252. https://doi.org/10.1002/anie.201712499.

[4] M. Mohamed Abouelela, G. Kawamura, A. Matsuda, Metal chalcogenide-based photoelectrodes for photoelectrochemical water splitting, Journal of Energy Chemistry 73 (2022) 189–213. https://doi.org/10.1016/j.jechem.2022.05.022.

[5] M. Farahi, F. Fathirad, T. Shamspur, A. Mostafavi, A novel Z-scheme heterojunction g-C_3N_4/WS_2@rGONR$_{(x)}$ nanocomposite for efficient photoelectrochemical water splitting, Mater Chem Phys 293 (2023) 126941. https://doi.org/10.1016/j.matchemphys.2022.126941.

[6] T. Li, Y. Zou, Z. Liu, Magnetic-thermal external field activate the pyro-magnetic effect of pyroelectric crystal ($NaNbO_3$) to build a promising multi-field coupling-assisted photoelectrochemical water splitting system, Appl Catal B 328 (2023) 122486. https://doi.org/10.1016/j.apcatb.2023.122486.

[7] T. Li, M. Ruan, Z. Guo, C. Wang, Z. Liu, Modulation of Lewis and Brønsted Acidic Sites to Enhance the Redox Ability of Nb_2O_5 Photoanodes for Efficient Photoelectrochemical Performance, ACS Appl Mater Interfaces 15 (2023) 11914–11926. https://doi.org/10.1021/acsami.2c23284.

[8] T.W. Kim, Y. Ping, G.A. Galli, K.-S. Choi, Simultaneous enhancements in photon absorption and charge transport of bismuth vanadate photoanodes for solar water splitting, Nat Commun 6 (2015) 8769. https://doi.org/10.1038/ncomms9769.

[9] J. Yadav, J.P. Singh, WO_3/Ag_2S type-II hierarchical heterojunction for improved charge carrier separation and photoelectrochemical water splitting performance, J Alloys Compd 925 (2022) 166684. https://doi.org/10.1016/j.jallcom.2022.166684.

[10] P. Lianos, Review of recent trends in photoelectrocatalytic conversion of solar energy to electricity and hydrogen, Appl Catal B 210 (2017) 235–254. https://doi.org/10.1016/j.apcatb.2017.03.067.

[11] C. Ma, Z. Liu, Q. Cai, C. Han, Z. Tong, ZnO photoelectrode simultaneously modified with Cu_2O and Co-Pi based on broader light absorption and efficiently photogenerated carrier separation, Inorg Chem Front 5 (2018) 2571–2578. https://doi.org/10.1039/C8QI00596F.

[12] S. Wang, P. Liu, C. Meng, Y. Wang, L. Zhang, L. Pan, Z. Yin, N. Tang, J.-J. Zou, Boosting photoelectrochemical water splitting by Au@Pt modified ZnO/CdS with synergy of Au-S bonds and surface plasmon resonance, J Catal 408 (2022) 196–205. https://doi.org/10.1016/j.jcat.2022.03.003.

[13] S. Zhang, Z. Liu, M. Ruan, Z. Guo, L. E, W. Zhao, D. Zhao, X. Wu, D. Chen, Enhanced piezoelectric-effect-assisted photoelectrochemical performance in ZnO modified with dual cocatalysts, Appl Catal B 262 (2020) 118279. https://doi.org/10.1016/j.apcatb.2019.118279.

[14] J. Lin, X. Han, S. Liu, Y. Lv, X. Li, Y. Zhao, Y. Li, L. Wang, S. Zhu, Nitrogen-doped cobalt-iron oxide cocatalyst boosting photoelectrochemical water splitting of $BiVO_4$ photoanodes, Appl Catal B 320 (2023) 121947. https://doi.org/10.1016/j.apcatb.2022.121947.

[15] Z. Zhou, J. Chen, Q. Wang, X. Jiang, Y. Shen, Enhanced photoelectrochemical water splitting using a cobalt-sulfide-decorated $BiVO_4$ photoanode, Chinese Journal of Catalysis 43 (2022) 433–441. https://doi.org/10.1016/S1872-2067(21)63845-7.

[16] V. Madhavi, P. Kondaiah, H. Shaik, K.N. Kumar, T.S.S. Kumar Naik, G.M. Rao, P.C. Ramamurthy, Fabrication of porous 1D WO_3 NRs and $WO_3/BiVO_4$ hetero junction photoanode for efficient photoelectrochemical water splitting, Mater Chem Phys 274 (2021) 125095. https://doi.org/10.1016/j.matchemphys.2021.125095.

[17] J. Xiao, C. Li, X. Jia, B. Du, R. Li, B. Wang, Enabling high low-bias performance of Fe_2O_3 photoanode for photoelectrochemical water splitting, J Colloid Interface Sci 633 (2023) 555–565. https://doi.org/10.1016/j.jcis.2022.11.134.

[18] X. Zhang, S. Zhang, X. Cui, W. Zhou, W. Cao, D. Cheng, Y. Sun, Recent Advances in TiO_2-based Photoanodes for Photoelectrochemical Water Splitting, Chem Asian J 17 (2022). https://doi.org/10.1002/asia.202200668.

[19] N. Khatun, S. Dey, G.C. Behera, S.C. Roy, Ti_3C_2T MXene functionalization induced enhancement of photoelectrochemical performance of TiO_2 nanotube arrays, Mater Chem Phys 278 (2022) 125651. https://doi.org/10.1016/j.matchemphys.2021.125651.

[20] Y. Li, Q. Mei, Z. Liu, X. Hu, Z. Zhou, J. Huang, B. Bai, H. Liu, F. Ding, Q. Wang, Fluorine-doped iron oxyhydroxide cocatalyst: promotion on the WO_3 photoanode conducted photoelectrochemical water splitting, Appl Catal B 304 (2022) 120995. https://doi.org/10.1016/j.apcatb.2021.120995.

[21] M.M. Abouelela, G. Kawamura, W.K. Tan, A. Matsuda, Anodic nanoporous WO_3 modified with Bi2S3 quantum dots as a photoanode for photoelectrochemical water splitting, J Colloid Interface Sci 629 (2023) 958–970. https://doi.org/10.1016/j.jcis.2022.09.041.

[22] Y. Li, Z. Liu, Z. Guo, M. Ruan, X. Li, Y. Liu, Efficient WO_3 Photoanode Modified by Pt Layer and Plasmonic Ag for Enhanced Charge Separation and Transfer To Promote Photoelectrochemical Performances, ACS Sustain Chem Eng (2019) acssuschemeng.9b02450. https://doi.org/10.1021/acssuschemeng.9b02450.

[23] X. Xie, R. Wang, Y. Ma, J. Chen, Z. Shi, Q. Cui, Z. Li, C. Xu, Sulfate-Functionalized Core–Shell ZnO/CdS/Ag_2 S Nanorod Arrays with Dual-Charge-Transfer Channels for Enhanced Photoelectrochemical Performance, ACS Appl Energy Mater 5 (2022) 6228–6237. https://doi.org/10.1021/acsaem.2c00608.

[24] Z. Kang, H. Si, S. Zhang, J. Wu, Y. Sun, Q. Liao, Z. Zhang, Y. Zhang, Interface Engineering for Modulation of Charge Carrier Behavior in ZnO Photoelectrochemical Water Splitting, Adv Funct Mater 29 (2019) 1808032. https://doi.org/10.1002/adfm.201808032.

[25] S. Banerjee, S. Padhan, R. Thangavel, Dopant inculcated ZnO based photoelectrodes for revitalizing photoelectrochemical water splitting, Mater Chem Phys 277 (2022) 125548. https://doi.org/10.1016/j.matchemphys.2021.125548.

[26] H. Han, F. Karlicky, S. Pitchaimuthu, S.H.R. Shin, A. Chen, Highly Ordered N-Doped Carbon Dots Photosensitizer on Metal–Organic Framework-Decorated ZnO Nanotubes for Improved Photoelectrochemical Water Splitting, Small 15 (2019) 1902771. https://doi.org/10.1002/smll.201902771.

[27] X. Long, C. Wang, S. Wei, T. Wang, J. Jin, J. Ma, Layered Double Hydroxide onto Perovskite Oxide-Decorated ZnO Nanorods for Modulation of Carrier Transfer Behavior in Photoelectrochemical Water Oxidation, ACS Appl Mater Interfaces 12 (2020) 2452–2459. https://doi.org/10.1021/acsami.9b17965.

[28] M. Kolaei, M. Tayebi, Z. Masoumi, B.-K. Lee, A novel approach for improving photoelectrochemical water splitting performance of ZnO-CdS photoanodes: Unveiling the effect of surface roughness of ZnO nanorods on distribution of CdS nanoparticles, J Alloys Compd 906 (2022) 164314. https://doi.org/10.1016/j.jallcom.2022.164314.

[29] A.P. Yengantiwar, M.S. Deo, A.D. Sheikh, $ZnFe_2O_4$/ZnO 0D-1D heterojunction for efficient photoelectrochemical water splitting, Materials Science and Engineering: B 284 (2022) 115854. https://doi.org/10.1016/j.mseb.2022.115854.

[30] Z. Masoumi, M. Tayebi, M. Kolaei, B.-K. Lee, Improvement of surface light absorption of ZnO photoanode using a double heterojunction with α–Fe_2O_3/g–C_3N_4 composite to enhance photoelectrochemical water splitting, Appl Surf Sci 608 (2023) 154915. https://doi.org/10.1016/j.apsusc.2022.154915.

[31] P.-Y. Kuang, X.-J. Zheng, J. Lin, X.-B. Huang, N. Li, X. Li, Z.-Q. Liu, Facile Construction of Dual p–n Junctions in CdS/Cu_2 O/ZnO Photoanode with Enhanced Charge Carrier Separation and Transfer Ability, ACS Omega 2 (2017) 852–863. https://doi.org/10.1021/acsomega.6b00507.

[32] S.I. Sadovnikov, A.I. Gusev, Recent progress in nanostructured silver sulfide: from synthesis and nonstoichiometry to properties, J Mater Chem A Mater 5 (2017) 17676–17704. https://doi.org/10.1039/C7TA04949H.

[33] S. Shuang, R. Lv, X. Cui, Z. Xie, J. Zheng, Z. Zhang, Efficient photocatalysis with graphene oxide/Ag/Ag_2S–TiO_2 nanocomposites under visible light irradiation, RSC Adv 8 (2018) 5784–5791. https://doi.org/10.1039/C7RA13501G.

[34] T. ben Nasrallah, H. Dlala, M. Amlouk, S. Belgacem, J.C. Bernède, Some physical investigations on Ag_2S thin films prepared by sequential thermal evaporation, Synth Met 151 (2005) 225–230. https://doi.org/10.1016/j.synthmet.2005.05.005.

[35] J. Xue, J. Liu, Y. Liu, H. Li, Y. Wang, D. Sun, W. Wang, L. Huang, J. Tang, Recent advances in synthetic methods and applications of Ag_2S-based heterostructure photocatalysts, J Mater Chem C Mater 7 (2019) 3988–4003. https://doi.org/10.1039/C9TC00008A.

[36] D. Solís-Cortés, F.M. Jiménez, G. Jauregui, D. Gau, J. Pereyra, R. Henríquez, R.E. Marotti, J.R. Ramos-Barrado, E.A. Dalchiele, Optimization of Ag_2S Quantum Dots Decorated ZnO Nanorod Array Photoanodes for Enhanced Photoelectrochemical Performances, J Electrochem Soc 168 (2021) 056516. https://doi.org/10.1149/1945-7111/ac001a.

[37] Y.-C. Chen, H.-T. Kuo, R. Popescu, Y.-K. Hsu, Ultralow–biased solar photoelectrochemical hydrogen generation by Ag_2S/ZnO heterojunction with high efficiency, J Taiwan Inst Chem Eng 140 (2022) 104554. https://doi.org/10.1016/j.jtice.2022.104554.

[38] A.A. Al-Zahrani, Z. Zainal, Z.A. Talib, H.N. Lim, A.M. Holi, N.N. Bahrudin, Enhanced photoelectrochemical performance of Bi_2S_3/Ag_2S/ZnO novel ternary heterostructure nanorods, Arabian Journal of Chemistry 13 (2020) 9166–9178. https://doi.org/10.1016/j.arabjc.2020.10.040.

[39] Y. Lan, Z. Liu, G. Liu, Z. Guo, M. Ruan, H. Rong, X. Li, 1D $ZnFe_2O_4$ nanorods coupled with plasmonic Ag, Ag_2S nanoparticles and Co-Pi cocatalysts for efficient

photoelectrochemical water splitting, Int J Hydrogen Energy 44 (2019) 19841–19854. https://doi.org/10.1016/j.ijhydene.2019.05.184.
[40] M.Z. Toe, A.T. Le, S.S. Han, K.A.B. Yaacob, S.-Y. Pung, Silver nanoparticles coupled ZnO nanorods array prepared using photo-reduction method for localized surface plasmonic effect study, J Cryst Growth 547 (2020) 125806. https://doi.org/10.1016/j.jcrysgro.2020.125806.
[41] Y. Liu, N. Jiang, M. Lyu, J. Wei, G. Wei, X. Han, Q. Shang, Q. Zhang, Y. Liu, H. Liu, X. Shi, TiO_2/black phosphorus heterojunction modified by Ag nanoparticles for efficient photoelectrochemical water splitting, Mater Chem Phys 301 (2023) 127624. https://doi.org/10.1016/j.matchemphys.2023.127624.
[42] M.M. Abouelela, G. Kawamura, W.K. Tan, M. Amiruldin, K. Maegawa, J. Nishida, A. Matsuda, Ag nanoparticles decorated ZnO nanopagodas for Photoelectrochemical application, Electrochem Commun 158 (2024) 107645. https://doi.org/10.1016/j.elecom.2023.107645.
[43] M.M. Abouelela, G. Kawamura, A. Matsuda, A review on plasmonic nanoparticle-semiconductor photocatalysts for water splitting, J Clean Prod 294 (2021) 126200. https://doi.org/10.1016/j.jclepro.2021.126200.
[44] P. Subramanyam, B. Meena, V. Biju, H. Misawa, S. Challapalli, Emerging materials for plasmon-assisted photoelectrochemical water splitting, Journal of Photochemistry and Photobiology C: Photochemistry Reviews 51 (2022) 100472. https://doi.org/10.1016/j.jphotochemrev.2021.100472.
[45] P. Peerakiatkhajohn, J.-H. Yun, T. Butburee, W. Nisspa, S. Thaweesak, Surface plasmon-driven photoelectrochemical water splitting of a Ag/TiO_2 nanoplate photoanode, RSC Adv 12 (2022) 2652–2661. https://doi.org/10.1039/D1RA09070D.
[46] Ch.V. Reddy, I.N. Reddy, A. Sreedhar, J. Shim, Investigation of dopant and Ag plasmonic effect on α-Fe_2O_3 photoelectrode for photoelectrochemical water splitting activity, Appl Surf Sci 488 (2019) 629–638. https://doi.org/10.1016/j.apsusc.2019.05.316.
[47] S. Qi, Z. Yin, Z. Liu, K. Xu, M. Zhang, Z. Sun, Construction of In_2S_3/Ag-Ag_2 S-$AgInS_2$ /TNR Nanoarrays with Excellent Photoelectrochemical and Photocatalytic Properties, J Electrochem Soc 168 (2021) 126517. https://doi.org/10.1149/1945-7111/ac4056.
[48] I.-C. Yao, P. Lin, T.-Y. Tseng, Field Emission Properties and Reliability of ZnO Nanorod, Nanopagoda, and Nanotip Current Emitters, IEEE Trans Nanotechnol 11 (2012) 746–750. https://doi.org/10.1109/TNANO.2012.2195502.
[49] H.-M. Chiu, J.-M. Wu, Opto-electrical properties and chemisorption reactivity of Ga-doped ZnO nanopagodas, J Mater Chem A Mater 1 (2013) 5524. https://doi.org/10.1039/c3ta01209c.
[50] W. Li, S. Gao, L. Li, S. Jiao, H. Li, J. Wang, Q. Yu, Y. Zhang, D. Wang, L. Zhao, Hydrothermal synthesis of a 3D double-sided comb-like ZnO nanostructure and its growth mechanism analysis, Chemical Communications 52 (2016) 8231–8234. https://doi.org/10.1039/C6CC02072K.
[51] M.A. Desai, A.N. Vyas, G.D. Saratale, S.D. Sartale, Zinc oxide superstructures: Recent synthesis approaches and application for hydrogen production via photoelectrochemical water splitting, Int J Hydrogen Energy 44 (2019) 2091–2127. https://doi.org/10.1016/j.ijhydene.2018.08.042.

[52] Y. Kong, H. Sun, W. Fan, L. Wang, H. Zhao, X. Zhao, S. Yuan, Enhanced photoelectrochemical performance of tungsten oxide film by bifunctional Au nanoparticles, RSC Adv 7 (2017) 15201–15210. https://doi.org/10.1039/C7RA01426K.
[53] A. Azam, S. Babkair, Low-temperature growth of well-aligned zinc oxide nanorod arrays on silicon substrate and their photocatalytic application, Int J Nanomedicine (2014) 2109. https://doi.org/10.2147/IJN.S60839.
[54] D. Solís-Cortés, F.M. Jiménez, G. Jauregui, D. Gau, J. Pereyra, R. Henríquez, R.E. Marotti, J.R. Ramos-Barrado, E.A. Dalchiele, Optimization of Ag $_2$ S Quantum Dots Decorated ZnO Nanorod Array Photoanodes for Enhanced Photoelectrochemical Performances, J Electrochem Soc 168 (2021) 056516. https://doi.org/10.1149/1945-7111/ac001a.
[55] J.R. Ansari, N. Singh, S. Mohapatra, R. Ahmad, N.R. Saha, D. Chattopadhyay, M. Mukherjee, A. Datta, Enhanced near infrared luminescence in Ag@Ag_2S core-shell nanoparticles, Appl Surf Sci 463 (2019) 573–580. https://doi.org/10.1016/j.apsusc.2018.08.244.
[56] Y. Du, B. Xu, T. Fu, M. Cai, F. Li, Y. Zhang, Q. Wang, Near-Infrared Photoluminescent Ag_2S Quantum Dots from a Single Source Precursor, J Am Chem Soc 132 (2010) 1470–1471. https://doi.org/10.1021/ja909490r.
[57] T. Majumder, S. Dhar, P. Chakraborty, K. Debnath, S.P. Mondal, Advantages of ZnO nanotaper photoanodes in photoelectrochemical cells and graphene quantum dot sensitized solar cell applications, Journal of Electroanalytical Chemistry 813 (2018) 92–101. https://doi.org/10.1016/j.jelechem.2018.02.015.
[58] W.K. Tan, K. Abdul Razak, Z. Lockman, G. Kawamura, H. Muto, A. Matsuda, Photoluminescence properties of rod-like Ce-doped ZnO nanostructured films formed by hot-water treatment of sol–gel derived coating, Opt Mater (Amst) 35 (2013) 1902–1907. https://doi.org/10.1016/j.optmat.2013.01.011.
[59] X. Li, D. Liu, Z. Shi, J. Yang, Effect of Ag_2S shell thickness on the photocatalytic properties of ZnO/Ag_2S core–shell nanorod arrays, J Mater Sci 54 (2019) 1226–1235. https://doi.org/10.1007/s10853-018-2930-z.
[60] W. Fan, S. Jewell, Y. She, M.K.H. Leung, In situ deposition of Ag–Ag_2S hybrid nanoparticles onto TiO_2 nanotube arrays towards fabrication of photoelectrodes with high visible light photoelectrochemical properties, Phys. Chem. Chem. Phys. 16 (2014) 676–680. https://doi.org/10.1039/C3CP54098G.
[61] A. Das, T. Deka, P.M. Kumar, M. Bhagavathiachari, R.G. Nair, Ag-modified ZnO nanorods and its dual application in visible light-driven photoelectrochemical water oxidation and photocatalytic dye degradation: A correlation between optical and electrochemical properties, Advanced Powder Technology 33 (2022) 103434. https://doi.org/10.1016/j.apt.2022.103434.
[62] W.K. Tan, H. Muto, T. Ito, G. Kawamura, Z. Lockman, A. Matsuda, Facile Fabrication of Plasmonic Enhanced Noble-Metal-Decorated ZnO Nanowire Arrays for Dye-Sensitized Solar Cells, J Nanosci Nanotechnol 20 (2020) 359–366. https://doi.org/10.1166/jnn.2020.17223.
[63] J. Feng, Y. Li, Z. Gao, H. Lv, X. Zhang, D. Fan, Q. Wei, Visible-light driven label-free photoelectrochemical immunosensor based on TiO_2/S-$BiVO_4$@Ag_2S nanocomposites for sensitive detection OTA, Biosens Bioelectron 99 (2018) 14–20. https://doi.org/10.1016/j.bios.2017.07.029.

[64] P. Guan, H. Bai, F. Wang, H. Yu, D. Xu, B. Chen, T. Xia, W. Fan, W. Shi, Boosting Water Splitting Performance of $BiVO_4$ Photoanode through Selective Surface Decoration of Ag_2S, ChemCatChem 10 (2018) 4927–4933. https://doi.org/10.1002/cctc.201801199.

[65] M. Karyaoui, D. ben Jemia, M. Daoudi, A. Bardaoui, A. Boukhachem, M. Amlouk, R. Chtourou, Physical properties of graphene oxide GO-doped ZnO thin films for optoelectronic application, Applied Physics A 127 (2021) 134. https://doi.org/10.1007/s00339-020-04269-9.

[66] R.K. Chava, M. Kang, Ag_2S quantum dot sensitized zinc oxide photoanodes for environment friendly photovoltaic devices, Mater Lett 199 (2017) 188–191. https://doi.org/10.1016/j.matlet.2017.04.078.

[67] Y. Liu, X. Yan, Z. Kang, Y. Li, Y. Shen, Y. Sun, L. Wang, Y. Zhang, Synergistic Effect of Surface Plasmonic particles and Surface Passivation layer on ZnO Nanorods Array for Improved Photoelectrochemical Water Splitting, Sci Rep 6 (2016) 29907. https://doi.org/10.1038/srep29907.

[68] F. Yan, Y. Wang, J. Zhang, Z. Lin, J. Zheng, F. Huang, Schottky or Ohmic Metal-Semiconductor Contact: Influence on Photocatalytic Efficiency of Ag/ZnO and Pt/ZnO Model Systems, ChemSusChem 7 (2014) 101–104. https://doi.org/10.1002/cssc.201300818.

Chapter 5. TiO_2 nanotube arrays/Bi_2Se_3 quantum dots as an efficient and stable photoanode for photoelectrochemical H_2 generation

5.1. Introduction

Utilizing PEC and PC devices to split water using solar energy is seen as a potential approach to producing green H_2 in a scalable and economically sustainable way [1–6]. PEC-WS is more efficient than its PC counterpart due to the following causes: (1) photogenerated electrons and holes are migrated in opposite directions, mitigating e^-/h^+ pairs recombination; (2) active sites are separated for water oxidation and reduction to lessen the possibility of the reverse reaction; and (3) external bias potential can be applied to enhance the built-in electric field to accelerate e^-/h^+ pairs mobility [7]. The essential component in the PEC-WS cell is the semiconductor photoelectrode that can absorb solar energy and produce e^-/h^+ pairs which are consumed in redox reactions. It also significantly affects the solar-to-hydrogen conversion efficiency [8–12]. Fujishima and Honda performed the initial research on TiO_2 as an electrode for the electrochemical photolysis of H_2O to H_2 and O_2 [13]. After that time, various studies have been done using TiO_2-based photoanodes for H_2 production from H_2O [14–17]. A lot of TiO_2 nanostructures such as nanotube arrays [18], nanofibers [19], nanoparticles [20], nanorods [21,22], and nanowires [23] were applied as photoanodes for PEC-WS. TiO_2 nanotube arrays (TNTAs) have distinctive properties, such as controlled morphology and minimal contact resistance at the interface between NTAs and substrate [24]. As well as a large surface area, promoting the diffusion of light and reactants through the full tubular depth with optimized morphology [25,26]. Well-aligned TNTAs are created on the Ti foil substrate using the anodization process and have been applied for numerous photocatalytic applications [27–30], moreover, the anodization is suitable for commercialization and scalability [31]. Though TNTAs have been extensively investigated as photoanodes because of their low cost and consistent photoconversion, their properties still need to be developed to boost their PEC performance. Great efforts have been made to overcome this issue, some studies concentrated on the decrease of the bandgap energy using chemical doping [32,33] and heterojunction with narrow bandgap semiconductors to improve the separation efficiency of e^-/h^+ pairs and mitigate their recombination [34,35]. Additionally, sensitization of TNTAs with plasmonic metals NPs [36], and QDs materials [27,37] can significantly improve the

light absorption ability. Among these diverse approaches, the sensitization of TNTAs with QDs materials is an excellent way to increase the efficiency of PEC system owing to the bandgap energy's flexibility, which varies according to the size of the QDs [38]. QDs materials have unique optoelectronic features due to the quantum confinement effect, involving adjustable bandgap energy, high extinction coefficient, and probability for multiple exciton generation [39–41].

Recently, PEC devices that used QDs-based photoelectrodes have advanced rapidly [42–44], through synthesizing QDs materials with adequate band structure and light absorption capability to improve the solar energy conversion [45], preparation of photoelectrodes with certain morphologies [46], improving the deposition techniques of QDs to optimize the loading [47,48], and designing the surface of photoelectrodes to ameliorate the charge mobility and maintain stability over time [49,50]. QDs photoelectrodes based on Pb and Cd chalcogenides are the most widely used in PEC-WS systems [51,52], due to the efficient charge mobility under Vis light excitation. Since these QDs are too harmful and unsuitable for large-scale applications, the use of QDs based on less hazardous and plentiful materials is necessary [53]. Bismuth-based QDs photoelectrodes are favorable due to their low toxicity and excellent electronic properties, such as small bandgap and high absorption coefficient [54]. Bi_2Se_3 has superb physical properties, involving adequate bandgap which can absorb a broad portion of the solar spectrum (~1.03–1.7 eV), and effective charge mobility. Additionally, it is more plentiful and less poisonous [55,56]. Recently, Bi_2Se_3 has gained attention for a variety of uses, including optoelectronics, solar cells, and PEC devices [55,57,58]. However, the Bi_2Se_3 QDs haven't yet been studied as a sensitizer with TNTAs for H_2 production through the PEC-WS technique. We expected that the heterojunction between Bi_2Se_3 QDs and TNTAs would increase the light absorption to the Vis region, offering an efficient photoelectrode for PEC H_2 generation.

In this study, we used a two-step anodization process to synthesize well-ordered TNTAs on Ti foil. Following that, we applied the SILAR technique to generate an efficient heterojunction with Bi_2Se_3 QDs. TNTAs/Bi_2Se_3 QDs photoanode displayed excellent PEC performance. The quantity of deposited Bi_2Se_3 QDs had a direct impact on the generated photocurrent density. The TNTAs/Bi_2Se_3 QDs fabricated by two SILAR cycles (2) achieved the highest photocurrent density at 1.23 V vs. RHE. The IPCE was 73% at 345 nm for TNTAs/Bi_2Se_3 QDs (2) and 53% for pristine TNTAs. Moreover, TNTAs/Bi_2Se_3 QDs (2) extended the light response to the Vis range owing to

the superb ability of deposited Bi_2Se_3 QDs to absorb the Vis light. TNTAs/Bi_2Se_3 QDs (2) also manifested excellent chemical stability for PEC H_2 production over 7 hours. It is obvious that the type II heterojunction constructed at the interface between TNTAs and Bi_2Se_3 QDs ameliorated the e^-/h^+ pairs separation and improved the transfer of excited electrons to the Ti substrate, resulting in enhancing the PEC performance.

5.2. Experimental

5.2.1. Fabrication of TiO_2 nanotube arrays

TNTAs were grown on a Ti foil two-step anodization process [59]. A Ti foil (40 × 25 × 2 mm^3) was sonicated in acetone for 1 hour to be clean and then air dried. The first step of anodization was carried out using a two-electrode system, the Ti foil acted as the anode, and a Pt rod was used as the cathode. The electrolyte was ethylene glycol comprising 0.08 M NH_4F and 1.3 M deionized (DI) H_2O. It was carried out under an applied potential of 60 V and at room temperature for 2 hours. The obtained anodized Ti foil was immediately treated in DI H_2O under sonication for 1 hour to eliminate the formed oxide layer including disordered TNTAs and to gain periodic nanovoids on the Ti foil surface. The second step of anodization was carried out using the obtained nanovoid Ti foil as the anode and a plain Ti foil as the cathode. The electrolyte was ethylene glycol and dimethyl sulfoxide with a 1:1 volume ratio comprising 0.1 M NH_4F and 1.5 M DI H_2O. it was carried out at 30 V for 30 minutes at 53°C. Following, the second anodization, the anodized Ti foil was kept in the electrolyte under stirring for 8 minutes at 53°C to remove the carbon-contaminated surface layer from TNTAs without destroying the nanotube arrays structure. This process is named post-anodization treatment [60]. The obtained sample was washed with 2-propanol, air-dried, and annealed at 550°C for 1 hour in air to enhance the crystallinity of TNTAs. Lastly, the sample was washed with an aqueous solution of 0.05 M HCl.

5.2.2. Fabrication of TNTAs/Bi_2Se_3 QDs

The SILAR process was used to deposit various quantities of Bi_2Se_3 QDs over TNTAs. It included the immersion of TNTAs formed on Ti foil in a cationic precursor of $Bi(NO_3)_3$•$5H_2O$ and an anionic precursor of chemically prepared sodium selenosulfate (Na_2SeSO_3). Firstly, 0.2 M Na_2SeSO_3 solution was freshly synthesized by refluxing 6.30 g of Na_2SO_3 and 1.57 g of Se powder in 100 mL of DI H_2O under vigorous stirring at 70°C for 24 hours. The prepared solution was covered and kept overnight. The solution was then filtrated using filter paper to eliminate the unwanted sediment and was stored in a dark place for later use. The SILAR procedure involved sequential immersion of TNTAs for 1 minute in four solutions at room temperature; (1) cationic solution of 50 mM of $Bi(NO_3)_3$•$5H_2O$ (DI H_2O: methanol (40 ml, 1:1 volume ratio)) added with 4 mL of glycerol to enhance the solubility of $Bi(NO_3)_3$. (2) 40 mL of DI H_2O: methanol (1:1 volume ratio). (3) anionic solution of 50 mM Na_2SeSO_3 in 40 mL of DI H_2O. (4) 40 mL of DI H_2O. The second and fourth solutions were necessary to remove the unreacted ions leading to the homogeneous growth of Bi_2Se_3 QDs. These four consecutive immersions formed one SILAR cycle. We deposited various cycles of Bi_2Se_3 QDs (one, two, and three) over TNTAs surface and expressed them as TNTAs/Bi_2Se_3 QDs (1), TNTAs/Bi_2Se_3 QDs (2), and TNTAs/Bi_2Se_3 QDs (3), respectively. To improve the interaction between Bi_2Se_3 QDs and TNTAs, the prepared TNTAs/Bi_2Se_3 QDs samples were then heated at 100 °C for 1 hour.

5.2.3. Characterization

The crystallographic structure, morphology, Elemental composition, valence states, and UV-Vis diffuse reflectance spectroscopy of the prepared samples were investigated using the same devices explained in Chapter 2 in section 2.2.2. Moreover, PL properties were studied with the same device displayed in Chapter 3 in section 3.2.2.

5.2.4. Photoelectrochemical measurements

The PEC performance was investigated using a three-electrode cell with TNTAs or TNTAs decorated with Bi_2Se_3 QDs as the working electrode, Hg/HgO (1 M NaOH) as the reference electrode, and Pt coil as the counter electrode. Data were recorded using a potentiostat (BioLogic, VSP-300, France). The working electrode was irradiated (1 cm^2 irradiated area) from the front side

utilizing a 300 W xenon lamp as a solar simulator with an air mass 1.5 global filter, adjusting the light intensity to 100 mW cm^{-2}. 0.1 M Na_2SO_3/Na_2S (pH = 12.4) was employed as the electrolyte, and it was purged with argon before the PEC determination. The LSV curves were determined at a scan rate of 10 mV/s. The EIS was measured at open circuit potential under irradiation and at 10^5–10^{-2} Hz with 10 mV amplitude. The M-S curves were recorded under dark at 1 kHz. The EIS and M-S curves were recorded in 0.2 M Na_2SO_4 aqueous electrolyte (pH = 6.5) using Ag/AgCl (3 M KCl) as the reference electrode. The rate of H_2 production was measured using gas chromatography (Shimadzu, GC-8A, Japan) directly linked to a gas circulation apparatus (Makuhari Rikagaku Garasu Seisakujo, Japan) with argon as the carrier gas. The chronoamperometry test was measured by recording photocurrent-time curves to evaluate the stability of the prepared samples. The ABPE was calculated from the LSV results as previously explained in Chapter 2 in section 2.3.2.6.

The IPCE was determined through photocurrent density measurement in a wavelength range of 325–850 nm by applying a monochromator light source at 1.23 V vs. RHE and estimated using equation (1) [61]:

$$IPCE\ (\%) = \frac{j_p\ X1240}{\lambda\ XI_o} \times\ 100, \qquad \text{(Eq. 5-1)}$$

where j_p , λ, and I_o are the photocurrent density, incident wavelength, and light power density, respectively.

The Potential versus RHE was calculated by transforming the applied potential versus Hg/HgO and the applied potential versus Ag/AgCl as illustrated in Chapter 2 in section 2.2.3.

5.3. Results and discussion

5.3.1. Characterization of prepared samples

The crystalline structure of pure TNTAs after the annealing process and TNTAs decorated with different SILAR cycles (1,2, and 3) of Bi_2Se_3 QDs was investigated using XRD analysis as depicted in **Figure 5-1**. All investigated samples manifested diffraction peaks regarding to the Ti foil substrate (JCPDS no. 44-1294) and the anatase phase of TiO_2 (JCPDS no. 73-1764) [62].

However, the distinctive peaks of Bi_2Se_3 QDs were not noticed maybe owing to their lower amount and smaller particle size than TNTAs.

The morphology of the synthesized samples was studied through SEM analysis. **Figure 5-2a** illustrates the successful preparation of TNTAs manifesting well-aligned nanoporous structure with 50–60 nm diameter. The cross-section view showed that TNTAs were grown with a well-ordered nanoporous surface and vertically aligned nanotubes with ~5 µm length (**Figure 5-2b**). **Figure 5-2c–h** illustrates the top and cross-section views of TNTAs decorated with different SILAR cycles (1,2, and 3). It is obvious that, even after several SILAR cycles, the nanotube array structure was preserved, and the TNTAs' surface became rough. This result verified the deposition of Bi_2Se_3 QDs on the internal and external surfaces of TNTAs without significant agglomeration. Additionally, TNTAs diameter was noticeably shrunk to 30–50 nm after raising the amount of Bi_2Se_3 QDs (**Figure 5-2g**).

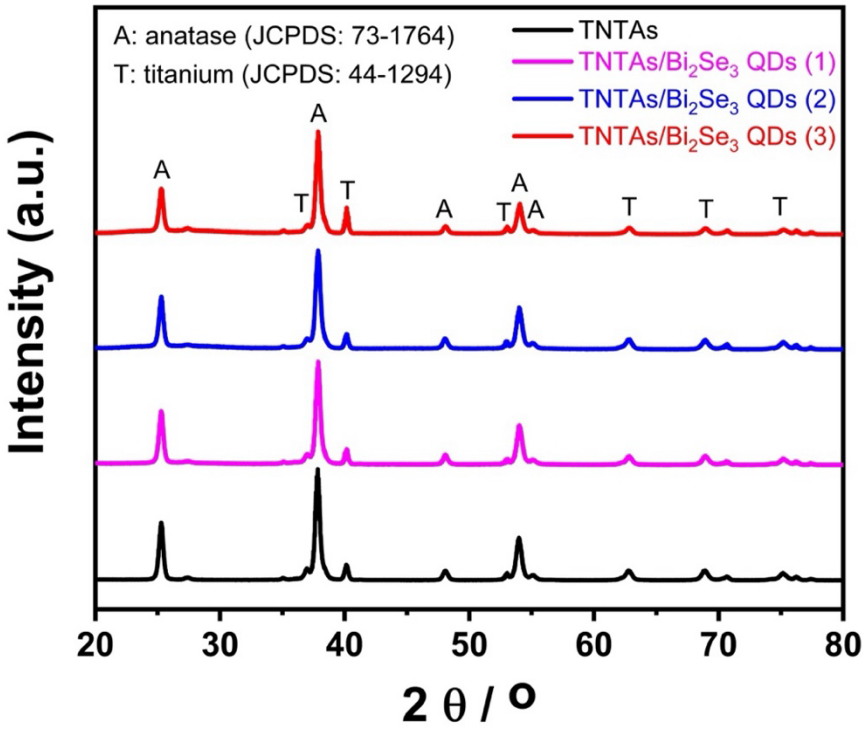

Figure 5-1. XRD patterns of pure TNTAs and TNTAs decorated with different SILAR cycles of Bi_2Se_3 QDs.

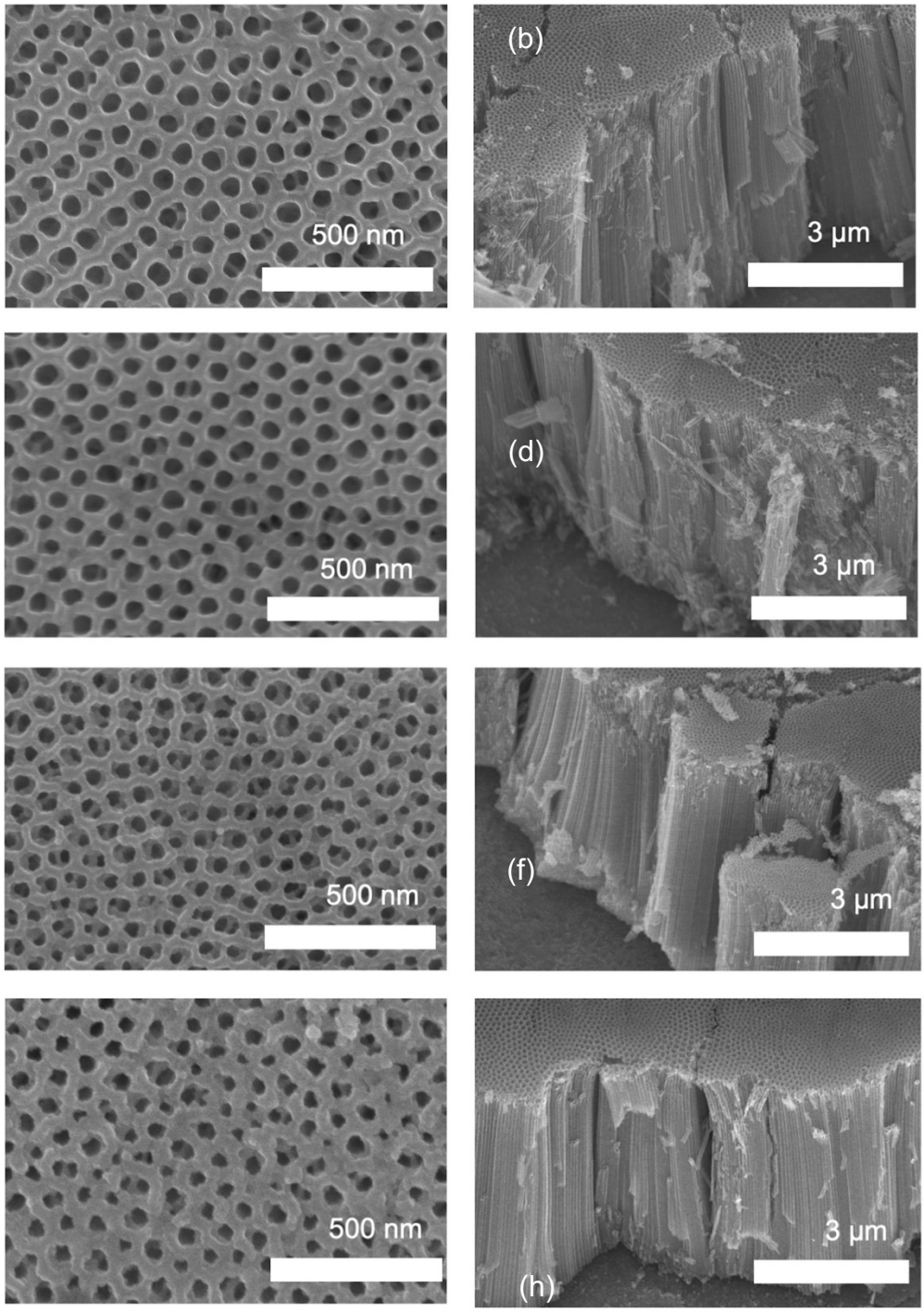

Figure 5-2. SEM images of (a, b) pure TNTAs, (c, d) one cycle, (e, f) two cycles, and (g, h) three cycles of the SILAR process for depositing Bi_2Se_3 QDs.

STEM-EDX investigation was carried out to examine the microscopic structure of the prepared TNTAs/Bi_2Se_3 QDs sample. **Figure 5-3a–c** illustrates the homogeneous dispersion of Bi_2Se_3 QDs on the walls of TNTAs. Bi_2Se_3 QDs were deposited with particle size less than 2 nm without agglomeration. The EDX analysis (**Figure 5-3d**) confirmed the existence of Bi and Se elements. Ti was found in greater quantity than O because Ti foil was utilized as the substrate. Additionally, a larger quantity of Bi was found than Se. This point will be elucidated in the next section with the discussion of XPS data.

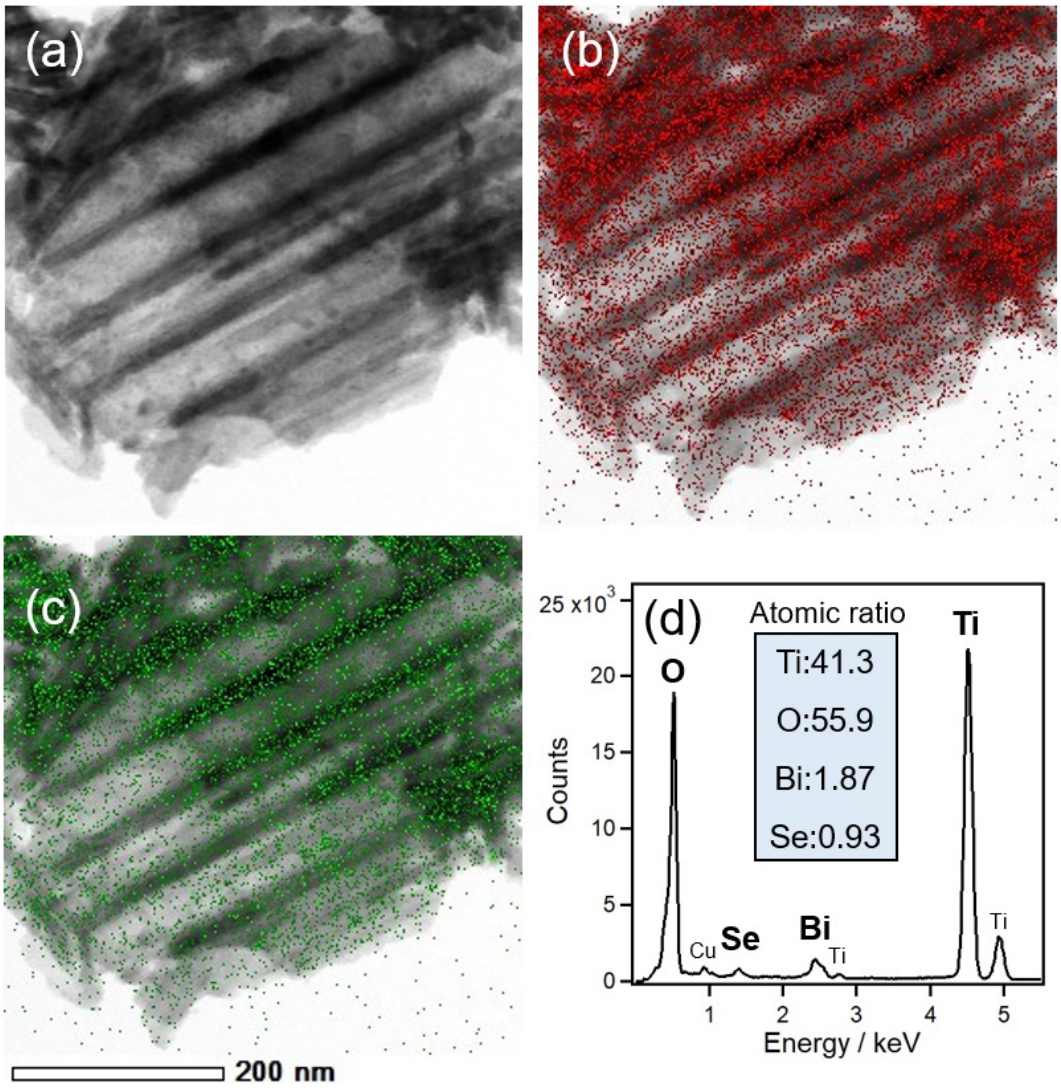

Figure 5-3. STEM-EDX analysis of TNTAs/Bi_2Se_3 QDs (2). (a) Dark-field STEM image overlapped with (b) Bi and (c) Se EDX mappings. (d) Corresponding EDX spectrum.

XPS analysis was employed to study the surface composition and elemental chemical states of the synthesized samples. The survey spectrum of TNTAs/Bi_2Se_3 QDs (2) approved the existence of Ti, O, Bi, and Se elements in addition to C contaminants, clarifying the successful deposition of Bi_2Se_3 QDs on the surface of TNTAs. **Figure 5-4** presents the high-resolution spectrum of all present elements. Ti 2p demonstrated two peaks at 464.7 and 458.9 eV matched to Ti $2p_{1/2}$ and Ti $2p_{3/2,}$ respectively; this was ascribed to the existence of Ti in Ti^{4+} oxidation state (**Figure 5-4a**). O 1s displayed a peak at 530.2 eV attributed to the lattice oxygen from TiO_2 (**Figure 5-4b**). The Bi 4f peaks split into two doublet states (**Figure 5-4c**). Bi $4f_{7/2}$ peaks at 164.6 and 163.3 eV and Bi $4f_{5/2}$ peaks at 159.4 and 158.0 eV verified the existence of Bi-Se bonding in the Bi^{3+} oxidation state and Bi-O bonding, which has stronger binding energies than Bi-Se [56,63,64]. This data indicated that a bismuth oxide thin layer formed on the Bi_2Se_3 QDs surface during QDs deposition in the ambient atmosphere. This result further elucidated the observation that Bi is present in larger quantity than Se in the EDX analysis in **Figure 5-3d**. Se 3d exhibited two peaks at 54 and 53.2 eV corresponding to Se $3d_{3/2}$ and Se $3d_{5/2}$, respectively (**Figure 5-4d**), approving Se^{2-} presence in Bi_2Se_3 QDs [55].

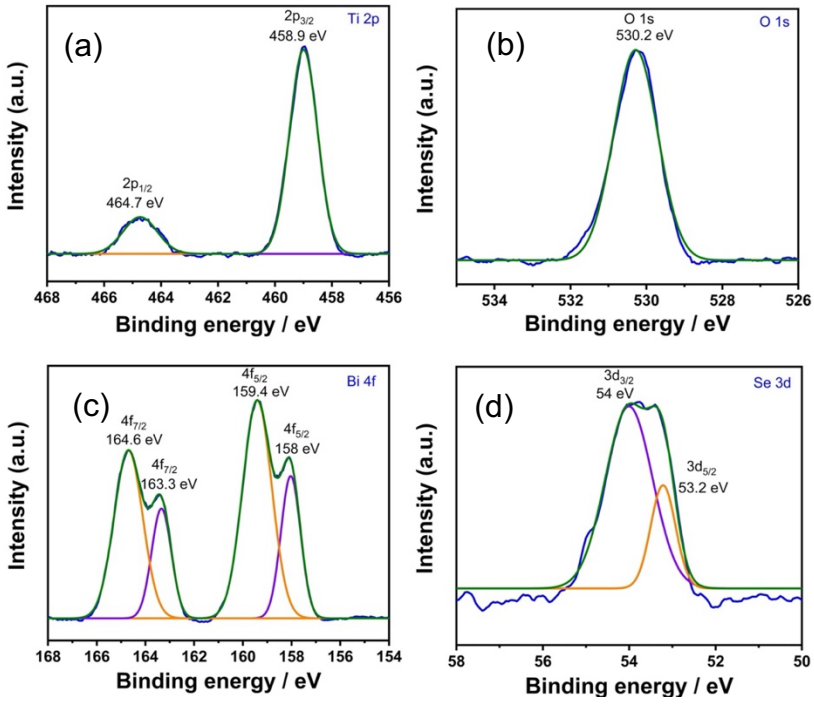

Figure 5-4. XPS spectra of TNTAs/Bi_2Se_3 QDs (2) presenting the high-resolution spectra of (a) Ti 2p, (b) O 1s, (c) Bi 4f, and (d) Se 3d elements.

The diffuse reflectance UV-Vis spectra were measured to study the optical properties of pure TNTAs, TNTAs/Bi_2Se_3 QDs (1), TNTAs/Bi_2Se_3 QDs (2), and TNTAs/Bi_2Se_3 QDs (3) samples as exhibited in **Figure 5-5a.** The presence of multi-absorption peaks in the UV and Vis zones, especially for pure TNTAs and TNTAs/Bi_2Se_3 QDs (1), was assigned to the periodic nanoporous structure of TNTAs, which can cause strong optical interference in the top photonic layer of TNTAs [65]. Bi_2Se_3 QDs deposition over TNTAs, improved the Vis light absorption, especially after two and three SILAR cycles. The bandgap energy of bare TNTAs and TNTAs/Bi_2Se_3 QDs (2) was calculated using Kubelka–Munk function [66]. **Figure 5-5b** reveals that the deposition of Bi_2Se_3 QDs (2) over TNTAs dramatically decreased the bandgap energy from 3.2 eV to 1.3 eV, resulting in enhancing Vis light absorption.

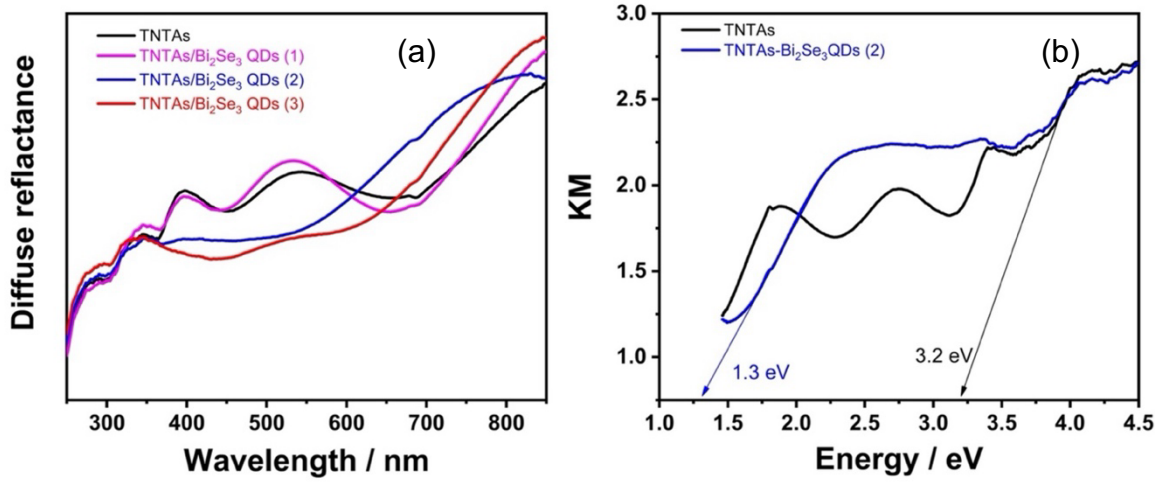

Figure 5-5. (a) Diffuse reflectance UV-Vis spectra of pure TNTAs, TNTAs/Bi_2Se_3 QDs (1), TNTAs/Bi_2Se_3 QDs (2), and TNTAs/Bi_2Se_3 QDs (3) samples; (b) bandgap energy of pure TNTAs and TNTAs/Bi_2Se_3 QDs (2).

Figure 5-6 exhibits the PL spectra of pure TNTAs and TNTAs decorated with different SILAR (1, 2, and 3) cycles of Bi_2Se_3 QDs. All investigated samples displayed a broad and strong emission peak between 400 and 850 nm. The PL intensity raised in the order of TNTAs/Bi_2Se_3 QDs (3) < TNTAs/Bi_2Se_3 QDs (2) < TNTAs/Bi_2Se_3 QDs (1) < bare TNTAs. This behavior was inversely correlated to the e^-/h^+ pairs separation efficiency. The e^-/h^+ pairs separation efficiency was the lowest in pure TNTAs and was enhanced by increasing the SILAR cycles of Bi_2Se_3 QDs. This result verified that the recombination rate of e^-/h^+ pairs decreased with increasing the deposited amount of Bi_2Se_3 QDs.

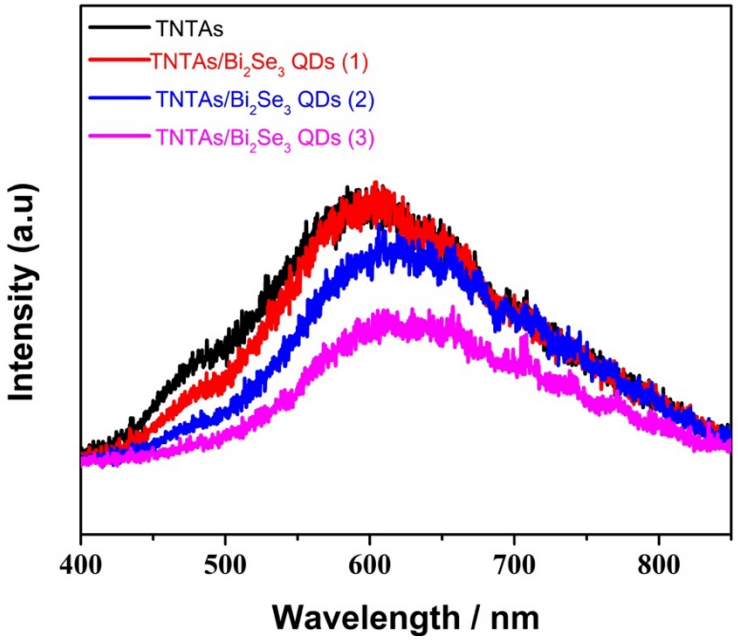

Figure 5-6. PL spectra of pure TNTAs, TNTAs/Bi_2Se_3 QDs (1), TNTAs/Bi_2Se_3 QDs (2), and TNTAs/Bi_2Se_3 QDs (3).

5.3.2. Photoelectrochemical performance

5.3.2.1. Linear sweep voltammetry

Figure 5-7a presents the LSV curves of pure TNTAs, TNTAs/Bi_2Se_3 QDs (1), TNTAs/Bi_2Se_3 QDs (2), and TNTAs/Bi_2Se_3 QDs (3) photoanodes under dark conditions (dot lines) and light irradiation (solid lines). All studied samples attained a low current density of $\leq$ 0.034 mA cm^{-2} at 1.23 V vs. RHE under dark conditions. While, under light irradiation, the photocurrent density of all investigated samples was significantly enhanced. Pure TNTAs demonstrated the lowest photocurrent density (0.46 mA cm^{-2}), however, the deposition of Bi_2Se_3 QDs remarkably improved the photocurrent. TNTAs/Bi_2Se_3 QDs (1), TNTAs/Bi_2Se_3 QDs (2), and TNTAs/Bi_2Se_3 QDs (3) photoanodes achieved photocurrent density of 1.04, 1.75, and 1.11 mA cm^{-2}, respectively. The TNTAs/Bi_2Se_3 QDs (2) photoanode exhibited the highest photocurrent density which was ~3.8 times higher than pure TNTAs. This improved photocurrent density can be attributed to the extended light absorption to the Vis zone and the developed electronic properties after the deposition of Bi_2Se_3 QDs. Moreover, the onset potential of all samples of TNTAs decorated with different cycles of Bi_2Se_3 QDs was negatively shifted compared to pure TNTAs, confirming that

the heterojunction constructed between TNTAs and Bi_2Se_3 QDs reduced the band bend necessary for e^-/h^+ pairs separation.

The transient photocurrent versus the applied potential was recorded for pure TNTAs and TNTAs decorated with different SILAR cycles (1,2, and 3) of Bi_2Se_3 QDs as depicted in **Figure 5-7b.** Bi_2Se_3 QDs deposition over TNTAs surface considerably enhanced the photocurrent density. It was observed that there is a relationship between the deposited amount of Bi_2Se_3 QDs and the generated photocurrent density. The generated photocurrent density in the case of TNTAs/Bi_2Se_3 QDs (2) photoanode was ~ 3.8 folds higher than pure TNTAs.

5.3.2.2.Photoconversion efficiency

Figure 5-7c illustrates the ABPE plots as a function of applied potential versus RHE of pure TNTAs and TNTAs decorated with different SILAR cycles of Bi_2Se_3 QDs. Pure TNTAs demonstrated the lowest photoconversion efficiency of 0.47% at 0.18 V vs. RHE, and TNTAs/Bi_2Se_3 QDs (2) significantly improved it to 1.13% at 0.38 V vs. RHE. This result is consistent with the LSV results and further verified that the Bi_2Se_3 QDs deposition over TNTAs can efficiently boost the PEC performance. **Figure 5-7d** presents the IPCE of pure TNTAs and TNTAs/Bi_2Se_3 QDs (2) photoanodes with values of 53% and 73%, respectively, at 345 nm. Additionally, TNTAs/Bi_2Se_3 QDs (2) photoanode exhibited the photoresponse until 800 nm. This behavior was ascribed to the low charge recombination rate and Vis light absorption provided by deposited Bi_2Se_3 QDs.

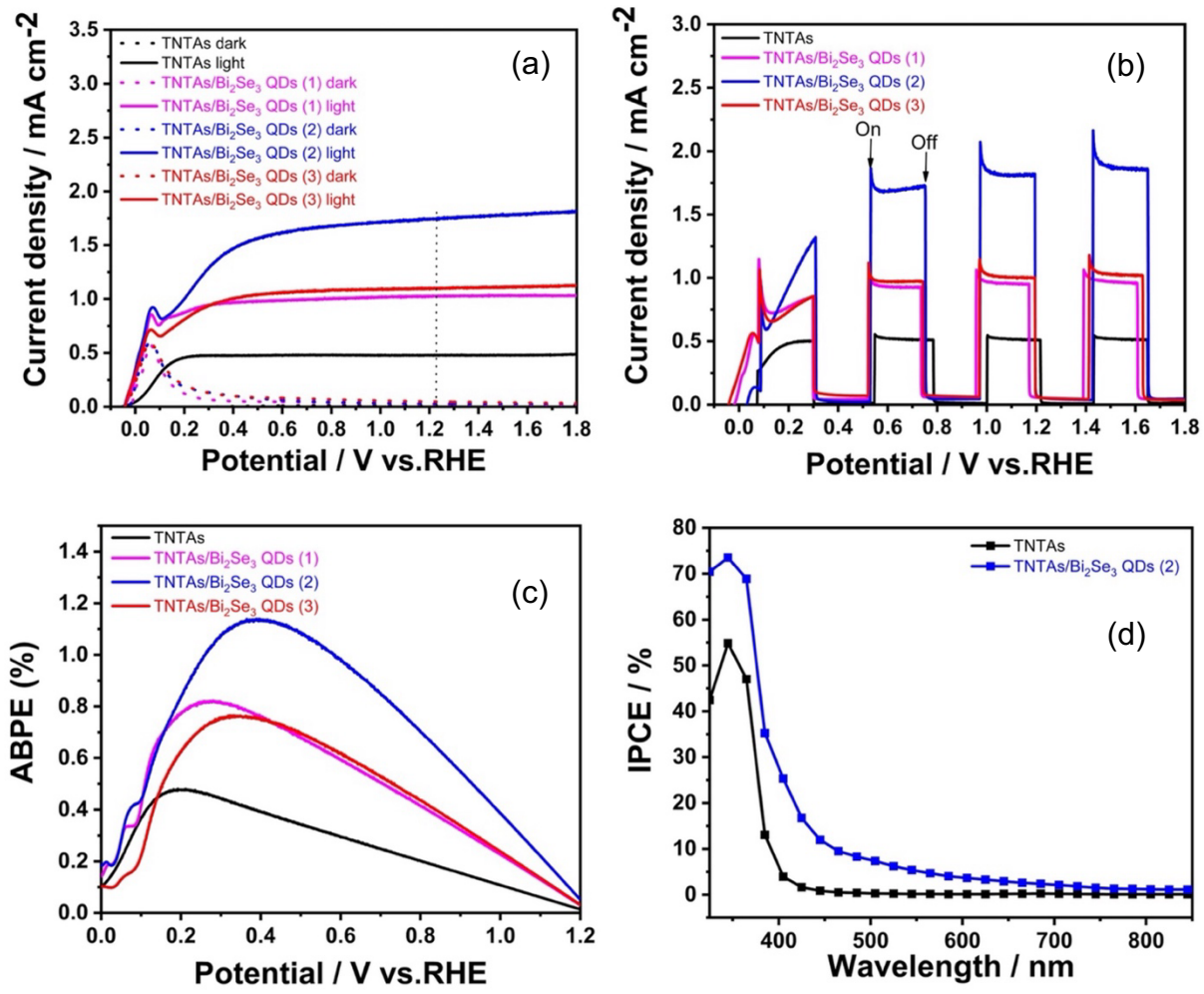

Figure 5-7. (a) LSV curves; (b) dark/photocurrent density as a variable of applied potential in different on/off cycles interrupted illumination; (c) ABPE curves as a variable of the applied potential of pure TNTAs and TNTAs decorated with different SILAR cycles for Bi_2Se_3 QDs; (d) IPCE spectra (1.23 V vs. RHE) of pure TNTAs and TNTAs/Bi_2Se_3 QDs (2).

5.3.2.3. Mott–Schottky

The M-S plots were recorded to investigate the type and conductivity of the studied samples. **Figure 5-8a** displays the positive slopes of pure TNTAs and TNTAs/Bi_2Se_3 QDs (2), approving that both photoelectrodes are n-type semiconductors. The E_{fb} of TNTAs and TNTAs/Bi_2Se_3 QDs (2) was 0.20 V and 0.05 V vs. RHE, respectively. The E_{fb} of TNTAs/Bi_2Se_3 QDs (2) was negatively shifted dramatically compared to pure TNTAs, indicating that the efficient e^-/h^+ pairs mobility would enhance the PEC performance.

5.3.2.4. Electrochemical impedance spectroscopy

EIS measurement is a powerful technique to investigate interfacial properties between the photoelectrode and electrolyte. The Nyquist plots of pure TNTAs and TNTAs/Bi_2Se_3 QDs (2) photoanodes are shown in **Figure 5-8b,c,** respectively. The recorded data were fitted with the ZView software (Scribner Associates, USA) utilizing the corresponding equivalent circuit model, which helped in estimating the R_{ct}. The obtained R_{ct} for TNTAs and TNTAs/Bi_2Se_3 QDs (2) was 5400 Ω and 47.72 Ω, respectively. The smaller R_{ct} of the TNTAs/Bi_2Se_3 QDs (2) photoanode than pure TNTAs approved the facile charge carrier separation and transfer following the deposition of Bi_2Se_3 QDs.

5.3.2.5.Chronoamperometry and H_2 generation

The photoelectrode's long-term stability is an important factor in reducing the price of the PEC H_2 generation. Thus, the stability of pure TNTAs and TNTAs/Bi_2Se_3 QDs (2) photoanodes was recorded through the chronoamperometry measurement at 1.23 V vs. RHE under light illumination. **Figure 5-8d** illustrates that pure TNTAs and TNTAs/Bi_2Se_3 QDs (2) were stable over 7 hours. During the chronoamperometry measurement, the H_2 production amount using pure TNTAs and TNTAs/Bi_2Se_3 QDs (2) photoanodes was measured as a function of time under light irradiation (**Figure 5-9a**). Regarding TNTAs, the produced amount of H_2 increased over time, although the quantity was difficult to determine during the first and second hours probably because it was very small. The total amount of H_2 produced using TNTAs/Bi_2Se_3 QDs (2) photoanode was 355.8 µmol after 5 hours, which is ~ 3.3 times higher than pure TNTAs (105.3 µmol). This can be attributed to the efficient band alignment, which mitigated e^-/h^+ pairs recombination. Moreover, the deposited Bi_2Se_3 QDs acted as a photosensitizer transforming the incident photons to electrons, resulting in a rise in photocurrent density and H_2 production amount.

5.3.2.6. Characterization of used samples after chronoamperometry test

After chronoamperometry, the used samples of pure TNTAs and TNTAs/Bi_2Se_3 QDs (2) were studied using XRD and SEM analyses. The XRD pattern (**Figure 5-9b**) and SEM images of TNTAs (**Figure 5-9c**) and TNTAs/Bi_2Se_3 QDs (2) (**Figure 5-9d**) illustrated that the crystal

structure and surface morphology of both samples did not deteriorate after 7 hours of PEC reactions.

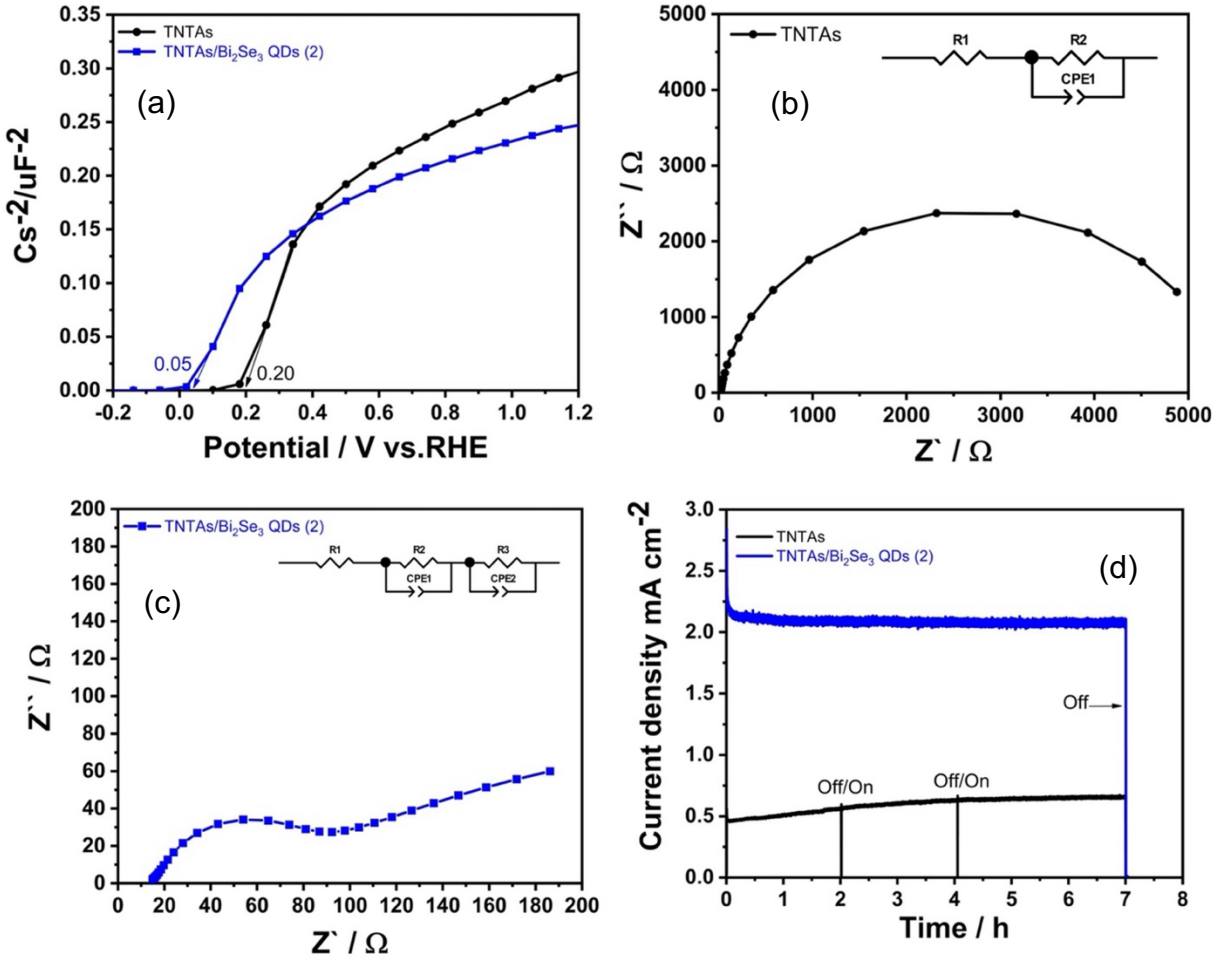

Figure 5-8. (a) Mott–Schottky curves of pure TNTAs and TNTAs/Bi_2Se_3 QDs (2); Nyquist plots of (b) pure TNTAs and (c) TNTAs/Bi_2Se_3 QDs (2) photoanodes; (d) chronoamperometry measurement of pure TNTAs and TNTAs/Bi_2Se_3 QDs (2) photoanodes.

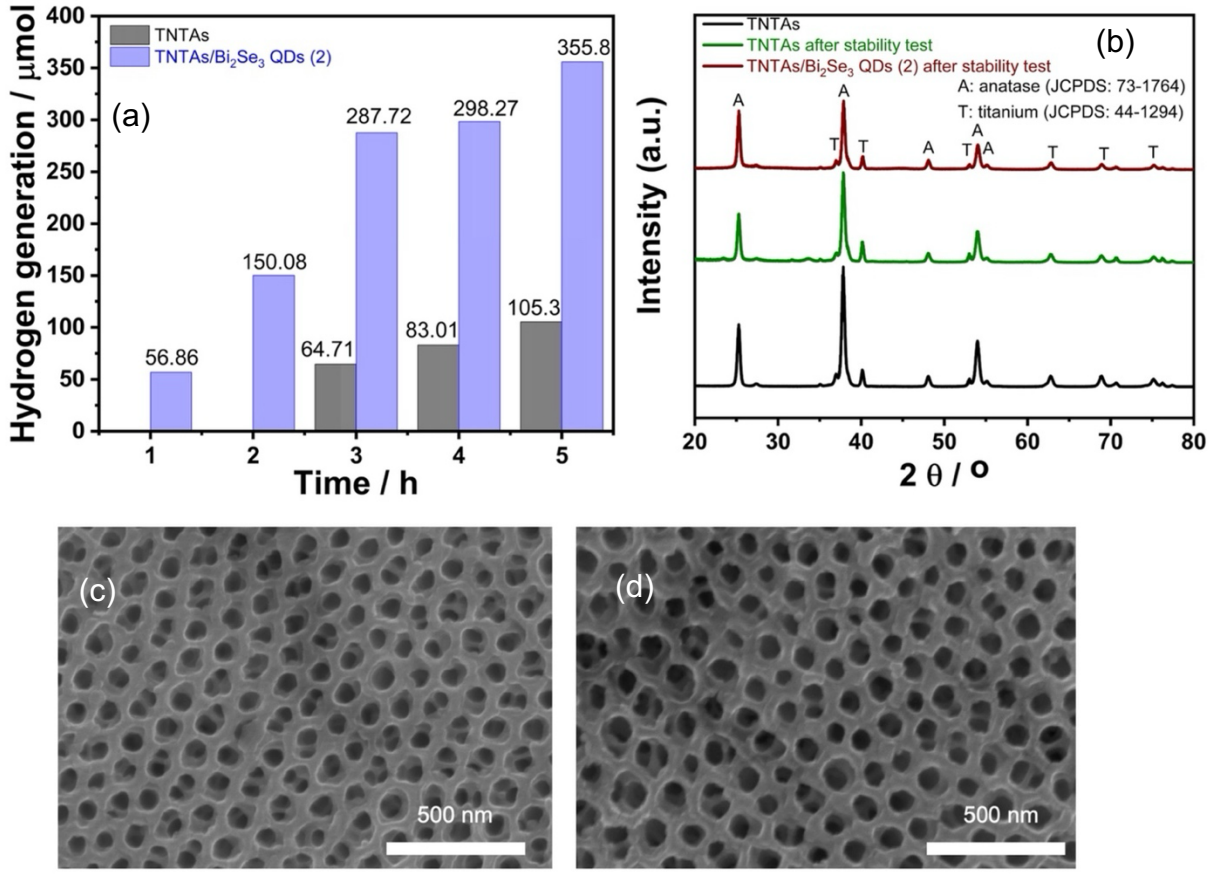

Figure 5-9. (a) H_2 production amount at 1.23 V vs. RHE. (b) XRD pattern and SEM images of (c) pure TNTAs, and (d) TNTAs/Bi_2Se_3 QDs (2) after chronoamperometry test.

5.3.3. Photoelectrochemical mechanism

The suggested mechanism of PEC H_2 production using the TNTAs/Bi_2Se_3 QDs photoanode is depicted in **Figure 5-10**. A type II heterojunction was created between TNTAs and Bi_2Se_3 QDs due to their appropriate energy band positions. The photogenerated electrons migrated from the CB of Bi_2Se_3 to the CB of TNTAs and then drifted through the Ti substrate and external circuit to the Pt counter electrode to reduce H_2O to H_2. The photogenerated holes migrated from the VB of TNTAs to the VB of Bi_2Se_3 where they were captured by the sacrificial reagent. The recombination rate of e^-/h^+ pairs was significantly decreased owing to the opposite directions of electrons and holes transfer. Consequently, the created type II heterojunction facilitated the e^-/h^+ pairs mobility and inhibited their recombination rate, resulting in boosted PEC performance and increased H_2 production.

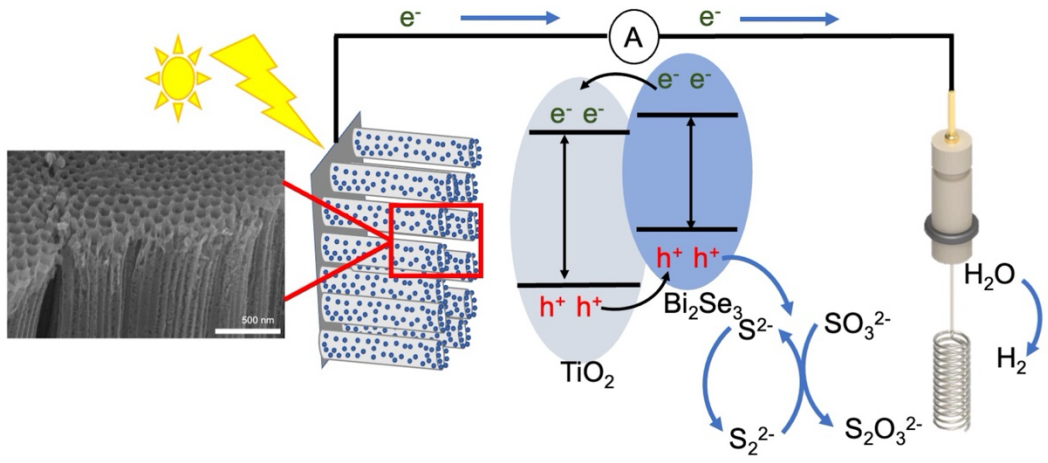

Figure 5-10. Schematic illustration of the PEC H_2 production mechanism on TNTAs/Bi_2Se_3 QDs photoanode.

5.4. Conclusions

TNTAs were successfully decorated with various quantities of Bi_2Se_3 QDs using the SILAR procedure to construct TNTAs/Bi_2Se_3 QDs heterojunction composite. STEM-EDX study revealed the homogeneous dispersion of Bi_2Se_3 QDs with particle size less than 2 nm on TNTAs walls. Additionally, the PL spectra clarified that the efficiency of e^-/h^+ pairs separation was improved by increasing the SILAR cycles of Bi_2Se_3 QDs. The type II heterojunction generated at the TNTAs/Bi_2Se_3 QDs interface improved the PEC performance and H_2 production. The TNTAs/Bi_2Se_3 QDs (2) photoanode achieved the highest photocurrent density of 1.75 mA cm^{-2}, which is 3.8 folds higher than pure TNTAs (0.46 mA cm^{-2}) at 1.23 V vs. RHE. The ABPE and IPCE of the TNTAs/Bi_2Se_3 QDs (2) photoanode were significantly enhanced compared with those of pure TNTAs. The M-S plots manifested that the E_{fb} of TNTAs/Bi_2Se_3 QDs (2) negatively shifted remarkably compared with that of pure TNTAs, confirming that the efficient e^-/h^+ pairs mobility enhanced the PEC performance. The EIS determination revealed that TNTAs/Bi_2Se_3 QDs (2) have lower R_{ct} (47.72 Ω) than pure TNTAs (5400 Ω) which implied the improvement of e^-/h^+ pairs separation and mobility after the deposition Bi_2Se_3 QDs. TNTAs/Bi_2Se_3 QDs (2) extended the light response to the Vis zone (up to 800 nm) and boosted the H_2 production amount of 355.8 µmol after 5 hours; this quantity is 3.3 folds greater than in case of pure TNTAs (105.3 µmol) at 1.23 V vs. RHE. Moreover, the TNTAs/Bi_2Se_3 QDs (2) photoanode demonstrated excellent stability for PEC

performance over 7 hours. Several characterizations disclosed the fundamental causes for improving the PEC performance and H_2 production quantity using TNTAs/Bi_2Se_3 QD photoanode as follows; (1) the enhanced Vis light absorption assigned to the deposited Bi_2Se_3 QDs, (2) the rise of charge carrier density and the reduction of the flat band potential, and (3) the decline of the charge transfer resistance and facile charge mobility.

References

[1] D. Zhang, H. Cho, J. Yum, M. Mensi, K. Sivula, An Organic Semiconductor Photoelectrochemical Tandem Cell for Solar Water Splitting, Adv Energy Mater 12 (2022) 2202363. https://doi.org/10.1002/aenm.202202363.

[2] C. Wu, Y. Dong, Y.H. Ng, Y. Liu, J. Deng, L. Jing, H. Dai, Nickel-assisted synthesis of elemental crystalline phosphorus photocatalyst for efficient hydrogen evolution, Sustainable Materials and Technologies 35 (2023) e00551. https://doi.org/10.1016/j.susmat.2022.e00551.

[3] J.Z. Hassan, A. Zaheer, A. Raza, G. Li, Au-based heterostructure composites for photo and electro catalytic energy conversions, Sustainable Materials and Technologies 36 (2023) e00609. https://doi.org/10.1016/j.susmat.2023.e00609.

[4] Y. Xiao, Q.-L. Mo, G. Wu, K. Wang, X.-Z. Ge, S.-R. Xu, J.-L. Li, Y. Wu, F.-X. Xiao, Charge modulation over atomically precise metal nanoclusters *via* non-conjugated polymers for photoelectrochemical water oxidation, J Mater Chem A Mater 11 (2023) 2402–2411. https://doi.org/10.1039/D2TA08547J.

[5] B. Tang, S.-C. Zhu, H. Liang, S. Li, B.-J. Liu, F.-X. Xiao, Tuning atomically precise metal nanocluster mediated photoelectrocatalysis *via* a non-conjugated polymer, J Mater Chem A Mater 10 (2022) 4032–4042. https://doi.org/10.1039/D1TA10284B.

[6] M.M. Abouelela, G. Kawamura, A. Matsuda, A review on plasmonic nanoparticle-semiconductor photocatalysts for water splitting, J Clean Prod 294 (2021) 126200. https://doi.org/10.1016/j.jclepro.2021.126200.

[7] J. Xiao, C. Li, X. Jia, B. Du, R. Li, B. Wang, Enabling high low-bias performance of Fe_2O_3 photoanode for photoelectrochemical water splitting, J Colloid Interface Sci 633 (2023) 555–565. https://doi.org/10.1016/j.jcis.2022.11.134.

[8] K. Sivula, R. van de Krol, Semiconducting materials for photoelectrochemical energy conversion, Nat Rev Mater 1 (2016) 15010. https://doi.org/10.1038/natrevmats.2015.10.

[9] P. Lianos, Review of recent trends in photoelectrocatalytic conversion of solar energy to electricity and hydrogen, Appl Catal B 210 (2017) 235–254. https://doi.org/10.1016/j.apcatb.2017.03.067.

[10] P. Arunachalam, K. Nagai, M.S. Amer, M.A. Ghanem, R.J. Ramalingam, A.M. Al-Mayouf, Recent Developments in the Use of Heterogeneous Semiconductor Photocatalyst Based Materials for a Visible-Light-Induced Water-Splitting System—A Brief Review, Catalysts 11 (2021) 160. https://doi.org/10.3390/catal11020160.

[11] L. Wang, W. Si, X. Hou, M. Wang, X. Liu, Y. Ye, F. Hou, J. Liang, Novel integrated strategies toward efficient and stable unassisted photoelectrochemical water splitting, Sustainable Materials and Technologies 25 (2020) e00209. https://doi.org/10.1016/j.susmat.2020.e00209.

[12] L. Wang, Y. Tong, J. Feng, J. Hou, J. Li, X. Hou, J. Liang, G-C_3N_4-based films: A rising star for photoelectrochemical water splitting, Sustainable Materials and Technologies 19 (2019) e00089. https://doi.org/10.1016/j.susmat.2018.e00089.

[13] A. FUJISHIMA, K. HONDA, Electrochemical Photolysis of Water at a Semiconductor Electrode, Nature 238 (1972) 37–38. https://doi.org/10.1038/238037a0.

[14] X. Zhang, S. Zhang, X. Cui, W. Zhou, W. Cao, D. Cheng, Y. Sun, Recent Advances in TiO_2-based Photoanodes for Photoelectrochemical Water Splitting, Chem Asian J 17 (2022). https://doi.org/10.1002/asia.202200668.

[15] M. Meng, C. Li, J. Li, J. Wu, Y. Feng, L. Sun, H. Yuan, K. Liu, 3D TiO_2 nanotube arrays with anatase-rutile phase junction and oxygen vacancies for promoted photoelectrochemical water splitting, J Phys D Appl Phys 56 (2023) 055502. https://doi.org/10.1088/1361-6463/acade9.

[16] S.-W. Lin, M.-H. Tong, Y.-X. Chen, R. Chen, H.-P. Zhao, X. Jiang, K. Yang, C.-Z. Lu, CeO_2/TiO_2 Heterojunction Nanotube Arrays for Highly Efficient Visible-Light Photoelectrochemical Water Splitting, ACS Appl Energy Mater 6 (2023) 1093–1102. https://doi.org/10.1021/acsaem.2c03723.

[17] X.-C. Dai, M.-H. Huang, Y.-B. Li, T. Li, B.-B. Zhang, Y. He, G. Xiao, F.-X. Xiao, Regulating spatial charge transfer over intrinsically ultrathin-carbon-encapsulated photoanodes toward solar water splitting, J Mater Chem A Mater 7 (2019) 2741–2753. https://doi.org/10.1039/C8TA10379H.

[18] L. Zheng, X. Ye, X. Deng, Y. Wang, Y. Zhao, X. Shi, H. Zheng, Black Phosphorus Quantum Dot-Sensitized TiO_2 Nanotube Arrays with Enriched Oxygen Vacancies for Efficient Photoelectrochemical Water Splitting, ACS Sustain Chem Eng 8 (2020) 15906–15914. https://doi.org/10.1021/acssuschemeng.0c04819.

[19] A. Thakur, P. Kumar, S. Bagchi, R.K. Sinha, P. Devi, Green synthesized plasmonic nanostructure decorated TiO_2 nanofibers for photoelectrochemical hydrogen production, Solar Energy 193 (2019) 715–723. https://doi.org/10.1016/j.solener.2019.10.022.

[20] H.-S. Sajjadizadeh, H. Ahmadzadeh, E.K. Goharshadi, M. Aziznezhad, Engineering of a high-efficiency water splitting photoanode by synergistic effects of doping, compositing, and coupling on TiO_2 nanoparticles, Electrochim Acta 362 (2020) 137149. https://doi.org/10.1016/j.electacta.2020.137149.

[21] Q. Yi, S. Cong, H. Wang, X. Zhou, J. Chen, K. Li, Y. Liu, J.-M. Lee, Heterostructure-Induced Light Absorption and Charge-Transfer Optimization of a TiO_2 Photoanode for Photoelectrochemical Water Splitting, ACS Appl Energy Mater 4 (2021) 14440–14446. https://doi.org/10.1021/acsaem.1c03112.

[22] Y. Zhang, Y. Lei, T. Zhu, Z. Li, S. Xu, J. Huang, X. Li, W. Cai, Y. Lai, X. Bao, Surface plasmon resonance metal-coupled biomass carbon modified TiO_2 nanorods for photoelectrochemical water splitting, Chin J Chem Eng 41 (2022) 403–411. https://doi.org/10.1016/j.cjche.2021.10.022.

[23] S. Huo, Y. Wu, C. Zhao, F. Yu, J. Fang, Y. Yang, Core–Shell TiO_2 @Au_{25} /TiO_2 Nanowire Arrays Photoanode for Efficient Photoelectrochemical Full Water Splitting, Ind Eng Chem Res 59 (2020) 14224–14233. https://doi.org/10.1021/acs.iecr.0c02119.

[24] M. Ye, J. Gong, Y. Lai, C. Lin, Z. Lin, High-Efficiency Photoelectrocatalytic Hydrogen Generation Enabled by Palladium Quantum Dots-Sensitized TiO_2 Nanotube Arrays, J Am Chem Soc 134 (2012) 15720–15723. https://doi.org/10.1021/ja307449z.

[25] K. Arifin, R.M. Yunus, L.J. Minggu, M.B. Kassim, Improvement of TiO_2 nanotubes for photoelectrochemical water splitting: Review, Int J Hydrogen Energy 46 (2021) 4998–5024. https://doi.org/10.1016/j.ijhydene.2020.11.063.

[26] K. Inoue, A. Matsuda, G. Kawamura, Tube length optimization of titania nanotube array for efficient photoelectrochemical water splitting, Sci Rep 13 (2023) 103. https://doi.org/10.1038/s41598-022-27278-5.

[27] O. Abdelkarim, A. Mirzaei, G.S. Selopal, A. Yurtsever, G. Bassioni, Z.M. Wang, M. Chaker, F. Rosei, Constructing quantum dots sensitized TiO_2 nanotube p-n heterojunction for

photoelectrochemical hydrogen generation, Chemical Engineering Journal 446 (2022) 137312. https://doi.org/10.1016/j.cej.2022.137312.
[28] W. Krengvirat, S. Sreekantan, A.-F.M. Noor, G. Kawamura, H. Muto, A. Matsuda, Single-step growth of carbon and potassium-embedded TiO_2 nanotube arrays for efficient photoelectrochemical hydrogen generation, Electrochim Acta 89 (2013) 585–593. https://doi.org/10.1016/j.electacta.2012.11.079.
[29] W. Krengvirat, S. Sreekantan, A.-F. Mohd Noor, N. Negishi, G. Kawamura, H. Muto, A. Matsuda, Low-temperature crystallization of TiO_2 nanotube arrays via hot water treatment and their photocatalytic properties under visible-light irradiation, Mater Chem Phys 137 (2013) 991–998. https://doi.org/10.1016/j.matchemphys.2012.11.013.
[30] W. Krengvirat, S. Sreekantan, A.-F. Mohd Noor, N. Negishi, S.Y. Oh, G. Kawamura, H. Muto, A. Matsuda, Carbon-incorporated TiO_2 photoelectrodes prepared via rapid-anodic oxidation for efficient visible-light hydrogen generation, Int J Hydrogen Energy 37 (2012) 10046–10056. https://doi.org/10.1016/j.ijhydene.2012.04.004.
[31] A. Matsuda, S. Sreekantan, W. Krengvirat, Well-aligned TiO_2 nanotube arrays for energy-related applications under solar irradiation, Journal of Asian Ceramic Societies 1 (2013) 203–219. https://doi.org/10.1016/j.jascer.2013.07.001.
[32] M.P. Kumar, R. Jagannathan, S. Ravichandran, Photoelectrochemical System for Unassisted High-Efficiency Water-Splitting Reactions Using N-Doped TiO_2 Nanotubes, Energy & Fuels 34 (2020) 9030–9036. https://doi.org/10.1021/acs.energyfuels.0c00634.
[33] G. Mohammadnezhad, M.M. Momeni, F. Nasiriani, Enhanced photoelectrochemical performance of tin oxide decorated tungsten oxide doped TiO_2 nanotube by electrodeposition for water splitting, Journal of Electroanalytical Chemistry 876 (2020) 114505. https://doi.org/10.1016/j.jelechem.2020.114505.
[34] T. Liu, C. Hu, M. Geng, S. Yuan, Z. Zhao, C. Kong, M. Sun, G. Yin, Fabrication of unique three-dimensional CdS nanosheets/TiO_2 nanosheets hierarchical heterostructure as photoelectrode for enhancing photoelectrochemical performance, J Cryst Growth 606 (2023) 127098. https://doi.org/10.1016/j.jcrysgro.2023.127098.
[35] F. Zhang, J. Liu, H. Yue, G. Cheng, X. Xue, Construction of g-C_3N_4 nanoparticles modified TiO_2 nanotube arrays with Z-scheme heterojunction for enhanced photoelectrochemical properties, J Mater Sci (2023). https://doi.org/10.1007/s10853-022-07730-7.
[36] W. Qi, N. Wang, X. Chen, H. Liang, Plasmon-assisted partially reduced TiO_2 nanotube arrays for photoelectrochemical water splitting, Mater Res Express 6 (2020) 1250h9. https://doi.org/10.1088/2053-1591/ab6d2a.
[37] K. Basu, H. Zhang, H. Zhao, S. Bhattacharya, F. Navarro-Pardo, P.K. Datta, L. Jin, S. Sun, F. Vetrone, F. Rosei, Highly stable photoelectrochemical cells for hydrogen production using a SnO_2–TiO_2/quantum dot heterostructured photoanode, Nanoscale 10 (2018) 15273–15284. https://doi.org/10.1039/C8NR02286K.
[38] A. Kongkanand, K. Tvrdy, K. Takechi, M. Kuno, P. V. Kamat, Quantum Dot Solar Cells. Tuning Photoresponse through Size and Shape Control of CdSe−TiO_2 Architecture, J Am Chem Soc 130 (2008) 4007–4015. https://doi.org/10.1021/ja0782706.
[39] J.-Y. Kim, J. Yang, J.H. Yu, W. Baek, C.-H. Lee, H.J. Son, T. Hyeon, M.J. Ko, Highly Efficient Copper–Indium–Selenide Quantum Dot Solar Cells: Suppression of Carrier Recombination by Controlled ZnS Overlayers, ACS Nano 9 (2015) 11286–11295. https://doi.org/10.1021/acsnano.5b04917.

[40] J.-Y. Kim, W. Baek, S. Kim, G. Kang, I.K. Han, T. Hyeon, M. Park, Moisture proof hole transport layers based on CISe quantum dots for highly stable and large active area perovskite solar cells, Appl Surf Sci 496 (2019) 143610. https://doi.org/10.1016/j.apsusc.2019.143610.

[41] Y. Yan, R.W. Crisp, J. Gu, B.D. Chernomordik, G.F. Pach, A.R. Marshall, J.A. Turner, M.C. Beard, Multiple exciton generation for photoelectrochemical hydrogen evolution reactions with quantum yields exceeding 100%, Nat Energy 2 (2017) 17052. https://doi.org/10.1038/nenergy.2017.52.

[42] G. Liu, X. Wang, B. Liu, G. Han, W. Jiang, Y. Zhang, H. Zhao, Band engineering enables highly efficient and stable photoelectrochemical hydrogen evolution, Chemical Engineering Journal 450 (2022) 137813. https://doi.org/10.1016/j.cej.2022.137813.

[43] M.M. Abouelela, M.S. Sayed, G. Kawamura, W.K. Tan, A. Matsuda, Enhancing the photoelectrochemical performance of ZnO nanopagoda photoanode through sensitization with Ag and Ag2S NPs co-deposition, Mater Chem Phys 305 (2023) 127984. https://doi.org/10.1016/j.matchemphys.2023.127984.

[44] X. Wang, Y. Zhang, J. Li, G. Liu, M. Gao, S. Ren, B. Liu, L. Zhang, G. Han, J. Yu, H. Zhao, F. Rosei, Platinum Cluster/Carbon Quantum Dots Derived Graphene Heterostructured Carbon Nanofibers for Efficient and Durable Solar-Driven Electrochemical Hydrogen Evolution, Small Methods 6 (2022). https://doi.org/10.1002/smtd.202101470.

[45] J. Liu, S. Yue, H. Zhang, C. Wang, D. Barba, F. Vidal, S. Sun, Z.M. Wang, J. Bao, H. Zhao, G.S. Selopal, F. Rosei, Efficient Photoelectrochemical Hydrogen Generation Using Eco-Friendly "Giant" InP/ZnSe Core/Shell Quantum Dots, ACS Appl Mater Interfaces 15 (2023) 34797–34808. https://doi.org/10.1021/acsami.3c04900.

[46] N. Manh Hung, V. Thi Bich, N. Duc Quang, N. Tien Hiep, C. V. Nguyen, S. Majumder, P. Tien Hung, P. Dinh Hoat, N. Van Hoang, N. Minh Hieu, T.D. Nguyen, CuS–CdS@TiO_2 multi-heterostructure-based photoelectrode for highly efficient photoelectrochemical water splitting, Ceram Int 49 (2023) 23796–23804. https://doi.org/10.1016/j.ceramint.2023.04.220.

[47] L. Jin, J. Liu, X. Liu, D. Benetti, G.S. Selopal, X. Tong, E. Hamzehpoor, F. Li, D.F. Perepichka, Z.M. Wang, F. Rosei, Rational Control of Near-Infrared Colloidal Thick-Shell Eco-Friendly Quantum Dots for Solar Energy Conversion, Small Methods (2023). https://doi.org/10.1002/smtd.202300133.

[48] L. Jin, H. Zhao, D. Ma, A. Vomiero, F. Rosei, Dynamics of semiconducting nanocrystal uptake into mesoporous TiO_2 thick films by electrophoretic deposition, J Mater Chem A Mater 3 (2015) 847–856. https://doi.org/10.1039/C4TA05549G.

[49] L. Jin, H. Zhao, Z.M. Wang, F. Rosei, Quantum Dots-Based Photoelectrochemical Hydrogen Evolution from Water Splitting, Adv Energy Mater 11 (2021) 2003233. https://doi.org/10.1002/aenm.202003233.

[50] H. Kim, A. Choe, S.B. Ha, G.M. Narejo, S.W. Koo, J.S. Han, W. Chung, J. Kim, J. Yang, S. In, Quantum Dots, Passivation Layer and Cocatalysts for Enhanced Photoelectrochemical Hydrogen Production, ChemSusChem 16 (2023). https://doi.org/10.1002/cssc.202201925.

[51] M. Mohamed Abouelela, G. Kawamura, A. Matsuda, Metal chalcogenide-based photoelectrodes for photoelectrochemical water splitting, Journal of Energy Chemistry 73 (2022) 189–213. https://doi.org/10.1016/j.jechem.2022.05.022.

[52] J.-W. Seo, S.-B. Ha, I.-C. Song, J.-Y. Kim, PbS Quantum Dots-Decorated $BiVO_4$ Photoanodes for Highly Efficient Photoelectrochemical Hydrogen Production, Nanomaterials 13 (2023) 799. https://doi.org/10.3390/nano13050799.

[53] D. V. Freitas, J.R. González-Moya, T.A.S. Soares, R.R. Silva, D.M. Oliveira, H.S. Mansur, G. Machado, M. Navarro, Enhanced Visible-Light Photoelectrochemical Conversion on TiO_2 Nanotubes with Bi_2S_3 Quantum Dots Obtained by in Situ Electrochemical Method, ACS Appl Energy Mater 1 (2018) 3636–3645. https://doi.org/10.1021/acsaem.8b00375.

[54] M.M. Abouelela, G. Kawamura, W.K. Tan, A. Matsuda, Anodic nanoporous WO_3 modified with Bi2S3 quantum dots as a photoanode for photoelectrochemical water splitting, J Colloid Interface Sci 629 (2023) 958–970. https://doi.org/10.1016/j.jcis.2022.09.041.

[55] P. Subramanyam, B. Meena, D. Suryakala, C. Subrahmanyam, TiO_2 Photoanodes Sensitized with Bi_2Se_3 Nanoflowers for Visible–Near-Infrared Photoelectrochemical Water Splitting, ACS Appl Nano Mater 4 (2021) 739–745. https://doi.org/10.1021/acsanm.0c03041.

[56] A.C. Mendhe, P. Babar, P. Koinkar, B.R. Sankapal, Process optimization for decoration of Bi2Se3 nanoparticles on CdS nanowires: Twofold power conversion solar cell efficiency, J Taiwan Inst Chem Eng 133 (2022) 104251. https://doi.org/10.1016/j.jtice.2022.104251.

[57] N.F. Patel, S.A. Bhakhar, H.S. Jagani, G.K. Solanki, P.M. Pataniya, Synthesis, characterization and optoelectronic application of Bi_2Se_3 thin film prepared by thermal evaporation technique, Opt Mater (Amst) 136 (2023) 113403. https://doi.org/10.1016/j.optmat.2022.113403.

[58] A. Abdolhay, A. Kashaninia, M. Banihashemi, Effect of a Metal–Semiconductor Hetero Nanostructure of Cu/Bi_2Se_3 on Optical Properties of Perovskite Solar Cells, Physica Status Solidi (b) (2023) 2200482. https://doi.org/10.1002/pssb.202200482.

[59] G. Kawamura, K. Oura, W.K. Tan, T. Goto, Y. Nakamura, D. Yokoe, F.L. Deepak, K. El Hajraoui, X. Wei, M. Inoue, H. Muto, K. Yamaguchi, A.R. Boccaccini, A. Matsuda, Nanotube array-based barium titanate–cobalt ferrite composite film for affordable magnetoelectric multiferroics, J Mater Chem C Mater 7 (2019) 10066–10072. https://doi.org/10.1039/C9TC02442E.

[60] H. Mirabolghasemi, N. Liu, K. Lee, P. Schmuki, Formation of 'single walled' TiO_2 nanotubes with significantly enhanced electronic properties for higher efficiency dye-sensitized solar cells, Chemical Communications 49 (2013) 2067. https://doi.org/10.1039/c3cc38793c.

[61] W. Bai, Y. Zhou, G. Peng, J. Wang, A. Li, P.F.-X. Corvini, Engineering efficient hole transport layer Ferrihydrite-MXene on $BiVO_4$ photoanodes for photoelectrochemical water splitting: Work function and conductivity regulated, Appl Catal B 315 (2022) 121606. https://doi.org/10.1016/j.apcatb.2022.121606.

[62] X. Wei, P.S. Nbelayim, G. Kawamura, H. Muto, A. Matsuda, Ag nanoparticle-filled TiO_2 nanotube arrays prepared by anodization and electrophoretic deposition for dye-sensitized solar cells, Nanotechnology 28 (2017) 135207. https://doi.org/10.1088/1361-6528/aa5f11.

[63] S. Gautam, V. Aggarwal, B. Singh, V.P.S. Awana, R. Ganesan, S.S. Kushvaha, Signature of weak-antilocalization in sputtered topological insulator Bi_2Se_3 thin films with varying thickness, Sci Rep 12 (2022) 9770. https://doi.org/10.1038/s41598-022-13600-8.

[64] L. Gao, H. Li, W. Ren, G. Wang, H. Li, Z. Zhou, H. Ji, X. Niu, Z. Wang, Patterning Bi_2Se_3 single-crystalline thin films on Si(111) substrates using strong oxidizing acids, RSC Adv 7 (2017) 32294–32299. https://doi.org/10.1039/C7RA05317G.

[65] Y. Xin, Z. Li, W. Wu, B. Fu, Z. Zhang, Pyrite FeS_2 Sensitized TiO_2 Nanotube Photoanode for Boosting Near-Infrared Light Photoelectrochemical Water Splitting, ACS Sustain Chem Eng 4 (2016) 6659–6667. https://doi.org/10.1021/acssuschemeng.6b01533.
[66] P. Makuła, M. Pacia, W. Macyk, How To Correctly Determine the Band Gap Energy of Modified Semiconductor Photocatalysts Based on UV–Vis Spectra, J Phys Chem Lett 9 (2018) 6814–6817. https://doi.org/10.1021/acs.jpclett.8b02892.

Chapter 6. General Conclusions

In this thesis, we focused on improving the PEC performance of metal oxide semiconductors through two pathways; (1) plasmonic metal NPs doping. (2) heterojunction with MCs QDs materials which have narrow bandgap energy. Chapters 1 to 6 illustrated a general overview about PEC-WS technology and various studies for developing efficient photoelectrodes and their application for PEC-WS as follows;

Chapter 1

This chapter explains an overview about the PEC-WS technique and substance requirements to achieve high PEC efficiency.

Chapter 2

ANPor WO_3 was successfully grown on a W sheet through an anodization process, followed by heterojunction formation with Bi_2S_3 QDs using SILAR procedure, and investigated for PEC-WS. The ANPor WO_3/Bi_2S_3 QDs (10) photoanode achieved the highest photocurrent density of 16.28 mA cm^{-2} at 0.95 V vs. RHE, which is ~ 19 folds higher than that of pure ANPor WO_3 (0.85 mA cm^{-2}). Additionally, it displayed a maximum photoconversion efficiency of 4.1% at 0.66 V vs. RHE and formed 3.59 mmol of H_2 after 5 h. This was attributed to the suitable deposited quantity and uniform distribution of Bi_2S_3 QDs on the WO_3 surface. Furthermore, the ANPor WO_3/Bi_2S_3 QDs (10) heterojunction demonstrated higher Vis light absorption capability, higher charge density, and lower charge transfer resistance than pure ANPor WO_3 verified by UV–Vis DRS, M-S, and EIS results respectively. This significantly improved PEC-WS performance was also due to the generation of type-II heterojunction between ANPor WO_3 and Bi_2S_3 QDs, ameliorating the e^-/h^+ pairs separation and mobility.

Chapter 3

A facile and efficient procedure for synthesizing distinct ZnO NPGs by an aqueous chemical downward technique was developed. Subsequently, ZnO NPGs were decorated with various amounts of Ag NPs using the SILAR procedure. The quantity of Ag NPs was controlled

by adjusting the number of SILAR cycles (2, 4, 6, 8, and 10). The quantity of Ag NPs deposited on the surface of ZnO NPGs substantially affected the PEC performance. The ZnO NPGs/Ag NPs photoanode with an optimum eight cycles deposition of Ag NPs demonstrated the highest photocurrent of 2.15 mA cm^{-2} at 1.23 V vs RHE and remarkably boosted the photoconversion efficiency. The hot electrons transfer from Ag NPs to the CB of ZnO NPGs under Vis light due to the LSPR effect. The enhanced PEC performance using ZnO NPGs/Ag NPs photoanode was attributed to the following reasons: (1) the unique superstructure characteristics of ZnO NPGs that increased scattering, enhanced light absorption, and inhibited e^-/h^+ pairs recombination. (2) The deposition of plasmonic Ag NPs ameliorated the interfacial mobility of charge carriers between photoelectrode and electrolyte, as well as enhanced the Vis light response owing to their LSPR effect.

Chapter 4

The unique morphology of ZnO NPGs was decorated with different quantities of Ag-Ag_2S NPs utilizing the SILAR procedure. The morphological investigation revealed that the deposited amount of Ag-Ag_2S NPs on the surface of ZnO NPGs raised with the number of SILAR cycles and covered the whole ZnO NPGs' surface and edges, keeping them grainy and rough. The deposited quantity of Ag-Ag_2S NPs on ZnO NPGs considerably influenced the PEC performance. The deposition of 8 SILAR cycles of Ag-Ag_2S NPs on ZnO NPGs attained the maximum photocurrent of 2.91 mA cm^{-2} at 1.23 V vs. RHE, five folds greater than pristine ZnO NPGs. Moreover, it exhibited the highest ABPE of 0.43% at 0.6 V vs. RHE. This boosted PEC efficiency was assigned to the vital role of co-deposited Ag and Ag_2S NPs, which synergistically increased Vis light absorption and ameliorated e^-/h^+ pairs separation that inhibited their recombination.

Chapter 5

TNTAs were successfully grown on a Ti sheet through two steps anodization process and decorated with different quantities of Bi_2Se_3 QDs using the SILAR procedure to construct TNTAs/Bi_2Se_3 QDs heterojunction composite. STEM-EDX study disclosed the homogeneous dispersion of Bi_2Se_3 QDs with particle size less than 2 nm on TNTAs walls. Additionally, the PL spectra clarified that the efficiency of e^-/h^+ pairs separation was improved by increasing the SILAR

cycles of Bi_2Se_3 QDs. The type II heterojunction generated at the TNTAs/Bi_2Se_3 QDs interface enhanced the PEC performance and H_2 production. The TNTAs/Bi_2Se_3 QDs (2) photoanode attained the highest photocurrent density of 1.75 mA cm^{-2}, which is 3.8 folds higher than pure TNTAs (0.46 mA cm^{-2}) at 1.23 V vs. RHE. The ABPE and IPCE of the TNTAs/Bi_2Se_3 QDs (2) photoanode were significantly enhanced compared with those of pure TNTAs. The M-S plots manifested that the E_{fb} of TNTAs/Bi_2Se_3 QDs (2) negatively shifted remarkably compared with that of pure TNTAs, proving that the efficient mobility of e^-/h^+ pairs enhanced the PEC performance. The EIS measurement revealed that TNTAs/Bi_2Se_3 QDs (2) have lower R_{ct} (47.72 Ω) than pure TNTAs (5400 Ω) which implied the improvement of e^-/h^+ pairs separation and mobility after the deposition Bi_2Se_3 QDs. TNTAs/Bi_2Se_3 QDs (2) extended the light response to the Vis zone (up to 800 nm) and boosted the H_2 production amount of 355.8 µmol after 5 hours; this quantity is ~ 3.3 folds greater than pure TNTAs (105.3 µmol) at 1.23 V vs. RHE. Moreover, the TNTAs/Bi_2Se_3 QDs (2) photoanode exhibited excellent stability for PEC performance over 7 hours. Several characterizations disclosed the main causes for improving the PEC performance and H_2 production using TNTAs/Bi_2Se_3 QDs photoanode as follows; (1) the enhanced Vis light absorption assigned to the deposited Bi_2Se_3 QDs, (2) the rise of charge carrier density and the reduction of the E_{fb}, and (3) the decline of the charge transfer resistance and facile charge mobility.

Future perspectives

1- Design hybrid (organic and inorganic) photoelectrodes to absorb a wide range of solar spectrum, demonstrate high stability, and achieve high photoconversion efficiency.
2- Exploring semiconductors with quantum structures to ameliorate charge carrier separation/mobility and reduce charge recombination rate by quantum confinement.

Acknowledgment

First of all, all praise to Allah SWT, and the prophet Muhammad SAW. I am grateful to Allah SWT who has given me the grace and strength to reach this point and achieve my goal.

I would like to express my deepest gratitude to the Egyptian Cultural Affairs and Missions' Sector, Ministry of Higher Education, Egypt for giving me the PhD scholarship and financial support.

I would like to deeply thank my supervisor Professor Atsunori Matsuda from the Department of Electrical and Electronic Information Engineering, Toyohashi University of Technology for his consistent support and whose knowledge of the topic and insight guided me during all stages of research. His guidance, unwavering support, and encouragement have been invaluable throughout this work.

I want to express my sincere gratitude and appreciation to my supervisor Associate Professor Go Kawamura from the Department of Electrical and Electronic Information Engineering, Toyohashi University of Technology who has been incredibly kind and helpful in giving me advice, suggestions, guidance, and valuable time during the experimental work and writing process of this dissertation.

I would like to express my gratitude toward Professor Takanori Mizushima from the Department of Applied Chemistry and Life Science, Toyohashi University of Technology for his invaluable contribution as the reviewer and examiner of my dissertation defense. His rigorous evaluation, insightful suggestions, and constructive comments have increased my knowledge and improved the quality of my research.

I would like to thank my supervisor Associate Professor Tan Wai Kian from the Institute of Liberal Arts and Science, Toyohashi University of Technology for his dedicated support, guidance, thoughtful comments, and recommendations during the experimental work and writing process for this dissertation. The meetings and conversations with my three supervisors were beneficial in motivating me to think creatively, from multiple perspectives to improve my research plan. I would like to extend my heartfelt appreciation to my three supervisors for their kind assistance beyond the scope of research. They played a vital role in facilitating my academic journey and life with my kids in Japan.

I would like to express my gratitude towards Professor Hiroyuki Muto, Dr. Jin Nishida, Dr. Kazuhiro Hikima, Ms. Reiko Matsuda, Dr. Atsushi Yokoi, and Ms. Masayo Takahashi from the

Department of Electrical and Electronic Information Engineering, Toyohashi University of Technology, for their unconditional help, providing advice for analysis and enabled this research to be possible.

I would also like to thank my colleagues, Keiichiro Maegawa, Radian Febi Indrawan, Mohamed Hamada Mohamed Abdelkodous, Inoue Kazuki, and Irine Yunhafita Malya for providing me with a lot of assistance during the experimental work and discussions.

I would like to express my deepest appreciation and thanks to all members of the laboratories of Professor Matsuda and Associate Professor Kawamura, colleagues, and friends who gave me guidance, support, and assistance in completing this dissertation.

I would like to express my gratitude towards laboratory secretary Chifumi Iwase and previous secretary Ms. Mayumi Ookawara For their hard work and kind help.

I would like to thank all members of the Petrochemical Technology Laboratory, from the Petrochemical Department, Egyptian Petroleum Research Institute, Egypt, especially, Professor Fatma Zakaria, Professor Abdelrahman Mohamed Rabie, and Assistant Professor Amr Hussien Mady for their generosity, and encouragement, as well as without their support I would not have been able to reach this point.

I am indebted to my colleague Mustafa Saad from the Analysis and Evaluation Department, Egyptian Petroleum Research Institute, Egypt for guidance, advice, and kind assistance during the photoelectrochemical measurements.

Special thanks to my beloved parents, my sisters & brother for their endless loving support, encouragement, and prayers in all stages of my study. Lastly, I want to express my gratitude to my husband Ahmed Gamal, my son Omar, and my daughter Khadija for their moral support and inspiration in helping me to complete this dissertation.

Marwa Mohamed Mohamed Abouelela

List of Publications

[1] M.M. Abouelela, G. Kawamura, A. Matsuda, A review on plasmonic nanoparticle-semiconductor photocatalysts for water splitting, J Clean Prod 294 (2021) 126200. https://doi.org/10.1016/j.jclepro.2021.126200.

[2] M. Mohamed Abouelela, G. Kawamura, A. Matsuda, Metal chalcogenide-based photoelectrodes for photoelectrochemical water splitting, Journal of Energy Chemistry 73 (2022) 189–213. https://doi.org/10.1016/j.jechem.2022.05.022.

[3] M.M. Abouelela, G. Kawamura, W.K. Tan, A. Matsuda, Anodic nanoporous WO_3 modified with Bi_2S_3 quantum dots as a photoanode for photoelectrochemical water splitting, J Colloid Interface Sci 629 (2023) 958–970. https://doi.org/10.1016/j.jcis.2022.09.041.

[4] M.M. Abouelela, M.S. Sayed, G. Kawamura, W.K. Tan, A. Matsuda, Enhancing the photoelectrochemical performance of ZnO nanopagoda photoanode through sensitization with Ag and Ag_2S NPs co-deposition, Mater Chem Phys 305 (2023) 127984. https://doi.org/10.1016/j.matchemphys.2023.127984.

[5] M.M. Abouelela, K. Inoue, G. Kawamura, W.K. Tan, A. Matsuda, Heterojunction of TiO_2 nanotubes arrays/Bi_2Se_3 quantum dots as an effective and stable photoanode for photoelectrochemical H_2 generation, Sustainable Materials and Technologies 38 (2023) e00718. https://doi.org/10.1016/j.susmat.2023.e00718.

[6] M.M. Abouelela, G. Kawamura, W.K. Tan, M. Amiruldin, K. Maegawa, J. Nishida, A. Matsuda, Ag nanoparticles decorated ZnO nanopagodas for Photoelectrochemical application, Electrochem Commun 158 (2024) 107645. https://doi.org/10.1016/j.elecom.2023.107645.